

Diss. ETH No. 27011

Associated Higgs Boson Production at NNLO QCD

A thesis submitted to attain the degree of
Doctor of Sciences of ETH Zurich
(Dr. sc. ETH Zurich)

presented by

Imre Majer

MSc ETH, ETH Zurich

born on 09.10.1989

citizen of Hungary

accepted on the recommendation of

Prof. Dr. A. Gehrmann–De Ridder,	examiner
Prof. Dr. C. Anastasiou,	co-examiner
Prof. Dr. S. Pozzorini,	co-examiner

2020

Declaration of Originality

I hereby confirm that I have not submitted the material presented in this thesis for any other degree at this or at any other university.

The results presented in this dissertation have been obtained in collaboration with my supervisor Prof. Dr. Aude Gehrmann–De Ridder, and primarily three other members of the NNLOJET collaboration: Dr. Rhorry Gauld, Prof. Dr. Nigel Glover, and Dr. Alexander Huss.

Chapter 1 relies mostly on the publication

- [1] Gauld, R. and Gehrmann-De Ridder, A. and Glover, E.W.N. and Huss, A. and Majer, I. “Associated production of a Higgs boson decaying into bottom quarks and a weak vector boson decaying leptonically at NNLO in QCD.” *JHEP* 10 (2019), p. 002. DOI: [10.1007/JHEP10\(2019\)002](https://doi.org/10.1007/JHEP10(2019)002). arXiv: [1907.05836](https://arxiv.org/abs/1907.05836) [hep-ph].

The research work presented in Chapter 2 is the object of the forthcoming publication:

- [2] Gauld, R. and Gehrmann-De Ridder, A. and Glover, E.W.N. and Huss, A. and Majer, I. “NNLO predictions for WH plus jet production at LHC (in preparation).” 2020

Finally, most of the work presented in Chapter 3 has been extensively used to obtain results presented in

- [3] Gauld, R. and Gehrmann-De Ridder, A. and Glover, E.W. N. and Huss, A. and Majer, I. “Predictions for Z-boson production in association with a b-jet at $\mathcal{O}(\alpha_s^3)$ ” (May 2020). arXiv: [2005.03016](https://arxiv.org/abs/2005.03016) [hep-ph].

Abstract

In this dissertation, I will present the calculation of next-to-next-to-leading order perturbative QCD corrections to the production of a Higgs boson in association with a leptonically decaying weak vector boson: $pp \rightarrow V(\rightarrow \ell\bar{\ell}) + H + X$ with $V = W^\pm$ and $V = Z$. Two subclasses of the processes are considered in two subsequent chapters:

- 1 The Higgs boson decays as $H \rightarrow b\bar{b}$ to a bottom quark–antiquark pair with no additional restrictions on X . NNLO QCD corrections are also included in the decay, which is identified by requiring at least two b-jets among the final states.
- 2 The Higgs boson is produced on shell and X must contain at least one single unflavoured hadronic jet.

A fully differential calculation is attained in both cases by implementing the processes into the parton-level event generator NNLOJET, using the antenna subtraction formalism to regulate infrared singularities. Numerical predictions for fiducial cross sections and differential distributions at 13 TeV LHC collision energies are presented for both associated Higgs production classes. In most cases, the inclusion of NNLO corrections leads to a clear stabilization of the predictions and they contribute substantially to the reduction of residual theoretical uncertainties inherent to perturbative calculations.

Lastly, the implementation of a brand new flavour-tagging layer into NNLOJET is considered in a separate chapter. This was quintessential for identifying b-jets and computing flavour-sensitive jet observables for LHC processes at NNLO precision in QCD.

Abrégé

Dans cette thèse de doctorat, je compte présenter le calcul de corrections perturbatives de second ordre (NNLO) survenant dans le cadre de la théorie de la chromodynamique quantique (QCD) et liées à la production d'un boson de Higgs associé à un boson caractérisant l'interaction faible et se désintégrant en leptons : $pp \rightarrow V(\rightarrow \ell\bar{\ell}) + H + X$ avec $V = W^\pm$ et $V = Z$.

Dans les deux chapitres à venir, je considérerai deux catégories de réactions :

- 1 Le boson de Higgs se désintègre en une paire de bottom–anti-bottom quarks et aucune autre restriction sur la nature de X n'est appliquée. Dans ce cas, les corrections perturbatives de second ordre (NNLO) sont considérés également dans le processus de désintégration du boson de Higgs qui est lui même identifié par la présence d'au moins deux jets contenant un quark bottom dans l'état final de la réaction considérée.
- 2 Le boson de Higgs est produit sur sa couche de masse (on-shell) et l'état final (X) doit au moins contenir un jet hadronique dont la saveur (flavour) n'est pas déterminée.

Dans les deux cas, un calcul entièrement différentiel est effectué en utilisant le formalisme de subtraction appelé : antenna subtraction nécessaire au traitement des singularités infra-rouges et considéré dans le cadre du contexte théorique appelé : NNLOJET. Ce calcul est réalisé à l'aide d'un code numérique, simulant les évènements au niveau des partons intervenant dans les réactions de particules élémentaires. Des prédictions numériques pour les sections efficaces et distributions différentielles sont ainsi obtenues et présentées pour ces deux types de réactions liées à la production d'un boson de Higgs au LHC et correspondant à des énergies de collisions de 13 TeV. Dans la plus part des cas, l'inclusion de corrections perturbatives de second ordre conduit à une claire stabilisation des prédictions et contribue à une nette réduction des incertitudes théoriques résiduelles et inhérentes aux calculs perturbatifs.

Finalement, le développement et l'intégration d'une toute nouvelle méthode de traçage de la saveur des partons dans le code NNLOJET est considérée dans un chapitre à part. Cette méthode, permettant l'identification des jets contenant un quark de saveur particulière est essentielle à la réalisation des calculs mentionnés précédemment ainsi que pour le calcul de toute quantité physique au LHC incluant des corrections perturbatives de second ordre et impliquant la production de jets hadroniques dont la saveur du quark présent dans ceux-ci est bien déterminée.

Acknowledgments

First and foremost, I wish to express my gratitude to my supervisor Prof. Dr. Aude Gehrmann–De Ridder for her regular feedback and constructive guidance that helped me finish and publish my research projects. Thanks to her, I had the opportunity to present my work in conferences all over the world and experience being part of the international NNLOJET collaboration. Special thanks to Rhorry Gauld and Alexander Huss from the collaboration, without whom I would not have progressed this far and the projects certainly would not have reached their fruitful completion. Monday beers (and Tuesday regrets) with them were a special highlight of my doctoral years I will not forget.

I also want to thank Xuan Chen, Juan Cruz-Martinez, James Currie, Thomas Gehrmann, Nigel Glover, Marius Höfer, Tom Morgan, Jonathan Mo, Jan Niehues, João Pires, Duncan Walker, and James Whitehead for useful discussions and their many contributions to the NNLOJET code. Furthermore, I would also like to express my thanks to Jonas Lindert for his swift and invaluable assistance on OpenLoops.

Finally, I want to thank Antal Martinecz for the absolutely awesome times we always end up having wherever we meet, Ryuta Yoshimatsu for the fun and interesting sauna and running sessions, and last but not least, Christian Somody and Simon Gyllenhammar for the life-defining trips we had during my doctoral years. Thank you guys!

Contents

Introduction	21
1 Associated Higgs Boson Production	25
1.1 Process Introduction	26
1.2 General Framework	28
1.3 Leading Order	30
1.3.1 Leading-Order Production $d\sigma_{VH}^B(1_q, 2_{\bar{q}}; 3_\ell, 4_{\bar{\ell}})$	31
1.3.2 No Momentum Conservation	33
1.3.3 Leading-Order Decay $d\sigma_{H\rightarrow b\bar{b}}^B(i_b, j_{\bar{b}})$	35
1.4 Next-to-Leading Order	36
1.4.1 Real Production $d\sigma_{VH}^R(1, 2, 3; 4_\ell, 5_{\bar{\ell}})$	38
1.4.2 Virtual Production $d\sigma_{VH}^V(1_q, 2_{\bar{q}}; 3_\ell, 4_{\bar{\ell}})$	41
1.4.3 Real Decay $d\sigma_{H\rightarrow b\bar{b}}^R(i_b, j_g, k_{\bar{b}})$	43
1.4.4 Virtual Decay $d\sigma_{H\rightarrow b\bar{b}}^V(i_b, j_{\bar{b}})$	44
1.5 Next-to-Next-to-Leading Order	46
1.5.1 Double-Real Production $d\sigma_{VH}^{RR}(1, 2, 3, 4; 5_\ell, 6_{\bar{\ell}})$	48
1.5.2 Real-Virtual Production $d\sigma_{VH}^{RV}(1, 2, 3; 4_\ell, 5_{\bar{\ell}})$	54
1.5.3 Double-Virtual Production $d\sigma_{VH}^{VV}(1, 2; 3_\ell, 4_{\bar{\ell}})$	58
1.5.4 Double-Real Decay $d\sigma_{H\rightarrow b\bar{b}}^{RR}(i_b, j, k, l_{\bar{b}})$	61
1.5.5 Real-Virtual Decay $d\sigma_{H\rightarrow b\bar{b}}^{RV}(i_b, j_g, k_{\bar{b}})$	65
1.5.6 Double-Virtual Decay $d\sigma_{H\rightarrow b\bar{b}}^{VV}(i_b, k_{\bar{b}})$	66
1.6 Jet Clustering for the VH Process	69
1.7 Numerical Results	70

TABLE OF CONTENTS

1.7.1	General Setup	70
1.7.2	Fiducial Cross Section	71
1.7.3	Scale Variations	74
1.7.4	Distributions	78
1.8	Summary and Conclusions	79
2	Associated Higgs Boson Plus Jet Production	85
2.1	Process Background	86
2.2	General Framework	86
2.3	Next-to-Next-to-Leading Order	89
2.3.1	Double-Real Cross Section	90
2.3.2	Real-Virtual Cross Section	102
2.3.3	Double-Virtual Cross Section	109
2.4	Numerical Results	112
2.4.1	General Setup	112
2.4.2	Fiducial Cross Sections	112
2.4.3	Distributions	113
2.5	Summary and Outlook	114
3	Flavour Tagging	119
3.1	Introduction	120
3.2	Flavoured Jet Algorithm	122
3.3	Flavour Dressing	124
3.4	Implementation	126
3.4.1	Driver	126
3.4.2	Autogeneration	134
3.5	Summary	137
	Closing Thoughts	139
A	Amplitudes	141
A.1	$B_0^{V,0}$	142
A.2	$B_1^{V,0}$	143

A.3	$B_0^{V,1}$	143
A.4	$B_2^{V,0}$	144
A.5	$C_0^{V,0}$	145
A.6	$D_0^{V,0}$	146
A.7	$B_1^{V,1}$ and $B_1^{V,2}$	147
A.8	$B_1^{VH,1top}$	149
A.9	$B_0^{V,2}$	151
A.10	$B_3^{V,0}$	151
A.11	$B_0^{H,0}$	154
A.12	$B_1^{H,0}$	154
A.13	$B_0^{H,1}$	155
A.14	$C_0^{H,0}$	155
A.15	$D_0^{H,0}$	156
A.16	$B_1^{H,1}$	156
A.17	$B_0^{H,2}$	157
B Effects of Even-Tag Exclusion		159

List of Figures

1.1	Associated Higgs Boson Production with $H \rightarrow b\bar{b}$ Decay	29
1.2	Leading-Order VH Production	31
1.3	Leading-Order $H \rightarrow b\bar{b}$ Decay	34
1.4	Real VH Production	38
1.5	SNLO Subtraction for VH Production	39
1.6	SNLO Spike Tests for VH Production	40
1.7	Virtual VH Production	41
1.8	Real $H \rightarrow b\bar{b}$ Decay	43
1.9	SNLO Subtraction for $H \rightarrow b\bar{b}$ Decay	44
1.10	SNLO $H \rightarrow b\bar{b}$ Spike Tests	45
1.11	Virtual $H \rightarrow b\bar{b}$ Decay	46
1.12	Double-Real VH Production	48
1.13	S Spike Tests for VH Production	55
1.14	Real-Virtual VH Production	56
1.15	Excluded Real-Virtual VH Top Loops	57
1.16	T Spike Tests for VH Production	58
1.17	Double-Virtual VH Production	59
1.18	Double-Virtual VH Top Loops	60
1.19	Excluded Double-Virtual VH Top Loops	61
1.20	Double-Real $H \rightarrow b\bar{b}$ Decay	62
1.21	S Spike Tests for $H \rightarrow b\bar{b}$ Decay	64
1.22	Real-Virtual $H \rightarrow b\bar{b}$ Decay	65
1.23	T Spike Tests for $H \rightarrow b\bar{b}$ Decay	67

LIST OF FIGURES

1.24	Double-Virtual $H \rightarrow b\bar{b}$ Decay	68
1.25	W^+H Scale Variations	81
1.26	W^+H Distributions	82
1.27	W^-H Distributions	83
1.28	ZH Distributions	84
2.1	Double-Real VH +jet Production	90
2.2	S Spike Tests for VH +jet Production	101
2.3	Real-Virtual VH +jet Production	102
2.4	T Spike Tests for VH +jet Production	109
2.5	Double-Virtual VH +jet Production	110
2.6	Double-Virtual VH Top Loops	111
2.7	W^+H +jet Distributions	116
2.8	W^-H +jet Distributions	117
3.1	Flavour Storage Scheme in NNLOJET	135
3.2	Flavour Autogeneration Strategy in NNLOJET	138
B.1	Effect of Even-Tag Exclusion on W^+H Distributions	160

List of Tables

1.1	VH Fiducial Cross Sections	71
1.2	Scaled VH Fiducial Cross Sections	73
2.1	W^+H +jet Fiducial Cross Sections	113
B.1	Effect of Even-Tag Exclusion on the W^+H Fiducial Cross Section	159

List of Snippets

3.1	Number of Subprocesses	127
3.2	Flavour Dressing	128
3.3	Autogenerated Subtraction Term	130
3.4	Flavour Tagging in <code>qcdnorm</code>	132
3.5	Matrix Element Library	135
3.6	Flavour List of Reduced Matrix Elements	136

Introduction

I have been working on a theory aspect of high-energy physics where one of many primary goals is to be able to produce precise predictions that are directly comparable to experiments, which in this field usually mean collider experiments, specifically, as far as this thesis is concerned, proton–proton collisions performed at the Large Hadron Collider (LHC) located in Switzerland and France.

According to the current overall status of the field as of 2020, most of the crucial theoretical predictions of the Standard Model of particle physics [4] have been confirmed by various experiments. The LHC has played a major role in validating core predictions of the Standard Model, a prime example of this is the discovery of the Higgs boson, which was the last missing particle of the Standard Model back in 2012. Due to cosmological and theoretical considerations [5], the Standard Model is ruled out as a final theory, therefore a major goal of the collider experiments is to find evidence for physics beyond the Standard Model. Despite all the effort, no striking new discovery has been made in recent years, for example in the form of a new particle previously not predicted by the Standard Model. Currently there are only tensions with respect to the predictions, which have only been observed in a few cases that need more confirmation.

A discovery of a new particle is usually made by identifying a clear resonance pattern in a differential distribution of an observable quantity. The evident lack of such a clear signal brought about continued efforts in precision physics, since effects beyond the Standard Model might manifest in various other small systematic deviations than just a clear resonance signal. For example, systematic deviations might appear if collision energies are insufficient and the resonance pattern lies just barely outside the range of detection, or if the new resonance is too wide to identify it clearly, etc. The key point is that if the theoretical predictions are not precise enough then systematic deviations might fall within the uncertainty of the calculations, making them very difficult to detect.

Observables in collider experiments are often expressed via cross sections: either differential in one or more variables or integrated over the fiducial region of the detector surrounding

the particle collision site. Without delving into detailed derivations of the basics of Quantum Chromodynamics [6] (QCD) and collider physics, let us review the core concepts that are required for the work presented in the upcoming chapters of the thesis.

The renormalized cross-section element [7] of a proton–proton collision can be written as

$$d\sigma = \sum_{a,b} \int \frac{d\xi_1}{\xi_1} \frac{d\xi_2}{\xi_2} f_{a/p_1}(\xi_1, \mu_F) f_{b/p_2}(\xi_2, \mu_F) d\hat{\sigma}_{ab}(\alpha_s(\mu_R), \mu_F, \mu_R). \quad (1)$$

The factorized partonic cross section for partons (i.e. quarks and gluons) a and b from protons p_1 and p_2 is defined as $d\hat{\sigma}_{ab}$, the parton distribution functions (PDFs) of parton c from proton p_i is labeled as f_{c/p_i} , the momentum fractions ξ_i carried by the partons are integrated over, and finally we have to perform a sum for all contributing partonic channels (a, b =quarks, antiquarks, gluons) where there is a valid (nonzero) partonic cross section.

This thesis focuses on perturbative calculations in QCD, i.e. expansions of the partonic cross section in the strong coupling constant α_s as

$$d\hat{\sigma}_{ab} = d\hat{\sigma}_{ab}^{(0)} + \left(\frac{\alpha_s}{2\pi}\right) d\hat{\sigma}_{ab}^{(1)} + \left(\frac{\alpha_s}{2\pi}\right)^2 d\hat{\sigma}_{ab}^{(2)} + \left(\frac{\alpha_s}{2\pi}\right)^3 d\hat{\sigma}_{ab}^{(3)} + \mathcal{O}(\alpha_s^4). \quad (2)$$

Consequently, we talk about leading-order (LO), next-to-leading order (NLO), and next-to-next-to-leading order (NNLO) cross sections, depending on up to how many orders the partonic cross section is included in eq. (2). The leading-order, or in other words the Born cross section, includes all underlying partonic cross sections associated with minimally describing the process in question. Higher order cross sections include radiative and virtual corrections, manifesting in extra partonic emissions and the inclusion of loops in the underlying Feynman diagrams. An all-order calculation would not depend on the factorization (μ_F) or renormalization (μ_R) scales, but due to the finite truncation of the perturbative series, such a dependence is unavoidable. Nevertheless, it is expected that the magnitude of this dependence reduces as higher orders are included in the calculation. The theoretical uncertainty of the prediction is usually associated with the change in value of the cross section when manually varying the factorization and renormalization scales. Therefore higher-order predictions come hand-in-hand with a better handle on the theoretical uncertainties, enabling more accurate comparisons to experimental data.

The excellent precision of the LHC experiments nowadays necessitates the inclusion of perturbative QCD corrections at least up to NNLO but often to even higher orders for a meaningful comparison between theory predictions and experiments. However, these calculations come at the price of exponentially increasing computational complexity both on the

analytical and numerical sides. At higher perturbative orders one faces two basic obstacles:

- the ever-increasing number of Feynman loop amplitudes carrying ultraviolet and infrared divergences are more and more demanding to evaluate;
- the additional partonic radiation can involve soft or collinear partons that lead to complex infrared structures in loop and tree-level amplitudes.

These divergences cannot be handled numerically and require complex evaluation schemes to get rid of. The effort of many collaborations are focused on methodically tackling and automating these obstacles so that higher-order predictions for collider physics may become more accessible.

Doctoral Research

During my PhD program I was part of the NNLOJET collaboration, a collaboration built-around the NNLOJET framework that specializes in systematically treating the aforementioned radiative infrared singularities arising in higher-order amplitudes up to NNLO precision. While there exist various slicing and subtraction techniques that handle these infrared divergences, the primary choice of the NNLOJET collaboration is *antenna subtraction*, detailed in a plethora of publications [8–16]. As its name suggests, it is a subtraction technique that captures and subtracts the infrared divergences with so-called antenna functions, leaving the amplitudes that build-up the cross section divergence-free and ready for numerical evaluation. The antenna function only depends on the number and type of partons involved in an infrared configuration, essentially making them universal building blocks for a subtraction scheme that is applicable to many different processes that occur during proton–proton collisions at the LHC. As long as the relevant loop amplitudes are known, antenna subtraction opens up the way to achieving NNLO predictions for a variety of physical processes.

All QCD antenna functions have been calculated and implemented into the *multiprocess parton-level event generator* software called NNLOJET, sharing the name with that of the framework and collaboration. The main focus of my research was on developing this software to extend its predictive powers to new types of processes. The research projects I worked on can be separated into three well-defined, yet interdependent pieces that I will address in three different chapters of this thesis. These are

- 1 **Associated Higgs Boson Production:** an implementation of the parton-level process up to NNLO precision where a Higgs boson is created in association with a leptonically decaying vector boson and the Higgs boson itself decays into a bottom–antibottom

quark pair. I will give a detailed introduction describing the importance and relevance of this process, then I will recount the elements of the calculation within the NNLOJET framework, including the clustering process of flavoured (bottom-tagged) jets used to identify the decay of the Higgs boson. Lastly, I will present and validate results in the form of fiducial cross sections and differential distributions.

- 2 **Associated Higgs Boson Plus Jet Production:** this is an extension of the previous project where we additionally require a resolved hard jet among the produced final states. I will also describe the relevance and implementation up to a NNLO precision before presenting the results, again in the form of fiducial cross sections and a few selected differential distributions. A difference compared to the previous project is that decays of the Higgs boson are not included and numerical results will only be shown for the case when the associated gauge boson in question is either the charged W^+ or W^- boson.
- 3 **Flavour Tagging:** a core infrastructural update to NNLOJET that enabled particle-collision simulations for cases when we wish to detect flavoured particles among the produced final states. It was an essential upgrade that made it possible to calculate flavour-dependent differential observables for associated Higgs and Z plus b-jet productions [3], but it is also a layer that is generic enough to be invoked for any processes already implemented into NNLOJET. As this is a completely new feature of the software, I will go into details of the under-the-hood workings of the implementation besides the theoretical background. From the phenomenological perspective, parts of this chapter can be considered an addendum but nevertheless it resulted in one of the biggest changes in the codebase of NNLOJET and occupied a large portion of my work as a doctoral student. Therefore, I intend for this chapter to act not only as part of the report on my doctoral research but also as a reference manual on flavour tagging in NNLOJET. I believe this will also be useful for other members of the NNLOJET collaboration who wish to understand and perhaps further extend it in the future.

Chapter 1

Associated Higgs Boson Production

In this chapter, I intend to describe the details of the implementation that went into producing NNLO predictions of observables related to the production of a Higgs boson in association with a leptonically decaying charged (W^\pm) or neutral (Z) vector boson. I will focus on the new work I added myself but as the implementation is done in the NNLOJET framework, the introduction of some established elements are required for a consistent context. Throughout this chapter, I will use excerpts from ref. [1], my publication with other members of the NNLOJET collaboration on associated Higgs production. The excerpts are often modified to fit the logical flow of this thesis better.

Firstly, I will introduce the experimental relevance and the current theory status of associated Higgs boson production with $H \rightarrow b\bar{b}$ decay in Section 1.1. Next, I will move on to describing the general framework of our theoretical predictions in Section 1.2. I will enumerate all the ingredients that went into calculating the cross sections at leading order, next-to-leading order, and next-to-next-to leading order through Sections 1.3–1.5. In these chapters I will heavily rely on the notational conventions of the NNLOJET framework, especially for the amplitudes and subtraction terms concerned. I will discuss the amplitudes we included in our prediction in detail but also mention those that we omitted due to negligible numerical contributions. While the theoretical background and technical implementation of flavour tagging in NNLOJET is the main topic of Chapter 3, the framework for identifying b-jets in VH production is immediately relevant in this chapter before we can move onto the discussion of numerical results. A brief discourse specifically concerning flavour-tagging characteristics of the VH process will already be the main topic of Section 1.6 of this chapter. The remaining Section 1.7 will present and analyze the numerical results acquired from NNLOJET. The numerical setup for the simulations is presented in Section 1.7.1, the resulting fiducial cross sections in Section 1.7.2, along with their analysis on renormalization scale

dependence in 1.7.3. Lastly, I will present and discuss a few selected differential distributions in Section 1.7.4 before concluding and summarizing this chapter in Section 1.8.

1.1 Process Introduction

One of the highest priorities of the LHC physics program is the detailed exploration of the mechanism of electroweak symmetry breaking that predicts the existence of the Higgs boson and its interactions with the fermions and gauge bosons of the Standard Model. In July 2012, the ATLAS and CMS Collaborations at the LHC reported the discovery of a resonance with a mass close to 125 GeV [17, 18]. At the current level of accuracy, the discovered particle is consistent with the Standard Model Higgs boson but the limited precision of some of the measurements still leaves room for possible alternative interpretations. Measurements of various properties of the Higgs boson have been carried out since then. One of the main goals of the completed Run II at $\sqrt{s} = 13$ TeV and the future Run III at $\sqrt{s} = 14$ TeV of the LHC is to test the coupling strength of the discovered Higgs-like particle to known SM particles through the study of a variety of processes at increased luminosity and collisions energies.

At LHC energies the VH processes are the third ($W^\pm H$) and fourth (ZH) largest production channels after the dominant gluon–gluon and vector-boson fusion ones. These Higgs production modes probe the gauge boson–Higgs vertex (VVH) separately for the charged W^\pm and neutral Z bosons. Moreover, a particularly relevant feature of associated Higgs production is the possibility to study the Higgs boson’s decay into a pair of bottom–antibottom quarks. Via this decay, it is possible to directly measure the Higgs boson’s coupling to fermions, thereby testing the mechanism of fermion mass generation in the Standard Model. Furthermore, since this decay mode dominates the total width of the Higgs boson, the uncertainty on this branching ratio enters into other studies as well, for instance in measurements of the decay of the Higgs boson to invisible final states, which are relevant for dark-matter searches [19]. Such a decay is hard to measure in inclusive Higgs production through the leading production modes like the gluon–gluon or vector-boson fusion channels due to the presence of enormous QCD backgrounds. In associated Higgs production, the presence of a vector boson decaying leptonically provides a clean experimental signature, which means experimental analyses looking for a $H \rightarrow b\bar{b}$ decay have a manageable background.

Direct searches for the Standard Model Higgs boson through VH production and $H \rightarrow b\bar{b}$ decay have been carried out at the LHC at center-of-mass energies of 7 TeV, 8 TeV, and 13 TeV. While the use of Run I data at $\sqrt{s} = 7$ TeV and 8 TeV by the ATLAS and CMS Collaborations was not able to firmly establish the discovery of a Standard Model Higgs

boson through this channel [20, 21], the use of Run II data at $\sqrt{s} = 13$ TeV enabled to do so. In 2017, The LHC experiments [22, 23] announced the observation of a Standard Model Higgs-like particle decaying to a pair of bottom–antibottom quarks precisely through these *VH* channels, with a significance of 5.6 and 5.3 standard deviations for CMS and ATLAS respectively. First differential measurements concerning a simplified template cross section as a function of the transverse momentum of the vector boson have been reported in ref. [24] and updated most recently with considerable reduction of the experimental uncertainty in ref. [25].

In view of prospective measurements of associated Higgs production including data from Run II and III at the LHC, it is important to have precise theoretical predictions for cross sections and differential distributions in the kinematic regimes probed by the experiments. This includes, in particular, taking QCD effects into account in both the production and decay. The present status of theoretical predictions for observables related to *VH* production with the vector boson decaying leptonically and the Higgs boson decaying into a bottom–antibottom quark pair can be summarized as follows:

The total inclusive cross section for associated *VH* production is known at NNLO QCD precision. It is available through the numerical program *VH@NNLO* [26] whose ingredients have been reported in refs. [27, 28]. The electroweak corrections to the total cross section are known at NLO [29, 30]. Differential distributions have also been computed at NNLO QCD, including the computation of $H \rightarrow b\bar{b}$ decay at different orders. In refs. [31–33], the Higgs decay has been included at NLO while it is included up to NNLO in refs. [34, 35]. In addition, for massless bottom quarks, the fully differential decay rate for $H \rightarrow b\bar{b}$ known so far at NNLO QCD [36, 37] has recently been computed at N³LO accuracy in ref. [38], although jet flavour is not identified in this calculation. Furthermore, a differential computation at NNLO QCD of this Higgs decay rate using massive bottom quarks has been performed in [39]. The combination of fixed-order QCD computations with parton showers has also been the subject of phenomenological studies in refs. [40–42].

Fully differential NNLO predictions for *VH* observables obtained via the combination of Higgs production and decay to bottom–antibottom processes have been presented in ref. [34] for W^+H and ZH and in ref. [35] for $V = W^-H$. These computations have essential features in common: at parton level, both consider massless bottom quarks except for the Higgs Yukawa coupling and use the same flavour- k_t algorithm [43] to define b-jets. Furthermore, the Higgs decay is treated in the narrow-width approximation and the Higgs Yukawa coupling y_b is computed at fixed scale $\mu_R^{\text{dec.}} = m_H$. Renormalization and factorization scale variations are only considered in the production subprocess, using the central scale choice $\mu_R^{\text{prod.}} = \mu_F^{\text{prod.}} = M_{VH}$, the dynamical mass of the *VH* system.

The aforementioned computations differ instead in the theoretical framework employed to regulate infrared divergences at NNLO level: in ref. [34] the q_T -subtraction formalism [44] is used for the VH production cross section combined with the CoLoRFulNNLO subtraction method [45] for the $H \rightarrow b\bar{b}$ decay. In ref. [35] the nested soft-collinear subtraction scheme [46, 47] is used—an extension of the residue subtraction scheme [48]—in both production and decay subprocesses.

The aim of this thesis is to present fully differential computations of VH observables for all three processes, i.e. $V = W^+, W^-$ and Z, including NNLO corrections to both production and decay. These are calculated using the antenna subtraction formalism [8–16] via the NNLOJET framework [49].

1.2 General Framework

In this section, I will present the main ingredients that enter the calculation. The collision process we consider is $pp \rightarrow VH + X$, where the vector boson further decays as $V \rightarrow \ell\bar{\ell}$ and the Higgs boson as $H \rightarrow b\bar{b}$. The X in both the production and the Higgs decay side indicates the possibility of additional partonic emissions that can be recombined into final-state jets. In all cases, we demand the process to always produce at least two hard b-jets as part of its definition, because phenomenologically this identifies the Higgs boson. Two basic configurations at different orders of α_s are depicted diagrammatically in Figure 1.1.

The NNLO QCD observables include radiative (real) and loop (virtual) corrections up to $\mathcal{O}(\alpha_s^2)$ in both production and decay subprocesses. The cross section element at $\mathcal{O}(\alpha_s^k)$ can be expressed in the factorized form

$$d\sigma_{\text{N}^k\text{LO}} = \sum_{\substack{i,j=0 \\ i+j \leq k}}^k \int \frac{d^d p_H}{(2\pi)^d} d\sigma_{\text{VH}}^{(i)} \times d\sigma_{\text{H} \rightarrow b\bar{b}}^{(j)} \mathcal{J}_{2_b}. \quad (1.1)$$

The term $d\sigma_{\text{VH}}^{(i)}$ corresponds to the production part at $\mathcal{O}(\alpha_s^i)$ and encompasses the matrix elements and Lorentz-invariant phase-space elements for the creation of a leptonically decaying vector boson and an on-shell Higgs boson. The term denoted by $d\sigma_{\text{H} \rightarrow b\bar{b}}^{(j)}$ corresponds to the decay part at $\mathcal{O}(\alpha_s^j)$ and includes the Higgs propagator connecting the production to the decay and matrix elements and phase space for the subsequent decay of the Higgs boson to a bottom-antibottom quark pair. The decay does not contain initial states, therefore it does not involve any convolution with PDFs, such as the one shown in eq. (1). This factorized form does not allow crosstalk between the production and decay subprocesses, in other

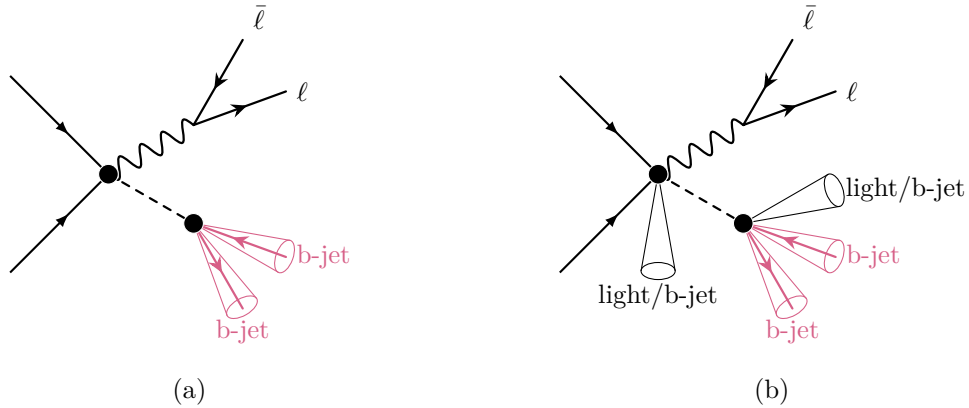


Figure 1.1: Possible event configurations for associated Higgs boson production. The arrows on the left in (a) represent incoming partons sampled from the colliding protons, the wavy and dashed lines indicate the vector and Higgs bosons, respectively. The former decays into a lepton–antilepton pair, while the latter into a pair of bottom–antibottom quarks. The presence of at least two hard b-jets is always demanded but higher order corrections can bring about additional emissions, resulting in additional jets. For example, at NNLO, i.e. $\mathcal{O}(\alpha_s^2)$, the configuration (b) is permitted, where multiple b-jets and/or light jets can be emitted from both the production and decay sides.

words there are no amplitudes describing interference between them. This is a reasonable approximation due to the extremely narrow decay width of the Higgs boson.

While the matrix elements and phase-space factors factorize as production \times decay and are encapsulated in their respective subprocess cross sections, overall momentum conservation must be demanded on the entire process level. This is ensured by the term $\int d^d p_H / (2\pi)^d$ in eq. (1.1) which will connect the phase spaces via the momentum of the Higgs boson. I would note at this point that all final-state quarks and leptons are considered massless, which is a reasonable approximation at energies as high as $\sqrt{s} = 13$ TeV. The jet function \mathcal{J}_{2_b} is responsible for assembling at least two b-jets in the final state and it is a non-factorizable term because we have to allow the jet algorithm to recombine radiated partons into final-state jets, regardless of whether they are emitted from production or decay sides. In fact, identifying flavoured jets needed major infrastructural changes in NNLOJET which I will describe in Chapter 3. As the number of particles at each order varies for real and virtual corrections, \mathcal{J}_{2_b} in eq. (1.1) is merely a shorthand notation whose exact form depends on each subcontribution. This will be indicated precisely while investigating the cross sections at each order in Sections 1.3 through 1.5.

In the aforementioned sections, I will go through all the amplitudes and subtraction terms needed for the NNLO calculation order-by-order, while introducing the workings of

the NNLOJET framework whenever needed. I will rely heavily on the notations and conventions used in the NNLOJET framework in order to directly reflect the implementation of the calculation inside the codebase so that these sections can also be used as a documentation of all the work I did on the VH process. All amplitudes presented in the next few chapters have been independently validated against established particle-physics tools, such as MadGraph [50], MCFM 8 [51], and OpenLoops [52, 53], where it was possible.

1.3 Leading Order

The leading-order or Born cross section is built with contributions related to the underlying basic partonic processes that characterize the process under consideration. Beyond leading order, at higher orders in $\mathcal{O}(\alpha_s)$, additional partonic processes that possibly involve more partons will have to be taken into account to compute the cross section. Understanding all elements of a leading-order cross-section calculation is necessary before we can proceed to higher orders. Therefore this section will introduce all elements and guiding principles step-by-step, some of which will be important in efficiently constructing higher-order terms as well.

The leading-order cross section in the production \times decay framework outlined in Section 1.2 can be written as

$$d\sigma_{\text{LO}} = \int \frac{d^d p_{\text{H}}}{(2\pi)^d} d\sigma_{\text{VH}}^{(0)} \times d\sigma_{\text{H} \rightarrow \text{b}\bar{\text{b}}}^{(0)} \mathcal{J}_{2_{\text{b}}} \quad (1.2)$$

$$= \int \frac{d^d p_{\text{H}}}{(2\pi)^d} d\sigma_{\text{VH}}^{\text{B}}(\hat{1}_q, \hat{2}_{\bar{q}}; 3_{\ell}, 4_{\bar{\ell}}) \times d\sigma_{\text{H} \rightarrow \text{b}\bar{\text{b}}}^{\text{B}}(5_{\text{b}}, 6_{\bar{\text{b}}}) \mathcal{J}_{2_{\text{b}}}^{(2)}(5_{\text{b}}, 6_{\bar{\text{b}}}). \quad (1.3)$$

It has only a single Born production \times Born decay subcontribution. The arguments of the cross sections and the jet function are shorthand notations for particle momenta and flavour while the extra circumflex accents on the numbers indicate that the given particle is in the initial state. In the NNLOJET framework these are always numbered as particles 1 and 2. The jet function $\mathcal{J}_{2_{\text{b}}}^{(2)}$ has two QCD final-state partons available (indicated by the upper index) for flavoured jet reconstruction.

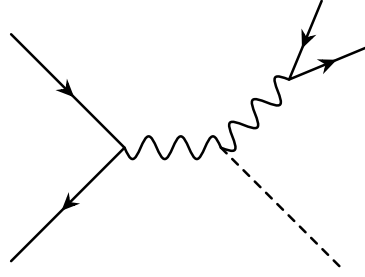


Figure 1.2: Leading-order VH production amplitude.

1.3.1 Leading-Order Production $d\sigma_{VH}^B(1_q, 2_{\bar{q}}; 3_\ell, 4_{\bar{\ell}})$

The leading-order or Born cross section for the production subprocess has only the contribution of the $q\bar{q}$ -initiated channel

$$d\hat{\sigma}_{VH,q\bar{q}}^B = \frac{\mathcal{N}_{VH}^B}{(2N_c)^2} d\Phi_2^{\text{prod.}}(p_1, p_2; p_3, p_4; p_H) B_0^{VH,0}(\hat{1}_q, \hat{2}_{\bar{q}}; 3_\ell, 4_{\bar{\ell}}). \quad (1.4)$$

The normalization factor \mathcal{N}_{VH}^B contains most of the constant factors that do not depend on the given kinematics. This can be separated into the normalization factor of the Drell–Yan (vector-boson production) process and an additional vector-boson–Higgs coupling according to

$$\mathcal{N}_{VH}^B = \mathcal{N}_V^B \lambda_{VH}^2 = \frac{1}{2s} (2\mathcal{C}_V)^2 N_c \lambda_{VH}^2, \quad (1.5)$$

where the vector-boson–fermion couplings are¹

$$\mathcal{C}_W = \frac{1}{2} \frac{4\pi\alpha}{\sin^2\theta_W} \quad \text{and} \quad \mathcal{C}_Z = \frac{4\pi\alpha}{\sin^2\theta_W \cos^2\theta_W} \quad (1.6)$$

and the vector-boson–Higgs couplings are

$$\lambda_{WWH} = m_W \sqrt{\frac{4\pi\alpha}{\sin^2\theta_W}} \quad \text{and} \quad \lambda_{ZZH} = m_Z \sqrt{\frac{4\pi\alpha}{\sin^2\theta_W \cos^2\theta_W}}, \quad (1.7)$$

for W^\pm and Z , respectively. The constants appearing are the electromagnetic fine-structure constant α , the Weinberg angle θ_W , the masses of the charged and neutral vector bosons m_W and m_Z , and finally the number of colours $N_c = 3$. The symbol s appearing in eq. (1.5) is

¹The part that is independent of the handedness in the Z case. The helicity-dependent factors are absorbed into the amplitude $B_0^{VH,0}$ as shown in eq. (A.11) of Appendix A.1.

the hadronic center-of-mass energy, therefore the factor $1/2s$ combines with the momentum fractions x_1 and x_2 in the PDF convolution (1) to yield the partonic flux factor.

The factor $1/(2N_c)^2$ in eq. (1.4) comes from averaging over the colours and spins of the incoming quarks as the detector is agnostic towards this information.

The phase-space notation chosen in eq. (1.4) is slightly unconventional in the NNLOJET framework. It is a two-particle phase-space element for the final-state massless leptons with a conservation term that allows momenta to flow out via p_H , the momentum of the Higgs boson. In general, this type of $(n - 2)$ -particle production phase space that we will use for higher production orders as well is written as

$$d\Phi_{n-2}^{\text{prod.}}(p_1, p_2; \{p_f\}_{f=3}^n; p_H) = \left[\prod_{f=3}^n \frac{d^{d-1}p_f}{(2\pi)^{d-1} 2E_f} \right] (2\pi)^d \delta^{(d)}(p_1 + p_2 - p_H - \sum_{f=3}^n p_f). \quad (1.8)$$

The phase space populated by the decay products of the Higgs boson is explicitly accounted for in the decay cross sections. Overall momentum conservation is taken care of by the integral over p_H during the assembly of the production and decay subprocess cross sections as seen in eq. (1.3).

The symbol $B_0^{VH,0}$ is the squared amplitude² describing this process. The only Feynman diagram contributing to it is depicted in Figure 1.2. The labeling of the amplitudes follows the conventions of the NNLOJET framework: a B -type amplitude has a single quark current; the upper index indicates the extra VH production and that 0 loops are present; the lower index marks the presence of 0 radiated gluons. The amplitude can be expanded as

$$B_0^{VH,0}(\hat{1}_q, \hat{2}_{\bar{q}}; 3_\ell, 4_{\bar{\ell}}) = |\mathcal{P}_V(s_{34})|^2 B_0^{V,0}(\hat{1}_q, \hat{2}_{\bar{q}}; 3_\ell, 4_{\bar{\ell}}), \quad (1.9)$$

where we separated the vector boson propagator

$$\mathcal{P}_V(s_{\ell\bar{\ell}}) = \frac{1}{s_{\ell\bar{\ell}} - m_V^2 + im_V\Gamma_V} \quad (1.10)$$

between the Higgs VVH and the lepton $V\ell\bar{\ell}$ vertices. The remaining term is the Drell–Yan amplitude $B_0^{V,0}$ found in Appendix A.1.

²Amplitudes in general mean real-valued squared amplitudes in the main body of the thesis even if the word “squared” is omitted. Complex-valued helicity amplitudes are only presented in Appendix A and they are consistently labelled with a calligraphic typeface.

1.3.2 No Momentum Conservation

One of the key ideas of this project was to formulate the production amplitudes and related cross sections in a way that are just extensions of the already fully implemented and validated Drell–Yan process in NNLOJET. At leading order, this deconstruction works trivially by the insertion of a gauge-boson propagator in eq. (1.9) and accounting for the difference in normalization factors due to the additional VVH coupling in eq. (1.5). This extension is possible owing to the scalar nature of the Higgs boson: spin correlations between the initial-state partons and the final-state leptons are not affected by the insertion of a Higgs vertex.

Furthermore, higher-order corrections in the production only affect initial-state QCD particles and therefore we can define Drell–Yan-like amplitudes similarly to eq. (1.9) at all orders accordingly, i.e.

$$M_{\text{DY-like}}^{VH}(\hat{1}, \hat{2}, 3, \dots; (n-1)_\ell, n_{\bar{\ell}}) = |\mathcal{P}_V(s_{\ell\bar{\ell}})|^2 M_{\text{nmc.}}^V(\hat{1}, \hat{2}, 3, \dots; (n-1)_\ell, n_{\bar{\ell}}). \quad (1.11)$$

These Drell–Yan-like amplitudes contribute to the bulk of the cross section up to NNLO precision. This is mainly because other contributions are simply not allowed until $\mathcal{O}(\alpha_s^2)$ —there are no contributing Feynman diagrams besides Drell–Yan-like ones at $\mathcal{O}(\alpha_s^0)$ and $\mathcal{O}(\alpha_s^1)$. Additional contributions related to closed fermion loops of top and bottom quarks become relevant at $\mathcal{O}(\alpha_s^2)$ and therefore we will recount them in the appropriate sections of NNLO production. Their numerical contribution however is only a small percentage of the Drell–Yan-like amplitudes, which makes the latter ones crucial and the cornerstone of this thesis.

These Drell–Yan-like amplitudes, however, have two important caveats and they are not equivalent to the amplitudes implemented for the actual Drell–Yan process. These distinguishing features are the following:

1. Momentum conservation between the initial- and final-state particles for Drell–Yan-like amplitudes is *not allowed* because momentum has to flow through the Higgs boson vertex, into the decay as well. The subscript “nmc.” in eq. (1.11) thus stands for “no momentum conservation”.

Generally speaking, utilizing momentum-conservation relations during the calculation of amplitudes allow for final formulæ with simpler analytic expressions. This simplification is a loss of information that cannot be reverse-engineered: besides being able to exploit the same generic properties as those of the conventional Drell–Yan helicity amplitudes, the non-momentum-conserving ones need to be derived anew.

Overall momentum conservation is guaranteed numerically on the entire process level at

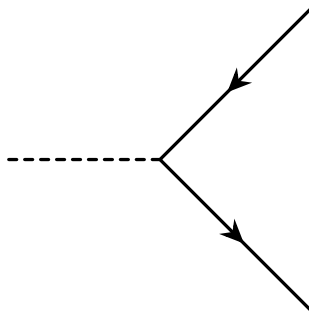


Figure 1.3: Leading-order $H \rightarrow b\bar{b}$ decay amplitude.

all orders. It is taken care of by integrating with respect to the Higgs boson momentum p_H as outlined for leading order in eq. (1.3).³

2. The Drell–Yan process is conventionally defined for a neutral current mediation of Z/γ^* bosons between the initial-state partons and final-state leptons. The Higgs boson however does not couple to photons, therefore we need to restrict the gauge boson to a Z only. For the sake of convenience, we also overload the term “Drell–Yan-like” to encompass charged current interactions of W^\pm mediators as well.

Although these aforementioned caveats require recalculating the amplitudes from near a priori considerations, the infrared structure of the non-momentum-conserving Drell–Yan-like amplitudes are identical to the regular Drell–Yan ones. This permits us to reuse all subtraction terms which were originally calculated and implemented for standard Drell–Yan production. I will introduce the basics of antenna subtraction in Section 1.4 where it will be apparent that subtraction terms are essentially constructed from universal antenna functions and reduced matrix elements, which are lower-order amplitudes of the same process. Consequently, swapping out the original Drell–Yan reduced matrix elements with their non-momentum-conserving counterparts makes the subtraction scheme of the Drell–Yan process readily available for VH production as well.

This fundamental concept behind the project naturally extends to VH +jet production as well, which will be the topic of the next chapter.

1.3.3 Leading-Order Decay $d\sigma_{H \rightarrow b\bar{b}}^B(i_b, j_{\bar{b}})$

As the $H \rightarrow b\bar{b}$ decay concerns only final states, there is always only a single channel, and naturally, no PDF convolution. The leading-order cross section for the $H \rightarrow b\bar{b}$ decay is

$$d\sigma_{H \rightarrow b\bar{b}}^{(0)} = d\sigma_{H \rightarrow b\bar{b}}^B = \mathcal{N}_{H \rightarrow b\bar{b}}^B d\Phi_2^{\text{dec.}}(p_H; p_i, p_j) \left| \mathcal{P}_H(p_H^2) \right|^2 B_0^{\text{H},0}(i_b, j_{\bar{b}}). \quad (1.12)$$

This decay will be attached to higher-order production cross sections as well, which could shift the particle numbering depending on the number of particles in the production subprocess. Consequently, instead of fixed alphanumeric shorthand notations for the momenta and flavour assignments of the decay particles, I am using generic Latin-character placeholders.

The normalization prefactor

$$\mathcal{N}_{H \rightarrow b\bar{b}}^B = N_c \mathcal{Y}_b^2 \quad \text{with} \quad \mathcal{Y}_b = \frac{\overline{m}_b(\mu_R^{\text{dec.}})}{2m_W} \sqrt{\frac{4\pi\alpha}{\sin^2\theta_W}} \quad (1.13)$$

contains the Yukawa coupling that gives rise to the Higgs–bottom-quark interaction, which can be expressed in terms of the mass of the b quark. The coupling—and therefore the mass \overline{m}_b —is subject to renormalization in the $\overline{\text{MS}}$ scheme, which is the scheme we used for higher-order virtual amplitudes as well. It thus depends on our choice for the renormalization scale $\mu_R^{\text{dec.}}$ of the decay.

Despite the presence of a non-zero $\overline{\text{MS}}$ mass in the Yukawa coupling, we still treat the bottom quarks as light quarks from the kinematic perspective, i.e. massless as far as the phase space and the amplitudes are concerned. The expression for the massless two-body decay phase space $d\Phi_2^{\text{dec.}}$ allows for momenta inflow via p_H . In general, such an n -body decay phase space is written as

$$d\Phi_2^{\text{dec.}}(p_H; p_{i_1}, \dots, p_{i_n}) = \left[\prod_{f=i_1}^{i_n} \frac{d^{d-1}p_f}{(2\pi)^{d-1} 2E_f} \right] (2\pi)^d \delta^{(d)}\left(p_H - \sum_{f=i_1}^{i_n} p_f\right). \quad (1.14)$$

The Higgs boson propagator

$$\mathcal{P}_H(s_H) = \frac{1}{s_H - m_H^2 + im_H\Gamma_H} \quad (1.15)$$

³In practice, it is manifest by appropriate phase-space sampling.

in eq. (1.12) is required to connect the production and decay subprocesses. As the Dirac delta in the phase space (1.14) implies, the Higgs momentum is always expressed as

$$p_H = \sum_{f=i_1}^{i_n} p_f \quad \text{and} \quad s_H = p_H^2. \quad (1.16)$$

At leading order this is just $s_H = 2p_i \cdot p_j$.

The only Feynman diagram contributing to the leading-order amplitude $B_0^{H,0}$ is shown in Figure 1.3 and given explicitly in Appendix A.11.

1.4 Next-to-Leading Order

The aim of this section is to go through all the elements in detail for a next-to-leading order calculation. First, I will write down the formula that assembles an NLO production \times decay cross section. Real corrections to production are found in Section 1.4.1, virtual corrections to production in Section 1.4.2. Sections 1.4.3 and 1.4.4 contain real and virtual corrections to the decay subprocess, respectively.

Through the detailed description of real and virtual subtraction terms in this section, we will confirm what I have already outlined previously in Section 1.3.2: it is indeed possible to recycle most elements of the regular Drell–Yan process when calculating subtraction terms for the production part. As these principles will hold at NNLO as well, I will not address production subtraction terms as thoroughly at $\mathcal{O}(\alpha_s^2)$ —converting them from ordinary Drell–Yan ones follows the exact same principles. Nevertheless, I think it is necessary to understand how this conversion is done and why it holds at a lower order, where the analytic expressions are more compact. Therefore, I will present all required elements here and build upon this when discussing formulation at NNLO in the next section.

The additional cross section at next-to-leading order—also called NLO coefficient—contains a combination of real and virtual cross sections from the production with the Born decay cross section and vice versa:

$$\begin{aligned} d\sigma_{\text{NLO coef.}} &= \int \frac{d^d p_H}{(2\pi)^d} \left[d\sigma_{VH}^{(1)} \times d\sigma_{H \rightarrow b\bar{b}}^{(0)} + d\sigma_{VH}^{(0)} \times d\sigma_{H \rightarrow b\bar{b}}^{(1)} \right] \mathcal{J}_{2_b} \quad (1.17) \\ &= \int \frac{d^d p_H}{(2\pi)^d} \left\{ \left(d\sigma_{VH}^R - d\sigma_{VH}^{\text{SNLO}} \right) \times d\sigma_{H \rightarrow b\bar{b}}^B \mathcal{J}_{2_b}^{(3)}(3; 6_b, 7_{\bar{b}}) \right. \\ &\quad \left. + \left(d\sigma_{VH}^V - d\sigma_{VH}^{\text{TNLO}} \right) \times d\sigma_{H \rightarrow b\bar{b}}^B \mathcal{J}_{2_b}^{(2)}(5_b, 6_{\bar{b}}) \right\} \end{aligned}$$

$$\begin{aligned}
& + d\sigma_{VH}^B \times \left(d\sigma_{H \rightarrow b\bar{b}}^R - d\sigma_{H \rightarrow b\bar{b}}^{\text{SNLO}} \right) \mathcal{J}_{2_b}^{(3)}(5_b, 6_g, 7_{\bar{b}}) \\
& + d\sigma_{VH}^B \times \left(d\sigma_{H \rightarrow b\bar{b}}^V - d\sigma_{H \rightarrow b\bar{b}}^{\text{TNLO}} \right) \mathcal{J}_{2_b}^{(2)}(5_b, 6_{\bar{b}}) \}. \quad (1.18)
\end{aligned}$$

The arguments indicating particle momenta and flavour are omitted for the cross sections and kept only for the jet functions for the sake of readability. The flavour of the particles is not indicated when it can take multiple values depending on the partonic channel and the amplitude, in which cases, the flavour association with the momenta is implicitly implied based on the amplitudes.

Both the real (R) and virtual (V) cross sections contain infrared singularities, which need to be regulated by the real (SNLO) and virtual (TNLO) subtraction terms, following the notational convention of antenna subtraction used in the NNLOJET framework. Upon integration over the appropriate particle phase spaces, these subtraction terms cancel, essentially helping the evaluation of the individual real or virtual subcontributions but not modifying the final integrated result:

$$\sigma = \int_{\Phi_{n+1}} d\sigma^R + \int_{\Phi_n} d\sigma^V = \int_{\Phi_{n+1}} \underbrace{\left(d\sigma^R - d\sigma^{\text{SNLO}} \right)}_{\text{infrared finite}} + \int_{\Phi_n} \underbrace{\left(d\sigma^V - d\sigma^{\text{TNLO}} \right)}_{\text{infrared finite}}. \quad (1.19)$$

This is due to the Kinoshita–Lee–Nauenberg (KLN) theorem that tells us that at a given perturbative order infrared divergences coming from loop integrals cancel with those coming from phase-space integrals.

Let us summarize the normalization factors at NLO before proceeding to the individual subcontributions.

$$\mathcal{N}_{VH}^R = \mathcal{N}_{VH}^B \left(\frac{\alpha_s N_c}{2\pi} \right) \frac{\bar{C}(\epsilon)}{C(\epsilon)}, \quad \mathcal{N}_{VH}^V = \mathcal{N}_{VH}^B \left(\frac{\alpha_s N_c}{2\pi} \right) \bar{C}(\epsilon), \quad (1.20)$$

$$\mathcal{N}_{H \rightarrow b\bar{b}}^R = \mathcal{N}_{H \rightarrow b\bar{b}}^B \left(\frac{\alpha_s N_c}{2\pi} \right) \frac{\bar{C}(\epsilon)}{C(\epsilon)}, \quad \mathcal{N}_{H \rightarrow b\bar{b}}^V = \mathcal{N}_{H \rightarrow b\bar{b}}^B \left(\frac{\alpha_s N_c}{2\pi} \right) \bar{C}(\epsilon), \quad (1.21)$$

with constants

$$\bar{C}(\epsilon) = (4\pi)^\epsilon e^{-\epsilon\gamma_E} \quad \text{and} \quad C(\epsilon) = \frac{\bar{C}(\epsilon)}{8\pi^2} \quad (1.22)$$

carrying the dimensional regularization parameter $d = 4 - 2\epsilon$ and the Euler–Mascheroni constant γ_E arising from the $\overline{\text{MS}}$ renormalization scheme.

A common feature of all appearing amplitudes at NLO is that the leading-colour ampli-

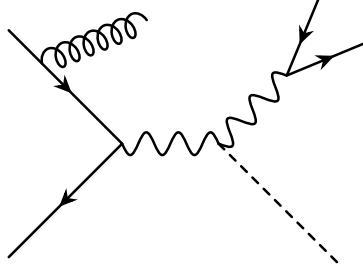


Figure 1.4: Real VH production amplitude.

tudes, which carry a prefactor 1, are equal to their subleading-colour counterparts, which carry a prefactor $1/N_c^2$. Therefore an overall prefactor $1 - \frac{1}{N_c^2}$ will be ubiquitous in front of all the amplitudes.

1.4.1 Real Production $d\sigma_{VH}^R(1, 2, 3; 4_\ell, 5_{\bar{\ell}})$

The production cross section now contains radiative corrections related to the emission of an additional gluon, which means that the production side has channels initiated by these gluons as well. The three partonic channels that contribute are

$$d\hat{\sigma}_{VH, q\bar{q}}^R = \frac{\mathcal{N}_{VH}^R \left(1 - \frac{1}{N_c^2}\right)}{(2N_c)^2} d\Phi_3^{\text{prod.}}(p_1, p_2; \{p_f\}_{f=3}^5; p_H) B_1^{VH,0}(\hat{1}_q, 3_g, \hat{2}_{\bar{q}}; 4_\ell, 5_{\bar{\ell}}), \quad (1.23)$$

$$d\hat{\sigma}_{VH, qg}^R = \frac{\mathcal{N}_{VH}^R \left(1 - \frac{1}{N_c^2}\right)}{(2N_c)[2(N_c^2 - 1)]} d\Phi_3^{\text{prod.}}(p_1, p_2; \{p_f\}_{f=3}^5; p_H) B_1^{VH,0}(\hat{1}_q, \hat{2}_g, 3_{\bar{q}}; 4_\ell, 5_{\bar{\ell}}), \quad (1.24)$$

$$d\hat{\sigma}_{VH, \bar{q}g}^R = \frac{\mathcal{N}_{VH}^R \left(1 - \frac{1}{N_c^2}\right)}{(2N_c)[2(N_c^2 - 1)]} d\Phi_3^{\text{prod.}}(p_1, p_2; \{p_f\}_{f=3}^5; p_H) B_1^{VH,0}(3_q, \hat{2}_g, \hat{1}_{\bar{q}}; 4_\ell, 5_{\bar{\ell}}). \quad (1.25)$$

The averaging factors in the denominators depend on the initial state and account for the two spin and N_c colour states of quarks; and the two polarization and $N_c^2 - 1$ colour states of gluons.

A Feynman diagram representing the amplitude $B_1^{VH,0}$ is shown in Figure 1.4 with its exact expression found in Appendix A.2.

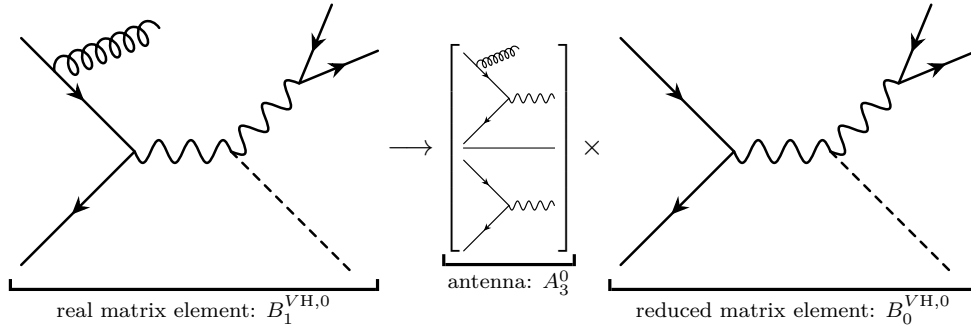


Figure 1.5: Structure of the SNLO VH production subtraction terms.

Subtraction Terms $d\sigma_{VH}^{\text{SNLO}}(1, 2, 3; 4_\ell, 5_{\bar{\ell}})$

The real subtraction terms for the production side, accompanying their respective real partonic cross-section channels are

$$d\hat{\sigma}_{VH, q\bar{q}}^{\text{SNLO}} = \frac{\mathcal{N}_{VH}^R \left(1 - \frac{1}{N_c^2}\right)}{(2N_c)^2} d\Phi_3^{\text{prod.}}(p_1, p_2; \{p_f\}_{f=3}^5; p_H) \text{qqbB1g}\theta\text{VHSNLO}(\hat{1}_q, 3_g, \hat{2}_{\bar{q}}; 4_\ell, 5_{\bar{\ell}}), \quad (1.26)$$

$$d\hat{\sigma}_{VH, qg}^{\text{SNLO}} = \frac{\mathcal{N}_{VH}^R \left(1 - \frac{1}{N_c^2}\right)}{(2N_c)[2(N_c^2 - 1)]} d\Phi_3^{\text{prod.}}(p_1, p_2; \{p_f\}_{f=3}^5; p_H) \text{qgB1g}\theta\text{VHSNLO}(\hat{1}_q, \hat{2}_g, 3_{\bar{q}}; 4_\ell, 5_{\bar{\ell}}), \quad (1.27)$$

$$d\hat{\sigma}_{VH, \bar{q}g}^{\text{SNLO}} = \frac{\mathcal{N}_{VH}^R \left(1 - \frac{1}{N_c^2}\right)}{(2N_c)[2(N_c^2 - 1)]} d\Phi_3^{\text{prod.}}(p_1, p_2; \{p_f\}_{f=3}^5; p_H) \text{qbgB1g}\theta\text{VHSNLO}(3_q, \hat{2}_g, \hat{1}_{\bar{q}}; 4_\ell, 5_{\bar{\ell}}). \quad (1.28)$$

The subtraction amplitudes indicated with monospace text are composed of antenna functions—which mimic the infrared structure of the corresponding real amplitude—and reduced matrix elements. Note that in the NNLOJET codebase these are present specifically for $V=Z$ or W but for the discussion here I am keeping the notation generic where possible. The subtraction amplitudes are

$$\text{qqbB1g}\theta\text{VHSNLO}(\hat{1}_q, 3_g, \hat{2}_{\bar{q}}; 4_\ell, 5_{\bar{\ell}}) = A_{3, q\bar{q}}^0(1, 3, 2) B_0^{VH,0}(\hat{1}_q, \hat{2}_{\bar{q}}, 4_\ell, 5_{\bar{\ell}}), \quad (1.29)$$

$$\text{qgB1g}\theta\text{VHSNLO}(\hat{1}_q, \hat{2}_g, 3_{\bar{q}}; 4_\ell, 5_{\bar{\ell}}) = -A_{3, qg \rightarrow q\bar{q}}^0(1, 2, 3) B_0^{VH,0}(\hat{1}_q, \hat{2}_{\bar{q}}, 4_\ell, 5_{\bar{\ell}}), \quad (1.30)$$

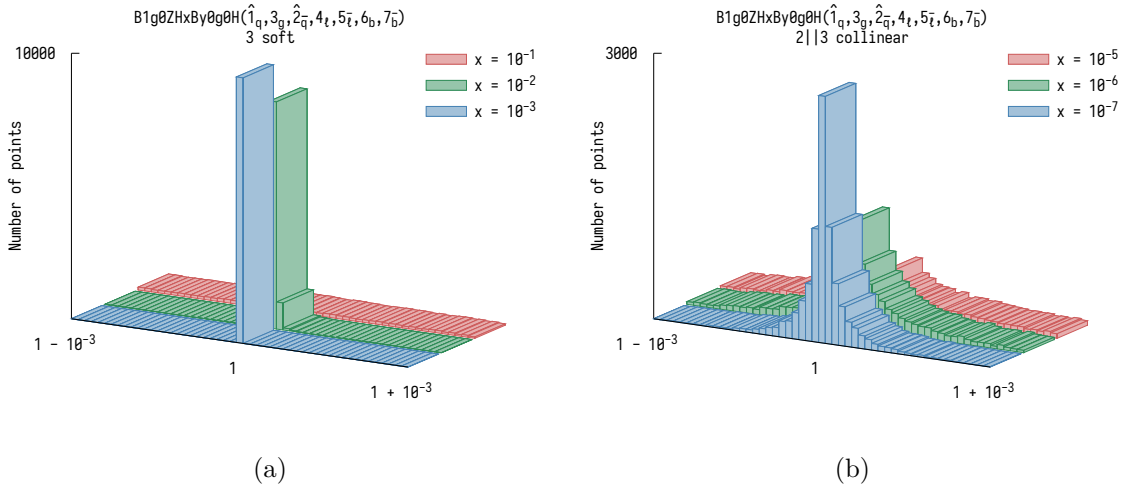


Figure 1.6: Spike tests for a soft 3_g gluon limit ($E_3 = x\sqrt{s} \rightarrow 0$) in (a) and a $\hat{2}_{\bar{q}} \parallel 3_g$ antiquark–gluon collinear limit ($E_{23} = x\sqrt{s} \rightarrow 0$) in (b) of the real production amplitude $B_1^{ZH,0}(\hat{1}_q, 3_g, \hat{2}_{\bar{q}}; 4_\ell, 5_{\bar{\ell}})$. A total of 10000 configurations were probed in all cases. As visible in the naming scheme and flavour assignment above the histograms, the amplitudes in the codebase already have the leading order $H \rightarrow b\bar{b}$ decay attached.

$$\text{qbqB1g0VHSNLO}(3_q, \hat{2}_g, \hat{1}_{\bar{q}}; 4_\ell, 5_{\bar{\ell}}) = -A_{3,qg \rightarrow q\bar{q}}^0(1, 2, 3) B_0^{VH,0}(\hat{2}_q, \hat{1}_{\bar{q}}, 4_\ell, 5_{\bar{\ell}}). \quad (1.31)$$

The A_3^0 -type (three partons and zero loops) antenna functions are one of the many antennae mimicking infrared structures and they are calculated as a ratio of essential matrix elements required to reproduce the given soft and collinear limits. Graphically the structure of these subtraction terms can be visualized in Figure 1.5. The full list and exact expression for the antenna functions up to NNLO are enumerated in refs. [8–15].

Besides the introduction necessary for a well-structured train of thought, it is not the intention of this thesis to go through all the peculiarities and details of antenna subtraction. For our purposes, it is enough to note that all subtraction terms contain universal antennae and process-specific reduced matrix elements of lower orders.

Eqs. (1.29)–(1.31) are exactly the same as the subtraction terms for the Drell–Yan process, except that the reduced matrix elements are swapped for those of VH production. As discussed earlier in Section 1.3.2, they are non-momentum-conserving Drell–Yan amplitudes decorated with some extra factors. Performing a replacement of reduced matrix elements readily yields all subtraction terms for the Drell–Yan-type VH production subcontributions. In practice, this meant creating a module for NNLOJET that recycles the implemented Drell–Yan subtraction terms by swapping out the reduced matrix elements.

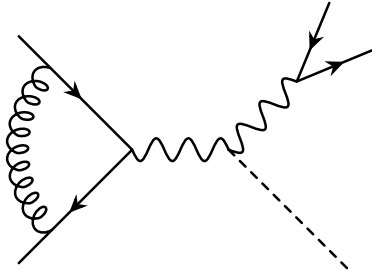


Figure 1.7: Virtual VH production amplitude.

While the aforementioned theoretical reasoning is without a doubt correct, the ultimate test for real subtraction terms are the so-called “spike tests” in the NNLOJET jargon. These are numerical tests designed to calculate the ratio of the real and real-subtraction amplitudes, probing random momentum configurations in all possible unresolved limits. The more we approach the unresolved limit, the closer the ratio should be to 1, regardless of the exact configuration.⁴ This results in a visually pronounced spike in the histogram of the ratio for a fixed number of configurations. Such test results are visualized in Figure 1.6 for a soft-gluon and an antiquark–gluon collinear limits as examples.

1.4.2 Virtual Production $d\hat{\sigma}_{VH,q\bar{q}}^V(1_q, 2_{\bar{q}}; 3_\ell, 4_{\bar{\ell}})$

Virtual cross sections are loop corrections to the Born amplitude, thus they contain only the same single $q\bar{q}$ partonic channel

$$d\hat{\sigma}_{VH,q\bar{q}}^V = \frac{\mathcal{N}_{VH}^V \left(1 - \frac{1}{N_c^2}\right)}{(2N_c)^2} d\Phi_2^{\text{prod.}}(p_1, p_2; p_3, p_4; p_H) B_0^{VH,1}(\hat{1}_q, \hat{2}_{\bar{q}}; 3_\ell, 4_{\bar{\ell}}), \quad (1.32)$$

The expression for the one-loop, zero-gluon amplitude $B_0^{VH,1}$ is found in Appendix A.3 and the new loop Feynman diagram contributing to it is illustrated in Figure 1.7. This diagram has to be interfered with the leading-order diagram of Figure 1.2 to get the expression for the $B_0^{VH,1}$ amplitude. It is already renormalized in the $\overline{\text{MS}}$ scheme and thus carries no ultraviolet divergences, but consequently depends on the renormalization scale $\mu_R^{\text{prod.}}$ of the production subprocess. However, it still has infrared divergences expressed as $1/\epsilon$ and $1/\epsilon^2$ poles in the dimensional regularization parameter, which need to be subtracted by the TNLO virtual subtraction term derived below.

⁴Up to limits in numerical precision. NNLOJET uses double precision everywhere.

Subtraction Term $d\sigma_{\text{VH}}^{\text{TNLO}}(1_q, 2_{\bar{q}}; 3_\ell, 4_{\bar{\ell}})$

Virtual subtraction terms not only need to subtract the explicit poles of the loop amplitudes but also the poles that appeared due to the phase-space integral of initial-state infrared singularities in the real-subtraction (SNLO) amplitude. These are the mass-factorization counterterms and they do not have a loop-amplitude equivalent; they are absorbed by redefinition of the physical PDFs. Therefore the virtual subtraction terms contain as many channels as their real counterpart:

$$d\hat{\sigma}_{\text{VH},q\bar{q}}^{\text{TNLO}} = \frac{\mathcal{N}_{\text{VH}}^{\text{V}} \left(1 - \frac{1}{N_c^2}\right)}{(2N_c)^2} \int \frac{dx_1}{x_1} \frac{dx_2}{x_2} d\Phi_2^{\text{prod.}}(x_1 p_1, x_2 p_2; p_3, p_4; p_{\text{H}}) \times$$

$$\text{qqbB}\theta\text{g1VHTNLO}(\hat{1}_q, \hat{2}_{\bar{q}}; 3_\ell, 4_{\bar{\ell}}), \quad (1.33)$$

$$d\hat{\sigma}_{\text{VH},qg}^{\text{TNLO}} = \frac{\mathcal{N}_{\text{VH}}^{\text{V}} \left(1 - \frac{1}{N_c^2}\right)}{(2N_c)[2(N_c^2 - 1)]} \int \frac{dx_1}{x_1} \frac{dx_2}{x_2} d\Phi_2^{\text{prod.}}(x_1 p_1, x_2 p_2; p_3, p_4; p_{\text{H}}) \times$$

$$\text{qgB}\theta\text{g1VHTNLO}(\hat{1}_q, \hat{2}_g; 3_\ell, 4_{\bar{\ell}}), \quad (1.34)$$

$$d\hat{\sigma}_{\text{VH},\bar{q}g}^{\text{TNLO}} = \frac{\mathcal{N}_{\text{VH}}^{\text{V}} \left(1 - \frac{1}{N_c^2}\right)}{(2N_c)[2(N_c^2 - 1)]} \int \frac{dx_1}{x_1} \frac{dx_2}{x_2} d\Phi_2^{\text{prod.}}(x_1 p_1, x_2 p_2; p_3, p_4; p_{\text{H}}) \times$$

$$\text{qbgB}\theta\text{g1VHTNLO}(\hat{2}_{\bar{q}}, \hat{1}_g; 3_\ell, 4_{\bar{\ell}}). \quad (1.35)$$

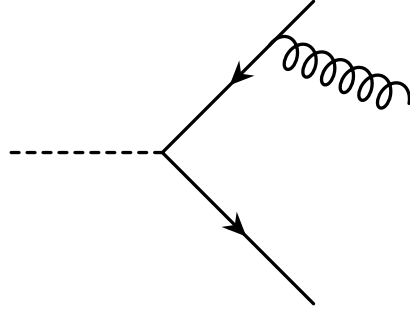
The subtraction amplitudes

$$\text{qqbB}\theta\text{g1VHTNLO}(\hat{1}_q, \hat{2}_{\bar{q}}; 3_\ell, 4_{\bar{\ell}}) = -J_{2,QQ}^{(1),II}(s_{12}) B_0^{\text{VH},0}(\hat{1}_q, \hat{2}_{\bar{q}}; 3_\ell, 4_{\bar{\ell}}), \quad (1.36)$$

$$\text{qgB}\theta\text{g1VHTNLO}(\hat{1}_q, \hat{2}_g; 3_\ell, 4_{\bar{\ell}}) = -J_{2,QQ,qg \rightarrow qq}^{(1),II}(s_{12}) B_0^{\text{VH},0}(\hat{1}_q, \hat{2}_{\bar{q}}; 3_\ell, 4_{\bar{\ell}}), \quad (1.37)$$

$$\text{qbgB}\theta\text{g1VHTNLO}(\hat{2}_{\bar{q}}, \hat{1}_g; 3_\ell, 4_{\bar{\ell}}) = -J_{2,QQ,qg \rightarrow qq}^{(1),II}(s_{12}) B_0^{\text{VH},0}(\hat{2}_q, \hat{1}_{\bar{q}}; 3_\ell, 4_{\bar{\ell}}) \quad (1.38)$$

are expressed with integrated dipoles $J_2^{(1)}$ and reduced matrix elements. The integrals over x_1 and x_2 in eqs. (1.33)–(1.35) indicate convolutions with the latter. It is implicitly understood that the momenta set appearing in the subtraction amplitudes—both in the reduced matrix elements and integrated dipoles—have initial-state momenta of $x_1 p_1$ and $x_2 p_2$. The dependence on the factorization scale μ_{F} and the production renormalization scale $\mu_{\text{R}}^{\text{prod.}}$ is

Figure 1.8: Real $H \rightarrow b\bar{b}$ decay amplitude.

also not indicated explicitly, but it is always understood that

$$J_2^{(1)}(s) = J_2^{(1)}(s, x_1, x_2, \mu_F, \mu_R^{\text{prod.}}). \quad (1.39)$$

The exact expressions for the integrated dipoles in terms of integrated antennæ and mass-factorization kernels are found in ref. [16] and I will not reiterate them here.

Overall, the same reasoning as for the real subtraction terms holds: virtual subtraction terms can be generated by replacing the original Drell–Yan reduced matrix elements with the non-momentum-conserving ones. Nevertheless, the expected $1/\epsilon$ and $1/\epsilon^2$ pole cancellations between the regenerated virtual amplitudes and their subtraction terms have been analytically validated with a built-in module of NNLOJET.

1.4.3 Real Decay $d\sigma_{H \rightarrow b\bar{b}}^R(i_b, j_g, k_{\bar{b}})$

Real corrections to the decay cross section are expressed as

$$d\sigma_{H \rightarrow b\bar{b}}^R = \mathcal{N}_{H \rightarrow b\bar{b}}^R \left(1 - \frac{1}{N_c^2}\right) d\Phi_3^{\text{dec.}}(p_H; p_i, p_j, p_k) B_1^{\text{H},0}(i_b, j_g, k_{\bar{b}}). \quad (1.40)$$

The amplitude $B_1^{\text{H},0}$ is illustrated in Figure 1.8 with its full form given in Appendix A.12.

Subtraction Term $d\sigma_{H \rightarrow b\bar{b}}^{\text{SNLO}}(i_b, j_g, k_{\bar{b}})$

The real subtraction term for the decay part is

$$d\sigma_{H \rightarrow b\bar{b}}^{\text{SNLO}} = \mathcal{N}_{H \rightarrow b\bar{b}}^R \left(1 - \frac{1}{N_c^2}\right) d\Phi_3^{\text{dec.}}(p_H; p_i, p_j, p_k) \text{By1g0HSNLO}(i_b, j_g, k_{\bar{b}}). \quad (1.41)$$

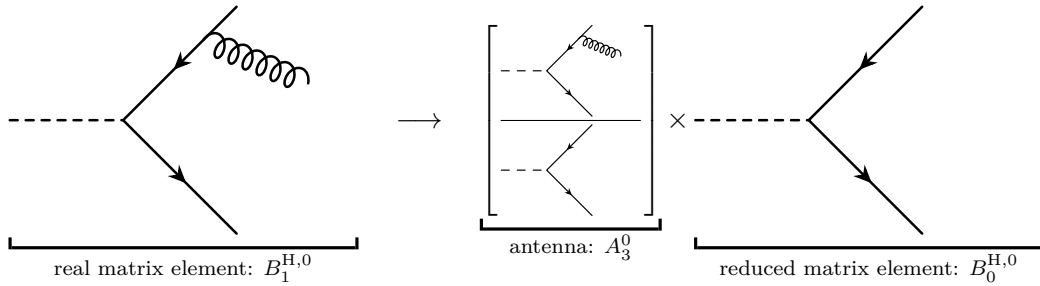


Figure 1.9: The simple, almost tautological structure of the SNLO subtraction term of the $H \rightarrow b\bar{b}$ decay.

The subtraction amplitude, whose structure is visualized in Figure 1.9 is expanded as

$$\text{By1g0HSNLO}(i_b, j_g, k_{\bar{b}}) = A_3^0(i, j, k) B_0^{H,0}(\bar{i}_b, \bar{j}_{\bar{b}}). \quad (1.42)$$

In the NNLOJET codebase the decay subtraction amplitudes never appear in the form above, but rather always together with their respective production channels. The Born production cross section contains only a $q\bar{q}$ channel, therefore a Born \times SNLO subtraction term is evaluated by the subroutine `qqbB0g0VHxBy1g0HSNLO` with $V=Z$ or W . The decay subtraction terms are completely new and not just replacements of reduced matrix elements. To verify these subtraction terms, we carried out spike tests, two of which are visualized in Figure 1.10.

1.4.4 Virtual Decay $d\sigma_{H \rightarrow b\bar{b}}^V(i_b, j_{\bar{b}})$

Virtual corrections for the decay cross section are written as

$$d\sigma_{H \rightarrow b\bar{b}}^V = \mathcal{N}_{H \rightarrow b\bar{b}}^V \left(1 - \frac{1}{N_c^2}\right) d\Phi_2^{\text{dec.}}(p_H; p_i, p_j) B_0^{H,1}(i_b, j_{\bar{b}}). \quad (1.43)$$

The amplitude $B_0^{H,1}$ is given in Appendix A.13 and the Feynman diagram that needs to be interfered with the leading-order decay of Figure 1.3 to get the amplitude is illustrated in Figure 1.11. Note that being a virtual amplitude renormalized in the $\overline{\text{MS}}$ scheme, it also depends on the renormalization scale $\mu_R^{\text{dec.}}$ of the decay side, independently from the production renormalization scale.

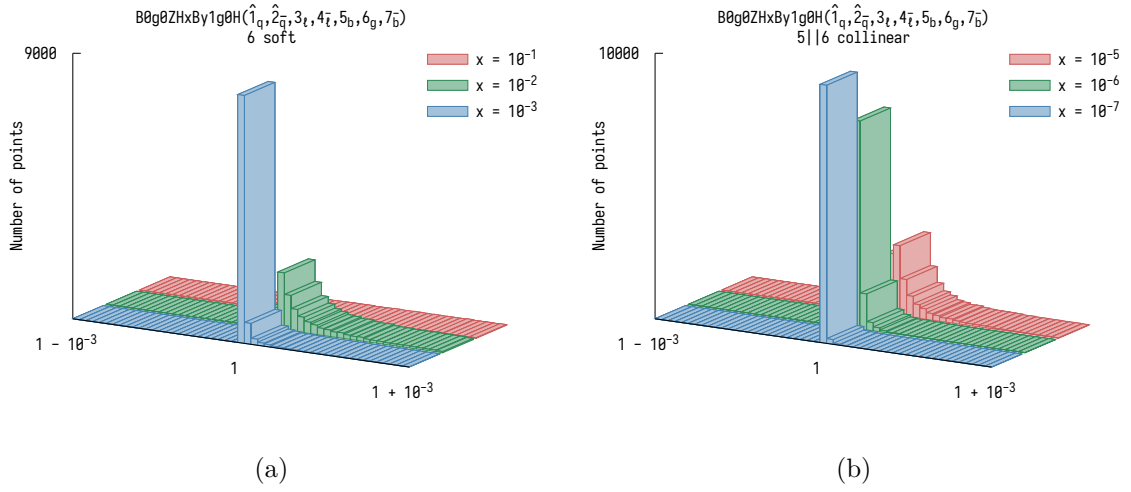


Figure 1.10: Spike tests for a soft 6_g gluon limit ($E_6 = x\sqrt{s} \rightarrow 0$) in (a) and a $5_b \parallel 6_g$ bottom-quark-gluon collinear limit ($E_{56} = x\sqrt{s} \rightarrow 0$) in (b) of the real decay amplitude $B_1^{H,0}(5_b, 6_g, 7_{\bar{b}})$. A total of 10000 configurations were probed in all cases. As visible in the naming scheme and flavour assignment above the histograms, the amplitudes shown here had the leading order ZH production attached to them.

Subtraction Term $d\sigma_{H \rightarrow b\bar{b}}^{\text{TNLO}}(i_b, j_{\bar{b}})$

The virtual subtraction term for the decay part is

$$d\sigma_{H \rightarrow b\bar{b}}^{\text{TNLO}} = \mathcal{N}_{H \rightarrow b\bar{b}}^{\text{V}} \left(1 - \frac{1}{N_c^2}\right) d\Phi_2^{\text{dec.}}(p_H; p_i, p_j) \text{By}\theta g1\text{HNSLO}(i_b, j_{\bar{b}}). \quad (1.44)$$

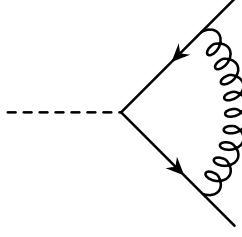
Mass-factorization counterterms only accompany initial-state integrated singularities, which are not present for decays as they only contain final-state configurations. Therefore, no convolution with the mass-factorization kernel is needed, such as in eqs. (1.33)–(1.35) and therefore the convolution variables x_1 and x_2 are missing as well. The subtraction amplitude is

$$\text{By}\theta g1\text{HTNLO}(i_b, j_{\bar{b}}) = -J_{2,QQ}^{(1),\text{FF}}(s_{ij}) B_0^{H,0}(i_b, j_{\bar{b}}), \quad (1.45)$$

which, being on the decay side, additionally depends on the decay renormalization scale:

$$J_{2,QQ}^{(1),\text{FF}}(s) = J_{2,QQ}^{(1),\text{FF}}(s, \mu_R^{\text{dec.}}). \quad (1.46)$$

With this, all ingredients necessary to evaluate VH production with $H \rightarrow b\bar{b}$ decay at NLO

Figure 1.11: Virtual $H \rightarrow b\bar{b}$ decay amplitude.

are given. We will now move onto the ingredients that are required for describing the cross section at NNLO.

1.5 Next-to-Next-to-Leading Order

There are many more elements that are required in order to consistently assemble VH production with $H \rightarrow b\bar{b}$ decay at $\mathcal{O}(\alpha_s^2)$. After expanding the main formula (1.1) for the NNLO coefficient, I will tackle the genuinely new ingredients step-by-step, channel-by-channel.

Ingredients to double-real production are found in Section 1.5.1, to real-virtual production in Section 1.5.2, and to double-virtual production in Section 1.5.3. Besides the $\mathcal{O}(\alpha_s^2)$ Drell-Yan-like amplitudes, there are also a set of completely new production processes appearing at real-virtual and double-virtual levels, induced by the Z boson or the Higgs boson coupling directly to closed fermion loops.

After enumerating the building blocks of the production subprocess, we will turn our attention towards new ingredients of the decay. Double-real decay correction are shown in Section 1.5.4, real-virtual and double-virtual ones in Sections 1.5.5 and 1.5.6, respectively. Whereas most of the Drell-Yan-like production subtraction amplitudes are recycled in the same manner as we have seen at NLO, subtraction terms for the decay are implemented into NNLOJET completely anew. Therefore I will give the expressions for them in terms of antennae and reduced matrix elements.

The production \times decay factorized NNLO coefficient contains all possible $\mathcal{O}(\alpha_s^2)$ contributions. These are

$$\begin{aligned} d\sigma_{\text{NNLO coef.}} &= \int \frac{d^d p_H}{(2\pi)^d} \left[d\sigma_{VH}^{(2)} \times d\sigma_{H \rightarrow b\bar{b}}^{(0)} + d\sigma_{VH}^{(1)} \times d\sigma_{H \rightarrow b\bar{b}}^{(1)} + d\sigma_{VH}^{(0)} \times d\sigma_{H \rightarrow b\bar{b}}^{(2)} \right] \mathcal{J}_{2_b} \quad (1.47) \\ &= \int \frac{d^d p_H}{(2\pi)^d} \left\{ \left(d\sigma_{VH}^{\text{RR}} - d\sigma_{VH}^{\text{S}} \right) \times d\sigma_{H \rightarrow b\bar{b}}^{\text{B}} \mathcal{J}_{2_b}^{(4)}(3, 4; 7_b, 8_{\bar{b}}) \right. \\ &\quad \left. + \left(d\sigma_{VH}^{\text{RV}} - d\sigma_{VH}^{\text{T}} \right) \times d\sigma_{H \rightarrow b\bar{b}}^{\text{B}} \mathcal{J}_{2_b}^{(3)}(3; 6_b, 7_{\bar{b}}) \right\} \end{aligned}$$

$$\begin{aligned}
& + \left(d\sigma_{VH}^{VV} - d\sigma_{VH}^U \right) \times d\sigma_{H \rightarrow b\bar{b}}^B \mathcal{J}_{2_b}^{(2)}(5_b, 6_{\bar{b}}) \\
& + \left(d\sigma_{VH}^R - d\sigma_{VH}^{\text{SNLO}} \right) \times \left(d\sigma_{H \rightarrow b\bar{b}}^R - d\sigma_{H \rightarrow b\bar{b}}^{\text{SNLO}} \right) \mathcal{J}_{2_b}^{(4)}(3; 6_b, 7_g, 8_{\bar{b}}) \\
& + \left(d\sigma_{VH}^R - d\sigma_{VH}^{\text{SNLO}} \right) \times \left(d\sigma_{H \rightarrow b\bar{b}}^V - d\sigma_{H \rightarrow b\bar{b}}^{\text{TNLO}} \right) \mathcal{J}_{2_b}^{(3)}(3; 6_b, 7_{\bar{b}}) \\
& + \left(d\sigma_{VH}^V - d\sigma_{VH}^{\text{TNLO}} \right) \times \left(d\sigma_{H \rightarrow b\bar{b}}^R - d\sigma_{H \rightarrow b\bar{b}}^{\text{SNLO}} \right) \mathcal{J}_{2_b}^{(3)}(5_b, 6_g, 7_{\bar{b}}) \\
& + \left(d\sigma_{VH}^V - d\sigma_{VH}^{\text{TNLO}} \right) \times \left(d\sigma_{H \rightarrow b\bar{b}}^V - d\sigma_{H \rightarrow b\bar{b}}^{\text{TNLO}} \right) \mathcal{J}_{2_b}^{(2)}(5_b, 6_{\bar{b}}) \\
& + d\sigma_{VH}^B \times \left(d\sigma_{H \rightarrow b\bar{b}}^{\text{RR}} - d\sigma_{H \rightarrow b\bar{b}}^S \right) \mathcal{J}_{2_b}^{(4)}(5_b, 6, 7, 8_{\bar{b}}) \\
& + d\sigma_{VH}^B \times \left(d\sigma_{H \rightarrow b\bar{b}}^{\text{RV}} - d\sigma_{H \rightarrow b\bar{b}}^T \right) \mathcal{J}_{2_b}^{(3)}(5_b, 6_g, 7_{\bar{b}}) \\
& + d\sigma_{VH}^B \times \left(d\sigma_{H \rightarrow b\bar{b}}^{\text{VV}} - d\sigma_{H \rightarrow b\bar{b}}^U \right) \mathcal{J}_{2_b}^{(2)}(5_b, 6_{\bar{b}}) \}. \tag{1.48}
\end{aligned}$$

The infrared singularities of the double-real (RR), real-virtual (RV), and double-virtual (VV) contributions at the subprocess level are cancelled by the subtraction terms S, T, and U, respectively. The KLN theorem within the antenna subtraction formalism at NNLO thus reads

$$\begin{aligned}
\sigma &= \int_{\Phi_{n+2}} d\sigma^{\text{RR}} + \int_{\Phi_{n+1}} d\sigma^{\text{RV}} + \int_{\Phi_n} d\sigma^{\text{VV}} \\
&= \int_{\Phi_{n+2}} \underbrace{\left(d\sigma^{\text{RR}} - d\sigma^S \right)}_{\text{infrared finite}} + \int_{\Phi_{n+1}} \underbrace{\left(d\sigma^{\text{RV}} - d\sigma^T \right)}_{\text{infrared finite}} + \int_{\Phi_n} \underbrace{\left(d\sigma^{\text{VV}} - d\sigma^U \right)}_{\text{infrared finite}}.
\end{aligned}$$

Genuinely new contributions are the NNLO \times LO and LO \times NNLO ones; the NLO \times NLO parts are assembled from the already discussed lower-order contributions.⁵

A new feature for the real-virtual and double-virtual production amplitudes will be the appearance of top quark induced loop contributions proportional to the Yukawa coupling of the top quark, where the Higgs boson is emitted from the loop and does not couple to the vector boson. The subtraction formalism for Drell-Yan is thus not applicable for these amplitudes but they are fortunately all infrared finite.

Let us summarize the normalization factors at NNLO before proceeding to the individual subcontributions.

$$\mathcal{N}_{VH}^{\text{RR}} = \mathcal{N}_{VH}^R \left(\frac{\alpha_s N_c}{2\pi} \right) \frac{\bar{C}(\epsilon)}{C(\epsilon)}, \tag{1.49}$$

⁵Note the products between subtraction terms as well in eq. (1.48), such as $d\sigma_{VH}^{\text{SNLO}} \times d\sigma_{H \rightarrow b\bar{b}}^{\text{TNLO}}$ etc.

real production. Moreover, channels that include amplitudes with two quark currents can get a little confusing, therefore I separated ZH and WH productions when necessary. Non-identical quark flavours are separated in notation with capitalization, i.e. q and Q with $q \neq Q$. The W coupling changes the quark flavour, which is indicated with the prime symbol, i.e. the quark current that couples to the charged vector boson is labelled as $q\bar{q}'$. Furthermore, it is always understood that $Q \neq q'$ with q being up-type and q' being down-type for W^+H production; and q being down-type and q' being up-type for W^-H production.

Quark–Quark Initiated (Non-Identical Flavour)

$$d\hat{\sigma}_{\text{ZH},qQ}^{\text{RR}} = \frac{\mathcal{N}_{\text{VH}}^{\text{RR}} \left(1 - \frac{1}{N_c^2}\right)}{(2N_c)^2} d\Phi_4^{\text{prod.}}(p_1, p_2; \{p_f\}_{f=3}^6; p_H) \frac{1}{N_c} C_0^{\text{ZH},0}(\hat{1}_q, 3_{\bar{Q}}, \hat{2}_Q, 4_{\bar{q}}; 5_\ell, 6_{\bar{\ell}}), \quad (1.55)$$

$$d\hat{\sigma}_{\text{WH},qQ}^{\text{RR}} = \frac{\mathcal{N}_{\text{VH}}^{\text{RR}} \left(1 - \frac{1}{N_c^2}\right)}{(2N_c)^2} d\Phi_4^{\text{prod.}}(p_1, p_2; \{p_f\}_{f=3}^6; p_H) \frac{1}{N_c} C_0^{\text{WH},0}(\hat{1}_q, 3_{\bar{Q}}, \hat{2}_Q, 4_{q'}; 5_\ell, 6_{\bar{\ell}}). \quad (1.56)$$

WH production has additional subleading-colour contributions when $Q = q'$,

$$d\hat{\sigma}_{\text{WH},qq'}^{\text{RR}} = \frac{\mathcal{N}_{\text{VH}}^{\text{RR}} \left(1 - \frac{1}{N_c^2}\right)}{(2N_c)^2} d\Phi_4^{\text{prod.}}(p_1, p_2; \{p_f\}_{f=3}^6; p_H) \times \\ \frac{1}{2!} \frac{1}{N_c} \left\{ C_0^{\text{WH},0}(\hat{1}_q, 3_{\bar{q}'}, \hat{2}_{q'}, 4_{\bar{q}'}; 5_\ell, 6_{\bar{\ell}}) + C_0^{\text{WH},0}(\hat{1}_q, 4_{\bar{q}'}, \hat{2}_{q'}, 3_{\bar{q}'}; 5_\ell, 6_{\bar{\ell}}) \right. \\ \left. - \frac{1}{N_c} D_{b,0}^{\text{WH},0}(\hat{1}_q, 3_{\bar{q}'}, \hat{2}_{q'}, 4_{\bar{q}'}; 5_\ell, 6_{\bar{\ell}}) \right\}. \quad (1.57)$$

A symmetry factor of $\frac{1}{2!}$ is present as final-state quarks $3_{\bar{q}'}$ and $4_{\bar{q}'}$ are identical. In practice the permutation $3_{\bar{q}'} \leftrightarrow 4_{\bar{q}'}$ is carried out by the phase-space integral, enabling contracting the two pieces into one in the codebase.

Quark–Quark Initiated (Identical Flavour)

$$d\hat{\sigma}_{\text{ZH},qq}^{\text{RR}} = \frac{\mathcal{N}_{\text{VH}}^{\text{RR}} \left(1 - \frac{1}{N_c^2}\right)}{(2N_c)^2} d\Phi_4^{\text{prod.}}(p_1, p_2; \{p_f\}_{f=3}^6; p_H) \times \\ \frac{1}{2!} \frac{1}{N_c} \left\{ C_0^{\text{ZH},0}(\hat{1}_q, 3_{\bar{q}}, \hat{2}_q, 4_{\bar{q}}; 5_\ell, 6_{\bar{\ell}}) + C_0^{\text{ZH},0}(\hat{1}_q, 4_{\bar{q}}, \hat{2}_q, 3_{\bar{q}}; 5_\ell, 6_{\bar{\ell}}) \right\}$$

$$-\frac{1}{N_c} D_0^{\text{ZH},0}(\hat{1}_q, 3_{\bar{q}}, \hat{2}_q, 4_{\bar{q}}; 5_\ell, 6_{\bar{\ell}}) \Big\}, \quad (1.58)$$

$$\begin{aligned} d\hat{\sigma}_{\text{WH},qq}^{\text{RR}} &= \frac{\mathcal{N}_{\text{VH}}^{\text{RR}} \left(1 - \frac{1}{N_c^2}\right)}{(2N_c)^2} d\Phi_4^{\text{prod.}}(p_1, p_2; \{p_f\}_{f=3}^6; p_{\text{H}}) \times \\ &\frac{1}{N_c} \left\{ C_0^{\text{WH},0}(\hat{1}_q, 3_{\bar{q}}, \hat{2}_q, 4_{\bar{q}}; 5_\ell, 6_{\bar{\ell}}) + C_0^{\text{WH},0}(\hat{2}_q, 3_{\bar{q}}, \hat{1}_q, 4_{\bar{q}}; 5_\ell, 6_{\bar{\ell}}) \right. \\ &\left. - \frac{1}{N_c} D_{a,0}^{\text{WH},0}(\hat{1}_q, 3_{\bar{q}}, \hat{2}_q, 4_{\bar{q}}; 5_\ell, 6_{\bar{\ell}}) \right\}. \end{aligned} \quad (1.59)$$

A symmetry factor of $\frac{1}{2!}$ is present for ZH production where the final-state quarks $3_{\bar{q}}$ and $4_{\bar{q}}$ are identical, whose permutation in practice is carried out by the phase-space integral. This factor is missing from WH production due to the change in flavour.

Antiquark–Antiquark Initiated (Non-Identical Flavour)

$$d\hat{\sigma}_{\text{ZH},\bar{Q}\bar{q}}^{\text{RR}} = \frac{\mathcal{N}_{\text{VH}}^{\text{RR}} \left(1 - \frac{1}{N_c^2}\right)}{(2N_c)^2} d\Phi_4^{\text{prod.}}(p_1, p_2; \{p_f\}_{f=3}^6; p_{\text{H}}) \frac{1}{N_c} C_0^{\text{ZH},0}(3_q, \hat{1}_{\bar{Q}}, 4_Q, \hat{2}_{\bar{q}}; 5_\ell, 6_{\bar{\ell}}), \quad (1.60)$$

$$d\hat{\sigma}_{\text{WH},\bar{Q}\bar{q}'}^{\text{RR}} = \frac{\mathcal{N}_{\text{VH}}^{\text{RR}} \left(1 - \frac{1}{N_c^2}\right)}{(2N_c)^2} d\Phi_4^{\text{prod.}}(p_1, p_2; \{p_f\}_{f=3}^6; p_{\text{H}}) \frac{1}{N_c} C_0^{\text{WH},0}(3_q, \hat{1}_{\bar{Q}}, 4_Q, \hat{2}_{\bar{q}'}; 5_\ell, 6_{\bar{\ell}}). \quad (1.61)$$

WH production has additional subleading-colour contributions when $Q = q$.

$$\begin{aligned} d\hat{\sigma}_{\text{WH},\bar{q}\bar{q}'}^{\text{RR}} &= \frac{\mathcal{N}_{\text{VH}}^{\text{RR}} \left(1 - \frac{1}{N_c^2}\right)}{(2N_c)^2} d\Phi_4^{\text{prod.}}(p_1, p_2; \{p_f\}_{f=3}^6; p_{\text{H}}) \times \\ &\frac{1}{2!} \frac{1}{N_c} \left\{ C_0^{\text{WH},0}(3_q, \hat{1}_{\bar{q}}, 4_q, \hat{2}_{\bar{q}'}; 5_\ell, 6_{\bar{\ell}}) + C_0^{\text{WH},0}(4_q, \hat{1}_{\bar{q}}, 3_q, \hat{2}_{\bar{q}'}; 5_\ell, 6_{\bar{\ell}}) \right. \\ &\left. - \frac{1}{N_c} D_{a,0}^{\text{WH},0}(3_q, \hat{1}_{\bar{q}}, 4_q, \hat{2}_{\bar{q}'}; 5_\ell, 6_{\bar{\ell}}) \right\}. \end{aligned} \quad (1.62)$$

A symmetry factor of $\frac{1}{2!}$ is present as the final-state quarks 3_q and 4_q are identical, whose permutation in practice is carried out by the phase-space integral.

Antiquark–Antiquark Initiated (Identical Flavour)

$$\begin{aligned}
d\hat{\sigma}_{\text{ZH},\bar{q}\bar{q}}^{\text{RR}} &= \frac{\mathcal{N}_{\text{VH}}^{\text{RR}} \left(1 - \frac{1}{N_c^2}\right)}{(2N_c)^2} d\Phi_4^{\text{prod.}}(p_1, p_2; \{p_f\}_{f=3}^6; p_{\text{H}}) \times \\
&\frac{1}{2!} \frac{1}{N_c} \left\{ C_0^{\text{ZH},0}(3_q, \hat{1}_{\bar{q}}, 4_q, \hat{2}_{\bar{q}}; 5_\ell, 6_{\bar{\ell}}) + C_0^{\text{ZH},0}(4_q, \hat{1}_{\bar{q}}, 3_q, \hat{2}_{\bar{q}}; 5_\ell, 6_{\bar{\ell}}) \right. \\
&\left. - \frac{1}{N_c} D_0^{\text{ZH},0}(3_q, \hat{1}_{\bar{q}}, 4_q, \hat{2}_{\bar{q}}; 5_\ell, 6_{\bar{\ell}}) \right\}, \tag{1.63}
\end{aligned}$$

$$\begin{aligned}
d\hat{\sigma}_{\text{WH},\bar{q}'\bar{q}'}^{\text{RR}} &= \frac{\mathcal{N}_{\text{VH}}^{\text{RR}} \left(1 - \frac{1}{N_c^2}\right)}{(2N_c)^2} d\Phi_4^{\text{prod.}}(p_1, p_2; \{p_f\}_{f=3}^6; p_{\text{H}}) \times \\
&\frac{1}{N_c} \left\{ C_0^{\text{WH},0}(3_q, \hat{1}_{\bar{q}'}, 4_{q'}, \hat{2}_{\bar{q}'}; 5_\ell, 6_{\bar{\ell}}) + C_0^{\text{WH},0}(3_q, \hat{2}_{\bar{q}'}, 4_{q'}, \hat{1}_{\bar{q}'}; 5_\ell, 6_{\bar{\ell}}) \right. \\
&\left. - \frac{1}{N_c} D_{b,0}^{\text{WH},0}(3_q, \hat{1}_{\bar{q}'}, 4_{q'}, \hat{2}_{\bar{q}'}; 5_\ell, 6_{\bar{\ell}}) \right\}. \tag{1.64}
\end{aligned}$$

A symmetry factor of $\frac{1}{2!}$ is present for ZH production for the identical final-state quarks 3_q and 4_q , whose permutation in practice is carried out by the phase-space integral. This is once again missing from WH production.

Quark–Antiquark Initiated (Non-Identical Flavour)

$$d\hat{\sigma}_{\text{ZH},q\bar{Q}}^{\text{RR}} = \frac{\mathcal{N}_{\text{VH}}^{\text{RR}} \left(1 - \frac{1}{N_c^2}\right)}{(2N_c)^2} d\Phi_4^{\text{prod.}}(p_1, p_2; \{p_f\}_{f=3}^6; p_{\text{H}}) \frac{1}{N_c} C_0^{\text{ZH},0}(\hat{1}_q, \hat{2}_{\bar{Q}}, 3_Q, 4_{\bar{q}}; 5_\ell, 6_{\bar{\ell}}), \tag{1.65}$$

$$d\hat{\sigma}_{\text{WH},q\bar{Q}}^{\text{RR}} = \frac{\mathcal{N}_{\text{VH}}^{\text{RR}} \left(1 - \frac{1}{N_c^2}\right)}{(2N_c)^2} d\Phi_4^{\text{prod.}}(p_1, p_2; \{p_f\}_{f=3}^6; p_{\text{H}}) \frac{1}{N_c} C_0^{\text{WH},0}(\hat{1}_q, \hat{2}_{\bar{Q}}, 3_Q, 4_{\bar{q}'}; 5_\ell, 6_{\bar{\ell}}). \tag{1.66}$$

WH production has additional leading- and subleading-colour contributions when $Q = q'$.

$$d\hat{\sigma}_{\text{WH},q\bar{q}'}^{\text{RR}} = \frac{\mathcal{N}_{\text{VH}}^{\text{RR}} \left(1 - \frac{1}{N_c^2}\right)}{(2N_c)^2} d\Phi_4^{\text{prod.}}(p_1, p_2; \{p_f\}_{f=3}^6; p_{\text{H}}) \times$$

$$\begin{aligned}
& \left\{ \frac{1}{2!} \left[\sum_{(3 \leftrightarrow 4)} B_2^{\text{WH},0}(\hat{1}_q, 3_g, 4_g, \hat{2}_{q'}, 5_\ell, 6_{\bar{\ell}}) - \frac{1}{N_c^2} \tilde{B}_2^{\text{WH},0}(\hat{1}_q, 3_g, 4_g, \hat{2}_{q'}, 5_\ell, 6_{\bar{\ell}}) \right] \right. \\
& + \frac{1}{N_c} \left[n_F C_0^{\text{WH},0}(\hat{1}_q, 4_{\bar{Q}}, 3_Q, \hat{2}_{q'}; 5_\ell, 6_{\bar{\ell}}) \right. \\
& + C_0^{\text{WH},0}(\hat{1}_q, \hat{2}_{q'}, 3_{q'}, 4_{q'}; 5_\ell, 6_{\bar{\ell}}) + C_0^{\text{WH},0}(3_q, 4_{\bar{q}}, \hat{1}_q, \hat{2}_{q'}; 5_\ell, 6_{\bar{\ell}}) \\
& \left. \left. - \frac{1}{N_c} \left[D_{a,0}^{\text{WH},0}(\hat{1}_q, 4_{\bar{q}}, 3_q, \hat{2}_{q'}; 5_\ell, 6_{\bar{\ell}}) + D_{b,0}^{\text{WH},0}(\hat{1}_q, \hat{2}_{q'}, 3_{q'}, 4_{q'}; 5_\ell, 6_{\bar{\ell}}) \right] \right] \right\}. \quad (1.67)
\end{aligned}$$

The symbol $\sum_{(3 \leftrightarrow 4)}$ indicates the sum over the two permutations of the final-state identical gluons 3_g and 4_g , hence the symmetry factor $\frac{1}{2!}$ as well. The expression assumes a diagonal CKM matrix with the number of flavours marked with $n_F = 5$.

Quark–Antiquark Initiated (Identical Flavour)

$$\begin{aligned}
d\hat{\sigma}_{\text{ZH},q\bar{q}}^{\text{RR}} &= \frac{\mathcal{N}_{\text{VH}}^{\text{RR}} \left(1 - \frac{1}{N_c^2}\right)}{(2N_c)^2} d\Phi_4^{\text{prod.}}(p_1, p_2; \{p_f\}_{f=3}^6; p_H) \times \\
& \left\{ \frac{1}{2!} \left[\sum_{(3 \leftrightarrow 4)} B_2^{\text{ZH},0}(\hat{1}_q, 3_g, 4_g, \hat{2}_{\bar{q}}, 5_\ell, 6_{\bar{\ell}}) - \frac{1}{N_c^2} \tilde{B}_2^{\text{ZH},0}(\hat{1}_q, 3_g, 4_g, \hat{2}_{\bar{q}}, 5_\ell, 6_{\bar{\ell}}) \right] \right. \\
& + \frac{1}{N_c} \left[n_{\text{up}} C_0^{\text{ZH},0}(\hat{1}_q, 4_{\bar{u}}, 3_u, \hat{2}_{\bar{q}}; 5_\ell, 6_{\bar{\ell}}) + n_{\text{down}} C_0^{\text{ZH},0}(\hat{1}_q, 4_{\bar{d}}, 3_d, \hat{2}_{\bar{q}}; 5_\ell, 6_{\bar{\ell}}) \right. \\
& \left. \left. + C_0^{\text{ZH},0}(\hat{1}_q, \hat{2}_{\bar{q}}, 3_q, 4_{\bar{q}}; 5_\ell, 6_{\bar{\ell}}) - \frac{1}{N_c} D_0^{\text{ZH},0}(\hat{1}_q, \hat{2}_{\bar{q}}, 3_q, 4_{\bar{q}}; 5_\ell, 6_{\bar{\ell}}) \right] \right\}. \quad (1.68)
\end{aligned}$$

The symbols u and d indicate up and down quarks with the number of up-type quarks $n_{\text{up}} = 2$ and down-type quarks $n_{\text{down}} = 3$. The separation is necessary because the Z boson couples with different strength to up- and down-type quarks, therefore we cannot just pull out a single $n_F = n_{\text{up}} + n_{\text{down}}$ term but rather have to separate up- and down-type contributions.

$$\begin{aligned}
d\hat{\sigma}_{\text{WH},q\bar{q}}^{\text{RR}} &= \frac{\mathcal{N}_{\text{VH}}^{\text{RR}} \left(1 - \frac{1}{N_c^2}\right)}{(2N_c)^2} d\Phi_4^{\text{prod.}}(p_1, p_2; \{p_f\}_{f=3}^6; p_H) \times \\
& \left\{ \frac{1}{N_c} \left[C_0^{\text{WH},0}(\hat{1}_q, \hat{2}_{\bar{q}}, 3_q, 4_{q'}; 5_\ell, 6_{\bar{\ell}}) + \left[\frac{n_F}{2} \right] C_0^{\text{WH},0}(3_q, \hat{2}_{\bar{q}}, \hat{1}_q, 4_{q'}; 5_\ell, 6_{\bar{\ell}}) \right. \right.
\end{aligned}$$

$$- \frac{1}{N_c} D_{a,0}^{\text{WH},0}(\hat{1}_q, \hat{2}_{\bar{q}}, 3_q, 4_{\bar{q}'}; 5_\ell, 6_{\bar{\ell}})] \Bigg\}. \quad (1.69)$$

The term $[n_F/2] = 2$ because the W^\pm only mediates up–down and charm–strange flavour changes with a diagonal CKM matrix in the 5-flavour scheme.

Quark–Gluon Initiated

There is only one quark line present, therefore—just like at NLO—the ZH and WH productions can be treated together without confusion.

$$\begin{aligned} d\hat{\sigma}_{\text{VH},qg}^{\text{RR}} &= \frac{\mathcal{N}_{\text{VH}}^{\text{RR}} \left(1 - \frac{1}{N_c^2}\right)}{(2N_c)[2(N_c^2 - 1)]} d\Phi_4^{\text{prod.}}(p_1, p_2; \{p_f\}_{f=3}^6; p_H) \times \\ &\frac{1}{2!} \left\{ \sum_{(\hat{2} \leftrightarrow 3)} B_2^{\text{VH},0}(\hat{1}_q, \hat{2}_g, 3_g, 4_{\bar{q}}; 5_\ell, 6_{\bar{\ell}}) - \frac{1}{N_c^2} \tilde{B}_2^{\text{VH},0}(\hat{1}_q, \hat{2}_{\bar{g}}, 3_{\bar{g}}, 4_{\bar{q}}; 5_\ell, 6_{\bar{\ell}}) \right\}. \quad (1.70) \end{aligned}$$

Antiquark–Gluon Initiated

We can once again easily treat the ZH and WH productions together.

$$\begin{aligned} d\hat{\sigma}_{\text{VH},\bar{q}g}^{\text{RR}} &= \frac{\mathcal{N}_{\text{VH}}^{\text{RR}} \left(1 - \frac{1}{N_c^2}\right)}{(2N_c)[2(N_c^2 - 1)]} d\Phi_4^{\text{prod.}}(p_1, p_2; \{p_f\}_{f=3}^6; p_H) \times \\ &\frac{1}{2!} \left\{ \sum_{(\hat{2} \leftrightarrow 3)} B_2^{\text{VH},0}(4_q, \hat{2}_g, 3_g, \hat{1}_{\bar{q}}; 5_\ell, 6_{\bar{\ell}}) - \frac{1}{N_c^2} \tilde{B}_2^{\text{VH},0}(4_q, \hat{2}_{\bar{g}}, 3_{\bar{g}}, \hat{1}_{\bar{q}}; 5_\ell, 6_{\bar{\ell}}) \right\}. \quad (1.71) \end{aligned}$$

Gluon–Gluon Initiated

The Z boson coupling is different based on whether it couples to up- or down-type quarks, therefore we need to list the contributions where up- or down-type quarks are in the final state separately as

$$\begin{aligned} d\hat{\sigma}_{\text{ZH},gg}^{\text{RR}} &= \frac{\mathcal{N}_{\text{ZH}}^{\text{RR}} \left(1 - \frac{1}{N_c^2}\right)}{[2(N_c^2 - 1)]^2} d\Phi_4^{\text{prod.}}(p_1, p_2; \{p_f\}_{f=3}^6; p_H) \times \\ &\left\{ \sum_{(\hat{1} \leftrightarrow \hat{2})} \left[n_{\text{up}} B_2^{\text{ZH},0}(3_u, \hat{1}_g, \hat{2}_g, 4_{\bar{u}}; 5_\ell, 6_{\bar{\ell}}) + n_{\text{down}} B_2^{\text{ZH},0}(3_d, \hat{1}_g, \hat{2}_g, 4_{\bar{d}}; 5_\ell, 6_{\bar{\ell}}) \right] \right\} \end{aligned}$$

$$- \frac{1}{N_c^2} \left[n_{\text{up}} \tilde{B}_2^{\text{ZH},0}(\mathfrak{3}_u, \hat{1}_{\tilde{g}}, \hat{2}_{\tilde{g}}, 4_{\bar{u}}; 5_\ell, 6_{\bar{\ell}}) + n_{\text{down}} \tilde{B}_2^{\text{ZH},0}(\mathfrak{3}_d, \hat{1}_{\tilde{g}}, \hat{2}_{\tilde{g}}, 4_{\bar{d}}; 5_\ell, 6_{\bar{\ell}}) \right] \Bigg\}. \quad (1.72)$$

Once again, we treat the CKM matrix as unity, resulting in the following expression for the WH case:

$$d\hat{\sigma}_{\text{WH,gg}}^{\text{RR}} = \frac{\mathcal{N}_{\text{WH}}^{\text{RR}} \left(1 - \frac{1}{N_c^2}\right)}{[2(N_c^2 - 1)]^2} d\Phi_4^{\text{prod.}}(p_1, p_2; \{p_f\}_{f=3}^6; p_H) \times \left[\frac{n_F}{2} \right] \left\{ \sum_{(\hat{1} \leftrightarrow \hat{2})} B_2^{\text{WH},0}(\mathfrak{3}_q, \hat{1}_{\tilde{g}}, \hat{2}_{\tilde{g}}, 4_{\bar{q}'}; 5_\ell, 6_{\bar{\ell}}) - \frac{1}{N_c^2} \tilde{B}_2^{\text{WH},0}(\mathfrak{3}_q, \hat{1}_{\tilde{g}}, \hat{2}_{\tilde{g}}, 4_{\bar{q}'}; 5_\ell, 6_{\bar{\ell}}) \right\}. \quad (1.73)$$

Subtraction Terms $d\sigma_{\text{VH}}^{\text{S}}(1, 2, 3, 4; 5_\ell, 6_{\bar{\ell}})$

These subtraction terms fully recycle the Drell–Yan subtraction terms in the NNLOJET codebase. The reduced matrix elements can be straightforwardly swapped with the non-momentum-conserving amplitudes. The necessary amplitudes are those of NLO production, which we already discussed with their explicit expressions found in Appendix A. As they would be just a repetition of already known results without gaining additional insight to the framework, I will not present them here.

Nevertheless, I carried out spike tests in all unresolved limits after the swap, such as those in Figure 1.13, to verify that everything is working as intended.

1.5.2 Real–Virtual Production $d\sigma_{\text{VH}}^{\text{RV}}(1, 2, 3; 4_\ell, 5_{\bar{\ell}})$

The real–virtual level includes only B -type amplitudes, however, we have to take into account not only the usual Drell–Yan-type Feynman amplitudes but new top quark induced Yukawa contributions as well, where the Higgs boson directly couples to the loop and not to the vector boson. These are called RI contributions in ref. [28], and we will adapt this notation in our case as well. Examples of Drell–Yan-like amplitudes and the RI-type top-quark ones are visualized in Figure 1.14. These amplitudes need to be interfered with tree-level real ones shown in Figure 1.4.

Leading-colour Drell–Yan-type amplitudes are denoted with $B_1^{\text{VH},1}$, their corresponding subleading-colour counterpart with $\tilde{B}_1^{\text{VH},1}$, and the part proportional to the number of flavours n_F with $\hat{B}_1^{\text{VH},1}$. The means of constructing them is found in Appendix A.7. The

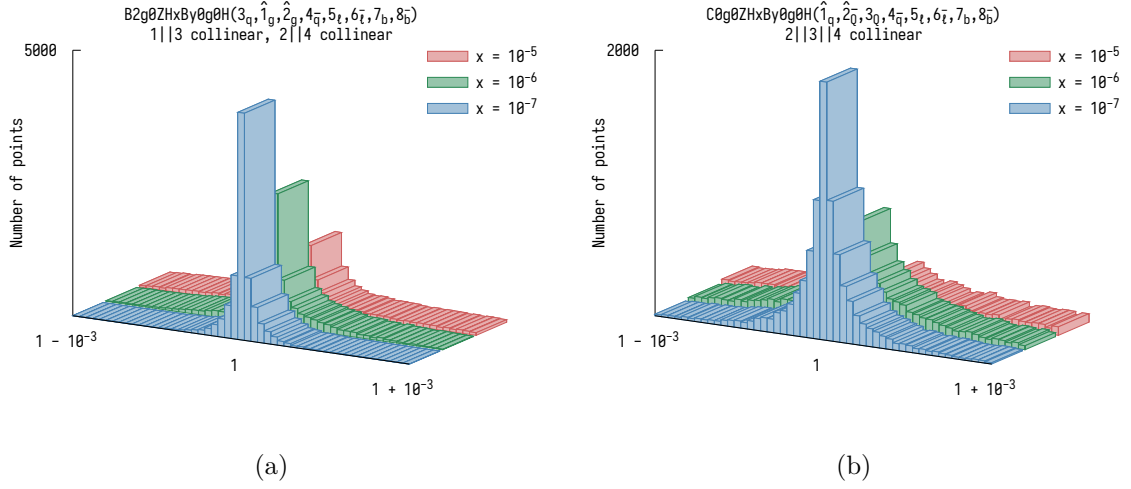


Figure 1.13: Two example spike tests: first a $\hat{1}_g \parallel 3_q$ and $\hat{2}_g \parallel 4_{\bar{q}}$ double collinear limit ($E_{13} = E_{24} = x\sqrt{s}$) in (a) for the gg-initiated double-real amplitude $B_2^{\text{ZH},0}(3_q, \hat{1}_g, \hat{2}_g, 4_{\bar{q}}; 5_\ell, 6_{\bar{\ell}})$; then a $\hat{2}_{\bar{Q}} \parallel 3_Q \parallel 4_{\bar{q}}$ triple collinear limit ($E_{234} = x\sqrt{s}$) in (b) for the $q\bar{Q}$ -initiated double-real amplitude $C_0^{\text{ZH},0}(\hat{1}_q, \hat{2}_{\bar{Q}}, 3_Q, 4_{\bar{q}}; 5_\ell, 6_{\bar{\ell}})$. A total of 10000 configurations were probed in all cases. As visible in the naming scheme and flavour assignment above the histograms, the amplitudes were tested with the leading-order $H \rightarrow b\bar{b}$ decay attached to them.

top loop contributions are named $B_1^{\text{VH},1\text{top}}$ and I recount them in Appendix A.8. We have the same three partonic cross-section channels as at real level, which read

$$\begin{aligned}
d\hat{\sigma}_{\text{VH},q\bar{q}}^{\text{RV}} &= \frac{\mathcal{N}_{\text{VH}}^{\text{RV}} \left(1 - \frac{1}{N_c^2}\right)}{(2N_c)^2} d\Phi_3^{\text{prod.}}(p_1, p_2; \{p_f\}_{f=3}^5; p_H) \times \\
&\left\{ B_1^{\text{VH},1}(\hat{1}_q, 3_g, \hat{2}_{\bar{q}}; 4_\ell, 5_{\bar{\ell}}) - \frac{1}{N_c^2} \tilde{B}_1^{\text{VH},1}(\hat{1}_q, 3_g, \hat{2}_{\bar{q}}; 4_\ell, 5_{\bar{\ell}}) \right. \\
&\left. + \frac{n_F}{N_c} \hat{B}_1^{\text{VH},1}(\hat{1}_q, 3_g, \hat{2}_{\bar{q}}; 4_\ell, 5_{\bar{\ell}}) + \frac{1}{N_c} \left(\frac{m_t^2}{8m_V^2}\right) B_1^{\text{VH},1\text{top}}(\hat{1}_q, 3_g, \hat{2}_{\bar{q}}; 4_\ell, 5_{\bar{\ell}}) \right\}, \quad (1.74)
\end{aligned}$$

$$\begin{aligned}
d\hat{\sigma}_{\text{VH},qg}^{\text{RV}} &= \frac{\mathcal{N}_{\text{VH}}^{\text{RV}} \left(1 - \frac{1}{N_c^2}\right)}{(2N_c)[2(N_c - 1)]} d\Phi_3^{\text{prod.}}(p_1, p_2; \{p_f\}_{f=3}^5; p_H) \times \\
&\left\{ B_1^{\text{VH},1}(\hat{1}_q, \hat{2}_g, 3_{\bar{q}}; 4_\ell, 5_{\bar{\ell}}) - \frac{1}{N_c^2} \tilde{B}_1^{\text{VH},1}(\hat{1}_q, \hat{2}_g, 3_{\bar{q}}; 4_\ell, 5_{\bar{\ell}}) \right. \\
&\left. + \frac{n_F}{N_c} \hat{B}_1^{\text{VH},1}(\hat{1}_q, \hat{2}_g, 3_{\bar{q}}; 4_\ell, 5_{\bar{\ell}}) + \frac{1}{N_c} \left(\frac{m_t^2}{8m_V^2}\right) B_1^{\text{VH},1\text{top}}(\hat{1}_q, \hat{2}_g, 3_{\bar{q}}; 4_\ell, 5_{\bar{\ell}}) \right\}, \quad (1.75)
\end{aligned}$$

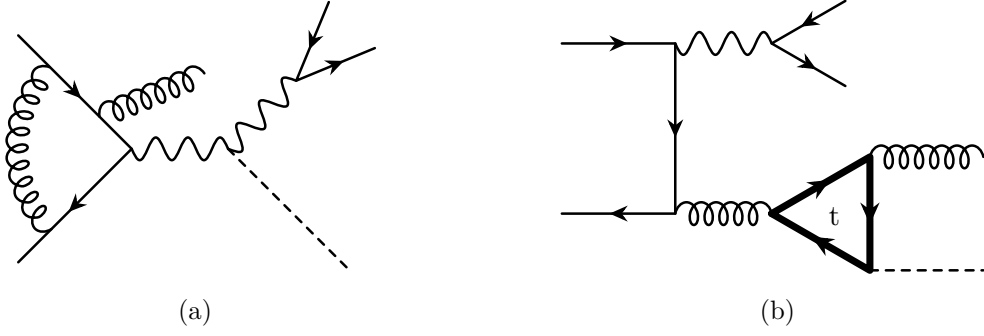


Figure 1.14: Examples of B -type Feynman diagrams contributing at real–virtual level. Besides the usual Drell–Yan-type diagrams (a) new RI-type top-quark loop induced ones (b) are present as well.

$$\begin{aligned}
d\hat{\sigma}_{VH,\bar{q}g}^{\text{RV}} &= \frac{\mathcal{N}_{VH}^{\text{RV}} \left(1 - \frac{1}{N_c^2}\right)}{(2N_c)[2(N_c^2 - 1)]} d\Phi_3^{\text{prod.}}(p_1, p_2; \{p_f\}_{f=3}^5; p_H) \times \\
&\left\{ B_1^{\text{VH},1}(3_q, \hat{2}_g, \hat{1}_{\bar{q}}; 4_\ell, 5_{\bar{\ell}}) - \frac{1}{N_c^2} \tilde{B}_1^{\text{VH},1}(3_q, \hat{2}_g, \hat{1}_{\bar{q}}; 4_\ell, 5_{\bar{\ell}}) \right. \\
&\left. + \frac{n_F}{N_c} \hat{B}_1^{\text{VH},1}(3_q, \hat{2}_g, \hat{1}_{\bar{q}}; 4_\ell, 5_{\bar{\ell}}) + \frac{1}{N_c} \left(\frac{m_t^2}{8m_V^2}\right) B_1^{\text{VH},1\text{top}}(3_q, \hat{2}_g, \hat{1}_{\bar{q}}; 4_\ell, 5_{\bar{\ell}}) \right\}. \quad (1.76)
\end{aligned}$$

The overall factor in front of the top-induced amplitudes is a result of exchanging a Higgs–vector-boson coupling to that of a Higgs–top-quark Yukawa coupling in the latter part of the tree \times loop interference, i.e.

$$\frac{\mathcal{Y}_t m_t}{2\lambda_{VH}} = \frac{m_t^2}{8m_V^2}, \quad (1.77)$$

with the Higgs–vector-boson coupling λ_{VH} shown in eq. (1.7) and

$$\mathcal{Y}_t = \frac{m_t}{2m_W} \sqrt{\frac{4\pi\alpha}{\sin^2\theta_W}}, \quad (1.78)$$

in analogy with the coupling of the bottom quark to the Higgs in eq. (1.13). The mass of the top quark, however, is kept fixed and evaluated at its pole mass instead of being subject to renormalization.

In principle, we could consider bottom-quark loop contributions as well but we stick to a strict power counting of $\mathcal{O}(\mathcal{Y}_b^2)$, which is always satisfied by the decay. Bottom quark Yukawa-induced contributions in the production would contribute only from $\mathcal{O}(\mathcal{Y}_b^3)$.

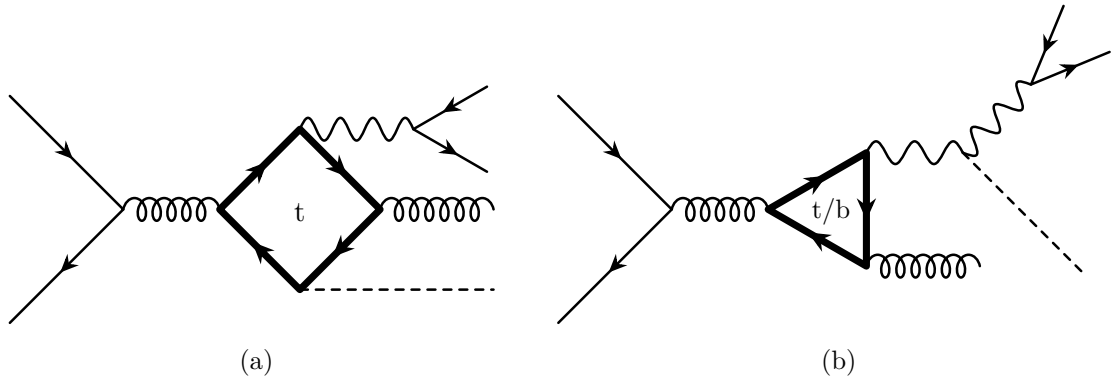


Figure 1.15: Examples of additional RII top-quark loop (a) and Drell–Yan-like top/bottom-quark loop amplitudes (b). They are *not included* in our calculations due to subpermille level numerical contributions.

As mentioned earlier, these contributions are infrared finite and do not require subtraction.

Additional Closed Fermion-Loop Contributions

While the RI top loop contributions are the only ones present for $W^\pm H$ production, there are additional amplitudes in case of ZH . These are all characterized by the neutral vector boson coupling to a closed fermion loop, which is allowed, as the Z coupling does not change quark flavours. For the sake of completeness, I will briefly recount them here but due to their negligible numerical contributions shown in ref. [28], they are *not included* in our predictions.

These infrared and ultraviolet finite closed fermion-loop contributions can be further separated into two subcategories. Yet again borrowing the notation of ref. [28], these are

1. **Yukawa-induced (RII):** both the Z and the Higgs boson directly couple to the fermion loop as shown in Figure 1.15a. As the only relevant Yukawa coupling is of the top quark, these are exclusively top loop contributions.
2. **Drell–Yan-like:** the Higgs couples to the Z boson. These amplitudes evaluate to zero in regular Drell–Yan production due to Furry’s theorem. The theorem does not apply however, when we replace the Drell–Yan amplitudes with non-momentum-conserving ones, yielding finite contributions. There is no dependence on the Yukawa coupling, and as such, all quark loops need to be evaluated but the up- and down-type light-quark loops cancel among each other. This cancellation is thwarted by the non-zero mass difference between the top and bottom quarks, as the top quark is evaluated at its pole mass while the bottom quark’s kinematic mass is kept zero. Therefore only

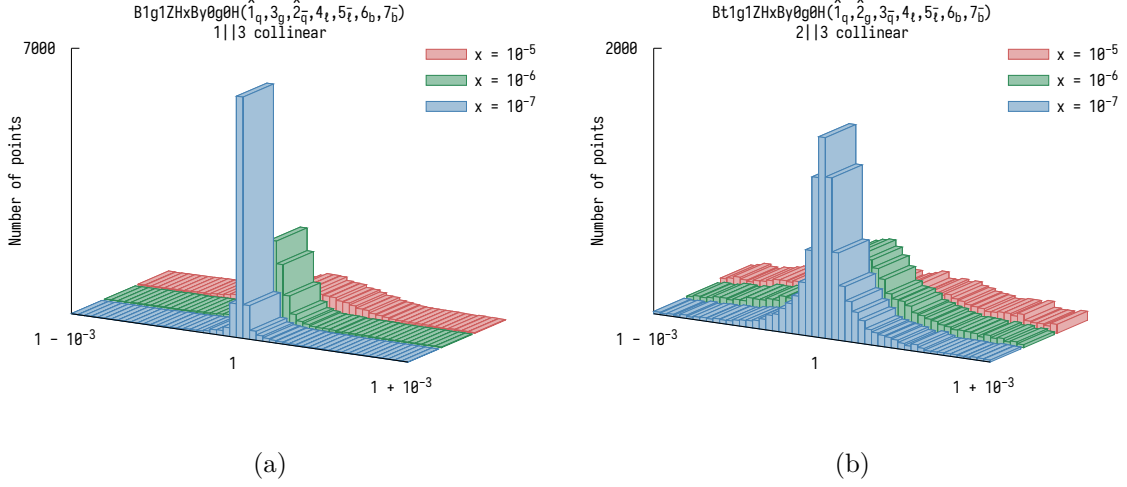


Figure 1.16: Spike tests for a $\hat{1}_q \parallel 3_g$ collinear limit in (a) for the $q\bar{q}$ -initiated leading-colour real-virtual amplitude $B_1^{\text{ZH},1}(\hat{1}_q, 3_g, \hat{2}_{\bar{q}}; 4_\ell, 5_{\bar{\ell}})$ and another one for the $\hat{2}_g \parallel 3_{\bar{q}}$ collinear limit in (b) for the qg -initiated subleading-colour real-virtual amplitude $\tilde{B}_1^{\text{ZH},1}(\hat{1}_q, \hat{2}_g, 3_{\bar{q}}; 4_\ell, 5_{\bar{\ell}})$. A total of 10000 configurations were probed in all cases. The amplitudes in the codebase already have the leading-order $H \rightarrow b\bar{b}$ decay attached.

the bottom- and top-quark loops shown in Figure 1.15b need to be evaluated.

Subtraction Terms $d\sigma_{\text{VH}}^{\text{T}}(1, 2, 3; 4_\ell, 5_{\bar{\ell}})$

Besides subtracting the infrared poles of the Drell-Yan-type loop amplitudes, these subtraction terms are also responsible for the mass factorization of the double-real cross sections and subtracting the soft and collinear limits of the real-virtual amplitudes. The subtraction terms are fully recycled from Drell-Yan production, therefore I will not reiterate them here. However, I note that pole cancellations have been tested analytically and spike tests, such as the ones shown in Figure 1.16 have been carried out in all unresolved limits.

The included RI top-loop amplitudes are infrared finite therefore no subtraction terms are needed for them.

1.5.3 Double-Virtual Production $d\sigma_{\text{VH}}^{\text{VV}}(1, 2; 3_\ell, 4_{\bar{\ell}})$

Double-virtual two-loop corrections are made of two components: (leading-order) \times (two-loop) and (one-loop) \times (one-loop) helicity-amplitude interferences. Therefore, besides the helicity amplitudes already derived at virtual level, we need genuine two-loop Feynman diagrams as well, such as the one shown in Figure 1.17. The two-loop Drell-Yan-like amplitudes denoted by $B_0^{\text{VH},2}$, along with their subleading-colour $\tilde{B}_0^{\text{VH},2}$, and n_{F} -proportional

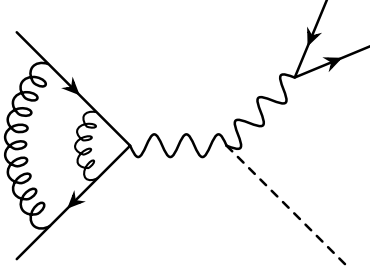


Figure 1.17: An example of a genuine Drell–Yan-like two-loop diagram that contributes to B -type amplitudes for double-virtual VH production.

$\hat{B}_0^{VH,2}$ companions are found in Appendix A.9. Just as with the leading-order and virtual cross sections, the only partonic channel contributing is

$$d\hat{\sigma}_{VH,q\bar{q}}^{VV} = \frac{\mathcal{N}_{VH}^{VV} \left(1 - \frac{1}{N_c^2}\right)}{(2N_c)^2} d\Phi_2^{\text{prod.}}(p_1, p_2; p_3, p_4; p_H) \times \left\{ B_0^{VH,2}(\hat{1}_q, \hat{2}_{\bar{q}}; 3_\ell, 4_{\bar{\ell}}) - \frac{1}{N_c} \tilde{B}_0^{VH,2}(\hat{1}_q, \hat{2}_{\bar{q}}; 3_\ell, 4_{\bar{\ell}}) + \frac{n_F}{N_c} \hat{B}_0^{VH,2}(\hat{1}_q, \hat{2}_{\bar{q}}; 3_\ell, 4_{\bar{\ell}}) \right\}. \quad (1.79)$$

Besides the B -type Drell–Yan-like amplitudes, there are important closed fermion-loop amplitudes present only for ZH production. The Z boson can couple directly to a fermion loop, which is not possible for the charged vector boson W^\pm due to the change in flavours. The phenomenologically important, i.e. numerically non-negligible ZH loop contributions are gluon–gluon-induced (one-loop)² amplitudes labelled collectively as $A_0^{ZH,2}$ in the NNLOJET framework. Thus the additional partonic cross section exclusively for ZH production is

$$d\hat{\sigma}_{ZH,gg}^{VV} = \frac{\mathcal{N}_{ZH}^{VV} \left(1 - \frac{1}{N_c^2}\right)}{[2(N_c^2 - 1)]^2} d\Phi_2^{\text{prod.}}(p_1, p_2; p_3, p_4; p_H) \frac{1}{16N_c} A_0^{ZH,2}(\hat{1}_g, \hat{2}_g; 3_\ell, 4_{\bar{\ell}}). \quad (1.80)$$

The averaging factor in the first denominator accounts for all possible polarization and colour states of the initial-state gluons. This time around, the amplitude $A_0^{ZH,2}$ also includes the top Yukawa coupling. This is due to the mixing of components with different dependence on it, therefore no single constant could be pulled out besides the factor $1/16N_c$ preceding the amplitude in eq. (1.80). These components, which are infrared and ultraviolet finite, are

1. **Yukawa-induced:** both the Z and the Higgs boson directly couple to the fermion loop as shown in Figure 1.18a. Only the top-quark loop is present due to the power counting of $\mathcal{O}(\mathcal{Y}_b^2)$ being already satisfied by the $H \rightarrow b\bar{b}$ decay.
2. **Drell–Yan-like:** the Higgs couples to the Z boson as shown in Figure 1.18b This is

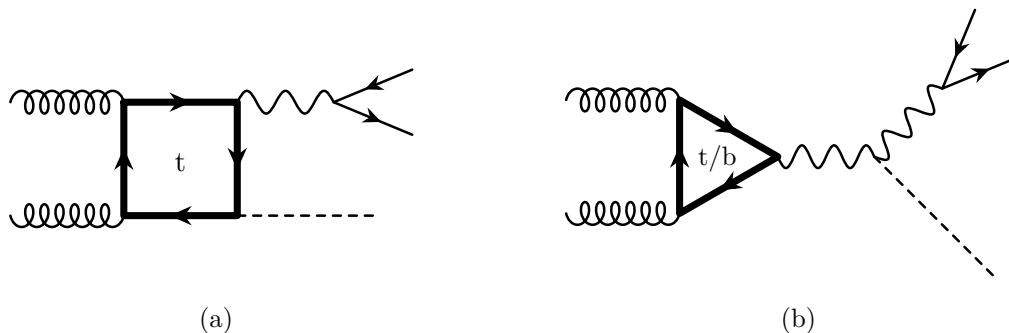


Figure 1.18: One-loop amplitudes contributing exclusively to the gluon–gluon-induced (one-loop)² double-virtual $A_0^{\text{ZH},2}$ production amplitude.

also a diagram that vanishes for the regular Drell–Yan process due to Furry’s theorem but is present here because some of the momenta is taken away by the Higgs boson, excluding it from the validity of mentioned theorem. Both bottom- and top-quark loops need to be evaluated.

In fact, we will see that these gluon–gluon-initiated contributions represent the dominant component of the ZH NNLO prediction due to the high gluon luminosity in LHC collisions; their phenomenological importance will be further emphasized by their distinguishing features when comparing ZH to $W^\pm H$ differential distributions.

The exact expressions for the helicity amplitudes comprising $A_0^{\text{ZH},2}$ are taken from the MCFM [51] codebase based on the work presented in ref. [33]. Although we could simplify this amplitude substantially compared to its original formulation⁶ it is still too long to include it meaningfully in this thesis, even for the appendices. Its implementation is nevertheless found in the A0g2ZH.f90 Fortran file in the NNLOJET codebase, in which we rely on the ONELOOP [54] library to evaluate the scalar integrals present in the amplitude.

Additional Closed Fermion-Loop Contributions

There are additional genuine two-loop amplitudes that we did not include in the calculations. They are not known in the full theory but were shown to be very tiny and phenomenologically irrelevant in ref. [28] with an approximation using an expansion around an infinite top-quark mass limit. Once again using the notation in the aforementioned publication, these include the following type of amplitudes

1. **Yukawa-induced (VI):** only the Higgs boson couples to the top loop, the vector boson W^\pm or Z does not, as shown in Figure 1.19a.

⁶We even uncovered a factor of 2 bug in the source MCFM formula.

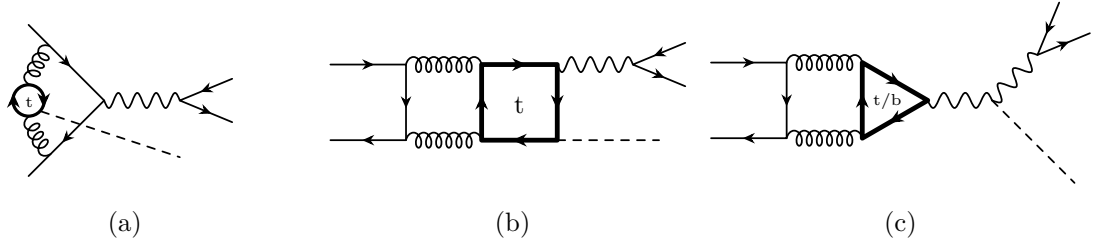


Figure 1.19: Example configurations of negligible genuine two-loop VI-type (a), VII-type (b), and Drell–Yan-like (c) contributions we *omit* from our calculation.

2. **Yukawa-induced (VII):** the Higgs and the Z boson both couple to the top loop as illustrated in Figure 1.19b. There are no corresponding W^\pm amplitude due to the change in flavours.
3. **Drell–Yan-like amplitudes:** these vanish in a regular Drell–Yan process due to Furry’s theorem but are present for ZH production as shown in Figure 1.19c where only the Z boson couples to the top- and bottom-quark loops, and the Higgs couples to the vector boson. There are no corresponding W^\pm amplitude here either.

Subtraction Terms $d\sigma_{VH}^U(1, 2; 3_\ell, 4_{\bar{\ell}})$

As the included new gg-induced (one-loop)² contributions are infrared finite, these subtraction terms are fully recycled from the already implemented Drell–Yan ones too, therefore I will not list them here. The number of channels are equal to the double-real case, because besides subtracting the poles coming from the Drell–Yan-like loop amplitudes, they also take care of infrared singularities related to mass factorization.

1.5.4 Double-Real Decay $d\sigma_{H\rightarrow b\bar{b}}^{\text{RR}}(i_b, j, k, l_{\bar{b}})$

Double-real corrections to the decay subprocess are written as

$$\begin{aligned}
 d\sigma_{H\rightarrow b\bar{b}}^{\text{RR}} &= \mathcal{N}_{H\rightarrow b\bar{b}}^{\text{RR}} \left(1 - \frac{1}{N_c^2}\right) d\Phi_4^{\text{dec.}}(p_H; p_i, p_j, p_k, p_l) \times \\
 &\quad \left\{ \frac{1}{2!} \left[\sum_{(j\leftrightarrow k)} B_2^{\text{H},0}(i_b, j_g, k_g, l_{\bar{b}}) - \frac{1}{N_c^2} \tilde{B}_2^{\text{H},0}(i_b, j_{\bar{g}}, k_{\bar{g}}, l_{\bar{b}}) \right] \right. \\
 &\quad \left. + \frac{1}{N_c} \left[(n_F - 1) C_0^{\text{H},0}(i_b, j_q, k_{\bar{q}}, l_{\bar{b}}) + \frac{1}{(2!)^2} \left(C_0^{\text{H},0}(i_b, j_b, k_{\bar{b}}, l_{\bar{b}}) + C_0^{\text{H},0}(i_b, j_b, l_{\bar{b}}, k_{\bar{b}}) \right) \right] \right\}
 \end{aligned}$$

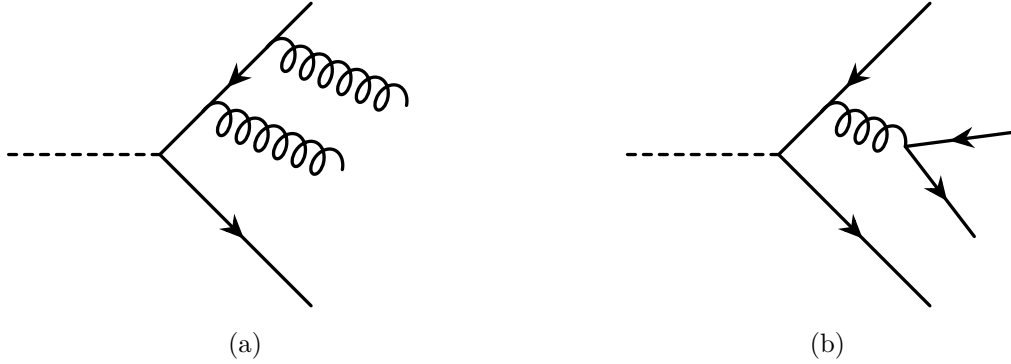


Figure 1.20: Examples contributing to B -type (a), and C - and D -type (b) double-real $H \rightarrow b\bar{b}$ decay amplitudes.

$$+ \left. \left. \left. \left. C_0^{\text{H},0}(j_b, i_b, k_{\bar{b}}, l_{\bar{b}}) + C_0^{\text{H},0}(j_b, i_b, l_{\bar{b}}, k_{\bar{b}}) - \frac{1}{N_c^2} D_0^{\text{H},0}(i_b, j_q, k_{\bar{q}}, l_{\bar{b}}) \right) \right] \right\}. \quad (1.81)$$

The amplitude $B_2^{\text{H},0}$ is the leading-colour contribution with one quark line and two gluon radiations; its subleading-colour counterpart is $\tilde{B}_2^{\text{H},0}$. Similarly, $C_0^{\text{H},0}$ is the leading-colour contribution with two quark lines and its subleading-colour identical-quark interference counterpart is $D_0^{\text{H},0}$. The denominators with the factorials account for the correct symmetry factors due to identical final-state particles. We omitted the bottom quark from the first C -type amplitude, i.e. $q \neq b$ and hence the $(n_F - 1)$ prefactor. This is due to the different symmetry factor we get when the $q = b$ quark is involved, as indicated by the prefactor in front of the rest of the C - and D -type contributions. In practice—as every particle is in the final state—the phase-space integral will automatically carry out the full permutation, therefore we can contract all the $B_2^{\text{H},0}$ and $C_0^{\text{H},0}$ terms with different particle orderings into single ones with a fixed one. This is how the implementation is done in the NNLOJET codebase.

Here, I must give credit to Sandro Della Torre and Andrew Lifson, who worked as master students in our group and their semester [55] and master-thesis [56] projects involved deriving the amplitudes $B_2^{\text{H},0}$, $\tilde{B}_2^{\text{H},0}$ and $C_0^{\text{H},0}$, $D_0^{\text{H},0}$, respectively. Contributing Feynman diagrams are visualized in Figure 1.20 and expressions for $C_0^{\text{H},0}$ and $D_0^{\text{H},0}$ are given in Appendices A.14 and A.15, respectively.

Double-Real Decay Subtraction $d\sigma_{H \rightarrow b\bar{b}}^{\text{S}}(i_b, j, k, l_{\bar{b}})$

These subtraction terms are completely new and did not recycle any of the past implementations in the codebase. Therefore I will give the full expression for them. Every amplitude

in eq. (1.81) needs a single subtraction term, and as such, the full expression is

$$\begin{aligned}
d\sigma_{H\rightarrow b\bar{b}}^S &= \mathcal{N}_{H\rightarrow b\bar{b}}^{\text{RR}} \left(1 - \frac{1}{N_c^2}\right) d\Phi_4^{\text{dec.}}(p_H; p_i, p_j, p_k, p_l) \times \\
&\left\{ \frac{1}{2!} \left[\sum_{(j\leftrightarrow k)} \text{By}2\text{g}\theta\text{H}(i_b, j_g, k_g, l_{\bar{b}}) - \frac{1}{N_c^2} \text{Bty}2\text{g}\theta\text{H}(i_b, j_{\bar{g}}, k_{\bar{g}}, l_{\bar{b}}) \right] \right. \\
&+ \frac{1}{N_c} \left[(n_F - 1) \text{Cy}\theta\text{g}\theta\text{H}(i_b, j_q, k_{\bar{q}}, l_{\bar{b}}) + \frac{1}{(2!)^2} \left(\text{Cy}\theta\text{g}\theta\text{H}(i_b, j_b, k_{\bar{b}}, l_{\bar{b}}) + \text{Cy}\theta\text{g}\theta\text{H}(i_b, j_b, l_{\bar{b}}, k_{\bar{b}}) \right. \right. \\
&\left. \left. + \text{Cy}\theta\text{g}\theta\text{H}(j_b, i_b, k_{\bar{b}}, l_{\bar{b}}) + \text{Cy}\theta\text{g}\theta\text{H}(j_b, i_b, l_{\bar{b}}, k_{\bar{b}}) - \frac{1}{N_c^2} \text{Dy}\theta\text{g}\theta\text{H}(i_b, j_q, k_{\bar{q}}, l_{\bar{b}}) \right) \right] \left. \right\}. \quad (1.82)
\end{aligned}$$

The three different subtraction amplitudes appearing are

$$\begin{aligned}
\text{By}2\text{g}\theta\text{HS}(i_b, j_g, k_g, l_{\bar{b}}) &= d_3^0(i, k, l) B_1^{\text{H},0}(\bar{i}_b, \bar{l}_g, j_{\bar{b}}) \\
&+ d_3^0(j, l, k) B_1^{\text{H},0}(i_b, \bar{k}_g, \bar{j}_{\bar{b}}) \\
&+ A_4^0(i, k, l, j) B_0^{\text{H},0}(\bar{i}_b, \bar{j}_{\bar{b}}) \\
&- d_3^0(i, k, l) A_3^0(\bar{i}, \bar{l}, j) B_0^{\text{H},0}(\bar{i}_b, \bar{j}_{\bar{b}}) \\
&- d_3^0(j, l, k) A_3^0(i, \bar{k}, \bar{j}) B_0^{\text{H},0}(\bar{i}_b, \bar{j}_{\bar{b}}), \quad (1.83)
\end{aligned}$$

$$\begin{aligned}
\text{Bty}2\text{g}\theta\text{HS}(i_b, j_{\bar{g}}, k_{\bar{g}}, l_{\bar{b}}) &= A_3^0(i, k, j) B_1^{\text{H},0}(\bar{i}_b, l_g, \bar{j}_{\bar{b}}) \\
&+ A_3^0(i, l, j) B_1^{\text{H},0}(\bar{i}_b, k_g, \bar{j}_{\bar{b}}) \\
&+ \tilde{A}_4^0(i, k, l, j) B_0^{\text{H},0}(\bar{i}_b, \bar{j}_{\bar{b}}) \\
&- A_3^0(i, k, j) A_3^0(\bar{i}, l, \bar{j}) B_0^{\text{H},0}(\bar{i}_b, \bar{j}_{\bar{b}}) \\
&- A_3^0(i, l, j) A_3^0(\bar{i}, k, \bar{j}) B_1^{\text{H},0}(\bar{i}_b, k_g, \bar{j}_{\bar{b}}), \quad (1.84)
\end{aligned}$$

$$\begin{aligned}
\text{Cy}\theta\text{g}\theta\text{HS}(i_b, j_q, k_{\bar{q}}, l_{\bar{b}}) &= \frac{1}{2} E_3^0(i, k, l) B_1^{\text{H},0}(\bar{i}_b, \bar{l}_g, j_{\bar{b}}) \\
&+ \frac{1}{2} E_3^0(j, l, k) B_1^{\text{H},0}(i_b, \bar{k}_g, \bar{j}_{\bar{b}}) \\
&+ B_4^0(i, k, l, j) B_0^{\text{H},0}(\bar{i}_b, \bar{j}_{\bar{b}})
\end{aligned}$$

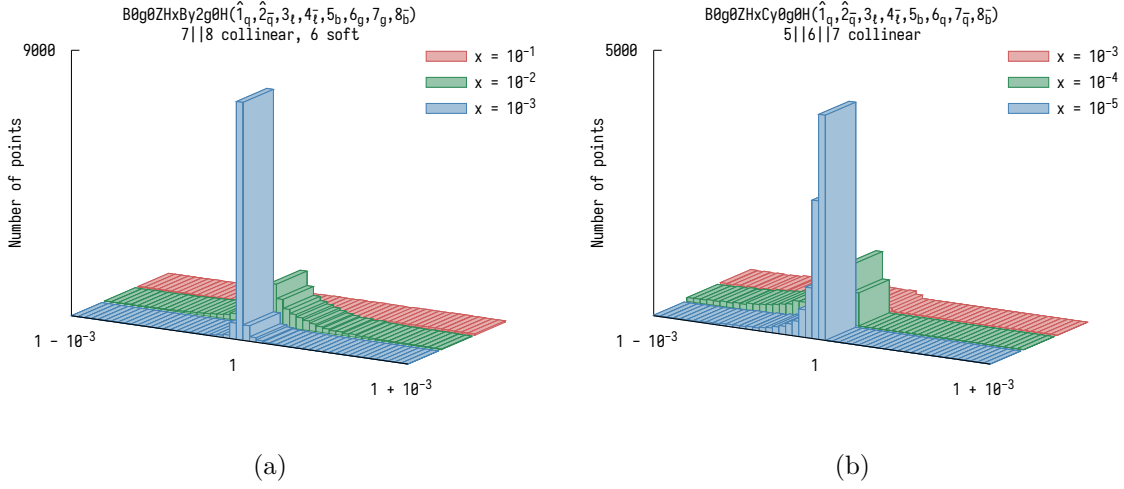


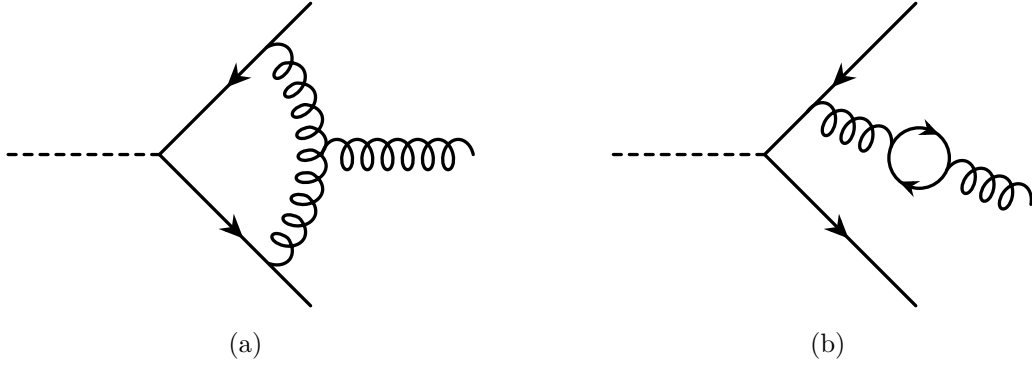
Figure 1.21: Spike tests for a simultaneous $7_g \parallel 8_{\bar{b}}$ collinear and 6_g soft limit in (a) for the double-real decay amplitude $B_2^{H,0}(5_b, 6_g, 7_g, 8_{\bar{b}})$; and a $5_b \parallel 6_q \parallel 7_q$ triple collinear limit in (b) for the double-real decay amplitude $C_0^{H,0}(5_b, 6_q, 7_q, 8_{\bar{b}})$. A total of 10000 configurations were probed in all cases. The amplitudes shown here all had leading-order ZH production attached to them.

$$\begin{aligned}
& -\frac{1}{2}E_3^0(i, k, l)A_3^0(\bar{i}, \bar{l}, j)B_0^{H,0}(\bar{i}_b, \bar{j}_{\bar{b}}) \\
& -\frac{1}{2}E_3^0(j, l, k)A_3^0(i, \bar{k}, \bar{j})B_0^{H,0}(\bar{i}_b, \bar{j}_{\bar{b}}), \tag{1.85}
\end{aligned}$$

$$\begin{aligned}
\text{Dy0g0HS}(i_b, j_b, k_{\bar{b}}, l_{\bar{b}}) &= 2C_4^0(i, k, l, j)B_0^{H,0}(\bar{i}_b, \bar{j}_{\bar{b}}) \\
& + 2C_4^0(j, l, k, i)B_0^{H,0}(\bar{j}_b, \bar{i}_{\bar{b}}) \\
& + 2C_4^0(l, j, i, k)B_0^{H,0}(\bar{l}_b, \bar{k}_{\bar{b}}) \\
& + 2C_4^0(k, i, j, l)B_0^{H,0}(\bar{k}_b, \bar{l}_{\bar{b}}). \tag{1.86}
\end{aligned}$$

The appearing final-final antennæ can be found in ref. [8] and the reduced matrix elements are all of lower order which have been discussed previously in Section 1.4.

Spike tests in all unresolved limits have also been carried out to affirm the validity of these subtraction terms, of which two examples are shown in Figure 1.21.

Figure 1.22: Examples contributing to the B -type real-virtual $H \rightarrow b\bar{b}$ decay amplitudes.

1.5.5 Real-Virtual Decay $d\sigma_{H \rightarrow b\bar{b}}^{\text{RV}}(i_b, j_g, k_{\bar{b}})$

The real-virtual decay cross section is

$$d\sigma_{H \rightarrow b\bar{b}}^{\text{RV}} = \mathcal{N}_{H \rightarrow b\bar{b}}^{\text{RV}} \left(1 - \frac{1}{N_c^2}\right) d\Phi_3^{\text{dec.}}(p_H; p_i, p_j, p_k) \times \left\{ B_1^{\text{H},1}(i_b, j_g, k_{\bar{b}}) - \frac{1}{N_c^2} \tilde{B}_1^{\text{H},1}(i_b, j_g, k_{\bar{b}}) + \frac{n_F}{N_c} \hat{B}_1^{\text{H},1}(i_b, j_g, k_{\bar{b}}) \right\}, \quad (1.87)$$

where $B_1^{\text{H},1}$ is the leading-colour, $\tilde{B}_1^{\text{H},1}$ is the subleading-colour amplitude, and $\hat{B}_1^{\text{H},1}$ is the piece proportional to the number of flavours. The amplitudes have been taken from ref. [37] and modified to fit the NNLOJET framework. The expression for all three of them is present in Appendix A.16 and examples of contributing diagrams that need to be interfered with the tree-level decay diagrams of Figure 1.8 are illustrated in Figure 1.22.

Real-Virtual Decay Subtraction $d\sigma_{H \rightarrow b\bar{b}}^{\text{T}}(i_b, j_g, k_{\bar{b}})$

The subtraction term responsible for subtracting the infrared limits and the explicit poles of the real-virtual amplitude (1.87) can be written as

$$d\sigma_{H \rightarrow b\bar{b}}^{\text{T}} = \mathcal{N}_{H \rightarrow b\bar{b}}^{\text{RV}} \left(1 - \frac{1}{N_c^2}\right) d\Phi_3^{\text{dec.}}(p_H; p_i, p_j, p_k) \times \left\{ \text{By1g1HT}(i_b, j_g, k_{\bar{b}}) - \frac{1}{N_c^2} \text{Bty1g1HT}(i_b, j_g, k_{\bar{b}}) + \frac{n_F}{N_c} \text{Bhy1g1HT}(i_b, j_g, k_{\bar{b}}) \right\}, \quad (1.88)$$

where the subtraction amplitudes explicitly are

$$\text{By1g1HT}(i_b, j_g, k_{\bar{b}}) = - \left[J_{2,qg}^{(1),\text{FF}}(i, k) + J_{2,qg}^{(1),\text{FF}}(j, k) \right] B_1^{\text{H},0}(i_b, k_g, j_{\bar{b}})$$

$$\begin{aligned}
& + A_3^0(i, k, j) B_0^{\text{H},1}(\bar{i}_b, \bar{j}_b) \\
& + A_3^1(i, k, j) B_0^{\text{H},0}(\bar{i}_b, \bar{j}_b) \\
& + \left[J_{2,qg}^{(1),\text{FF}}(i, k) + J_{2,qg}^{(1),\text{FF}}(j, k) \right] A_3^0(i, k, j) B_0^{\text{H},0}(\bar{i}_b, \bar{j}_b), \tag{1.89}
\end{aligned}$$

$$\begin{aligned}
\text{Bty1g1HT}(i_b, j_g, k_b) & = - J_{2,qq}^{(1),\text{FF}}(i, j) B_1^{\text{H},0}(i_b, k_g, j_b) \\
& + A_3^0(i, j, k) B_0^{\text{H},1}(\bar{i}_b, \bar{j}_b) \\
& + \tilde{A}_3^1(i, j, k) B_0^{\text{H},0}(\bar{i}_b, \bar{j}_b) \\
& + J_{2,qq}^{(1),\text{FF}}(i, j) A_3^0(i, k, j) B_0^{\text{H},0}(\bar{i}_b, \bar{j}_b), \tag{1.90}
\end{aligned}$$

$$\begin{aligned}
\text{Bhy1g1HT}(i_b, j_g, k_b) & = - \left[\hat{J}_{2,qg}^{(1),\text{FF}}(i, k) + \hat{J}_{2,qg}^{(1),\text{FF}}(j, k) \right] B_1^{\text{H},0}(i_b, k_g, j_b) \\
& + \hat{A}_3^1(i, k, j) B_0^{\text{H},0}(\bar{i}_b, \bar{j}_b) \\
& + \left[\hat{J}_{2,qg}^{(1),\text{FF}}(i, k) + \hat{J}_{2,qg}^{(1),\text{FF}}(j, k) \right] A_3^0(i, k, j) B_1^{\text{H},0}(i_b, k_g, j_b). \tag{1.91}
\end{aligned}$$

The integrated antennæ subtract poles of the loop amplitudes and the regular antennæ are responsible for mimicking the soft and collinear limits as usual. Explicit expressions for them are all found in ref. [8].

Once again, I tested that the poles of the real–virtual amplitudes and their corresponding subtraction terms cancel analytically and also carried out spike tests to verify the expected behaviour in all unresolved limits. Two examples of the latter are shown in Figure 1.23.

1.5.6 Double-Virtual Decay $d\sigma_{\text{H} \rightarrow \text{b}\bar{\text{b}}}^{\text{VV}}(i_b, k_b)$

The double-virtual decay cross section can be expressed as

$$\begin{aligned}
d\sigma_{\text{H} \rightarrow \text{b}\bar{\text{b}}}^{\text{VV}} & = \mathcal{N}_{\text{H} \rightarrow \text{b}\bar{\text{b}}}^{\text{VV}} \left(1 - \frac{1}{N_c^2} \right) d\Phi_2^{\text{dec.}}(p_H; p_i, p_j) \times \\
& \left\{ B_0^{\text{H},2}(i_b, j_b) - \frac{1}{N_c^2} \tilde{B}_0^{\text{H},2}(i_b, j_b) + \frac{n_F}{N_c} \hat{B}_0^{\text{H},2}(i_b, j_b) \right\}, \tag{1.92}
\end{aligned}$$

with the two-loop virtual amplitudes $B_0^{\text{H},2}$ standing for the leading-colour, $\tilde{B}_0^{\text{H},2}$ for the subleading-colour, and $\hat{B}_0^{\text{H},2}$ for the n_F -proportional contributions. An example of the genuine two-loop contributions that need to be interfered with the leading-order decay diagram

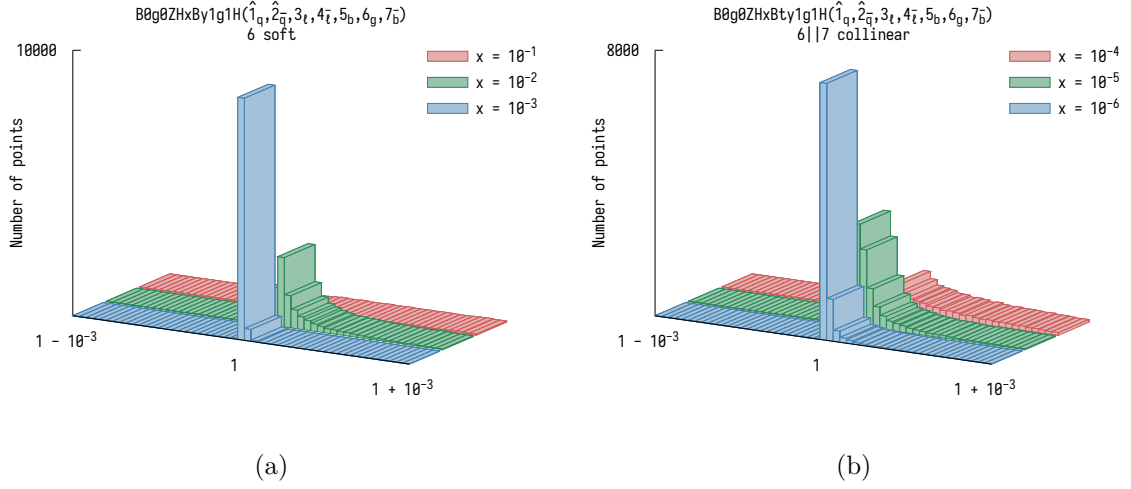


Figure 1.23: Spike tests for a soft 6_g limit in (a) for the leading-colour real-virtual decay amplitude $B_1^{\text{H},1}(5_{\bar{b}}, 6_g, 7_{\bar{b}})$; and a $6_g \parallel 7_{\bar{b}}$ collinear limit in (b) for the subleading-colour real-virtual decay amplitude $\tilde{B}_1^{\text{H},1}(5_{\bar{b}}, 6_q, 7_{\bar{b}})$. A total of 10000 configurations were probed in all cases. The amplitudes shown here all had leading-order ZH production attached to them.

of Figure 1.3 is illustrated in Figure 1.24. The amplitudes have been taken from ref. [37] and modified to fit the NNLOJET framework. In particular, the double-virtual U subtraction terms already had their Catani pole structure subtracted, therefore this had to be performed for the double-virtual matrix elements as well. I modified a script—originally written by Alexander Huss for Drell-Yan production—so that it is applicable to these $\text{H} \rightarrow \text{b}\bar{\text{b}}$ decay two-loop amplitudes as well. The resulting expressions for the B -type amplitudes appearing in (1.92) are found explicitly in Appendix A.17.

Double-Virtual Decay Subtraction $d\sigma_{\text{H} \rightarrow \text{b}\bar{\text{b}}}^{\text{U}}(i_{\text{b}}, k_{\bar{\text{b}}})$

The double-virtual decay subtraction term is the following:

$$d\sigma_{\text{H} \rightarrow \text{b}\bar{\text{b}}}^{\text{U}} = \mathcal{N}_{\text{H} \rightarrow \text{b}\bar{\text{b}}}^{\text{VV}} \left(1 - \frac{1}{N_c^2}\right) d\Phi_2^{\text{dec.}}(p_{\text{H}}; p_i, p_j) \times \left\{ \text{By}\theta\text{g}2\text{HU}(i_{\text{b}}, j_{\bar{\text{b}}}) - \frac{1}{N_c^2} \text{Bty}\theta\text{g}2\text{HU}(i_{\text{b}}, j_{\bar{\text{b}}}) + \frac{n_{\text{F}}}{N_c} \text{Bhy}\theta\text{g}2\text{HU}(i_{\text{b}}, j_{\bar{\text{b}}}) \right\}. \quad (1.93)$$

The individual subtraction amplitudes are

$$\text{By}\theta\text{g}2\text{HU}(i_{\text{b}}, j_{\bar{\text{b}}}) = -\mathcal{A}_3^0(i, j) \left[B_0^{\text{H},1}(i_{\text{b}}, j_{\bar{\text{b}}}) - \frac{b_0}{\epsilon} B_0^{\text{H},0}(i_{\text{b}}, j_{\bar{\text{b}}}) \right]$$

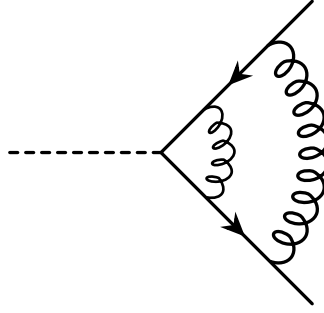


Figure 1.24: An example contribution to the double-virtual $H \rightarrow b\bar{b}$ decay amplitude.

$$-\frac{b_0}{\epsilon}(s_{ij})^{-\epsilon} \mathcal{A}_3^0(i, j) B_0^{\text{H},0}(i_b, j_{\bar{b}}), \quad (1.94)$$

$$\begin{aligned} \text{Bty0g2HU}(i_b, j_{\bar{b}}) &= -\mathcal{A}_3^0(i, j) B_0^{\text{H},1}(i_b, j_{\bar{b}}) \\ &\quad -\frac{1}{2} \tilde{\mathcal{A}}_4^0(i, j) B_0^{\text{H},0}(i_b, j_{\bar{b}}) \\ &\quad -2\mathcal{C}_4^0(i, j) B_0^{\text{H},0}(i_b, j_{\bar{b}}) \\ &\quad -\tilde{\mathcal{A}}_3^1(i, j) B_0^{\text{H},0}(i_b, j_{\bar{b}}), \end{aligned} \quad (1.95)$$

$$\begin{aligned} \text{Bhy0g2HU}(i_b, j_{\bar{b}}) &= +\frac{b_{0,\text{F}}}{\epsilon} \mathcal{A}_3^0(i, j) B_0^{\text{H},0}(i_b, j_{\bar{b}}) \\ &\quad -\mathcal{B}_4^0(i, j) B_0^{\text{H},0}(i_b, j_{\bar{b}}) \\ &\quad -\hat{\mathcal{A}}_3^1(i, j) B_0^{\text{H},0}(i_b, j_{\bar{b}}) \\ &\quad -\frac{b_{0,\text{F}}}{\epsilon} (s_{ij})^{-\epsilon} \mathcal{A}_3^0(i, j) B_0^{\text{H},0}(i_b, j_{\bar{b}}). \end{aligned} \quad (1.96)$$

The symbols b_0 and $b_{0,\text{F}}$ represent the colour decomposition of the first coefficient of the QCD β function

$$\beta_0 = b_0 N_c + b_{0,\text{F}} n_F \quad \text{with} \quad b_0 = \frac{11}{6} \quad \text{and} \quad b_{0,\text{F}} = -\frac{1}{3}. \quad (1.97)$$

Formulae for the integrated antennae are found in ref. [8].

Naturally, I tested the analytical pole cancellations between the double-virtual and their corresponding subtraction amplitudes here as well.

This concludes the list of all the contributions that are necessary for a combination of VH production with $H \rightarrow b\bar{b}$ decay at $\mathcal{O}(\alpha_s^2)$ precision. The next step was to produce integrated

cross sections and differential distributions in observables while using a jet algorithm suitable to this end.

1.6 Jet Clustering for the VH Process

The goal of this chapter of the thesis is to provide fixed-order predictions for the hadron-level process $pp \rightarrow \ell\bar{\ell} + 2 \text{ b-jets} + X$, i.e. yielding a final state that contains flavour-tagged bottom-quark jets (b-jets) and (charged) leptons. The presence of two identified b-jets with a combined invariant mass consistent with m_H allows us to associate this final state with the underlying process $pp \rightarrow VH + X \rightarrow \ell\bar{\ell} b\bar{b} + X$. The identification of jet flavour is an essential component of any experimental analysis of this process, which is required to reduce otherwise overwhelming background processes. It is therefore also an integral part of the requirements needed to obtain the corresponding theoretical predictions.

The computation of such observables at fixed order requires the application of a flavour-sensitive jet algorithm that—besides reconstructing flavour-insensitive properties such as four-momenta—identifies the flavour of the reconstructed jets based on some well-defined (infrared-safe) criteria. The theoretical discussion and specific implementation the flavour-tagging layer along with the infrared-safe flavour- k_t algorithm [43] into the NNLOJET code-base is described in detail in Chapter 3 of the thesis. Here we discuss a few specific points related to the application of the jet algorithm to the VH process, which will be relevant to the results presented in later sections of this thesis.

The first point is that we wish to apply the flavour- k_t algorithm to the partonic process $q\bar{q} \rightarrow VH \rightarrow \ell\bar{\ell} b\bar{b}$, including NNLO QCD corrections which were discussed in Section 1.5. When higher-order corrections are considered, additional light or b-quark partons can be emitted from both the production and decay sides, as illustrated in Figure 1.1. The jet clustering is performed by considering b-quarks to be flavoured (all other partons carrying zero flavour) and fully accounting for emissions from both production and decay during the jet clustering process. While our calculation focuses on the decay subprocess $H \rightarrow b\bar{b}$, it has been implemented in such a way that predictions for the hadronic process $pp \rightarrow \ell\bar{\ell} + 2 \text{ c-jets} + X$ can also be easily produced. This may be interesting in view of possible future measurements by the LHCb Collaboration [57].

The second point is that the definition of the transverse momentum of the beam k_{tB} in [43], also reviewed later in Section 3.2 is altered to account for the presence of a leptonically decaying gauge boson. This is done by modifying eq. (3.4) according to

$$\tilde{k}_{tB}(y) = k_{tB}(y) + E_{t,V} (\Theta(y_V - y) + \Theta(y - y_V)e^{y_V - y}), \quad (1.98)$$

where $E_{t,V}$ and y_V are the transverse energy and rapidity of the reconstructed gauge boson. A similar modification to the beam transverse momentum at negative rapidity (3.5) is assumed. This modification is introduced to provide a better estimate of the hardness of the beam, which can affect the clustering outcome. One could alternatively modify the beam hardness by including the charged leptons, which may be necessary in experimental situations where the gauge boson cannot be fully reconstructed.

1.7 Numerical Results

In this section I will present phenomenological results obtained for all three VH processes from our implementation in NNLOJET covered in previous sections. First, I will summarize the general setup in Section 1.7.1 then I will move on to discuss the obtained integrated fiducial cross sections in Section 1.7.2. Lastly, I devote Section 1.7.3 to the description and validation of the scale dependence of the numerical results and will present differential distributions for flavour-sensitive observables in Section 1.7.4.

1.7.1 General Setup

We have generated predictions for proton–proton collisions at $\sqrt{s} = 13$ TeV using the parton distribution function NNPDF31_nnlo_as_0118 provided via the LHAPDF library [58]. Each event was required to contain at least two b-jets with transverse momentum $p_{\perp,b} > 25$ GeV and rapidity $|y_b| < 2.5$. Charged leptons were required to have a transverse momentum above $p_{\perp,\ell} > 15$ GeV and their rapidity had to satisfy $|y_\ell| < 2.5$. For the $W^\pm H$ processes, we additionally demanded a minimum missing transverse energy of $E_{\perp,\text{miss}} > 15$ GeV to identify the neutrino in the final state. We used the flavour- k_t algorithm with an even-tag exclusion to cluster b-jets as described in Sections 3.2 and 1.6 with the parameters $R = 0.5$ and $\alpha = 2$.

We employed the G_μ scheme for the electroweak input parameters with the full set of independent parameters entering the computation given by

$$\begin{aligned} m_Z &= 91.1876 \text{ GeV}, & m_W &= 80.385 \text{ GeV}, & m_H &= 125.09 \text{ GeV}, \\ \Gamma_Z &= 2.4952 \text{ GeV}, & \Gamma_W &= 2.085 \text{ GeV}, & \Gamma_H &= 4.1 \text{ MeV}, \\ \overline{m}_b(\overline{m}_b) &= 4.18 \text{ GeV}, & m_t^{\text{pole}} &= 173.21 \text{ GeV}, & G_F &= 1.166\,378\,7 \times 10^{-5} \text{ GeV}^{-2}. \end{aligned} \quad (1.99)$$

The running of the strong coupling α_s was evaluated using the LHAPDF library with the associated PDF set, while the $\overline{\text{MS}}$ mass of the bottom quark \overline{m}_b at the given renormalization

	W ⁺ H	W ⁻ H	ZH
σ_{LO} [fb]	18.06 ^{+2.87} _{-2.41}	11.96 ^{+1.90} _{-1.60}	4.83 ^{+0.77} _{-0.65}
σ_{NLO} [fb]	21.52 ^{+0.88} _{-1.08}	14.21 ^{+0.58} _{-0.71}	5.71 ^{+0.22} _{-0.28}
σ_{NNLO} [fb]	20.68 ^{+0.16} _{-0.46}	13.64 ^{+0.11} _{-0.31}	5.92 ^{+0.13} _{-0.16}

Table 1.1: The fiducial cross sections for all VH processes according to the setup of Section 1.7.1. The error on the values represents the theoretical uncertainty which was obtained by taking the minimum and maximum values of the 21-point scale variation.

scale was directly computed within NNLOJET using an implementation of ref. [59]. Finally, in the case of W[±]H production, we assumed a diagonal CKM matrix for the vector-boson–quark couplings.

For the unphysical scales appearing in the calculation, we chose to set and vary them independently for the production and decay parts. The central factorization and renormalization scales of the production subprocesses were chosen as the invariant mass of the VH system M_{VH} , whereas the central renormalization scale of the decay was set to the Higgs-boson mass m_{H} . We evaluated the differential cross section for a total of 21 different scale settings that are obtained from all possible combinations of

$$\mu_{\text{F}} = M_{\text{VH}} \left[1, \frac{1}{2}, 2\right], \quad \mu_{\text{R}}^{\text{prod.}} = M_{\text{VH}} \left[1, \frac{1}{2}, 2\right], \quad \mu_{\text{R}}^{\text{dec.}} = m_{\text{H}} \left[1, \frac{1}{2}, 2\right], \quad (1.100)$$

with the additional constraint $\frac{1}{2} \leq \mu_{\text{F}}/\mu_{\text{R}}^{\text{prod.}} \leq 2$ following the conventional 7-point scale variation for the production subprocess.

1.7.2 Fiducial Cross Section

The integrated cross-section predictions including fiducial cuts for the different VH processes are summarized in Table 1.1 at the various orders in α_{S} .

Regarding the W[±]H fiducial values, we observe an $\mathcal{O}(20\%)$ increase in the cross section from the NLO corrections and a slight $\mathcal{O}(5\%)$ decrease when going from NLO to NNLO. The minimum and the maximum values of the 21-point scale variations yield the theoretical uncertainties of our predictions, which are $\mathcal{O}(15\%)$ at LO, $\mathcal{O}(5\%)$ at NLO, and reduce to only $\mathcal{O}(2\%)$ at NNLO with a three-fold asymmetry between the lower and upper bounds of the latter values. The decrease in the size of the theoretical uncertainty is apparent at each of these orders, demonstrating the perturbative convergence of these results in a satisfying

manner. This will be further accentuated for flavour-sensitive jet observables in Section 1.7.4.

For the ZH fiducial values we see a different behaviour beyond NLO: the gluon–gluon-induced (one-loop)² contributions of Figures 1.18a and 1.18b dominate the NNLO coefficient, such that there is an $\mathcal{O}(4\%)$ increase going from NLO to NNLO, contrasting the decrease seen for the $W^\pm H$ case. The ZH-exclusive channels open up at NNLO, and therefore the theoretical uncertainty does not exhibit such a strong reduction in size but remains around $\mathcal{O}(3\%)$.

The reduction of scale uncertainties observed here is spoiled in all cases when a rescaling prescription is employed that incorporates a fixed branching ratio for the $H \rightarrow b\bar{b}$ decay, as is commonly done in previous calculations, such as [33–35]. The cross sections in these calculations are assembled in a different manner compared to our expression of eq. (1.1). Specifically, the Higgs decay at the different orders is scaled up to a fixed value of the accurately known branching ratio of the $H \rightarrow b\bar{b}$ process. Let us review how the cross section is assembled in this case to better understand why we opted to use the more naïve formula of eq. (1.1) instead. Up to NNLO the cross sections in the scaled formulation of refs. [33–35] read

$$d\sigma_{\text{LO}}^{\text{scaled}} = \int \frac{d^d p_H}{(2\pi)^d} d\sigma_{VH}^{(0)} \times \left(d\sigma_{H \rightarrow b\bar{b}}^{(0)} \right) \times K^{(0)} \mathcal{J}_{2_b}, \quad (1.101)$$

$$d\sigma_{\text{NLO}}^{\text{scaled}} = \int \frac{d^d p_H}{(2\pi)^d} \left[d\sigma_{VH}^{(1)} \times d\sigma_{H \rightarrow b\bar{b}}^{(0)} \times K^{(0)} \right. \\ \left. + d\sigma_{VH}^{(0)} \times \left(d\sigma_{H \rightarrow b\bar{b}}^{(0)} + d\sigma_{H \rightarrow b\bar{b}}^{(1)} \right) \times K^{(1)} \right] \mathcal{J}_{2_b}, \quad (1.102)$$

$$d\sigma_{\text{NNLO}}^{\text{scaled}} = \int \frac{d^d p_H}{(2\pi)^d} \left[d\sigma_{VH}^{(2)} \times d\sigma_{H \rightarrow b\bar{b}}^{(0)} \times K^{(0)} \right. \\ \left. + d\sigma_{VH}^{(1)} \times \left(d\sigma_{H \rightarrow b\bar{b}}^{(0)} + d\sigma_{H \rightarrow b\bar{b}}^{(1)} \right) \times K^{(1)} \right. \\ \left. + d\sigma_{VH}^{(0)} \times \left(d\sigma_{H \rightarrow b\bar{b}}^{(0)} + d\sigma_{H \rightarrow b\bar{b}}^{(1)} + d\sigma_{H \rightarrow b\bar{b}}^{(2)} \right) \times K^{(2)} \right] \mathcal{J}_{2_b}. \quad (1.103)$$

The scaling factors $K^{(i)}$ contain the branching ratio and are given by

$$K^{(i)} = \frac{\text{Br}(H \rightarrow b\bar{b}) \Gamma_H}{\sum_{j=0}^i \Gamma_{H \rightarrow b\bar{b}}^{(j)}}. \quad (1.104)$$

The branching ratio $\text{Br}(H \rightarrow b\bar{b})$ is kept fixed and is not a subject to an α_s expansion. Let us elaborate on possible drawbacks that this prescription entails, in particular concerning

	W ⁺ H	W ⁻ H	ZH
$\sigma_{\text{LO}}^{\text{scaled}}$ [fb]	22.52 ^{+0.63} _{-0.80}	14.91 ^{+0.42} _{-0.54}	6.02 ^{+0.17} _{-0.21}
$\sigma_{\text{NLO}}^{\text{scaled}}$ [fb]	22.87 ^{+0.76} _{-0.87}	15.11 ^{+0.51} _{-0.58}	6.06 ^{+0.20} _{-0.23}
$\sigma_{\text{NNLO}}^{\text{scaled}}$ [fb]	20.93 ^{+0.61} _{-0.73}	13.80 ^{+0.41} _{-0.49}	6.10 ^{+0.31} _{-0.31}

Table 1.2: The scaled fiducial cross sections at each perturbative order up to $\mathcal{O}(\alpha_s^2)$ for all VH processes according to the setup of eqs. (1.101)–(1.103) used in refs. [33–35]. Contrast the values and their theoretical uncertainties with those presented in Table 1.1.

theory uncertainties estimated through scale variations.

Firstly, the scaling factors effectively divide out the Yukawa coupling $\mathcal{Y}_b \propto \overline{m}_b(\mu_R^{\text{dec.}})$ from the prediction. As a result, any running of the mass in the $\overline{\text{MS}}$ scheme exactly cancels in the final result. This can lead to underestimating the uncertainties, which is especially apparent at LO where the scale dependence of the Yukawa coupling otherwise dominates the uncertainties.

Secondly, analyzing the structure of the scaled cross sections at NLO (1.102) and NNLO (1.103), it is apparent that they are assembled as a sum of terms where different scaling factors $K^{(i)}$ accompany the different perturbative coefficients of the production cross section $d\sigma_{\text{VH}}^{(j)}$. This mismatch can interfere with the compensation mechanism between terms of different orders, possibly distorting the theory error estimate obtained through variations of the production scale $\mu_R^{\text{prod.}}$.

To quantify the differences between the two approaches, we reported the fiducial cross sections in Table 1.2 obtained according to (1.101)–(1.103) using $\text{Br}(\text{H} \rightarrow \text{b}\bar{\text{b}}) = 58.09\%$ [60]. Comparing these predictions with those given in Table 1.1 using the unscaled cross section of eq. (1.1), we observe that the central value of the LO prediction is substantially improved in the scaled predictions thanks to absorbing higher-order effects into the $\text{H} \rightarrow \text{b}\bar{\text{b}}$ decay through the branching ratio. At NLO, however, the scaled prediction appears to slightly overestimate the cross section, while the associated theory uncertainties are comparable in size between the two formulations. At NNLO, both prescriptions agree well in their respective central values, however, sizable differences can be seen in their associated uncertainties. The scaled predictions at NNLO show almost no reduction in scale uncertainties—even increasing for ZH—compared to the respective NLO number, whereas our formulation (1.1) exhibits a substantial reduction in theoretical uncertainties when going from NLO to NNLO. This difference can be attributed to the aforementioned compensation of scale dependences, which

is spoiled by the different rescaling factors used in eq. (1.103).

The effects of dividing out the Yukawa coupling in the decay and the scaling factor mismatch during the assembly of production cross sections are apparent as the theoretical uncertainties of the NNLO cross section barely change compared to their NLO values. In our opinion, the consistent treatment of theoretical uncertainties outweighs the precision gain that one might (or might not) get by scaling to a fixed branching ratio, especially in the case of NNLO-accurate observables. This further motivates our initial and simpler formulation we presented in eq. (1.1) where no scaling factors are applied.

1.7.3 Scale Variations

Verifying the dependence on the renormalization scales $\mu_R^{\text{prod.}}$ and $\mu_R^{\text{dec.}}$ can serve as a non-trivial check of the final results obtained from the numerical computation, in which cross sections are calculated independently at different scales. This is especially important after the previous section where we argued in favour of selecting a more naïve assembly convention of the factorized production and decay cross sections, in contrast to the one established in the literature, because this gave us a better handle at the theoretical uncertainties. To this end, we must validate that the different scale settings of eq. (1.100) are correctly reproduced by the analytic renormalization-group running starting from the central scale choice. The analytic expressions for the dependence on $\mu_R^{\text{prod.}}$ have been explicitly derived and given in ref. [61] and as such, I will not repeat them here.

The dependence (of the decay cross section) on $\mu_R^{\text{dec.}}$ can be derived in a similar fashion, so let us go through that instead, since I could not find it in existing literature. The running of the strong coupling α_s is governed by the β function

$$\mu^2 \frac{d\alpha_s(\mu)}{d\mu^2} = \beta(\alpha_s(\mu)) = -\alpha_s(\mu) \left[\beta_0 \left(\frac{\alpha_s(\mu)}{2\pi} \right) + \beta_1 \left(\frac{\alpha_s(\mu)}{2\pi} \right)^2 + \beta_2 \left(\frac{\alpha_s(\mu)}{2\pi} \right)^3 + \mathcal{O}(\alpha_s^4) \right], \quad (1.105)$$

with the QCD ($N_c = 3$) β function coefficients

$$\begin{aligned} \beta_0 &= \frac{1}{2} \left[11 - \frac{2}{3} n_F \right], \\ \beta_1 &= \frac{1}{4} \left[102 - \frac{38}{3} n_F \right], \\ \beta_2 &= \frac{1}{8} \left[\frac{2857}{2} - \frac{5033}{18} n_F + \frac{325}{54} n_F^2 \right]. \end{aligned} \quad (1.106)$$

By solving eq. (1.105), we get the formula

$$\alpha_s(\mu_0) = \alpha_s(\mu_R) \left[1 + \beta_0 L_R \left(\frac{\alpha_s(\mu_R)}{2\pi} \right) + \left(\beta_0^2 L_R^2 + \beta_1 L_R \right) \left(\frac{\alpha_s(\mu_R)}{2\pi} \right)^2 + \mathcal{O}(\alpha_s^3) \right], \quad (1.107)$$

where the strong coupling α_s at a fixed scale μ_0 is expressed order-by-order with α_s evaluated at a different scale μ_R , as seen in ref. [61], from where we also borrowed the notation

$$L_R = \ln \left(\frac{\mu_R}{\mu_0} \right). \quad (1.108)$$

The running of the $\overline{\text{MS}}$ mass \overline{m}_b is governed by the mass anomalous dimension γ_m via the differential equation

$$\begin{aligned} \mu^2 \frac{d\overline{m}_b(\mu)}{d\mu^2} &= \overline{m}_b(\mu) \gamma_m(\alpha_s(\mu)) \\ &= -\overline{m}_b(\mu) \left[\gamma_0 \left(\frac{\alpha_s(\mu)}{2\pi} \right) + \gamma_1 \left(\frac{\alpha_s(\mu)}{2\pi} \right)^2 + \gamma_2 \left(\frac{\alpha_s(\mu)}{2\pi} \right)^3 + \mathcal{O}(\alpha_s^4) \right], \end{aligned} \quad (1.109)$$

with the QCD mass anomalous dimension coefficients⁷

$$\begin{aligned} \gamma_0 &= 2, \\ \gamma_1 &= \frac{1}{2} \left[\frac{202}{3} - \frac{20}{9} n_F \right], \\ \gamma_2 &= \frac{1}{8} \left[1249 + \left(-\frac{2216}{27} - \frac{160}{3} \zeta_3 \right) n_F - \frac{140}{81} n_F^2 \right]. \end{aligned} \quad (1.110)$$

As seen in ref. [59], solving eq. (1.109) to express the mass \overline{m}_b at a fixed scale μ_0 can be written in the integral form

$$\overline{m}_b(\mu_0) = \overline{m}_b(\mu_R) \exp \left[\int_{\alpha_s(\mu_R)}^{\alpha_s(\mu_0)} d\alpha \frac{\gamma_m(\alpha)}{\beta(\alpha)} \right]. \quad (1.111)$$

Subsequently, the integrand can be expanded up to $\mathcal{O}(\alpha)$ using eqs. (1.105) and (1.109).

⁷The coefficients β_k in eqs. (1.106) and γ_k in eqs. (1.110) differ to those in ref. [59] with a factor 2^{k+1} due to our convention of expanding in $\frac{\alpha_s}{2\pi}$ instead of $\frac{\alpha_s}{\pi}$.

Performing the integral then gives

$$\bar{m}_b(\mu_0) = \bar{m}_b(\mu_R) \left(\frac{\alpha_s(\mu_0)}{\alpha_s(\mu_R)} \right)^{\frac{\gamma_0}{\beta_0}} \exp \left[A_1 \frac{\alpha_s(\mu_0) - \alpha_s(\mu_R)}{2\pi} + \frac{A_2}{2} \frac{\alpha_s^2(\mu_0) - \alpha_s^2(\mu_R)}{(2\pi)^2} + \mathcal{O}(\alpha_s^3) \right], \quad (1.112)$$

borrowing the notation of ref. [59] for the constants

$$A_1 = -\frac{\beta_1 \gamma_0}{\beta_0^2} + \frac{\gamma_1}{\beta_0} \quad \text{and} \quad A_2 = \frac{\gamma_0}{\beta_0^2} \left(\frac{\beta_1^2}{\beta_0} - \beta_2 \right) - \frac{\beta_1 \gamma_1}{\beta_0^2} + \frac{\gamma_2}{\beta_0}. \quad (1.113)$$

Plugging in eq. (1.107) into eq. (1.112) and then expanding in α_s up to second order yields the formula for the running of \bar{m}_b in terms of $\alpha_s(\mu_R)$:

$$\bar{m}_b(\mu_0) = \bar{m}_b(\mu_R) \left[1 + \gamma_0 L_R \left(\frac{\alpha_s(\mu_R)}{2\pi} \right) + \left(\frac{\gamma_0(\beta_0 + \gamma_0)}{2} L_R^2 + \gamma_1 L_R \right) \left(\frac{\alpha_s(\mu_R)}{2\pi} \right)^2 + \mathcal{O}(\alpha_s^3) \right]. \quad (1.114)$$

Let us change notation slightly for the formula of the $H \rightarrow b\bar{b}$ decay cross section by detaching the scale-dependent couplings, i.e. the strong coupling α_s and the $\overline{\text{MS}}$ bottom-quark mass \bar{m}_b . Indicating the scale dependences explicitly, the decay cross section up to NNLO is written as

$$\sigma_{H \rightarrow b\bar{b}}(\mu_0, \alpha_s(\mu_0), \bar{m}_b(\mu_0)) = \bar{m}_b^2(\mu_0) \times \left[\sigma_{H \rightarrow b\bar{b}}^{(0)} + \left(\frac{\alpha_s(\mu_0)}{2\pi} \right) \sigma_{H \rightarrow b\bar{b}}^{(1)}(\mu_0) + \left(\frac{\alpha_s(\mu_0)}{2\pi} \right)^2 \sigma_{H \rightarrow b\bar{b}}^{(2)}(\mu_0) + \mathcal{O}(\alpha_s^3) \right], \quad (1.115)$$

where it is always understood that $\mu_0 = \mu_{R_0}^{\text{dec.}}$ is the decay renormalization scale. Inserting eqs. (1.107) and (1.114) into eq. (1.115) and keeping terms up to $\mathcal{O}(\alpha_s^2)$ gives

$$\begin{aligned} \sigma_{H \rightarrow b\bar{b}}(\mu_R, \alpha_s(\mu_R), \bar{m}_b(\mu_R)) &= \bar{m}_b^2(\mu_R) \times \\ &\left[\sigma_{H \rightarrow b\bar{b}}^{(0)} + \left(\frac{\alpha_s(\mu_R)}{2\pi} \right) \left\{ 2\gamma_0 L_R \sigma_{H \rightarrow b\bar{b}}^{(0)} + \sigma_{H \rightarrow b\bar{b}}^{(1)}(\mu_0) \right\} \right. \\ &+ \left(\frac{\alpha_s(\mu_R)}{2\pi} \right)^2 \left\{ \left(\gamma_0(\beta_0 + 2\gamma_0) L_R^2 + 2L_R \gamma_1 \right) \sigma_{H \rightarrow b\bar{b}}^{(0)} \right. \\ &\left. \left. + (\beta_0 + 2\gamma_0) L_R \sigma_{H \rightarrow b\bar{b}}^{(1)}(\mu_0) + \sigma_{H \rightarrow b\bar{b}}^{(2)}(\mu_0) \right\} + \mathcal{O}(\alpha_s^3) \right]. \quad (1.116) \end{aligned}$$

If we compare eq. (1.116) to the decay cross section

$$\sigma_{\text{H}\rightarrow\text{b}\bar{\text{b}}}(\mu_{\text{R}}, \alpha_{\text{s}}(\mu_{\text{R}}), \bar{m}_{\text{b}}(\mu_{\text{R}})) = \bar{m}_{\text{b}}^2(\mu_{\text{R}}) \times \left[\sigma_{\text{H}\rightarrow\text{b}\bar{\text{b}}}^{(0)} + \left(\frac{\alpha_{\text{s}}(\mu_{\text{R}})}{2\pi} \right) \sigma_{\text{H}\rightarrow\text{b}\bar{\text{b}}}^{(1)}(\mu_{\text{R}}) + \left(\frac{\alpha_{\text{s}}(\mu_{\text{R}})}{2\pi} \right)^2 \sigma_{\text{H}\rightarrow\text{b}\bar{\text{b}}}^{(2)}(\mu_{\text{R}}) + \mathcal{O}(\alpha_{\text{s}}^3) \right], \quad (1.117)$$

evaluated a priori at renormalization scale μ_{R} , we can identify the analytic formulæ that define the running of decay cross-section pieces under scale variations. Explicitly these are

$$\sigma_{\text{H}\rightarrow\text{b}\bar{\text{b}}}^{(0)}(\mu_{\text{R}}) = \sigma_{\text{H}\rightarrow\text{b}\bar{\text{b}}}^{(0)}(\mu_0) = \sigma_{\text{H}\rightarrow\text{b}\bar{\text{b}}}^{(0)}, \quad (1.118)$$

$$\sigma_{\text{H}\rightarrow\text{b}\bar{\text{b}}}^{(1)}(\mu_{\text{R}}) = 2\gamma_0 L_{\text{R}} \sigma_{\text{H}\rightarrow\text{b}\bar{\text{b}}}^{(0)} + \sigma_{\text{H}\rightarrow\text{b}\bar{\text{b}}}^{(1)}(\mu_0), \quad (1.119)$$

$$\begin{aligned} \sigma_{\text{H}\rightarrow\text{b}\bar{\text{b}}}^{(2)}(\mu_{\text{R}}) &= \left[\gamma_0(\beta_0 + 2\gamma_0) L_{\text{R}}^2 + 2L_{\text{R}}\gamma_1 \right] \sigma_{\text{H}\rightarrow\text{b}\bar{\text{b}}}^{(0)} \\ &+ (\beta_0 + 2\gamma_0) L_{\text{R}} \sigma_{\text{H}\rightarrow\text{b}\bar{\text{b}}}^{(1)}(\mu_0) + \sigma_{\text{H}\rightarrow\text{b}\bar{\text{b}}}^{(2)}(\mu_0). \end{aligned} \quad (1.120)$$

The combined analytic variation of production and decay renormalization scales have been implemented into NNLOJET as a separate module for the first time, which we can use to double-check the cross sections that we obtained via independent numerical evaluations. The comparison between the analytic evolution and the 21 points obtained from the numerical computation using NNLOJET is shown in Figure 1.25 for the case of the W^+H process at NLO (a–c) and NNLO (d–f). We performed a scan in the two-dimensional $(\mu_{\text{R}}^{\text{prod.}}, \mu_{\text{R}}^{\text{dec.}})$ space by choosing three different slices that cover the combinations in eq. (1.100) where the three choices in the factorization scale $\mu_{\text{F}} = M_{\text{WH}} \left[1, \frac{1}{2}, 2 \right]$ are shown as separate curves:

(a,d) We keep the decay renormalization scale fixed to $\mu_{\text{R}}^{\text{dec.}} = m_{\text{H}}$ and vary the scale in the production subprocess according to

$$\mu_{\text{R}}^{\text{prod.}} = K_{\text{R}}^{\text{prod.}} \times M_{\text{WH}} \quad \text{with} \quad K_{\text{R}}^{\text{prod.}} \in \left[\frac{1}{2}, 2 \right]. \quad (1.121)$$

(b,e) We keep the production renormalization scale fixed to $\mu_{\text{R}}^{\text{prod.}} = M_{\text{WH}}$ and vary the scale in the decay subprocess according to

$$\mu_{\text{R}}^{\text{dec.}} = K_{\text{R}}^{\text{dec.}} \times m_{\text{H}} \quad \text{with} \quad K_{\text{R}}^{\text{dec.}} \in \left[\frac{1}{2}, 2 \right]. \quad (1.122)$$

(c,f) We choose a diagonal slice in the $(\mu_{\text{R}}^{\text{prod.}}, \mu_{\text{R}}^{\text{dec.}})$ plane setting $K_{\text{R}}^{\text{prod.}} = K_{\text{R}}^{\text{dec.}} \equiv K_{\text{R}}$ with

the individual scales given as

$$\mu_{\text{R}}^{\text{prod.}} = K_{\text{R}} \times M_{\text{WH}} \quad \text{and} \quad \mu_{\text{R}}^{\text{dec.}} = K_{\text{R}} \times m_{\text{H}} \quad \text{with} \quad K_{\text{R}} \in \left[\frac{1}{2}, 2\right]. \quad (1.123)$$

Note that the invariant mass M_{WH} constitutes a dynamical quantity that varies on an event-by-event basis. The curves in Figure 1.25 are obtained by picking the specific bin $M_{\text{WH}} \in [220, 230]$ GeV to assign a value to the production scale, where the widths of the bands in the smooth curves correspond to the uncertainty that arises from the finite bin width.

We observe an excellent agreement between the numerical results from NNLOJET and the curves predicted from the renormalization group equations. The dramatic reduction in scale uncertainties can be further appreciated by contrasting the vertical ranges in the figures at NLO (left) and NNLO (right). We carried out the same tests also for the W^-H and the ZH processes as well as for other individual M_{VH} bins in the distributions and found that the scale variation of the numerical results match the analytical formulæ in all cases.

1.7.4 Distributions

In Figures 1.26–1.28 we present differential distributions of flavour-sensitive observables for the three different associated Higgs boson production processes W^+H , W^-H , and ZH. We focused on this set of observables in order to allow for a qualitative comparison with refs. [34, 35]. The observables in question are

- (a) the transverse momentum $p_{\perp, \text{b}}$ of the leading b-jet,
- (b) the transverse momentum $p_{\perp, \text{bb}}$ of a pair of two b-jets,
- (c) the angular separation $\Delta R_{\text{bb}} = \sqrt{\Delta\eta_{\text{bb}}^2 + \Delta\phi_{\text{bb}}^2}$ of two b-jets,
- (d) and the invariant mass m_{bb} of two b-jets,

where in (b–d) the two b-jets are selected whose invariant mass is closest to m_{H} in order to identify the candidate pair that is most likely to originate from the Higgs decay.

Up to NLO, all three production modes of W^+H , W^-H , and ZH show similar qualitative behaviour for all four investigated distributions. However, there are significant phenomenological differences between the $W^\pm H$ and ZH distributions at NNLO.

NNLO corrections to the $W^\pm H$ cases lead to substantial stabilization of the predictions for the first three distributions shown in Figures 1.26–1.27, parts (a–c): size and shape are

only slightly modified at NNLO compared to the NLO predictions; the scale-variation bands, however, are reduced considerably. In contrast, the first three of the ZH distributions show an excess of events in the central regions throughout Figure 1.28, parts (a–c). This behaviour is attributed to threshold effects in the top-quark amplitudes in the dominant gluon–gluon-induced ZH-exclusive contributions of Figure 1.18. As mentioned earlier, these channels first contribute at NNLO, which also explains the widening of the theoretical uncertainty bands around the threshold regions of these distributions.

Concerning the invariant mass distribution of all three production modes shown in Figures 1.26d–1.28d, the features previously noted in refs. [34, 35] can be confirmed by our predictions as well: due to the very narrow width of the Higgs boson, the m_{bb} distribution has a natural kinematic threshold at $m_H = 125.09$ GeV and the phase space away from this value is barely populated at leading order. Consequently, NNLO corrections are effectively NLO-accurate for most of the bins, which explains the large corrections and relatively larger uncertainty bands for these distributions. The left shoulder below m_H is mainly the result of radiation from the decay, whereas the shoulder above m_H is due to radiative corrections to the production. Fixed-order predictions at the threshold region of $m_{bb} \approx m_H$, however, should not be trusted as they are prone to Sudakov-type instabilities. A proper treatment of this region would require the inclusion of resummation effects. In our case, the binning is sufficiently coarse so that such instabilities only manifest in larger uncertainty bands for the $m_{bb} = m_H$ bin and not as an explicit divergence.

1.8 Summary and Conclusions

This chapter of the thesis enumerated the new elements that were required for the calculation of NNLO corrections to the associated Higgs boson production processes W^+H , W^-H , and ZH. The calculation includes off-shell leptonic decay of the gauge bosons as well as the Higgs decaying into a bottom–antibottom quark pair. It consistently takes into account NNLO corrections to the production and decay subprocesses and fully retains the differential information on the final state.

The study of VH processes with $H \rightarrow b\bar{b}$ decay critically relies on the tagging of bottom jets in order to isolate the candidate pairs associated with the Higgs boson. The theoretical and technical details of our independent implementation of the infrared-safe flavour- k_t algorithm into the NNLOJET parton-level generation and the necessary modifications this entailed in the framework of the antenna subtraction formalism will be discussed in Chapter 3

A detailed account was given on the residual theory uncertainties by allowing the scales in the production and decay subprocesses to vary independently. This conservative approach

resulted in taking the envelope of 21 scale variations for the full process but allowed for a more comprehensive view into the impact of higher orders on the reduction of scale uncertainties. The NNLO corrections to the fiducial cross section were found to exhibit a good perturbative convergence with residual uncertainties at the percent level. We contrasted our naïve perturbative expansion of the cross section with a more commonly employed rescaling procedure using the branching ratio $\text{Br}(\text{H} \rightarrow \text{b}\bar{\text{b}})$, where we observed the latter to overestimate the residual scale uncertainties. This was attributed to a miscancellation in the scale dependence among the terms that receive different rescaling factors and it led us to advocate the simpler prescription in order to be more reliable beyond NLO.

Flavour-sensitive observables were studied by investigating differential distributions where a similar stabilization of the perturbative series was found as in the cross sections. Larger effects from higher-order corrections were seen in the invariant mass distributions of two b-jets, which can be attributed to these observables being only NLO-accurate away from $m_{\text{bb}} \sim m_{\text{H}}$. A comparison between the W^{\pm}H and ZH processes showed qualitatively similar behaviour but also emphasized the phenomenologically sizable impact that arose from the gluon-gluon-induced top quark loop amplitudes.

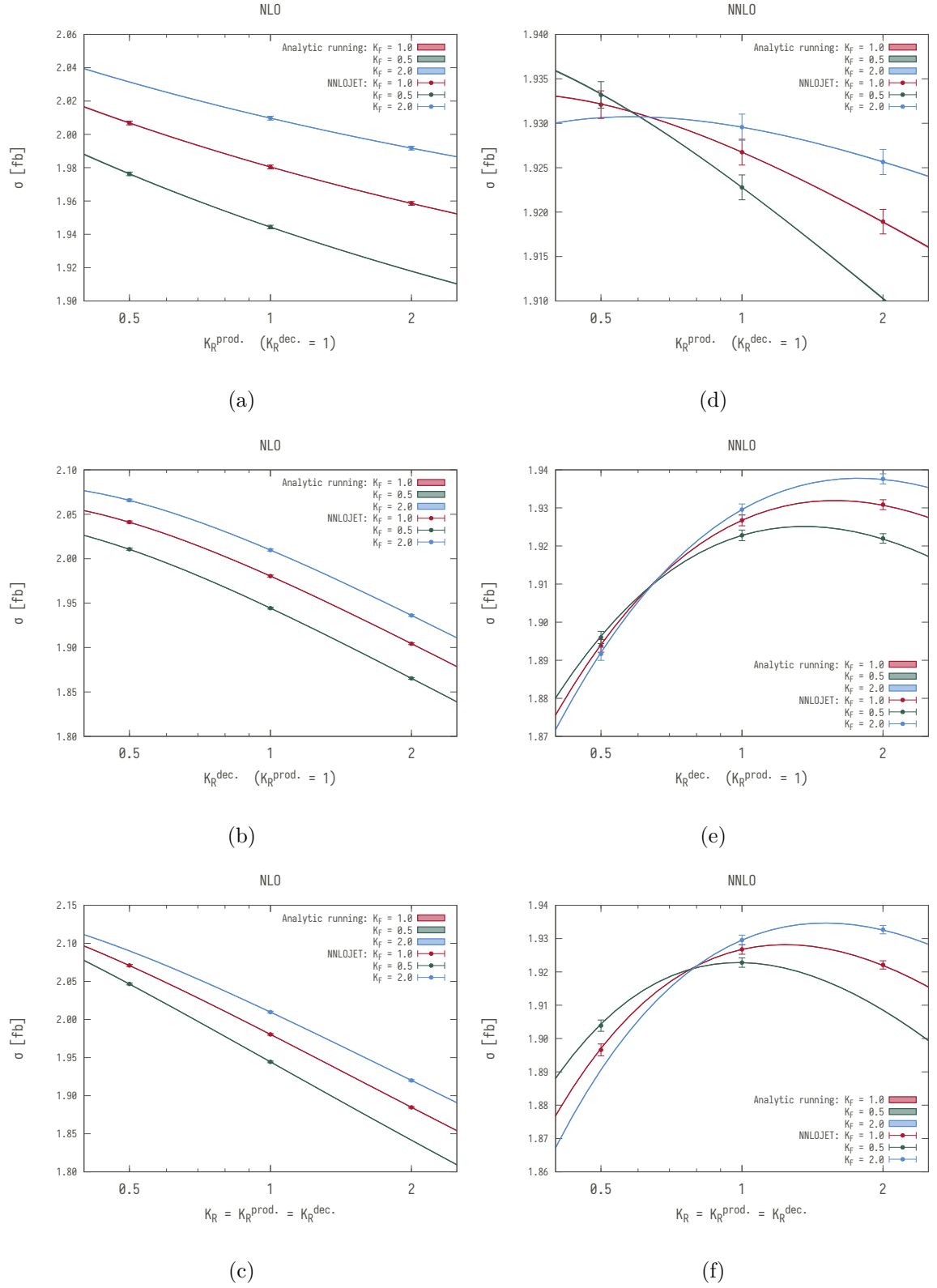


Figure 1.25: Numerical versus analytical scale variation of the W^+H process at NLO (left) and NNLO (right) for the bin $220 \text{ GeV} \leq M_{\text{WH}} \leq 230 \text{ GeV}$ and three different slices in the $(\mu_R^{\text{prod.}}, \mu_R^{\text{dec.}})$ plane.

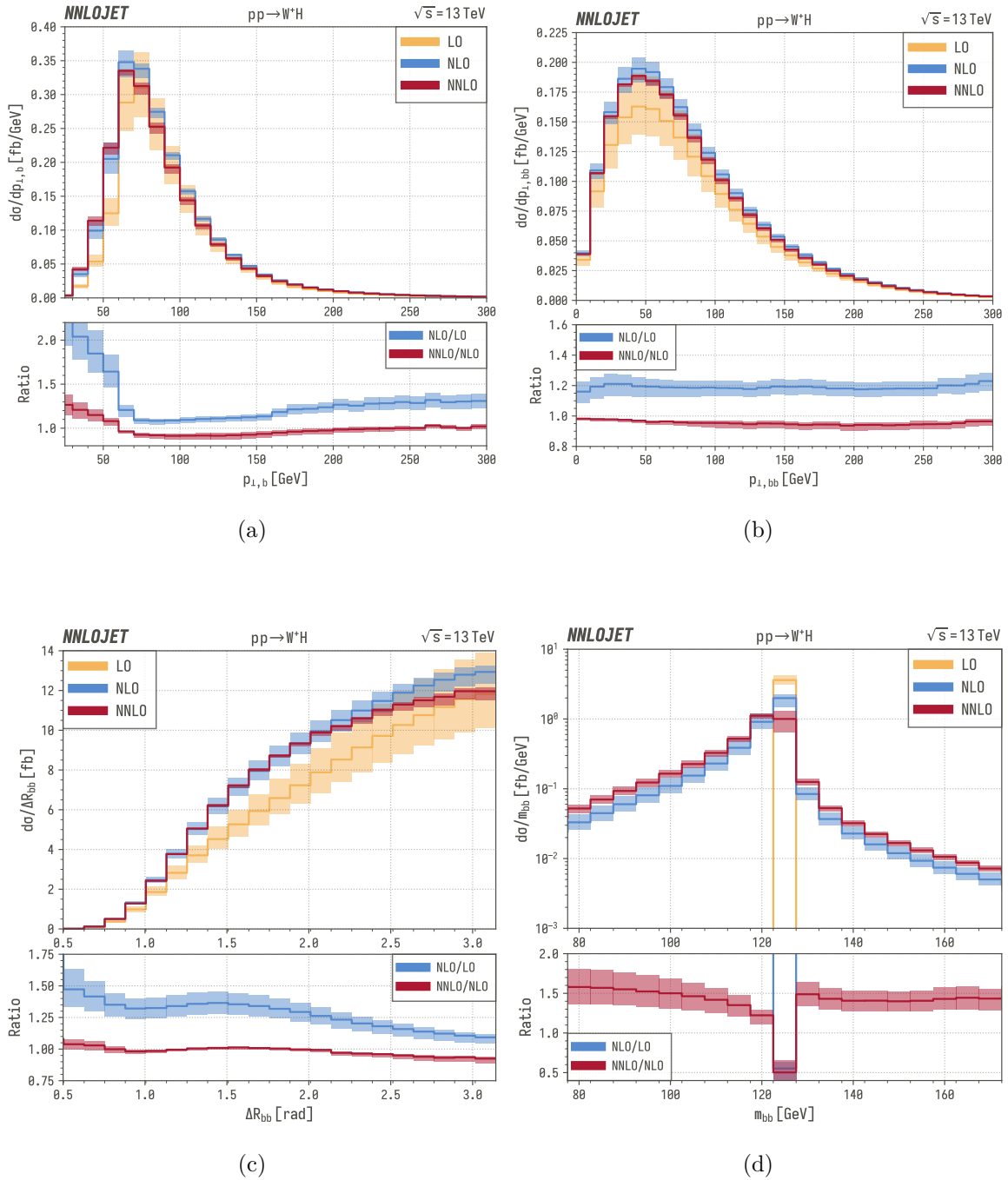


Figure 1.26: Flavour-sensitive jet distributions for the W^+H process showing (a) the transverse momentum of the leading b-jet, (b) the transverse momentum of the b-jet pair, (c) the angular separation of the b-jet pair, and (d) the invariant mass of the b-jet pair closest to the Higgs boson mass. The upper panel contains the absolute values while the lower panel shows the bin-by-bin ratios with respect to the previous order evaluated at the central scale.

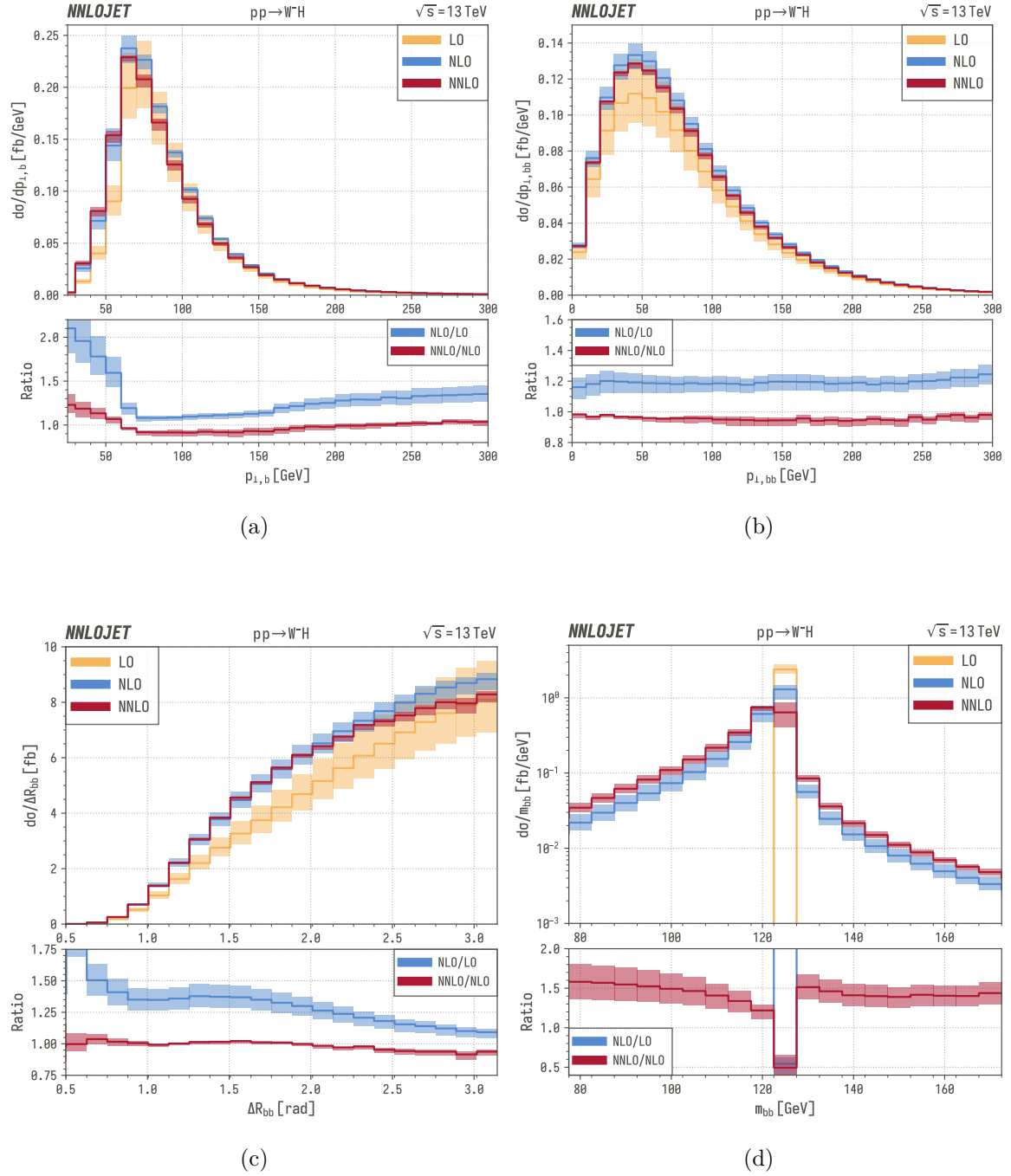


Figure 1.27: Flavour-sensitive jet distributions for the W^-H process showing (a) the transverse momentum of the leading b-jet, (b) the transverse momentum of the b-jet pair, (c) the angular separation of the b-jet pair, and (d) the invariant mass of the b-jet pair closest to the Higgs boson mass. The upper panel contains the absolute values while the lower panel shows the bin-by-bin ratios with respect to the previous order evaluated at the central scale.

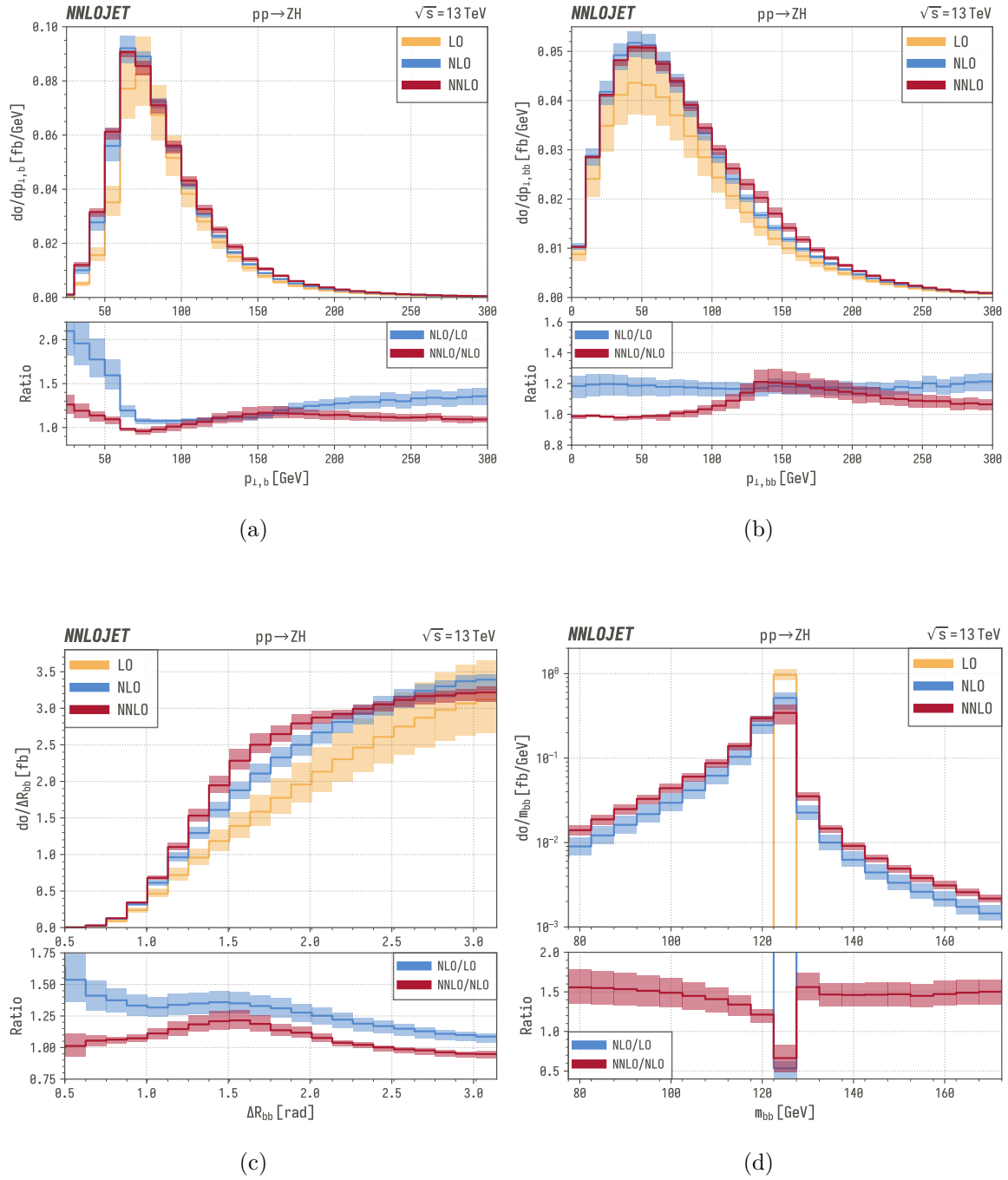


Figure 1.28: Flavour-sensitive jet distributions for the ZH process showing (a) the transverse momentum of the leading b-jet, (b) the transverse momentum of the b-jet pair, (c) the angular separation of the b-jet pair, and (d) the invariant mass of the b-jet pair closest to the Higgs boson mass. The upper panel contains the absolute values while the lower panel shows the bin-by-bin ratios with respect to the previous order evaluated at the central scale.

Chapter 2

Associated Higgs Boson Plus Jet Production

I will present $\mathcal{O}(\alpha_s^3)$ corrections to associated Higgs boson plus jet production in this chapter. This is a class of VH production that is defined by requiring at least a single hard jet among the final states in addition to a vector and a Higgs boson. Similarly to Chapter 1, our predictions are given with the mediating off-shell vector bosons—charged W^\pm or neutral Z bosons as before—decaying leptonically, keeping the spin correlations between the initial and final states. As this is the first time such a production process is calculated at NNLO precision, I will show results in which the Higgs boson is on shell and does not decay. A publication [2] of the results of this chapter is currently in preparation and I will often insert excerpts from its draft at the time of writing.

First, I will introduce the experimental and theoretical status of the VH +jet process in Section 2.1. It will be apparent that it is not as widely studied as VH without a resolved jet neither by the experimental nor by the theoretical community, making this thesis a pioneering work for VH +jet production. Section 2.2 will present the computational framework for our predictions, naturally carrying over essential concepts from VH production of Chapter 1. Moreover, we will ascertain that genuine new additions are only those of the $\mathcal{O}(\alpha_s^3)$ NNLO coefficient, which is the subject of Section 2.3. Specifically, its building blocks are enumerated in Section 2.3.1 for double-real, in Section 2.3.2 for real-virtual, and finally in Section 2.3.3 for double-virtual cross sections. The subsequent Section 2.4 is dedicated to presenting and analyzing numerical predictions of $W^\pm H$ +jet acquired from NNLOJET with the experimental setup of Section 2.4.1 for 13 TeV center-of-mass energy LHC runs. The resulting fiducial cross sections are found in Section 2.4.2, in which we also examine the phenomenological effect and validity of the included Yukawa-induced top loop contributions besides the usual Drell–

Yan-like ones. Last, but not least, a few selected differential distributions are displayed in Section 2.4.3. I will conclude the chapter in Section 2.5 with a brief summary and an outlook on possible useful extensions of this process within NNLOJET for future studies.

2.1 Process Background

Compared to VH production without a hard jet, the requirement of an additional hadronic jet has the potential of providing more differential information on the final state and being more sensitive to QCD radiation effects. While experimental data are becoming more and more available for VH production including specific Higgs decay modes, there is at present much less for VH +jet production. In fact, first experimental measurements of a simplified template cross section as a function of the vector boson transverse momentum for this category have only been reported recently by the ATLAS collaboration in refs. [23, 25].

The state of the art on the theoretical side is also notably different for the two VH production processes with or without a hard jet: fixed order VH +jet calculations were only available up to NLO QCD corrections so far for an on-shell Higgs boson, compared to the variety of higher-order predictions for VH including $H \rightarrow b\bar{b}$ decay we recounted in Section 1.1. Most recently the combination of NLO QCD computations for VH and VH +jet production have been merged in the context of parton showers to provide full NLO+PS simulations for the two on-shell Higgs production modes in refs. [40–42] and lately including electroweak corrections in ref. [62] as well.

The purpose of this chapter is to provide a new level of fixed-order theoretical precision for $W^\pm H$ +jet production observables where the charged vector boson decays leptonically and the Higgs boson is produced on-shell. We will include QCD corrections to the computation of Drell–Yan-type and non-Drell–Yan contributions up to $\mathcal{O}(\alpha_s^3)$ and $\mathcal{O}(\alpha_s^2)$, respectively. This is an important step towards computing VH +jet observables that eventually also include the decay of the Higgs boson into a bottom–antibottom pair, but this is beyond the scope of this thesis.

2.2 General Framework

Having at least a single hadronic jet among the final states, the parton-level Born contributions to VH +jet production are almost exactly the same as those present for real VH production listed in eqs. (1.23)–(1.25) of Section 1.4.1. However, there are some differences in the formulation due to the Higgs boson being on shell and simply because VH +jet is a process with different defining equations than VH without the resolved jet. Let us investi-

gate how the Born cross section can be written for VH+jet that will outline the similarities and differences of the framework compared to Chapter 1.2.

The Born cross sections for the contributing three different partonic channels are given by

$$d\hat{\sigma}_{VHj,q\bar{q}}^B = \frac{\mathcal{N}_{VHj}^B}{(2N_c)^2} d\Phi_3^H(p_1, p_2; \{p_f\}_{f=3}^5) \mathcal{J}_1^{(1)}(p_3) B_1^{VH,0}(\hat{1}_q, 3_g, \hat{2}_{\bar{q}}; 4_\ell, 5_{\bar{\ell}}), \quad (2.1)$$

$$d\hat{\sigma}_{VHj,qg}^B = \frac{\mathcal{N}_{VHj}^B}{(2N_c)[2(N_c^2 - 1)]} d\Phi_3^H(p_1, p_2; \{p_f\}_{f=3}^5) \mathcal{J}_1^{(1)}(p_3) B_1^{VH,0}(\hat{1}_q, \hat{2}_g, 3_{\bar{q}}; 4_\ell, 5_{\bar{\ell}}), \quad (2.2)$$

$$d\hat{\sigma}_{VHj,\bar{q}g}^B = \frac{\mathcal{N}_{VHj}^B}{(2N_c)[2(N_c^2 - 1)]} d\Phi_3^H(p_1, p_2; \{p_f\}_{f=3}^5) \mathcal{J}_1^{(1)}(p_3) B_1^{VH,0}(3_q, \hat{2}_g, \hat{1}_{\bar{q}}; 4_\ell, 5_{\bar{\ell}}). \quad (2.3)$$

The fundamental difference in the definition of the processes is indicated by the jet function $\mathcal{J}_1^{(1)}$. Whereas in Chapter 1 the presence of two flavoured b-jets were required—originating exclusively from the $H \rightarrow b\bar{b}$ decay—at leading order, the formulæ (2.1)–(2.3) demand the presence of a single unflavoured jet. The Higgs boson does not decay, therefore jets can only be reconstructed using partons radiated from the initial states. Not distinguishing any flavour also permits us to use flavour-insensitive jet algorithms from the k_t family, with our choice always falling onto the anti- k_t algorithm.

The on-shell condition of the Higgs boson is incorporated into the phase space element, which now takes the standard form of

$$d\Phi_{n-2}^H(p_1, p_2; \{p_f\}_{f=3}^n) = \left[\prod_{f=3}^n \frac{d^{d-1}p_f}{(2\pi)^{d-1} (2E_f)} \right] \left[\frac{d^d p_H}{(2\pi)^{d-1}} \delta^+(p_H^2 - m_H^2) \right] \times \\ (2\pi)^d \delta^{(d)}(p_1 + p_2 - p_H - \sum_{f=3}^n p_f). \quad (2.4)$$

Provided we formulate the amplitudes in a way in which they do not depend explicitly on the momentum p_H of the Higgs boson, we can integrate it out trivially using the Dirac delta distribution for momentum conservation, yielding

$$d\Phi_{n-2}^H(p_1, p_2; \{p_f\}_{f=3}^n) = (2\pi) \left[\prod_{f=3}^n \frac{d^{d-1}p_f}{(2\pi)^{d-1} (2E_f)} \right] \delta^+ \left[(p_1 + p_2 - \sum_{f=3}^n p_f)^2 - m_H^2 \right]. \quad (2.5)$$

Besides the addition of a factor of (2π) in front, the expression (2.5) describes an $(n - 2)$ -body massless phase space without momentum conservation and appropriate sampling of the momenta whose total invariant mass is m_H , the mass of the Higgs boson.

The amplitudes in Chapter 1 for VH production—both Drell–Yan-like and loop-induced contributions—were formulated in a way that do not depend explicitly on the momentum of the Higgs boson. As outlined in Section 1.3.2, these amplitudes do not conserve momentum between the QCD partons and final-state leptons, enabling their usage for VH+jet production of an on-shell Higgs boson with the phase-space formula (2.5).

The normalization factor in eqs. (2.1)–(2.3) can be expressed with that of VH production of one order higher in α_s . The expression

$$\mathcal{N}_{VHj} = \mathcal{N}_{VH} \left(\frac{\alpha_s N_c}{2\pi} \right) \left[1 - \frac{1}{N_c^2} \right] \quad (2.6)$$

holds at all levels for the normalization factors of VH+jet production.

The formulation of NLO $\mathcal{O}(\alpha_s^2)$ VH+jet production cross sections is thus a transition from the NNLO $\mathcal{O}(\alpha_s^2)$ VH ones. This is carried out in an identical fashion to the transition from NLO $\mathcal{O}(\alpha_s)$ VH cross sections to LO $\mathcal{O}(\alpha_s)$ VH+jet ones shown in eqs. (2.1)–(2.3). Accordingly, real VH+jet amplitudes are those of double-real VH production of Section 1.5.1 and virtual VH+jet amplitudes are those of real–virtual VH production of Section 1.5.3.

In principle, the subtraction terms can be converted in an identical manner as well. However, the jet function $\mathcal{J}_1^{(n)}$ for VH+jet production will always cut contributions without a single hard jet, essentially vetoing all unresolved limits in the SNLO $\mathcal{O}(\alpha_s)$ and T $\mathcal{O}(\alpha_s^2)$ VH subtraction terms and all double unresolved limits in the S $\mathcal{O}(\alpha_s^2)$ ones. One could argue that approaching the subtraction terms this way is slightly tautological: a process should not require any subtraction terms at its Born level and only single ones at NLO. From the practical perspective, however, this means that we can recycle the VH subtraction amplitudes up to $\mathcal{O}(\alpha_s^2)$ while omitting the terms which would anyway be vetoed by the jet function.

The genuine new contributions to VH+jet production are those of the $\mathcal{O}(\alpha_s^3)$ NNLO coefficient. In order to implement these, we followed a similar path to what we took for VH production without a resolved jet. The Drell–Yan-like contributions, in other words those of V+jet production are already available in NNLOJET with several phenomenological studies stemming from it in the literature [63–67]. The argument brought forward in Section 1.3.2 regarding non-momentum-conserving Drell–Yan-like amplitudes holds here as well. These amplitudes need to be derived independently, but once they are known, the subtraction terms of V+jet can be converted to those of VH+jet by swapping out the reduced matrix elements. For NNLO VH+jet production, these non-momentum-conserving Drell–Yan-type amplitudes are only partially derived (and validated) by us, a portion of them were evaluated

using libraries from OpenLoops 2 [53]. Interfacing OpenLoops 2 with NNLOJET carries some additional complications, mostly originating from OpenLoops not decomposing its amplitudes into different colour levels. This mismatch in conventions has to be mended by redefining subtraction terms to include all colour levels, a procedure I will describe in great detail, channel-by-channel in Section 2.3 whenever OpenLoops amplitudes are used.

The important non-Drell–Yan top loop contributions are only accounted for up to $\mathcal{O}(\alpha_s^2)$ NLO level. While all closed fermion-loop contributions for VH +jet production are known at real–virtual level, many of the required double-virtual, genuine two-loop amplitudes are presently unknown. They are both required for a gauge-invariant prediction and cannot be untangled from each other: not including the unknown double-virtual amplitudes necessarily prevents us from including any at real–virtual level either. Nevertheless, based on the results presented in Section 2.4, we will argue that including Yukawa-induced top loop contributions up to only NLO is phenomenologically sufficient and in fact necessary for a NNLO-accurate $W^\pm H$ +jet prediction.

An exception is the gauge-invariant subset of gluon–gluon-induced (one-loop)² amplitudes which are present exclusively for ZH +jet production, similar to those in Figure 1.18 for the ZH process without a hard jet. They are included in our calculation and likely to be phenomenologically relevant due to high gluon luminosity in LHC collisions. Having said that, only $W^\pm H$ +jet results will be presented in this thesis: at the time of writing these lines ZH +jet results are still pending. Nonetheless, for the sake of completion, I will cover all elements of the NNLO coefficient for both ZH +jet and $W^\pm H$ +jet production as both of these processes are fully implemented into NNLOJET.

2.3 Next-to-Next-to-Leading Order

In this section, I will go through the RR, RV, and VV contributions to the NNLO coefficient of VH +jet production in a similar fashion to Section 1.5 of the previous chapter. As shown in eq. (2.6), the normalization prefactors that appear throughout the VH +jet NNLO cross sections can be summarized in terms of the prefactors of the VH NNLO cross sections (1.49)–(1.51) as

$$\mathcal{N}_{VHj}^{\text{RR}} = \mathcal{N}_{VH}^{\text{RR}} \left(\frac{\alpha_s N_c}{2\pi} \right) \frac{N_c^2 - 1}{N_c^2}, \quad (2.7)$$

$$\mathcal{N}_{VHj}^{\text{RV}} = \mathcal{N}_{VH}^{\text{RV}} \left(\frac{\alpha_s N_c}{2\pi} \right) \frac{N_c^2 - 1}{N_c^2}, \quad (2.8)$$

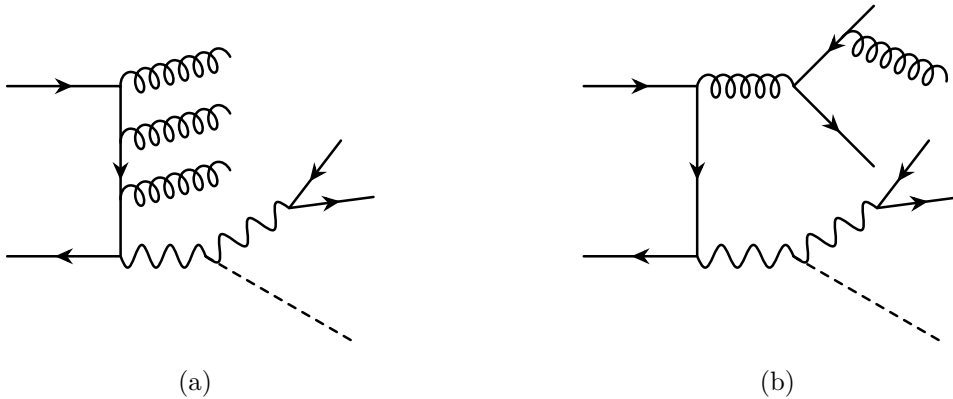


Figure 2.1: Example of a B -type diagram in (a) and a C -type one in (b) which contribute to double-real VH +jet production.

$$\mathcal{N}_{VHj}^{VV} = \mathcal{N}_{VH}^{VV} \left(\frac{\alpha_s N_c}{2\pi} \right) \frac{N_c^2 - 1}{N_c^2}. \quad (2.9)$$

Let us then move onto enumerating the different NNLO contributions.

2.3.1 Double-Real Cross Section

I will present all the partonic channels ordered in the same way as in Section 1.5.1. There are two different parton-level processes: a B -type one with one quark line and three gluons and a C -type process with two disconnected quark lines and a single gluon. Two examples of diagrams contributing to these amplitudes are depicted in Figure 2.1.

As usual in the NNLOJET formalism, the B -type amplitude is separated into colour-ordered pieces, which are denoted as $B_3^{VH,0}$ for the leading-colour piece, $\tilde{B}_3^{VH,0}$ for the subleading-colour piece, and $\tilde{\tilde{B}}_3^{VH,0}$ for the sub-subleading-colour piece. The formulæ for these B -type amplitudes is found in Appendix A.10.

The C -type amplitude, however, was evaluated using OpenLoops 2 [53] and the convention used there is not to separate the amplitude according to colour ordering. Nevertheless, I will indicate the way one would do such a separation, which is important to know when one wishes to assemble the subtraction terms for an OpenLoops amplitude implemented into NNLOJET. This is because the subtraction terms—which are recycled from the V +jet calculation—were originally created for amplitudes separated into various colour levels and we need to add them up accordingly for the correct subtraction.

The colour-level separation for the C -type partonic processes entails the following amplitudes: the leading-colour $C_1^{VH,0}$, the subleading-colour $\tilde{C}_1^{VH,0}$, the sub-subleading-colour $\tilde{\tilde{C}}_1^{VH,0}$, the leading-colour $D_1^{VH,0}$, and the subleading-colour $\tilde{D}_1^{VH,0}$. The D -type amplitudes

themselves are interference terms when the separate quark lines either are of identical flavour (present for ZH+jet) or contain at least one identical flavour (present for WH+jet). In order to avoid confusion, I will list the contributions separately for ZH+jet and WH+jet production and use the same notational convention concerning the labelling of quarks as established in Section 1.5.1, the section listing the double-real contributions for VH production.

The C -type OpenLoops amplitudes for a given parton-level ordering can be constructed according to

$$C_{1,\text{OL}}^{\text{ZH},0}(i_q, j_g, k_{\bar{Q}}, l_Q, m_{\bar{q}}; 6_\ell, 7_{\bar{\ell}}) = \frac{\mathcal{N}_{\text{ZHj}}^{\text{RR}}}{A} \frac{1}{N_c} \left\{ C_1^{\text{ZH},0}(i_q, j_g, k_{\bar{Q}}, l_Q, m_{\bar{q}}; 6_\ell, 7_{\bar{\ell}}) + \frac{1}{N_c^2} \left[\tilde{C}_1^{\text{ZH},0}(i_q, j_g, k_{\bar{Q}}, l_Q, m_{\bar{q}}; 6_\ell, 7_{\bar{\ell}}) - \tilde{\tilde{C}}_1^{\text{ZH},0}(i_q, j_g, k_{\bar{Q}}, l_Q, m_{\bar{q}}; 6_\ell, 7_{\bar{\ell}}) \right] \right\}, \quad (2.10)$$

$$C_{1,\text{OL}}^{\text{WH},0}(i_q, j_g, k_{\bar{Q}}, l_Q, m_{\bar{q}}; 6_\ell, 7_{\bar{\ell}}) = \frac{\mathcal{N}_{\text{WHj}}^{\text{RR}}}{A} \frac{1}{N_c} \left\{ C_1^{\text{WH},0}(i_q, j_g, k_{\bar{Q}}, l_Q, m_{\bar{q}'}; 6_\ell, 7_{\bar{\ell}}) + \frac{1}{N_c^2} \left[\tilde{C}_1^{\text{WH},0}(i_q, j_g, k_{\bar{Q}}, l_Q, m_{\bar{q}'}; 6_\ell, 7_{\bar{\ell}}) - \tilde{\tilde{C}}_1^{\text{WH},0}(i_q, j_g, k_{\bar{Q}}, l_Q, m_{\bar{q}'}; 6_\ell, 7_{\bar{\ell}}) \right] \right\}. \quad (2.11)$$

In general, the structure above always assumes that $Q \neq q$ and $Q \neq q'$. In case of flavour assignments containing identical quarks, the necessary symmetry factors are inserted and the permutations are carried out on the OpenLoops amplitude level, as this will be apparent later. Therefore the structure of eqs. (2.10) and (2.11) does not change even if $Q = q$ or $Q = q'$ inside their arguments. The averaging factor A that accounts for all the initial spin/polarization and colour states depends on which partons are in the initial state. For the above C -type amplitudes and the upcoming D -type ones, it is either $A = (2N_c)^2$ for (anti)quark–(anti)quark channels or $A = (2N_c)[2(N_c^2 - 1)]$ for (anti)quark–gluon ones.

The structure of the OpenLoops D -type identical-quark interference amplitudes is the following:

$$D_{1,\text{OL}}^{\text{ZH},0}(i_q, j_g, k_{\bar{q}}, l_q, m_{\bar{q}}; 6_\ell, 7_{\bar{\ell}}) = -\frac{\mathcal{N}_{\text{ZHj}}^{\text{RR}}}{A} \frac{1}{S} \times \frac{1}{N_c^2} \left\{ D_1^{\text{ZH},0}(i_q, j_g, k_{\bar{q}}, l_q, m_{\bar{q}}; 6_\ell, 7_{\bar{\ell}}) - \left[1 - \frac{1}{N_c^2} \right] \tilde{D}_1^{\text{ZH},0}(i_q, j_g, k_{\bar{q}}, l_q, m_{\bar{q}}; 6_\ell, 7_{\bar{\ell}}) \right\}, \quad (2.12)$$

$$D_{a,1,\text{OL}}^{\text{WH},0}(i_q, j_g, k_{\bar{q}}, l_q, m_{\bar{q}'}; 6_\ell, 7_{\bar{\ell}}) = -\frac{\mathcal{N}_{\text{WHj}}^{\text{RR}}}{A} \frac{1}{S} \times$$

$$\frac{1}{N_c^2} \left\{ D_{a,1}^{\text{WH},0}(i_q, j_g, k_{\bar{q}}, l_q, m_{\bar{q}'}; 6_\ell, 7_{\bar{\ell}}) - \left[1 - \frac{1}{N_c^2} \right] \tilde{D}_{a,1}^{\text{WH},0}(i_q, j_g, k_{\bar{q}}, l_q, m_{\bar{q}'}; 6_\ell, 7_{\bar{\ell}}) \right\}, \quad (2.13)$$

$$D_{b,1,\text{OL}}^{\text{WH},0}(i_q, j_g, k_{\bar{q}'}, l_{q'}, m_{\bar{q}'}; 6_\ell, 7_{\bar{\ell}}) = -\frac{\mathcal{N}_{\text{WHj}}^{\text{RR}}}{A} \frac{1}{S} \times \frac{1}{N_c^2} \left\{ D_{b,1}^{\text{WH},0}(i_q, j_g, k_{\bar{q}'}, l_{q'}, m_{\bar{q}'}; 6_\ell, 7_{\bar{\ell}}) - \left[1 - \frac{1}{N_c^2} \right] \tilde{D}_{b,1}^{\text{WH},0}(i_q, j_g, k_{\bar{q}'}, l_{q'}, m_{\bar{q}'}; 6_\ell, 7_{\bar{\ell}}) \right\}. \quad (2.14)$$

The sub-subleading-colour $\tilde{D}_1^{\text{VH},0}$ amplitudes are the same as the subleading-colour $\tilde{D}_1^{\text{VH},0}$ ones, explaining the $1 - 1/N_c^2$ prefactor in front of the amplitudes with the tilde accent. Similarly to WH production, we distinguish D_a - and D_b -type amplitudes for the WH+jet case, depending on which three quarks are of identical flavour. The symmetry factor S is built into the amplitudes (2.12)–(2.14) and depending on the channel it can be either $\frac{1}{S} = \frac{1}{2!}$ for two identical quarks or $\frac{1}{S} = 1$ when no identical particles are present in the final state.

Before moving onto the partonic channel breakdown, I would like to emphasize once again that only the left-hand side of eqs. (2.10)–(2.14), the OpenLoops amplitudes are implemented into NNLOJET. Knowing the right-hand side, the breakdown in colour structure, is important for constructing the subtraction terms.

Quark–Quark Initiated (Non-Identical Flavour)

$$d\hat{\sigma}_{\text{ZHj},qQ}^{\text{RR}} = d\Phi_5(p_1, p_2; \{p_i\}_{i=3}^7) \mathcal{J}_1^{(3)}(p_3, p_4, p_5) C_{1,\text{OL}}^{\text{ZH},0}(\hat{1}_q, 3_g, 4_{\bar{Q}}, \hat{2}_Q, 5_{\bar{q}}; 6_\ell, 7_{\bar{\ell}}), \quad (2.15)$$

$$d\hat{\sigma}_{\text{WHj},qQ}^{\text{RR}} = d\Phi_5(p_1, p_2; \{p_i\}_{i=3}^7) \mathcal{J}_1^{(3)}(p_3, p_4, p_5) C_{1,\text{OL}}^{\text{WH},0}(\hat{1}_q, 3_g, 4_{\bar{Q}}, \hat{2}_Q, 5_{\bar{q}'}; 6_\ell, 7_{\bar{\ell}}). \quad (2.16)$$

The WH+jet cross section has an additional permutation and subleading-colour interference term when $Q = q'$, in other words

$$d\hat{\sigma}_{\text{WHj},qq'}^{\text{RR}} = d\Phi_5(p_1, p_2; \{p_i\}_{i=3}^7) \mathcal{J}_1^{(3)}(p_3, p_4, p_5) \times \left\{ \frac{1}{2!} \left[C_{1,\text{OL}}^{\text{WH},0}(\hat{1}_q, 3_g, 4_{\bar{q}'}, \hat{2}_{q'}, 5_{\bar{q}'}; 6_\ell, 7_{\bar{\ell}}) + C_{1,\text{OL}}^{\text{WH},0}(\hat{1}_q, 3_g, 5_{\bar{q}'}, \hat{2}_{q'}, 4_{\bar{q}'}; 6_\ell, 7_{\bar{\ell}}) \right] + D_{b,1,\text{OL}}^{\text{WH},0}(\hat{1}_q, 3_g, 4_{\bar{q}'}, \hat{2}_{q'}, 5_{\bar{q}'}; 6_\ell, 7_{\bar{\ell}}) \right\}. \quad (2.17)$$

The symmetry factor $\frac{1}{2!}$ is present due to the identical $4_{\bar{q}'}$ and $5_{\bar{q}'}$ quarks in the final state.¹ In practice the ($4_{\bar{q}'} \leftrightarrow 5_{\bar{q}'}$) permutation is carried out by phase-space integration and thus the two terms are contracted into one in the codebase.

Quark–Quark Initiated (Identical Flavour)

$$\begin{aligned} d\hat{\sigma}_{\text{ZHj},qq}^{\text{RR}} &= d\Phi_5 \left(p_1, p_2; \{p_i\}_{i=3}^7 \right) \mathcal{J}_1^{(3)}(p_3, p_4, p_5) \times \\ &\quad \left\{ \frac{1}{2!} \left[C_{1,\text{OL}}^{\text{ZH},0} \left(\hat{1}_q, 3_g, 4_{\bar{q}}, \hat{2}_q, 5_{\bar{q}}; 6_\ell, 7_{\bar{\ell}} \right) + C_{1,\text{OL}}^{\text{ZH},0} \left(\hat{1}_q, 3_g, 5_{\bar{q}}, \hat{2}_q, 4_{\bar{q}}; 6_\ell, 7_{\bar{\ell}} \right) \right] \right. \\ &\quad \left. + D_{1,\text{OL}}^{\text{ZH},0} \left(\hat{1}_q, 3_g, 4_{\bar{q}}, \hat{2}_q, 5_{\bar{q}}; 6_\ell, 7_{\bar{\ell}} \right) \right\}, \end{aligned} \quad (2.18)$$

$$\begin{aligned} d\hat{\sigma}_{\text{WHj},qq}^{\text{RR}} &= d\Phi_5 \left(p_1, p_2; \{p_i\}_{i=3}^7 \right) \mathcal{J}_1^{(3)}(p_3, p_4, p_5) \times \\ &\quad \left\{ C_{1,\text{OL}}^{\text{WH},0} \left(\hat{1}_q, 3_g, 4_{\bar{q}}, \hat{2}_q, 5_{\bar{q}'}; 6_\ell, 7_{\bar{\ell}} \right) + C_{1,\text{OL}}^{\text{WH},0} \left(\hat{2}_q, 3_g, 4_{\bar{q}}, \hat{1}_q, 5_{\bar{q}'}; 6_\ell, 7_{\bar{\ell}} \right) \right. \\ &\quad \left. + D_{a,1,\text{OL}}^{\text{WH},0} \left(\hat{1}_q, 3_g, 4_{\bar{q}}, \hat{2}_q, 5_{\bar{q}'}; 6_\ell, 7_{\bar{\ell}} \right) \right\}. \end{aligned} \quad (2.19)$$

The symmetry factor $\frac{1}{2!}$ for ZH+jet production is due to the identical quarks $4_{\bar{q}}$ and $5_{\bar{q}}$ in the final state.² In practice, the permutation ($4_{\bar{q}} \leftrightarrow 5_{\bar{q}}$) is done via phase-space integration and the two terms are contracted into one in the codebase.

Identical quarks in the final state are not present for WH+jet production due to the flavour-changing effect of the W^\pm coupling.

Antiquark–Antiquark Initiated (Non-Identical Flavour)

$$d\hat{\sigma}_{\text{ZHj},\bar{Q}\bar{q}}^{\text{RR}} = d\Phi_5 \left(p_1, p_2; \{p_i\}_{i=3}^7 \right) \mathcal{J}_1^{(3)}(p_3, p_4, p_5) C_{1,\text{OL}}^{\text{ZH},0} \left(3_q, 4_g, \hat{1}_{\bar{Q}}, 5_Q, \hat{2}_{\bar{q}}; 6_\ell, 7_{\bar{\ell}} \right), \quad (2.20)$$

$$d\hat{\sigma}_{\text{WHj},\bar{Q}\bar{q}'}^{\text{RR}} = d\Phi_5 \left(p_1, p_2; \{p_i\}_{i=3}^7 \right) \mathcal{J}_1^{(3)}(p_3, p_4, p_5) C_{1,\text{OL}}^{\text{WH},0} \left(3_q, 4_g, \hat{1}_{\bar{Q}}, 5_Q, \hat{2}_{\bar{q}'}; 6_\ell, 7_{\bar{\ell}} \right). \quad (2.21)$$

The WH+jet cross section has an additional permutation and subleading-colour interference

¹This is built into $D_{b,1,\text{OL}}^{\text{WH},0}$ as shown in eq. (2.14).

²This is built into $D_{1,\text{OL}}^{\text{ZH},0}$ as shown in eq. (2.12).

term when $Q = q$, in other words

$$\begin{aligned} d\hat{\sigma}_{\text{WHj},\bar{q}q'}^{\text{RR}} &= d\Phi_5 \left(p_1, p_2; \{p_i\}_{i=3}^7 \right) \mathcal{J}_1^{(3)}(p_3, p_4, p_5) \times \\ &\quad \left\{ \frac{1}{2!} \left[C_{1,\text{OL}}^{\text{WH},0} \left(3_q, 4_g, \hat{1}_{\bar{q}}, 5_q, \hat{2}_{\bar{q}'}; 6_\ell, 7_{\bar{\ell}} \right) + C_{1,\text{OL}}^{\text{WH},0} \left(5_q, 4_g, \hat{1}_{\bar{q}}, 3_q, \hat{2}_{\bar{q}'}; 6_\ell, 7_{\bar{\ell}} \right) \right] \right. \\ &\quad \left. + D_{a,1,\text{OL}}^{\text{WH},0} \left(3_q, 4_g, \hat{1}_{\bar{q}}, 5_q, \hat{2}_{\bar{q}'}; 6_\ell, 7_{\bar{\ell}} \right) \right\}. \end{aligned} \quad (2.22)$$

The symmetry factor $\frac{1}{2!}$ is present due to the identical 3_q and 5_q quarks in the final state³ whose permutation in practice is carried out by phase-space integration.

Antiquark–Antiquark Initiated (Identical Flavour)

$$\begin{aligned} d\hat{\sigma}_{\text{ZHj},\bar{q}\bar{q}}^{\text{RR}} &= d\Phi_5 \left(p_1, p_2; \{p_i\}_{i=3}^7 \right) \mathcal{J}_1^{(3)}(p_3, p_4, p_5) \times \\ &\quad \left\{ \frac{1}{2!} \left[C_{1,\text{OL}}^{\text{ZH},0} \left(3_q, 4_g, \hat{1}_{\bar{q}}, 5_q, \hat{2}_{\bar{q}}; 6_\ell, 7_{\bar{\ell}} \right) + C_{1,\text{OL}}^{\text{ZH},0} \left(5_q, 4_g, \hat{1}_{\bar{q}}, 3_q, \hat{2}_{\bar{q}}; 6_\ell, 7_{\bar{\ell}} \right) \right] \right. \\ &\quad \left. + D_{1,\text{OL}}^{\text{ZH},0} \left(3_q, 4_g, \hat{1}_{\bar{q}}, 5_q, \hat{2}_{\bar{q}}; 6_\ell, 7_{\bar{\ell}} \right) \right\}, \end{aligned} \quad (2.23)$$

$$\begin{aligned} d\hat{\sigma}_{\text{WHj},\bar{q}'\bar{q}'}^{\text{RR}} &= d\Phi_5 \left(p_1, p_2; \{p_i\}_{i=3}^7 \right) \mathcal{J}_1^{(3)}(p_3, p_4, p_5) \times \\ &\quad \left\{ C_{1,\text{OL}}^{\text{WH},0} \left(3_q, 4_g, \hat{1}_{\bar{q}'}, 5_{q'}, \hat{2}_{\bar{q}'}; 6_\ell, 7_{\bar{\ell}} \right) + C_{1,\text{OL}}^{\text{WH},0} \left(3_q, 4_g, \hat{2}_{\bar{q}'}, 5_{q'}, \hat{1}_{\bar{q}'}; 6_\ell, 7_{\bar{\ell}} \right) \right. \\ &\quad \left. + D_{b,1,\text{OL}}^{\text{WH},0} \left(3_q, 4_g, \hat{1}_{\bar{q}'}, 5_{q'}, \hat{2}_{\bar{q}'}; 6_\ell, 7_{\bar{\ell}} \right) \right\} \end{aligned} \quad (2.24)$$

The symmetry factor $\frac{1}{2!}$ for ZH+jet production is due to the identical quarks 3_q and 5_q in the final state⁴ whose permutation in practice is carried out by phase-space integration. It is not present for WH+jet production due to the flavour-changing effect of the W^\pm coupling.

Quark–Antiquark Initiated (Non-Identical Flavour)

$$d\hat{\sigma}_{\text{ZHj},q\bar{Q}}^{\text{RR}} = d\Phi_5 \left(p_1, p_2; \{p_i\}_{i=3}^7 \right) \mathcal{J}_1^{(3)}(p_3, p_4, p_5) C_{1,\text{OL}}^{\text{ZH},0} \left(\hat{1}_q, 3_g, \hat{2}_{\bar{Q}}, 4_Q, 5_{\bar{q}}; 6_\ell, 7_{\bar{\ell}} \right), \quad (2.25)$$

$$d\hat{\sigma}_{\text{WHj},q\bar{Q}}^{\text{RR}} = d\Phi_5 \left(p_1, p_2; \{p_i\}_{i=3}^7 \right) \mathcal{J}_1^{(3)}(p_3, p_4, p_5) C_{1,\text{OL}}^{\text{WH},0} \left(\hat{1}_q, 3_g, \hat{2}_{\bar{Q}}, 4_Q, 5_{\bar{q}'}; 6_\ell, 7_{\bar{\ell}} \right). \quad (2.26)$$

³This is built into $D_{a,1,\text{OL}}^{\text{WH},0}$ as shown in eq. (2.13).

⁴This is built into $D_{1,\text{OL}}^{\text{ZH},0}$ as shown in eq. (2.12).

The WH+jet cross section has additional leading- and subleading-colour contributions when $Q = q'$ and takes the form

$$\begin{aligned}
d\hat{\sigma}_{\text{WHj},q\bar{q}'}^{\text{RR}} &= d\Phi_5 \left(p_1, p_2; \{p_i\}_{i=3}^7 \right) \mathcal{J}_1^{(3)}(p_3, p_4, p_5) \frac{\mathcal{N}_{\text{WHj}}^{\text{RR}}}{(2N_c)^2} \times \\
&\frac{1}{3!} \left\{ \sum_{(3,4,5)} \left[B_3^{\text{WH},0}(\hat{1}_q, 3_g, 4_g, 5_g, \hat{2}_{q'}, 6_\ell, 7_{\bar{\ell}}) - \frac{1}{N_c^2} \tilde{B}_3^{\text{WH},0}(\hat{1}_q, 3_{\bar{g}}, 4_g, 5_{\bar{g}}, \hat{2}_{q'}, 6_\ell, 7_{\bar{\ell}}) \right] \right. \\
&\quad \left. + \left(\frac{1}{N_c^2} + \frac{1}{N_c^4} \right) \tilde{\tilde{B}}_3^{\text{WH},0}(\hat{1}_q, 3_{\bar{g}}, 4_{\bar{g}}, 5_{\bar{g}}, \hat{2}_{q'}, 6_\ell, 7_{\bar{\ell}}) \right\} \\
&+ d\Phi_5 \left(p_1, p_2; \{p_i\}_{i=3}^7 \right) \mathcal{J}_1^{(3)}(p_3, p_4, p_5) \times \\
&\left\{ n_{\text{F}} C_{1,\text{OL}}^{\text{WH},0}(\hat{1}_q, 3_g, 4_{\bar{Q}}, 5_Q, \hat{2}_{q'}; 6_\ell, 7_{\bar{\ell}}) \right. \\
&\quad + C_{1,\text{OL}}^{\text{WH},0}(5_q, 3_g, 4_{\bar{q}}, \hat{1}_q, \hat{2}_{q'}; 6_\ell, 7_{\bar{\ell}}) + C_{1,\text{OL}}^{\text{WH},0}(\hat{1}_q, 3_g, \hat{2}_{q'}, 5_{q'}, 4_{q'}; 6_\ell, 7_{\bar{\ell}}) \\
&\quad \left. + D_{a,1,\text{OL}}^{\text{WH},0}(\hat{1}_q, 3_g, 4_{\bar{q}}, 5_q, \hat{2}_{q'}; 6_\ell, 7_{\bar{\ell}}) + D_{b,1,\text{OL}}^{\text{WH},0}(\hat{1}_q, 3_g, \hat{2}_{q'}, 4_{q'}, 5_{q'}; 6_\ell, 7_{\bar{\ell}}) \right\}. \quad (2.27)
\end{aligned}$$

The B -type contributions radiate the three gluons 3_g , 4_g , and 5_g into the final state, explaining the symmetry factor $\frac{1}{3!}$ in front of the sum of all six of their permutations, which is indicated by $\sum_{(3,4,5)}$.

Quark–Antiquark Initiated (Identical Flavour)

$$\begin{aligned}
d\hat{\sigma}_{\text{ZHj},q\bar{q}'}^{\text{RR}} &= d\Phi_5 \left(p_1, p_2; \{p_i\}_{i=3}^7 \right) \mathcal{J}_1^{(3)}(p_3, p_4, p_5) \frac{\mathcal{N}_{\text{ZHj}}^{\text{RR}}}{(2N_c)^2} \times \\
&\frac{1}{3!} \left\{ \sum_{(3,4,5)} \left[B_3^{\text{ZH},0}(\hat{1}_q, 3_g, 4_g, 5_g, \hat{2}_{q'}; 6_\ell, 7_{\bar{\ell}}) - \frac{1}{N_c^2} \tilde{B}_3^{\text{ZH},0}(\hat{1}_q, 3_{\bar{g}}, 4_g, 5_{\bar{g}}, \hat{2}_{q'}; 6_\ell, 7_{\bar{\ell}}) \right] \right. \\
&\quad \left. + \left(\frac{1}{N_c^2} + \frac{1}{N_c^4} \right) \tilde{\tilde{B}}_3^{\text{ZH},0}(\hat{1}_q, 3_{\bar{g}}, 4_{\bar{g}}, 5_{\bar{g}}, \hat{2}_{q'}; 6_\ell, 7_{\bar{\ell}}) \right\} \\
&+ d\Phi_5 \left(p_1, p_2; \{p_i\}_{i=3}^7 \right) \mathcal{J}_1^{(3)}(p_3, p_4, p_5) \times \\
&\left\{ n_{\text{up}} C_{1,\text{OL}}^{\text{ZH},0}(\hat{1}_q, 3_g, 4_{\bar{u}}, 5_u, \hat{2}_{q'}; 6_\ell, 7_{\bar{\ell}}) + n_{\text{down}} C_{1,\text{OL}}^{\text{ZH},0}(\hat{1}_q, 3_g, 4_{\bar{d}}, 5_d, \hat{2}_{q'}; 6_\ell, 7_{\bar{\ell}}) \right. \\
&\quad \left. + C_{1,\text{OL}}^{\text{ZH},0}(\hat{1}_q, 3_g, \hat{2}_{q'}, 5_q, 4_{q'}; 6_\ell, 7_{\bar{\ell}}) + D_{1,\text{OL}}^{\text{ZH},0}(\hat{1}_q, 3_g, \hat{2}_{q'}, 5_q, 4_{q'}; 6_\ell, 7_{\bar{\ell}}) \right\}, \quad (2.28)
\end{aligned}$$

$$\begin{aligned}
d\hat{\sigma}_{\text{WHj},q\bar{q}}^{\text{RR}} &= d\Phi_5(p_1, p_2; \{p_i\}_{i=3}^7) \mathcal{J}_1^{(3)}(p_3, p_4, p_5) \times \\
&\left\{ C_{1,\text{OL}}^{\text{WH},0}(\hat{1}_q, 3_g, \hat{2}_{\bar{q}}, 4_q, 5_{\bar{q}'}, 6_\ell, 7_{\bar{\ell}}) + \left[\frac{n_F}{2} \right] C_{1,\text{OL}}^{\text{WH},0}(4_q, 3_g, \hat{2}_{\bar{q}}, \hat{1}_q, 5_{\bar{q}'}, 6_\ell, 7_{\bar{\ell}}) \right. \\
&\left. + D_{a,1,\text{OL}}^{\text{WH},0}(\hat{1}_q, 3_g, \hat{2}_{\bar{q}}, 4_q, 5_{\bar{q}'}, 6_\ell, 7_{\bar{\ell}}) \right\}. \tag{2.29}
\end{aligned}$$

B -type amplitudes are only present for ZH+jet production in eq. (2.28); the three identical gluons in its final state explain the symmetry factor $\frac{1}{3!}$ in front of them. Due to the different coupling of the Z boson to quark lines, up- and down-type contributions need to be separately accounted for. This is shown in the second to last line of eq. (2.28) where $n_{\text{up}} = 2$, $n_{\text{down}} = 3$ with the symbols u and d labelling up and down quarks, respectively.

In the second term for WH+jet production (2.29) the quark current in the final state couples directly to the W^\pm boson. Assuming a diagonal CKM matrix, this allows for $\lfloor \frac{n_F}{2} \rfloor = 2$ identical amplitudes as the W^\pm boson only mediates up–down and charm–strange flavour changes in the $n_F = 5$ scheme.

Quark–Gluon Initiated

These channels are rather long, so let us look at the ZH+jet case first:

$$\begin{aligned}
d\hat{\sigma}_{\text{ZHj},qg}^{\text{RR}} &= d\Phi_5(p_1, p_2; \{p_i\}_{i=3}^7) \mathcal{J}_1^{(3)}(p_3, p_4, p_5) \frac{\mathcal{N}_{\text{ZHj}}^{\text{RR}}}{(2N_c)[2(N_c^2 - 1)]} \times \\
&\frac{1}{2!} \left\{ \sum_{(3 \leftrightarrow 4)} \left[B_3^{\text{ZH},0}(\hat{1}_q, \hat{2}_g, 3_g, 4_g, 5_{\bar{q}}, 6_\ell, 7_{\bar{\ell}}) + B_3^{\text{ZH},0}(\hat{1}_q, 3_g, \hat{2}_g, 4_g, 5_{\bar{q}}, 6_\ell, 7_{\bar{\ell}}) \right. \right. \\
&\quad \left. \left. + B_3^{\text{ZH},0}(\hat{1}_q, 3_g, 4_g, \hat{2}_g, 5_{\bar{q}}, 6_\ell, 7_{\bar{\ell}}) \right] \right. \\
&\quad \left. - \frac{1}{N_c^2} \sum_{(3 \leftrightarrow 4)} \left[\tilde{B}_3^{\text{ZH},0}(\hat{1}_q, \hat{2}_{\bar{g}}, 3_g, 4_g, 5_{\bar{q}}, 6_\ell, 7_{\bar{\ell}}) + \tilde{B}_3^{\text{ZH},0}(\hat{1}_q, 3_{\bar{g}}, \hat{2}_g, 4_g, 5_{\bar{q}}, 6_\ell, 7_{\bar{\ell}}) \right. \right. \\
&\quad \left. \left. + \tilde{B}_3^{\text{ZH},0}(\hat{1}_q, 3_{\bar{g}}, 4_g, \hat{2}_g, 5_{\bar{q}}, 6_\ell, 7_{\bar{\ell}}) \right] \right. \\
&\quad \left. + \left(\frac{1}{N_c^2} + \frac{1}{N_c^4} \right) \tilde{\tilde{B}}_3^{\text{ZH},0}(\hat{1}_q, \hat{2}_{\bar{g}}, 3_{\bar{g}}, 4_{\bar{g}}, 5_{\bar{q}}, 6_\ell, 7_{\bar{\ell}}) \right\} \\
&+ d\Phi_5(p_1, p_2; \{p_i\}_{i=3}^7) \mathcal{J}_1^{(3)}(p_3, p_4, p_5) \times \\
&\left\{ (n_{\text{up}} - \delta_{qu}) C_{1,\text{OL}}^{\text{ZH},0}(\hat{1}_q, \hat{2}_g, 3_{\bar{u}}, 4_u, 5_{\bar{q}}, 6_\ell, 7_{\bar{\ell}}) \right.
\end{aligned}$$

$$\begin{aligned}
& + (n_{\text{down}} - \delta_{qd}) C_{1,\text{OL}}^{\text{ZH},0}(\hat{1}_q, \hat{2}_g, 3_{\bar{d}}, 4_d, 5_{\bar{q}}; 6_\ell, 7_{\bar{\ell}}) \\
& + \frac{1}{2!} \left[C_{1,\text{OL}}^{\text{ZH},0}(\hat{1}_q, \hat{2}_g, 3_{\bar{q}}, 4_q, 5_{\bar{q}}; 6_\ell, 7_{\bar{\ell}}) + C_{1,\text{OL}}^{\text{ZH},0}(\hat{1}_q, \hat{2}_g, 5_{\bar{q}}, 4_q, 3_{\bar{q}}; 6_\ell, 7_{\bar{\ell}}) \right] \\
& + D_{1,\text{OL}}^{\text{ZH},0}(\hat{1}_q, \hat{2}_g, 3_{\bar{q}}, 4_q, 5_{\bar{q}}; 6_\ell, 7_{\bar{\ell}}) \Big\}. \tag{2.30}
\end{aligned}$$

The Kronecker delta δ_{qu} (δ_{qd}) is one if the quark q in question is up-type (down-type) and zero if it is not. The symmetry factor is $\frac{1}{2!}$ for the B -type contributions because of the two gluons 3_g and 4_g in the final state. For the C -type amplitudes of the last two lines, the symmetry factor is $\frac{1}{2!}$ due to the identical quarks $3_{\bar{q}}$ and $5_{\bar{q}}$ in the final state.⁵ The ($3_{\bar{q}} \leftrightarrow 5_{\bar{q}}$) permutation in the second-to-last line is carried out by phase-space integration inside the codebase and thus the terms are contracted into one.

Next, let us move onto the WH+jet case of

$$\begin{aligned}
d\hat{\sigma}_{\text{WHj},qg}^{\text{RR}} &= d\Phi_5(p_1, p_2; \{p_i\}_{i=3}^7) \mathcal{J}_1^{(3)}(p_3, p_4, p_5) \frac{\mathcal{N}_{\text{WHj}}^{\text{RR}}}{(2N_c)[2(N_c^2 - 1)]} \times \\
& \frac{1}{2!} \left\{ \sum_{(3 \leftrightarrow 4)} \left[B_3^{\text{WH},0}(\hat{1}_q, \hat{2}_g, 3_g, 4_g, 5_{\bar{q}'}, 6_\ell, 7_{\bar{\ell}}) + B_3^{\text{WH},0}(\hat{1}_q, 3_g, \hat{2}_g, 4_g, 5_{\bar{q}'}; 6_\ell, 7_{\bar{\ell}}) \right. \right. \\
& \quad \left. \left. + B_3^{\text{WH},0}(\hat{1}_q, 3_g, 4_g, \hat{2}_g, 5_{\bar{q}'}; 6_\ell, 7_{\bar{\ell}}) \right] \right. \\
& - \frac{1}{N_c^2} \sum_{(3 \leftrightarrow 4)} \left[\tilde{B}_3^{\text{WH},0}(\hat{1}_q, \hat{2}_{\bar{g}}, 3_g, 4_g, 5_{\bar{q}'}; 6_\ell, 7_{\bar{\ell}}) + \tilde{B}_3^{\text{WH},0}(\hat{1}_q, 3_{\bar{g}}, \hat{2}_g, 4_g, 5_{\bar{q}'}; 6_\ell, 7_{\bar{\ell}}) \right. \\
& \quad \left. + \tilde{B}_3^{\text{WH},0}(\hat{1}_q, 3_{\bar{g}}, 4_g, \hat{2}_g, 5_{\bar{q}'}; 6_\ell, 7_{\bar{\ell}}) \right] \\
& \left. + \left(\frac{1}{N_c^2} + \frac{1}{N_c^4} \right) \tilde{\tilde{B}}_3^{\text{WH},0}(\hat{1}_q, \hat{2}_{\bar{g}}, 3_{\bar{g}}, 4_{\bar{g}}, 5_{\bar{q}'}; 6_\ell, 7_{\bar{\ell}}) \right\} \\
& + d\Phi_5(p_1, p_2; \{p_i\}_{i=3}^7) \mathcal{J}_1^{(3)}(p_3, p_4, p_5) \times \\
& \left\{ (n_F - 1) C_{1,\text{OL}}^{\text{WH},0}(\hat{1}_q, \hat{2}_g, 3_{\bar{Q}}, 4_Q, 5_{\bar{q}'}; 6_\ell, 7_{\bar{\ell}}) + C_{1,\text{OL}}^{\text{WH},0}(4_q, \hat{2}_g, 3_{\bar{q}}, \hat{1}_q, 5_{\bar{q}'}; 6_\ell, 7_{\bar{\ell}}) \right. \\
& + \frac{1}{2!} \left[C_{1,\text{OL}}^{\text{WH},0}(\hat{1}_q, \hat{2}_g, 3_{\bar{q}'}, 4_{q'}, 5_{\bar{q}'}; 6_\ell, 7_{\bar{\ell}}) + C_{1,\text{OL}}^{\text{WH},0}(\hat{1}_q, \hat{2}_g, 5_{\bar{q}'}, 4_{q'}, 3_{\bar{q}'}; 6_\ell, 7_{\bar{\ell}}) \right] \\
& \left. + D_{b,1,\text{OL}}^{\text{WH},0}(\hat{1}_q, \hat{2}_g, 3_{\bar{q}'}, 4_{q'}, 5_{\bar{q}'}; 6_\ell, 7_{\bar{\ell}}) + D_{a,1,\text{OL}}^{\text{WH},0}(\hat{1}_q, \hat{2}_g, 3_{\bar{q}}, 4_q, 5_{\bar{q}'}; 6_\ell, 7_{\bar{\ell}}) \right\}. \tag{2.31}
\end{aligned}$$

⁵This is built into $D_{1,\text{OL}}^{\text{ZH},0}$ as shown in eq. (2.12).

The B -type amplitudes take an identical structure to those of ZH+jet. The C -type amplitudes are slightly more complicated, as all permutations and symmetry factors need to be taken into account when there are identical quarks in the final state.⁶ In practice, the $(3_{\bar{q}'} \leftrightarrow 5_{\bar{q}'})$ permutation inside the brackets is carried out by phase-space integration, therefore those C -type amplitudes are contracted with the $(n_F - 1)$ piece into a single term with an overall n_F prefactor inside the codebase.

Antiquark–Gluon Initiated

$$\begin{aligned}
d\hat{\sigma}_{\text{ZHj},\bar{q}\text{g}}^{\text{RR}} &= d\Phi_5(p_1, p_2; \{p_i\}_{i=3}^7) \mathcal{J}_1^{(3)}(p_3, p_4, p_5) \frac{\mathcal{N}_{\text{ZHj}}^{\text{RR}}}{(2N_c)[2(N_c^2 - 1)]} \times \\
&\frac{1}{2!} \left\{ \sum_{(4 \leftrightarrow 5)} \left[B_3^{\text{ZH},0}(3_q, \hat{2}_g, 4_g, 5_g, \hat{1}_{\bar{q}}; 6_\ell, 7_{\bar{\ell}}) + B_3^{\text{ZH},0}(3_q, 4_g, \hat{2}_g, 5_g, \hat{1}_{\bar{q}}; 6_\ell, 7_{\bar{\ell}}) \right. \right. \\
&\quad \left. \left. + B_3^{\text{ZH},0}(3_q, 4_g, 5_g, \hat{2}_g, \hat{1}_{\bar{q}}; 6_\ell, 7_{\bar{\ell}}) \right] \right. \\
&\quad \left. - \frac{1}{N_c^2} \sum_{(4 \leftrightarrow 5)} \left[\tilde{B}_3^{\text{ZH},0}(3_q, \hat{2}_{\bar{g}}, 4_g, 5_g, \hat{1}_{\bar{q}}; 6_\ell, 7_{\bar{\ell}}) + \tilde{B}_3^{\text{ZH},0}(3_q, 4_{\bar{g}}, \hat{2}_g, 5_g, \hat{1}_{\bar{q}}; 6_\ell, 7_{\bar{\ell}}) \right. \right. \\
&\quad \left. \left. + \tilde{B}_3^{\text{ZH},0}(3_q, 4_{\bar{g}}, 5_g, \hat{2}_g, \hat{1}_{\bar{q}}; 6_\ell, 7_{\bar{\ell}}) \right] \right. \\
&\quad \left. + \left(\frac{1}{N_c^2} + \frac{1}{N_c^4} \right) \tilde{\tilde{B}}_3^{\text{ZH},0}(3_q, \hat{2}_{\bar{g}}, 4_{\bar{g}}, 5_{\bar{g}}, \hat{1}_{\bar{q}}; 6_\ell, 7_{\bar{\ell}}) \right\} \\
&+ d\Phi_5(p_1, p_2; \{p_i\}_{i=3}^7) \mathcal{J}_1^{(3)}(p_3, p_4, p_5) \times \\
&\quad \left\{ (n_{\text{up}} - \delta_{qu}) C_{1,\text{OL}}^{\text{ZH},0}(3_q, \hat{2}_g, 4_{\bar{u}}, 5_{\bar{u}}, \hat{1}_{\bar{q}}; 6_\ell, 7_{\bar{\ell}}) \right. \\
&\quad + (n_{\text{down}} - \delta_{qd}) C_{1,\text{OL}}^{\text{ZH},0}(3_q, \hat{2}_g, 4_{\bar{d}}, 5_{\bar{d}}, \hat{1}_{\bar{q}}; 6_\ell, 7_{\bar{\ell}}) \\
&\quad + \frac{1}{2!} \left[C_{1,\text{OL}}^{\text{ZH},0}(3_q, \hat{2}_g, 4_{\bar{q}}, 5_q, \hat{1}_{\bar{q}}; 6_\ell, 7_{\bar{\ell}}) + C_{1,\text{OL}}^{\text{ZH},0}(5_q, \hat{2}_g, 4_{\bar{q}}, 3_q, \hat{1}_{\bar{q}}; 6_\ell, 7_{\bar{\ell}}) \right] \\
&\quad \left. + D_{1,\text{OL}}^{\text{ZH},0}(3_q, \hat{2}_g, 4_{\bar{q}}, 5_q, \hat{1}_{\bar{q}}; 6_\ell, 7_{\bar{\ell}}) \right\}. \tag{2.32}
\end{aligned}$$

For the C - and D -type amplitudes of the last two lines, the symmetry factor is $\frac{1}{2!}$ due to the

⁶The symmetry factor $\frac{1}{2!}$ is contained in $D_{b,1,\text{OL}}^{\text{WH},0}$ as shown in eq. (2.14). The $D_{a,1,\text{OL}}^{\text{WH},0}$ amplitude here does not require one.

identical quarks 3_q and 5_q in the final state⁷ whose permutation is carried out by phase-space integration inside the codebase and thus the terms are contracted into one.

$$\begin{aligned}
d\hat{\sigma}_{\text{WHj},\bar{q}'g}^{\text{RR}} &= d\Phi_5(p_1, p_2; \{p_i\}_{i=3}^7) \mathcal{J}_1^{(3)}(p_3, p_4, p_5) \frac{\mathcal{N}_{\text{WHj}}^{\text{RR}}}{(2N_c)[2(N_c^2 - 1)]} \times \\
&\frac{1}{2!} \left\{ \sum_{(4 \leftrightarrow 5)} \left[B_3^{\text{WH},0}(3_q, \hat{2}_g, 4_g, 5_g, \hat{1}_{\bar{q}'}; 6_\ell, 7_{\bar{\ell}}) + B_3^{\text{WH},0}(3_q, 4_g, \hat{2}_g, 5_g, \hat{1}_{\bar{q}'}; 6_\ell, 7_{\bar{\ell}}) \right] \right. \\
&\quad + \left[B_3^{\text{WH},0}(3_q, 4_g, 5_g, \hat{2}_g, \hat{1}_{\bar{q}'}; 6_\ell, 7_{\bar{\ell}}) \right] \\
&\quad - \frac{1}{N_c^2} \sum_{(4 \leftrightarrow 5)} \left[\tilde{B}_3^{\text{WH},0}(3_q, \hat{2}_{\bar{g}}, 4_g, 5_g, \hat{1}_{\bar{q}'}; 6_\ell, 7_{\bar{\ell}}) + \tilde{B}_3^{\text{WH},0}(3_q, 4_{\bar{g}}, \hat{2}_g, 5_g, \hat{1}_{\bar{q}'}; 6_\ell, 7_{\bar{\ell}}) \right] \\
&\quad + \tilde{B}_3^{\text{WH},0}(3_q, 4_{\bar{g}}, 5_g, \hat{2}_g, \hat{1}_{\bar{q}'}; 6_\ell, 7_{\bar{\ell}}) \left. \right\} \\
&+ \left(\frac{1}{N_c^2} + \frac{1}{N_c^4} \right) \tilde{\tilde{B}}_3^{\text{WH},0}(3_q, \hat{2}_{\bar{g}}, 4_{\bar{g}}, 5_{\bar{g}}, \hat{1}_{\bar{q}'}; 6_\ell, 7_{\bar{\ell}}) \left. \right\} \\
&+ d\Phi_5(p_1, p_2; \{p_i\}_{i=3}^7) \mathcal{J}_1^{(3)}(p_3, p_4, p_5) \times \\
&\quad \left\{ (n_F - 1) C_{1,\text{OL}}^{\text{WH},0}(3_q, \hat{2}_g, 4_{\bar{Q}}, 5_Q, \hat{1}_{\bar{q}'}; 6_\ell, 7_{\bar{\ell}}) + C_{1,\text{OL}}^{\text{WH},0}(3_q, \hat{2}_g, \hat{1}_{\bar{q}'}, 5_{q'}, 4_{\bar{q}'}; 6_\ell, 7_{\bar{\ell}}) \right. \\
&\quad + \frac{1}{2!} \left[C_{1,\text{OL}}^{\text{WH},0}(3_q, \hat{2}_g, 4_{\bar{q}}, 5_q, \hat{1}_{\bar{q}'}; 6_\ell, 7_{\bar{\ell}}) + C_{1,\text{OL}}^{\text{WH},0}(5_q, \hat{2}_g, 4_{\bar{q}}, 3_q, \hat{1}_{\bar{q}'}; 6_\ell, 7_{\bar{\ell}}) \right] \\
&\quad + D_{a,1,\text{OL}}^{\text{WH},0}(3_q, \hat{2}_g, 4_{\bar{q}}, 5_q, \hat{1}_{\bar{q}'}; 6_\ell, 7_{\bar{\ell}}) + D_{b,1,\text{OL}}^{\text{WH},0}(3_q, \hat{2}_g, \hat{1}_{\bar{q}'}, 5_{q'}, 4_{\bar{q}'}; 6_\ell, 7_{\bar{\ell}}) \left. \right\}. \tag{2.33}
\end{aligned}$$

Similarly to the quark–gluon channel, the $(3_q \leftrightarrow 5_q)$ permutation inside the braces is carried out by phase-space integration, therefore the C -type amplitudes there can be contracted with the $(n_F - 1)$ piece into a single term with an overall n_F prefactor.⁸

Gluon–Gluon Initiated

This channel does not contain any C - or D -type amplitudes, nevertheless we still need to distinguish the ZH+jet and the WH+jet cases because up- and down-type contributions have

⁷This is built into $D_{1,\text{OL}}^{\text{ZH},0}$ as shown in eq. (2.12).

⁸The symmetry factor $\frac{1}{2!}$ is contained in $D_{a,1,\text{OL}}^{\text{WH},0}$ as shown in eq. (2.13). The $D_{b,1,\text{OL}}^{\text{WH},0}$ amplitude here does not require one.

to be accounted for separately whenever the Z coupling is involved.

$$\begin{aligned}
d\hat{\sigma}_{\text{ZHj,gg}}^{\text{RR}} &= d\Phi_5(p_1, p_2; \{p_i\}_{i=3}^7) \mathcal{J}_1^{(3)}(p_3, p_4, p_5) \frac{\mathcal{N}_{\text{ZHj}}^{\text{RR}}}{[2(N_c^2 - 1)]^2} \times \\
&\left\{ n_{\text{up}} \sum_{(\hat{1} \leftrightarrow \hat{2})} \left[B_3^{\text{ZH},0}(4_{\text{u}}, \hat{1}_{\text{g}}, \hat{2}_{\text{g}}, 3_{\text{g}}, 5_{\bar{\text{u}}}; 6_{\ell}, 7_{\bar{\ell}}) + B_3^{\text{ZH},0}(4_{\text{u}}, 3_{\text{g}}, \hat{1}_{\text{g}}, \hat{2}_{\text{g}}, 5_{\bar{\text{u}}}; 6_{\ell}, 7_{\bar{\ell}}) \right. \right. \\
&\quad \left. \left. + B_3^{\text{ZH},0}(4_{\text{u}}, \hat{1}_{\text{g}}, 3_{\text{g}}, \hat{2}_{\text{g}}, 5_{\bar{\text{u}}}; 6_{\ell}, 7_{\bar{\ell}}) \right] \right. \\
&\quad n_{\text{down}} \sum_{(\hat{1} \leftrightarrow \hat{2})} \left[B_3^{\text{ZH},0}(4_{\text{d}}, \hat{1}_{\text{g}}, \hat{2}_{\text{g}}, 3_{\text{g}}, 5_{\bar{\text{d}}}; 6_{\ell}, 7_{\bar{\ell}}) + B_3^{\text{ZH},0}(4_{\text{d}}, 3_{\text{g}}, \hat{1}_{\text{g}}, \hat{2}_{\text{g}}, 5_{\bar{\text{d}}}; 6_{\ell}, 7_{\bar{\ell}}) \right. \\
&\quad \left. + B_3^{\text{ZH},0}(4_{\text{d}}, \hat{1}_{\text{g}}, 3_{\text{g}}, \hat{2}_{\text{g}}, 5_{\bar{\text{d}}}; 6_{\ell}, 7_{\bar{\ell}}) \right] \\
&\quad - \frac{n_{\text{up}}}{N_c^2} \sum_{(\hat{1} \leftrightarrow \hat{2})} \left[\tilde{B}_3^{\text{ZH},0}(4_{\text{u}}, \hat{1}_{\tilde{\text{g}}}, \hat{2}_{\tilde{\text{g}}}, 3_{\text{g}}, 5_{\bar{\text{u}}}; 6_{\ell}, 7_{\bar{\ell}}) + \tilde{B}_3^{\text{ZH},0}(4_{\text{u}}, 3_{\tilde{\text{g}}}, \hat{1}_{\text{g}}, \hat{2}_{\text{g}}, 5_{\bar{\text{u}}}; 6_{\ell}, 7_{\bar{\ell}}) \right. \\
&\quad \left. + \tilde{B}_3^{\text{ZH},0}(4_{\text{u}}, \hat{1}_{\tilde{\text{g}}}, 3_{\text{g}}, \hat{2}_{\text{g}}, 5_{\bar{\text{u}}}; 6_{\ell}, 7_{\bar{\ell}}) \right] \\
&\quad - \frac{n_{\text{down}}}{N_c^2} \sum_{(\hat{1} \leftrightarrow \hat{2})} \left[\tilde{B}_3^{\text{ZH},0}(4_{\text{d}}, \hat{1}_{\tilde{\text{g}}}, \hat{2}_{\tilde{\text{g}}}, 3_{\text{g}}, 5_{\bar{\text{d}}}; 6_{\ell}, 7_{\bar{\ell}}) + \tilde{B}_3^{\text{ZH},0}(4_{\text{d}}, 3_{\tilde{\text{g}}}, \hat{1}_{\text{g}}, \hat{2}_{\text{g}}, 5_{\bar{\text{d}}}; 6_{\ell}, 7_{\bar{\ell}}) \right. \\
&\quad \left. + \tilde{B}_3^{\text{ZH},0}(4_{\text{d}}, \hat{1}_{\tilde{\text{g}}}, 3_{\text{g}}, \hat{2}_{\text{g}}, 5_{\bar{\text{d}}}; 6_{\ell}, 7_{\bar{\ell}}) \right] \\
&\quad + n_{\text{up}} \left(\frac{1}{N_c^2} + \frac{1}{N_c^4} \right) \tilde{\tilde{B}}_3^{\text{ZH},0}(4_{\text{u}}, \hat{1}_{\tilde{\text{g}}}, \hat{2}_{\tilde{\text{g}}}, 3_{\tilde{\text{g}}}, 5_{\bar{\text{u}}}; 6_{\ell}, 7_{\bar{\ell}}) \\
&\quad \left. + n_{\text{down}} \left(\frac{1}{N_c^2} + \frac{1}{N_c^4} \right) \tilde{\tilde{B}}_3^{\text{ZH},0}(4_{\text{d}}, \hat{1}_{\tilde{\text{g}}}, \hat{2}_{\tilde{\text{g}}}, 3_{\tilde{\text{g}}}, 5_{\bar{\text{d}}}; 6_{\ell}, 7_{\bar{\ell}}) \right\}, \tag{2.34}
\end{aligned}$$

$$\begin{aligned}
d\hat{\sigma}_{\text{WHj,gg}}^{\text{RR}} &= d\Phi_5(p_1, p_2; \{p_i\}_{i=3}^7) \mathcal{J}_1^{(3)}(p_3, p_4, p_5) \frac{\mathcal{N}_{\text{WHj}}^{\text{RR}}}{[2(N_c^2 - 1)]^2} \times \\
&\left\{ \left[\frac{n_{\text{F}}}{2} \right] \sum_{(\hat{1} \leftrightarrow \hat{2})} \left[B_3^{\text{WH},0}(4_{\text{q}}, \hat{1}_{\tilde{\text{g}}}, \hat{2}_{\tilde{\text{g}}}, 3_{\text{g}}, 5_{\bar{\text{q}'}}}; 6_{\ell}, 7_{\bar{\ell}}) + B_3^{\text{WH},0}(4_{\text{q}}, 3_{\text{g}}, \hat{1}_{\tilde{\text{g}}}, \hat{2}_{\tilde{\text{g}}}, 5_{\bar{\text{q}'}}}; 6_{\ell}, 7_{\bar{\ell}}) \right. \right. \\
&\quad \left. \left. + B_3^{\text{WH},0}(4_{\text{q}}, \hat{1}_{\tilde{\text{g}}}, 3_{\text{g}}, \hat{2}_{\tilde{\text{g}}}, 5_{\bar{\text{q}'}}}; 6_{\ell}, 7_{\bar{\ell}}) \right] \right. \\
&\quad - \frac{[n_{\text{F}}/2]}{N_c^2} \sum_{(\hat{1} \leftrightarrow \hat{2})} \left[\tilde{B}_3^{\text{WH},0}(4_{\text{q}}, \hat{1}_{\tilde{\text{g}}}, \hat{2}_{\tilde{\text{g}}}, 3_{\text{g}}, 5_{\bar{\text{q}'}}}; 6_{\ell}, 7_{\bar{\ell}}) + \tilde{B}_3^{\text{WH},0}(4_{\text{q}}, 3_{\tilde{\text{g}}}, \hat{1}_{\tilde{\text{g}}}, \hat{2}_{\tilde{\text{g}}}, 5_{\bar{\text{q}'}}}; 6_{\ell}, 7_{\bar{\ell}}) \right. \\
&\quad \left. + \tilde{B}_3^{\text{WH},0}(4_{\text{q}}, \hat{1}_{\tilde{\text{g}}}, 3_{\text{g}}, \hat{2}_{\tilde{\text{g}}}, 5_{\bar{\text{q}'}}}; 6_{\ell}, 7_{\bar{\ell}}) \right] \left. \right\}
\end{aligned}$$

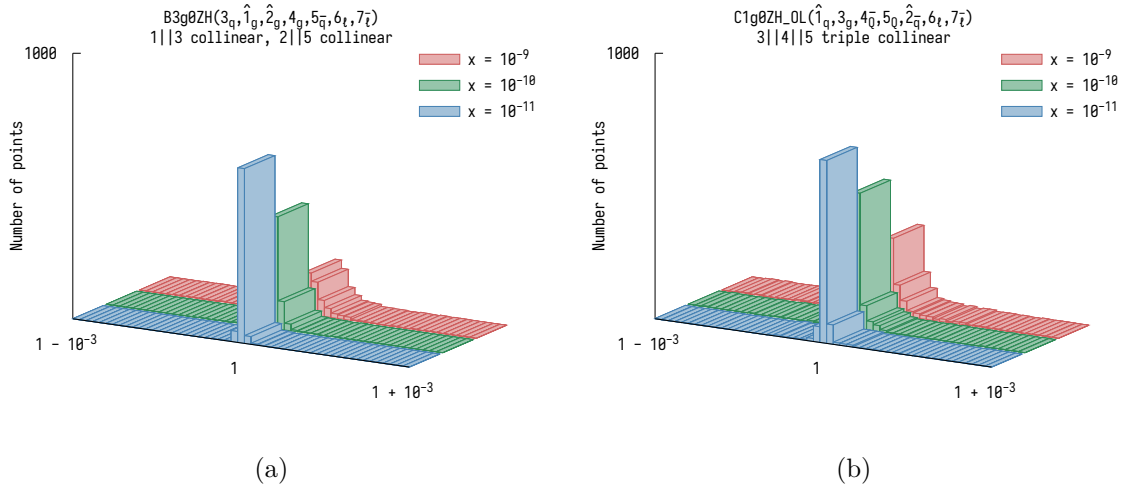


Figure 2.2: Spike tests for a $\hat{1}_g \parallel 3_q$ and $\hat{2}_g \parallel 5_{\bar{q}}$ double collinear limit in (a) for the gg-initiated leading-colour double-real amplitude $B_3^{\text{ZH},0}(3_q, \hat{1}_g, \hat{2}_g, 4_g, 5_{\bar{q}}, 6_\ell, 7_{\bar{\ell}})$ and another one for a $3_g \parallel 4_{\bar{q}} \parallel 5_Q$ triple collinear limit in (b) for the $q\bar{q}$ -initiated double-real OpenLoops amplitude $C_{1,OL}^{\text{ZH},0}(\hat{1}_q, 3_g, 4_{\bar{q}}, 5_Q, \hat{2}_{\bar{q}}, 6_\ell, 7_{\bar{\ell}})$. A total of 1000 configurations were probed in both cases.

$$+ \left[\frac{n_F}{2} \right] \left(\frac{1}{N_c^2} + \frac{1}{N_c^4} \right) \tilde{B}_3^{\text{WH},0}(4_q, \hat{1}_{\bar{g}}, \hat{2}_{\bar{g}}, 3_{\bar{g}}, 5_{\bar{q}'}; 6_\ell, 7_{\bar{\ell}}) \}. \quad (2.35)$$

A diagonal CKM matrix is once again assumed for WH+jet production when counting the number of possible quark pairs the W^\pm can couple to.

Subtraction Terms

The double-real S subtraction terms were fully recycled from the already implemented Z+jet and W^\pm +jet processes. I used the same module I already took advantage of for VH production to replace the reduced matrix elements in the subtraction terms with non-momentum-conserving ones, which are all of lower order and are implemented natively in NNLOJET. Next, I manually assembled the subtraction terms, which were originally intended for various colour levels, exactly as I listed them throughout the previous channel breakdowns.

The ultimate tests for whether real subtraction terms work as intended are the spike tests, therefore I carried them out in all unresolved limits. Two examples are shown in Figure 2.2. The successful spike tests guarantee a correct match—including all symmetry and normalization factors—between the OpenLoops amplitudes and the native NNLOJET subtraction terms which were assembled to encompass all colour levels.

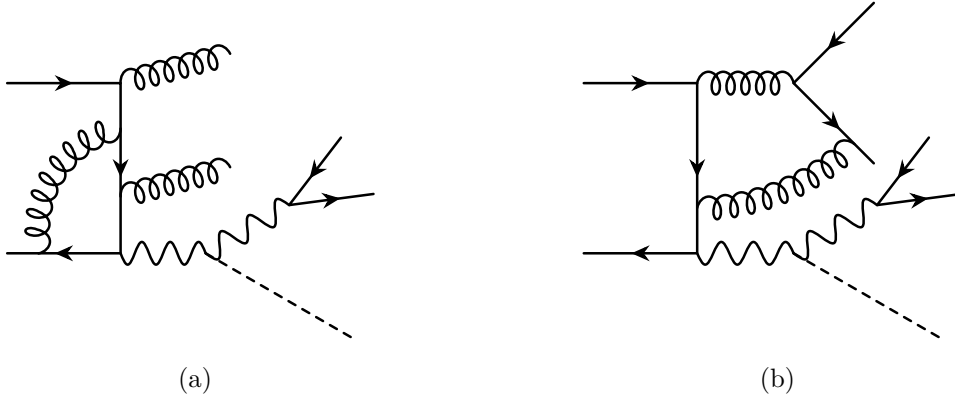


Figure 2.3: Example of a B -type diagram in (a) and a C -type one in (b) that contribute to real–virtual VH +jet production.

2.3.2 Real–Virtual Cross Section

In this section I will present all partonic channels that contribute to real–virtual VH +jet production. All of the amplitudes are evaluated via OpenLoops on this level, therefore I will follow the same strategy I already introduced previously. First, I will describe how the OpenLoops amplitudes can be constructed from native NNLOJET ones, which are only implemented for Z +jet and W^\pm +jet. This is in order to understand how the new subtraction terms need to be assembled from the native colour-ordered ones to successfully cancel the poles and unresolved limits present in the OpenLoops amplitudes. Next, I will put together the partonic cross sections for the various channels from these OpenLoops amplitudes, not unlike how it was done for the double-real C - and D -type amplitudes in the previous section. Two examples of diagrams that contribute to real–virtual VH +jet production are visualized in Figure 2.3.

The B -type amplitudes on the real–virtual level consist of the leading-colour $B_2^{VH,1}$ piece, the subleading-colour $\tilde{B}_2^{VH,1}$ piece, two sub-subleading-colour pieces: $\tilde{\tilde{B}}_2^{VH,1}$ and $\hat{\tilde{B}}_2^{VH,1}$, the sub-sub-subleading-colour $\tilde{\tilde{\tilde{B}}}_2^{VH,1}$ piece, the n_F -proportional $\hat{B}_2^{VH,1}$ piece, and finally the subleading-colour n_F -proportional $\hat{\hat{B}}_2^{VH,1}$ piece. The OpenLoops amplitudes encompass all of the colour levels and permutations that arise in the NNLOJET-native ones according to the following formula

$$B_{2,OL}^{VH,1}(i_q, j_g, k_g, l_{\bar{q}}; 5_\ell, 6_{\bar{\ell}}) = \frac{\mathcal{N}_{VHj}^{RV}}{A} \frac{1}{S} \times \left\{ \sum_{(j \leftrightarrow k)} \left[B_2^{VH,1}(i_q, j_g, k_g, l_{\bar{q}}; 5_\ell, 6_{\bar{\ell}}) - \frac{1}{N_c^2} \tilde{B}_2^{VH,1}(i_q, j_g, k_g, l_{\bar{q}}; 5_\ell, 6_{\bar{\ell}}) \right] \right.$$

$$\begin{aligned}
& + \frac{n_F}{N_c} \hat{B}_2^{VH,1}(i_q, j_{\bar{g}}, k_{\bar{g}}, l_{\bar{q}}; 5_\ell, 6_{\bar{\ell}}) \Big] \\
& - \frac{1}{N_c^2} \left[\tilde{\hat{B}}_2^{VH,1}(i_q, j_{\bar{g}}, k_{\bar{g}}, l_{\bar{q}}; 5_\ell, 6_{\bar{\ell}}) - \hat{B}_2^{VH,1}(i_q, j_{\bar{g}}, k_{\bar{g}}, l_{\bar{q}}; 5_\ell, 6_{\bar{\ell}}) \right. \\
& \quad \left. - \frac{1}{N_c^2} \tilde{\tilde{B}}_2^{VH,1}(i_q, j_{\bar{g}}, k_{\bar{g}}, l_{\bar{q}}; 5_\ell, 6_{\bar{\ell}}) + \frac{n_F}{N_c} \hat{B}_2^{VH,1}(i_q, j_{\bar{g}}, k_{\bar{g}}, l_{\bar{q}}; 5_\ell, 6_{\bar{\ell}}) \right] \Big\}, \quad (2.36)
\end{aligned}$$

where we treated the ZH+jet and WH+jet amplitudes together, because a single quark line is not confusing when we consider the flavour change due to the W^\pm boson. The averaging factor A depends on which partons are in the initial state and can take the values $A = (2N_c)^2$ for the quark–antiquark, $A = (2N_c)[2(N_c^2 - 1)]$ for the (anti)quark–gluon, and $A = [2(N_c^2 - 1)]^2$ for the gluon–gluon channels. Likewise, the symmetry factor S also depends on the particular channel and takes $\frac{1}{S} = \frac{1}{2!}$ for the quark–antiquark channels due to two identical gluons in the final state and $\frac{1}{S} = 1$ for all the other cases.

The C -type amplitudes, which consist of two non-identical quark lines, promptly separate into the leading-colour $C_0^{VH,1}$ piece, the subleading-colour $\tilde{C}_0^{VH,1}$ piece, and the n_F -proportional $\hat{C}_0^{VH,1}$ piece. The OpenLoops amplitudes assemble them as

$$\begin{aligned}
C_{0,OL}^{ZH,1}(i_q, j_{\bar{Q}}, k_Q, l_{\bar{q}}; 5_\ell, 6_{\bar{\ell}}) &= \frac{\mathcal{N}_{ZHj}^{RV}}{(2N_c)^2} \frac{1}{N_c} \left\{ C_0^{ZH,1}(i_q, j_{\bar{Q}}, k_Q, l_{\bar{q}}; 5_\ell, 6_{\bar{\ell}}) \right. \\
& \quad \left. - \frac{1}{N_c^2} \tilde{C}_0^{ZH,1}(i_q, j_{\bar{Q}}, k_Q, l_{\bar{q}}; 5_\ell, 6_{\bar{\ell}}) + \frac{n_F}{N_c} \hat{C}_0^{ZH,1}(i_q, j_{\bar{Q}}, k_Q, l_{\bar{q}}; 5_\ell, 6_{\bar{\ell}}) \right\}, \quad (2.37)
\end{aligned}$$

$$\begin{aligned}
C_{0,OL}^{WH,1}(i_q, j_{\bar{Q}}, k_Q, l_{\bar{q}'}; 5_\ell, 6_{\bar{\ell}}) &= \frac{\mathcal{N}_{WHj}^{RV}}{(2N_c)^2} \frac{1}{N_c} \left\{ C_0^{WH,1}(i_q, j_{\bar{Q}}, k_Q, l_{\bar{q}'}; 5_\ell, 6_{\bar{\ell}}) \right. \\
& \quad \left. - \frac{1}{N_c^2} \tilde{C}_0^{WH,1}(i_q, j_{\bar{Q}}, k_Q, l_{\bar{q}'}; 5_\ell, 6_{\bar{\ell}}) + \frac{n_F}{N_c} \hat{C}_0^{WH,1}(i_q, j_{\bar{Q}}, k_Q, l_{\bar{q}'}; 5_\ell, 6_{\bar{\ell}}) \right\}. \quad (2.38)
\end{aligned}$$

Similarly to the previous section, the formulæ above always assume that $Q \neq q$ and $Q \neq q'$. In case of identical quark contributions, permutations and the insertion of the correct symmetry factors are carried out on the OpenLoops amplitude level; the structure of eqs. (2.37) and (2.38) is left intact.

The D -type interference terms are subleading-colour to their corresponding C -type amplitudes and arise in the case when both quark lines are identical (ZH+jet production) or almost identical (WH+jet production). They also consist of the leading-colour $D_0^{VH,1}$ piece, the subleading-colour $\tilde{D}_0^{VH,1}$ piece, and the n_F -proportional $\hat{D}_0^{VH,1}$ piece. Specifically, we distinguish D_a -type and D_b -type amplitudes for WH+jet, as before, depending on which of

the three quarks are of identical flavour. The OpenLoops amplitudes for these are assembled as follows:

$$D_{0,\text{OL}}^{\text{ZH},1}(i_q, j_{\bar{q}}, k_q, l_{\bar{q}}; 5_\ell, 6_{\bar{\ell}}) = \frac{\mathcal{N}_{\text{ZHj}}^{\text{RV}}}{(2N_c)^2} \frac{1}{S} \frac{1}{N_c^2} \left\{ D_0^{\text{ZH},1}(i_q, j_{\bar{q}}, k_q, l_{\bar{q}}; 5_\ell, 6_{\bar{\ell}}) \right. \\ \left. - \frac{1}{N_c^2} \tilde{D}_0^{\text{ZH},1}(i_q, j_{\bar{q}}, k_q, l_{\bar{q}}; 5_\ell, 6_{\bar{\ell}}) + \frac{n_F}{N_c} \hat{D}_0^{\text{ZH},1}(i_q, j_{\bar{q}}, k_q, l_{\bar{q}}; 5_\ell, 6_{\bar{\ell}}) \right\}, \quad (2.39)$$

$$D_{a,0,\text{OL}}^{\text{WH},1}(i_q, j_{\bar{q}}, k_q, l_{\bar{q}'}; 5_\ell, 6_{\bar{\ell}}) = \frac{\mathcal{N}_{\text{WHj}}^{\text{RV}}}{(2N_c)^2} \frac{1}{S} \frac{1}{N_c^2} \left\{ D_0^{\text{WH},1}(i_q, j_{\bar{q}}, k_q, l_{\bar{q}'}; 5_\ell, 6_{\bar{\ell}}) \right. \\ \left. - \frac{1}{N_c^2} \tilde{D}_0^{\text{WH},1}(i_q, j_{\bar{q}}, k_q, l_{\bar{q}'}; 5_\ell, 6_{\bar{\ell}}) + \frac{n_F}{N_c} \hat{D}_0^{\text{WH},1}(i_q, j_{\bar{q}}, k_q, l_{\bar{q}'}; 5_\ell, 6_{\bar{\ell}}) \right\}, \quad (2.40)$$

$$D_{b,0,\text{OL}}^{\text{WH},1}(i_q, j_{\bar{q}'}, k_{q'}, l_{\bar{q}'}; 5_\ell, 6_{\bar{\ell}}) = \frac{\mathcal{N}_{\text{WHj}}^{\text{RV}}}{(2N_c)^2} \frac{1}{S} \frac{1}{N_c^2} \left\{ D_0^{\text{WH},1}(i_q, j_{\bar{q}'}, k_{q'}, l_{\bar{q}'}; 5_\ell, 6_{\bar{\ell}}) \right. \\ \left. - \frac{1}{N_c^2} \tilde{D}_0^{\text{WH},1}(i_q, j_{\bar{q}'}, k_{q'}, l_{\bar{q}'}; 5_\ell, 6_{\bar{\ell}}) + \frac{n_F}{N_c} \hat{D}_0^{\text{WH},1}(i_q, j_{\bar{q}'}, k_{q'}, l_{\bar{q}'}; 5_\ell, 6_{\bar{\ell}}) \right\}. \quad (2.41)$$

The accompanying symmetry factor S in these expressions depends on how many identical particles are in the final state and can either be $\frac{1}{S} = \frac{1}{2!}$ or $\frac{1}{S} = 1$ accordingly.

Quark–Quark Initiated (Non-Identical Flavour)

$$d\hat{\sigma}_{\text{ZHj},qQ}^{\text{RV}} = d\Phi_4(p_1, p_2; \{p_i\}_{i=3}^6) \mathcal{J}_1^{(2)}(p_3, p_4) C_{0,\text{OL}}^{\text{ZH},1}(\hat{1}_q, 3_{\bar{Q}}, \hat{2}_Q, 4_{\bar{q}}; 5_\ell, 6_{\bar{\ell}}), \quad (2.42)$$

$$d\hat{\sigma}_{\text{WHj},qQ}^{\text{RV}} = d\Phi_4(p_1, p_2; \{p_i\}_{i=3}^6) \mathcal{J}_1^{(2)}(p_3, p_4) C_{0,\text{OL}}^{\text{WH},1}(\hat{1}_q, 3_{\bar{Q}}, \hat{2}_Q, 4_{\bar{q}'}; 5_\ell, 6_{\bar{\ell}}). \quad (2.43)$$

The WH+jet cross section has an additional permutation and subleading-colour interference term when $Q = q'$, in other words

$$d\hat{\sigma}_{\text{WHj},qq'}^{\text{RV}} = d\Phi_4(p_1, p_2; \{p_i\}_{i=3}^6) \mathcal{J}_1^{(2)}(p_3, p_4) \times \\ \left\{ \frac{1}{2!} \left[C_{0,\text{OL}}^{\text{WH},1}(\hat{1}_q, 3_{\bar{q}'}, \hat{2}_{q'}, 4_{\bar{q}'}; 5_\ell, 6_{\bar{\ell}}) + C_{0,\text{OL}}^{\text{WH},1}(\hat{1}_q, 4_{\bar{q}'}, \hat{2}_{q'}, 3_{\bar{q}'}; 5_\ell, 6_{\bar{\ell}}) \right] \right. \\ \left. + D_{b,0,\text{OL}}^{\text{WH},1}(\hat{1}_q, 3_{\bar{q}'}, \hat{2}_{q'}, 4_{\bar{q}'}; 5_\ell, 6_{\bar{\ell}}) \right\}. \quad (2.44)$$

The symmetry factor $\frac{1}{2!}$ is present due to the identical $3_{\bar{q}'}$ and $4_{\bar{q}'}$ quarks in the final state.⁹ In practice the ($3_{\bar{q}'} \leftrightarrow 4_{\bar{q}'}$) permutation is carried out by phase-space integration and thus the two terms are contracted into one in the codebase.

Quark–Quark Initiated (Identical Flavour)

$$\begin{aligned} d\hat{\sigma}_{\text{ZHj},qq}^{\text{RV}} &= d\Phi_4(p_1, p_2; \{p_i\}_{i=3}^6) \mathcal{J}_1^{(2)}(p_3, p_4) \times \\ &\quad \left\{ \frac{1}{2!} \left[C_{0,\text{OL}}^{\text{ZH},1}(\hat{1}_q, 3_{\bar{q}}, \hat{2}_q, 4_{\bar{q}}; 5_\ell, 6_{\bar{\ell}}) + C_{0,\text{OL}}^{\text{ZH},1}(\hat{1}_q, 4_{\bar{q}}, \hat{2}_q, 3_{\bar{q}}; 5_\ell, 6_{\bar{\ell}}) \right] \right. \\ &\quad \left. + D_{0,\text{OL}}^{\text{ZH},1}(\hat{1}_q, 3_{\bar{q}}, \hat{2}_q, 4_{\bar{q}}; 5_\ell, 6_{\bar{\ell}}) \right\}, \end{aligned} \quad (2.45)$$

$$\begin{aligned} d\hat{\sigma}_{\text{WHj},qq}^{\text{RV}} &= d\Phi_4(p_1, p_2; \{p_i\}_{i=3}^6) \mathcal{J}_1^{(2)}(p_3, p_4) \times \\ &\quad \left\{ C_{0,\text{OL}}^{\text{WH},1}(\hat{1}_q, 3_{\bar{q}}, \hat{2}_q, 4_{\bar{q}'}; 5_\ell, 6_{\bar{\ell}}) + C_{0,\text{OL}}^{\text{WH},1}(\hat{2}_q, 3_{\bar{q}}, \hat{1}_q, 4_{\bar{q}'}; 5_\ell, 6_{\bar{\ell}}) \right. \\ &\quad \left. + D_{a,0,\text{OL}}^{\text{WH},1}(\hat{1}_q, 3_{\bar{q}}, \hat{2}_q, 4_{\bar{q}'}; 5_\ell, 6_{\bar{\ell}}) \right\}. \end{aligned} \quad (2.46)$$

The symmetry factor $\frac{1}{2!}$ for ZH+jet production is due to the identical quarks $3_{\bar{q}}$ and $4_{\bar{q}}$ in the final state.¹⁰ In practice, the permutation ($3_{\bar{q}} \leftrightarrow 4_{\bar{q}}$) is done via phase-space integration and the two terms are contracted into one in the codebase.

Identical quarks in the final state are not present for WH+jet production due to the flavour-changing effect of the W^\pm coupling.

Antiquark–Antiquark Initiated (Non-Identical Flavour)

$$d\hat{\sigma}_{\text{ZHj},\bar{Q}\bar{Q}}^{\text{RV}} = d\Phi_4(p_1, p_2; \{p_i\}_{i=3}^6) \mathcal{J}_1^{(2)}(p_3, p_4) C_{0,\text{OL}}^{\text{ZH},1}(3_q, \hat{1}_{\bar{Q}}, 4_Q, \hat{2}_{\bar{Q}}; 5_\ell, 6_{\bar{\ell}}), \quad (2.47)$$

$$d\hat{\sigma}_{\text{WHj},\bar{Q}\bar{Q}}^{\text{RV}} = d\Phi_4(p_1, p_2; \{p_i\}_{i=3}^6) \mathcal{J}_1^{(2)}(p_3, p_4) C_{0,\text{OL}}^{\text{WH},1}(3_q, \hat{1}_{\bar{Q}}, 4_Q, \hat{2}_{\bar{Q}}; 5_\ell, 6_{\bar{\ell}}). \quad (2.48)$$

The WH+jet cross section has an additional permutation and subleading-colour interference

⁹This is built into $D_{b,0,\text{OL}}^{\text{WH},1}$ as shown in eq. (2.41).

¹⁰This is built into $D_{0,\text{OL}}^{\text{ZH},1}$ as shown in eq. (2.39).

term when $Q = q$, in other words

$$\begin{aligned} d\hat{\sigma}_{\text{WHj},\bar{q}\bar{q}'}^{\text{RV}} &= d\Phi_4(p_1, p_2; \{p_i\}_{i=3}^6) \mathcal{J}_1^{(2)}(p_3, p_4) \times \\ &\quad \left\{ \frac{1}{2!} \left[C_{0,\text{OL}}^{\text{WH},1}(3_q, \hat{1}_{\bar{q}}, 4_q, \hat{2}_{\bar{q}'}; 5_\ell, 6_{\bar{\ell}}) + C_{0,\text{OL}}^{\text{WH},1}(4_q, \hat{1}_{\bar{q}}, 3_q, \hat{2}_{\bar{q}'}; 5_\ell, 6_{\bar{\ell}}) \right] \right. \\ &\quad \left. + D_{a,0,\text{OL}}^{\text{WH},1}(3_q, \hat{1}_{\bar{q}}, 4_q, \hat{2}_{\bar{q}'}; 5_\ell, 6_{\bar{\ell}}) \right\}. \end{aligned} \quad (2.49)$$

The symmetry factor $\frac{1}{2!}$ is present due to the identical 3_q and 4_q quarks in the final state¹¹ whose permutation in practice is carried out by phase-space integration.

Antiquark–Antiquark Initiated (Identical Flavour)

$$\begin{aligned} d\hat{\sigma}_{\text{ZHj},\bar{q}\bar{q}}^{\text{RV}} &= d\Phi_4(p_1, p_2; \{p_i\}_{i=3}^6) \mathcal{J}_1^{(3)}(p_3, p_4) \times \\ &\quad \left\{ \frac{1}{2!} \left[C_{0,\text{OL}}^{\text{ZH},1}(3_q, \hat{1}_{\bar{q}}, 4_q, \hat{2}_{\bar{q}}; 5_\ell, 6_{\bar{\ell}}) + C_{0,\text{OL}}^{\text{ZH},1}(4_q, \hat{1}_{\bar{q}}, 3_q, \hat{2}_{\bar{q}}; 5_\ell, 6_{\bar{\ell}}) \right] \right. \\ &\quad \left. + D_{0,\text{OL}}^{\text{ZH},1}(3_q, \hat{1}_{\bar{q}}, 4_q, \hat{2}_{\bar{q}}; 5_\ell, 6_{\bar{\ell}}) \right\}, \end{aligned} \quad (2.50)$$

$$\begin{aligned} d\hat{\sigma}_{\text{WHj},\bar{q}'\bar{q}'}^{\text{RV}} &= d\Phi_4(p_1, p_2; \{p_i\}_{i=3}^6) \mathcal{J}_1^{(2)}(p_3, p_4) \times \\ &\quad \left\{ C_{0,\text{OL}}^{\text{WH},1}(3_q, \hat{1}_{\bar{q}'}, 4_{q'}, \hat{2}_{\bar{q}'}; 5_\ell, 6_{\bar{\ell}}) + C_{0,\text{OL}}^{\text{WH},1}(3_q, \hat{2}_{\bar{q}'}, 4_{q'}, \hat{1}_{\bar{q}'}; 5_\ell, 6_{\bar{\ell}}) \right. \\ &\quad \left. + D_{b,0,\text{OL}}^{\text{WH},1}(3_q, \hat{1}_{\bar{q}'}, 4_{q'}, \hat{2}_{\bar{q}'}; 5_\ell, 6_{\bar{\ell}}) \right\}. \end{aligned} \quad (2.51)$$

The symmetry factor $\frac{1}{2!}$ for ZH+jet production is due to the identical quarks 3_q and 4_q in the final state¹² whose permutation in practice is carried out by phase-space integration. It is not present for WH+jet production due to the flavour-changing effect of the W^\pm coupling.

Quark–Antiquark Initiated (Non-Identical Flavour)

$$d\hat{\sigma}_{\text{ZHj},q\bar{Q}}^{\text{RV}} = d\Phi_4(p_1, p_2; \{p_i\}_{i=3}^6) \mathcal{J}_1^{(2)}(p_3, p_4) C_{0,\text{OL}}^{\text{ZH},1}(\hat{1}_q, \hat{2}_{\bar{Q}}, 3_Q, 4_{\bar{q}}; 5_\ell, 6_{\bar{\ell}}), \quad (2.52)$$

$$d\hat{\sigma}_{\text{WHj},q\bar{Q}}^{\text{RV}} = d\Phi_4(p_1, p_2; \{p_i\}_{i=3}^6) \mathcal{J}_1^{(2)}(p_3, p_4) C_{0,\text{OL}}^{\text{WH},1}(\hat{1}_q, \hat{2}_{\bar{Q}}, 3_Q, 4_{\bar{q}'}; 5_\ell, 6_{\bar{\ell}}). \quad (2.53)$$

¹¹This is built into $D_{a,0,\text{OL}}^{\text{WH},1}$ as shown in eq. (2.40).

¹²This is built into $D_{0,\text{OL}}^{\text{ZH},1}$ as shown in eq. (2.39).

The WH+jet cross section has additional leading- and subleading-colour contributions when $Q = q'$, namely

$$\begin{aligned}
d\hat{\sigma}_{\text{WHj},q\bar{q}'}^{\text{RV}} &= d\Phi_4(p_1, p_2; \{p_i\}_{i=3}^6) \mathcal{J}_1^{(2)}(p_3, p_4) \times \\
&\left\{ B_{2,\text{OL}}^{\text{WH},1}(\hat{1}_q, 3_g, 4_g, \hat{2}_{q'}; 5_\ell, 6_{\bar{\ell}}) + n_{\text{F}} C_{0,\text{OL}}^{\text{WH},1}(\hat{1}_q, 3_{\bar{Q}}, 4_Q, \hat{2}_{q'}; 5_\ell, 6_{\bar{\ell}}) \right. \\
&+ C_{0,\text{OL}}^{\text{WH},1}(4_q, 3_{\bar{q}}, \hat{1}_q, \hat{2}_{q'}; 5_\ell, 6_{\bar{\ell}}) + C_{0,\text{OL}}^{\text{WH},1}(\hat{1}_q, \hat{2}_{q'}, 4_{q'}, 3_{\bar{q}'}; 5_\ell, 6_{\bar{\ell}}) \\
&\left. + D_{a,0,\text{OL}}^{\text{WH},1}(\hat{1}_q, 3_{\bar{q}}, 4_q, \hat{2}_{q'}; 5_\ell, 6_{\bar{\ell}}) + D_{b,0,\text{OL}}^{\text{WH},1}(\hat{1}_q, \hat{2}_{q'}, 3_{q'}, 4_{\bar{q}'}; 5_\ell, 6_{\bar{\ell}}) \right\}. \quad (2.54)
\end{aligned}$$

Quark–Antiquark Initiated (Identical Flavour)

$$\begin{aligned}
d\hat{\sigma}_{\text{ZHj},q\bar{q}}^{\text{RV}} &= d\Phi_4(p_1, p_2; \{p_i\}_{i=3}^6) \mathcal{J}_1^{(2)}(p_3, p_4) \left\{ B_{2,\text{OL}}^{\text{ZH},1}(\hat{1}_q, 3_g, 4_g, \hat{2}_{\bar{q}}; 5_\ell, 6_{\bar{\ell}}) \right. \\
&+ n_{\text{up}} C_{0,\text{OL}}^{\text{ZH},1}(\hat{1}_q, 3_{\bar{u}}, 4_u, \hat{2}_{\bar{q}}; 5_\ell, 6_{\bar{\ell}}) + n_{\text{down}} C_{0,\text{OL}}^{\text{ZH},1}(\hat{1}_q, 3_{\bar{d}}, 4_d, \hat{2}_{\bar{q}}; 5_\ell, 6_{\bar{\ell}}) \\
&\left. + C_{1,\text{OL}}^{\text{ZH},0}(\hat{1}_q, \hat{2}_{\bar{q}}, 4_q, 3_{\bar{q}}; 5_\ell, 6_{\bar{\ell}}) + D_{1,\text{OL}}^{\text{ZH},0}(\hat{1}_q, \hat{2}_{\bar{q}}, 4_q, 3_{\bar{q}}; 5_\ell, 6_{\bar{\ell}}) \right\}, \quad (2.55)
\end{aligned}$$

$$\begin{aligned}
d\hat{\sigma}_{\text{WHj},q\bar{q}}^{\text{RV}} &= d\Phi_4(p_1, p_2; \{p_i\}_{i=3}^6) \mathcal{J}_1^{(2)}(p_3, p_4) \times \\
&\left\{ C_{0,\text{OL}}^{\text{WH},1}(\hat{1}_q, \hat{2}_{\bar{q}}, 3_q, 4_{\bar{q}'}; 5_\ell, 6_{\bar{\ell}}) + \left\lfloor \frac{n_{\text{F}}}{2} \right\rfloor C_{0,\text{OL}}^{\text{WH},1}(3_q, \hat{2}_{\bar{q}}, \hat{1}_q, 4_{\bar{q}'}; 5_\ell, 6_{\bar{\ell}}) \right. \\
&\left. + D_{a,0,\text{OL}}^{\text{WH},1}(\hat{1}_q, \hat{2}_{\bar{q}}, 3_q, 4_{\bar{q}'}; 5_\ell, 6_{\bar{\ell}}) \right\}. \quad (2.56)
\end{aligned}$$

B -type amplitudes are only present for ZH+jet production in eq. (2.55). Due to the different coupling of the Z boson to quark lines, up- and down-type C -type amplitudes need to be separately accounted for.

In the second term for WH+jet production (2.56) the quark current in the final state couples directly to the W^\pm boson with a diagonal CKM matrix as usual.

Quark–Gluon Initiated

Only B -type amplitudes are present, therefore ZH+jet and WH+jet cross sections can be treated together without confusion.

$$d\hat{\sigma}_{\text{VHj},qg}^{\text{RV}} = d\Phi_4(p_1, p_2; \{p_i\}_{i=3}^6) \mathcal{J}_1^{(2)}(p_3, p_4) B_{2,\text{OL}}^{\text{VH},1}(\hat{1}_q, \hat{2}_g, 3_g, 4_{\bar{q}}; 5_\ell, 6_{\bar{\ell}}). \quad (2.57)$$

Antiquark–Gluon Initiated

Similarly to the quark–gluon channel

$$d\hat{\sigma}_{VH_j, \bar{q}g}^{\text{RV}} = d\Phi_4(p_1, p_2; \{p_i\}_{i=3}^6) \mathcal{J}_1^{(2)}(p_3, p_4) B_{2, \text{OL}}^{VH, 1}(3_q, \hat{2}_g, 4_g, \hat{1}_{\bar{q}}; 5_\ell, 6_{\bar{\ell}}). \quad (2.58)$$

Gluon–Gluon Initiated

This channel does not contain any C - or D -type amplitudes either, nevertheless we still need to distinguish the ZH +jet and the WH +jet cases because up- and down-type contributions have to be accounted for separately whenever the Z coupling is involved.

$$d\hat{\sigma}_{ZH_j, gg}^{\text{RV}} = d\Phi_4(p_1, p_2; \{p_i\}_{i=3}^6) \mathcal{J}_1^{(2)}(p_3, p_4) \times \\ \left\{ n_{\text{up}} B_{2, \text{OL}}^{\text{ZH}, 1}(3_u, \hat{1}_g, \hat{2}_g, 4_{\bar{u}}; 5_\ell, 6_{\bar{\ell}}) + n_{\text{down}} B_{2, \text{OL}}^{\text{ZH}, 1}(3_d, \hat{1}_g, \hat{2}_g, 4_{\bar{d}}; 5_\ell, 6_{\bar{\ell}}) \right\}, \quad (2.59)$$

$$d\hat{\sigma}_{WH_j, gg}^{\text{RV}} = d\Phi_4(p_1, p_2; \{p_i\}_{i=3}^6) \mathcal{J}_1^{(2)}(p_3, p_4) \left[\frac{n_F}{2} \right] B_{2, \text{OL}}^{\text{WH}, 1}(3_q, \hat{1}_g, \hat{2}_g, 4_{q'}; 5_\ell, 6_{\bar{\ell}}). \quad (2.60)$$

Additional Closed Fermion-Loop Contributions

At the real–virtual level, there are closed fermion loop contributions that unfortunately cannot be included because the corresponding two-loop amplitudes on the double-virtual level are unknown at this point. These are radiative corrections to both Yukawa and Drell–Yan-like VH Feynman diagrams shown in Figures 1.14b, 1.15a, and 1.15b. Together with their respective double-virtual contributions they form gauge-invariant subsets of all amplitudes, thus can be omitted from the calculation without spoiling gauge invariance.

In Section 2.4 we will argue that not including NNLO Yukawa-induced corrections in the WH +jet cross sections—which are the only ones present when the charged gauge boson is involved—is phenomenologically not a serious omission.

Subtraction Terms

The real–virtual T subtraction terms fully recycle those of the Z +jet and W^\pm +jet processes to subtract unresolved limits, pole parts of the loop integrals, and perform the mass factorization. Knowing the colour structure of the amplitudes (2.36)–(2.41) evaluated via OpenLoops allows for constructing the subtraction terms for each partonic channel after replacing the reduced matrix elements with their non-momentum-conserving counterparts. All reduced

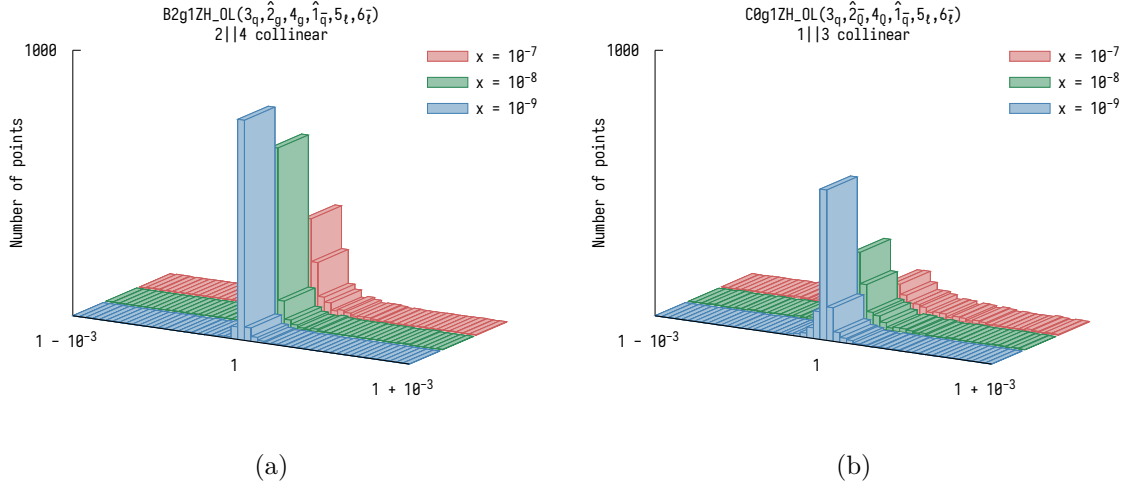


Figure 2.4: Spike tests for a $\hat{2}_g \parallel 4_g$ collinear limit in (a) for the $\bar{q}g$ -initiated real-virtual OpenLoops amplitude $B_{2,OL}^{ZH,1}(3_q, \hat{2}_g, 4_g, \hat{1}_{\bar{q}}, 5_\ell, 6_{\bar{\ell}})$ and another one for a $\hat{1}_{\bar{q}} \parallel 3_q$ collinear limit in (b) for the $\bar{q}\bar{Q}$ -initiated real-virtual OpenLoops amplitude $C_{0,OL}^{ZH,1}(3_q, \hat{2}_{\bar{Q}}, 4_Q, \hat{1}_{\bar{q}}, 5_\ell, 6_{\bar{\ell}})$. A total of 1000 configurations were probed in both cases.

matrix elements are of lower-order amplitudes, which we have covered for VH production and are written as part of the NNLOJET codebase.

Due to calling amplitudes from OpenLoops and not having access to the analytical formulæ, pole cancellations in the dimensional regularization parameter ϵ were tested only numerically. And as usual, spike tests in all unresolved limits as shown in Figure 2.4 have been successfully carried out. Successful spike tests indicate that subtraction terms constructed from multiple colour levels mimic the infrared structure of the OpenLoops amplitudes correctly.

2.3.3 Double-Virtual Cross Section

The common double-virtual cross sections for both ZH+jet and WH+jet production contain only B -type partonic contributions, i.e. amplitudes of one quark line and one gluon. As usual, they are made of (one-loop)² and genuine (two-loop) \times (tree-level) interferences. An example of a genuine two-loop diagram is shown in Figure 2.5. The cross sections for each partonic channel are

$$d\hat{\sigma}_{VH_j, q\bar{q}}^{VV} = d\Phi_3(p_1, p_2; \{p_i\}_{i=3}^5) \mathcal{J}_1^{(1)}(p_3) \frac{\mathcal{N}_{VH_j}^{VV}}{(2N_c)^2} \times$$

$$\left\{ B_1^{VH,2}(\hat{1}_q, 3_g, \hat{2}_{\bar{q}}, 4_\ell, 5_{\bar{\ell}}) - \frac{1}{N_c^2} \tilde{B}_1^{VH,2}(\hat{1}_q, 3_g, \hat{2}_{\bar{q}}, 4_\ell, 5_{\bar{\ell}}) + \frac{1}{N_c^4} \tilde{\tilde{B}}_1^{VH,2}(\hat{1}_q, 3_g, \hat{2}_{\bar{q}}, 4_\ell, 5_{\bar{\ell}}) \right\}$$

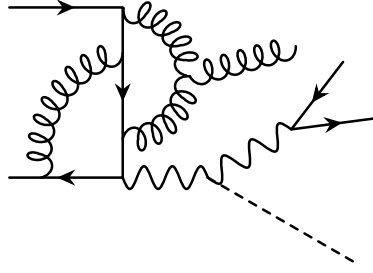


Figure 2.5: Example of a genuine two-loop B -type diagram that contributes to double-virtual VH +jet production.

$$+ \frac{n_F}{N_c} \hat{B}_1^{VH,2}(\hat{1}_q, 3_g, \hat{2}_{\bar{q}}; 4_\ell, 5_{\bar{\ell}}) + \frac{n_F}{N_c^3} \hat{\hat{B}}_1^{VH,2}(\hat{1}_q, 3_g, \hat{2}_{\bar{q}}; 4_\ell, 5_{\bar{\ell}}) + \frac{n_F^2}{N_c^2} \hat{\hat{\hat{B}}}_1^{VH,2}(\hat{1}_q, 3_g, \hat{2}_{\bar{q}}; 4_\ell, 5_{\bar{\ell}}) \Big\}, \quad (2.61)$$

$$\begin{aligned} d\hat{\sigma}_{VHj,gg}^{VV} &= d\Phi_3(p_1, p_2; \{p_i\}_{i=3}^5) \mathcal{J}_1^{(1)}(p_3) \frac{\mathcal{N}_{VHj}^{VV}}{(2N_c)[2(N_c^2 - 1)]} \times \\ &\left\{ B_1^{VH,2}(\hat{1}_q, \hat{2}_g, 3_{\bar{q}}; 4_\ell, 5_{\bar{\ell}}) - \frac{1}{N_c^2} \tilde{B}_1^{VH,2}(\hat{1}_q, \hat{2}_g, 3_{\bar{q}}; 4_\ell, 5_{\bar{\ell}}) + \frac{1}{N_c^4} \tilde{\tilde{B}}_1^{VH,2}(\hat{1}_q, \hat{2}_g, 3_{\bar{q}}; 4_\ell, 5_{\bar{\ell}}) \right. \\ &\left. + \frac{n_F}{N_c} \hat{B}_1^{VH,2}(\hat{1}_q, \hat{2}_g, 3_{\bar{q}}; 4_\ell, 5_{\bar{\ell}}) + \frac{n_F}{N_c^3} \hat{\hat{B}}_1^{VH,2}(\hat{1}_q, \hat{2}_g, 3_{\bar{q}}; 4_\ell, 5_{\bar{\ell}}) + \frac{n_F^2}{N_c^2} \hat{\hat{\hat{B}}}_1^{VH,2}(\hat{1}_q, \hat{2}_g, 3_{\bar{q}}; 4_\ell, 5_{\bar{\ell}}) \right\}, \quad (2.62) \end{aligned}$$

$$\begin{aligned} d\hat{\sigma}_{VHj,\bar{q}g}^{VV} &= d\Phi_3(p_1, p_2; \{p_i\}_{i=3}^5) \mathcal{J}_1^{(1)}(p_3) \frac{\mathcal{N}_{VHj}^{VV}}{(2N_c)[2(N_c^2 - 1)]} \times \\ &\left\{ B_1^{VH,2}(3_q, \hat{2}_g, \hat{1}_{\bar{q}}; 4_\ell, 5_{\bar{\ell}}) - \frac{1}{N_c^2} \tilde{B}_1^{VH,2}(3_q, \hat{2}_g, \hat{1}_{\bar{q}}; 4_\ell, 5_{\bar{\ell}}) + \frac{1}{N_c^4} \tilde{\tilde{B}}_1^{VH,2}(3_q, \hat{2}_g, \hat{1}_{\bar{q}}; 4_\ell, 5_{\bar{\ell}}) \right. \\ &\left. + \frac{n_F}{N_c} \hat{B}_1^{VH,2}(3_q, \hat{2}_g, \hat{1}_{\bar{q}}; 4_\ell, 5_{\bar{\ell}}) + \frac{n_F}{N_c^3} \hat{\hat{B}}_1^{VH,2}(3_q, \hat{2}_g, \hat{1}_{\bar{q}}; 4_\ell, 5_{\bar{\ell}}) + \frac{n_F^2}{N_c^2} \hat{\hat{\hat{B}}}_1^{VH,2}(3_q, \hat{2}_g, \hat{1}_{\bar{q}}; 4_\ell, 5_{\bar{\ell}}) \right\}. \quad (2.63) \end{aligned}$$

They consist of the leading-colour $B_1^{VH,2}$ piece, the subleading-colour $\tilde{B}_1^{VH,2}$ piece, the sub-subleading-colour $\tilde{\tilde{B}}_1^{VH,2}$ piece, the n_F -proportional $\hat{B}_1^{VH,2}$ piece, the subleading-colour n_F -proportional $\hat{\hat{B}}_1^{VH,2}$ piece, and finally the n_F^2 -proportional $\hat{\hat{\hat{B}}}_1^{VH,2}$ piece. An overview of the construction of these amplitudes is found in Appendix A.7.

For ZH +jet production, we included additional, separately gauge-invariant gluon–gluon-induced (one-loop)² pieces shown in Figure 2.6. The amplitude is evaluated via OpenLoops

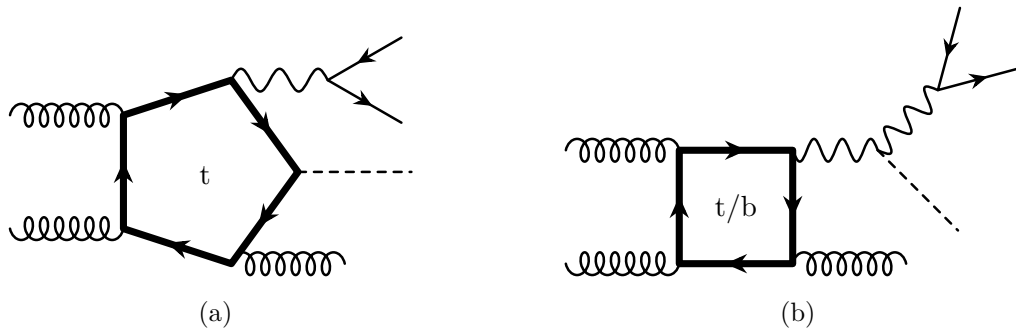


Figure 2.6: Examples of diagrams that contribute exclusively to the gluon–gluon-induced (one-loop)² double-virtual $A_{1,\text{OL}}^{\text{ZH},2}$ OpenLoops amplitude.

and thus the partonic cross section for this gg channel can be written as

$$d\hat{\sigma}_{\text{ZH,gg}}^{\text{VV}} = d\Phi_3(p_1, p_2; \{p_i\}_{i=3}^5) \mathcal{J}_1^{(1)}(p_3) A_{1,\text{OL}}^{\text{ZH},2}(\hat{1}_g, \hat{2}_g, 3_g; 4_\ell, 5_{\bar{\ell}}). \quad (2.64)$$

Similarly to ZH production without the resolved jet, this piece is phenomenologically important due to the high gluon luminosity in LHC proton–proton collisions. The amplitude encompasses the top quark Yukawa-induced and Drell–Yan-like terms along with their interference. As the vector boson couples directly to the closed fermion loop in all cases, this contribution is not present for WH+jet production.

Additional Closed Fermion-Loop Contributions

As we already discussed before in Section 2.3.2, there are gauge-invariant subsets of both Drell–Yan-like and Yukawa-induced two-loop contributions which are presently unknown and not included in our calculation. This is the reason why some known amplitudes at the real–virtual level cannot be included, as adding them alone would spoil the gauge invariance without their corresponding double-virtual amplitudes.

Subtraction Terms

The subtraction terms once again are fully recycled from the V +jet calculations and are present for each piece of the colour-decomposed amplitude. Analytic pole cancellation tests have been carried out to validate all of them after swapping out the reduced matrix elements with non-momentum-conserving ones.

2.4 Numerical Results

2.4.1 General Setup

I will present predictions of $W^\pm H + \text{jet}$ production which were generated for $\sqrt{s} = 13$ TeV proton–proton collisions using the parton distribution function NNPDF31_nnlo_as_0118 from the LHAPDF library [58]. Although all three of the $VH + \text{jet}$ processes are implemented, production runs are only completed for $W^\pm H + \text{jet}$ production at the time of writing this thesis. Runs for $ZH + \text{jet}$ are still pending.

Values for the parameters used in the calculation were set up exactly as in (1.99).¹³ The experimental setup can be summarized in the following: we required a hard cut of $p_\perp > 20$ GeV for each identified final-state jet, which were clustered with the anti- k_t algorithm using $\Delta R = 0.5$. We demanded at least a single such hard jet to be present in the final state. The charged leptons were also subject to a transverse momentum cut of $p_{\perp, \ell^\pm} > 25$ GeV and a cut $|y|_{\ell^\pm} < 2.5$ in the absolute value of their rapidity. Lastly—concerning the neutrinos from the W^\pm decay—a missing transverse energy cut $E_{\perp, \text{miss}} > 25$ GeV was also required for an event to be registered.

In order to estimate the theoretical uncertainty of the predictions at different perturbative orders, we varied the factorization and renormalization scales with a factor of two around the central value of the dynamical mass of the WH system according to the commonly used 7-point variation scheme:

$$\mu_F = M_{WH} \left[1, \frac{1}{2}, 2 \right], \quad \mu_R = M_{WH} \left[1, \frac{1}{2}, 2 \right],$$

with the constraint of $\frac{1}{2} \leq \mu_F/\mu_R \leq 2$. LHAPDF provided the value of the strong coupling constant α_s and managed its running to all scales.

2.4.2 Fiducial Cross Sections

The fiducial cross sections for $W^\pm H + \text{jet}$ production are summarized in Table 2.1 at the various orders in α_s . Verifying their analytic dependence on the renormalization scale have been carried out according to ref. [61], similarly to Section 1.7.3.

The behaviour of the fiducial cross sections for $W^+ H + \text{jet}$ and $W^- H + \text{jet}$ are very similar. We observe a drastic stabilization of the values at NNLO: the correction to the central value is merely of $\mathcal{O}(+1\%)$ and the theoretical uncertainty reduces from $\mathcal{O}(4\%)$ at NLO to only $\mathcal{O}(8\text{--}9\%)$ at NNLO. Furthermore, the NNLO values are all contained within the scale

¹³The bottom quark mass was not required as the Higgs boson is kept on shell without any decay.

	W ⁺ H+jet	W ⁻ H+jet
σ_{LO} [fb]	20.99 ^{+2.09} _{-1.83}	12.30 ^{+1.24} _{-1.09}
σ_{NLO} [fb]	26.12 ^{+0.94} _{-0.99}	15.18 ^{+0.52} _{-0.56}
σ_{NNLO} [fb]	26.36 ^{+0.04} _{-0.24}	15.37 ^{+0.03} _{-0.12}

Table 2.1: The fiducial cross sections for the experimental setup at 13 TeV detailed in Section 2.4.1. The lower and upper error estimates are acquired as the envelope of the cross-section values evaluated at the seven different scales.

uncertainty of the NLO predictions.

To study the impact of the top loop-induced parts, we compare the W⁺H+jet fiducial cross-section values of the included $\mathcal{O}(\alpha_s^2)$ top loop contributions of Figure 1.14b with the $\mathcal{O}(\alpha_s^3)$ NNLO coefficient of the Drell–Yan-like amplitudes at central scale $\mu_F = \mu_R = M_{\text{WH}}$:

$$\begin{aligned}\sigma_{\text{W}^+\text{Hj,NLO coef.}}^{\text{top}} &= 0.32^{+0.07}_{-0.06} \text{ fb}, \\ \sigma_{\text{W}^+\text{Hj,NNLO coef.}}^{\text{DY}} &= 0.24 \text{ fb}.\end{aligned}$$

We observe that the top Yukawa-induced contributions amount to one percent of the NLO fiducial cross section and are of similar magnitude as the NNLO coefficient not containing any effect of top quark loops. For precise phenomenology, their inclusion at this order, i.e. at $\mathcal{O}(\alpha_s^2)$, is therefore of crucial importance when the Drell–Yan-like parts are computed at $\mathcal{O}(\alpha_s^3)$. Furthermore, it is worth noticing that their theoretical uncertainties are better contained than the $\mathcal{O}(\alpha_s^3)$ Drell–Yan-like counterparts. It is therefore not unreasonable to expect that the $\mathcal{O}(\alpha_s^3)$ contributions to these top-induced contributions—presently mostly unknown—would become only relevant when combined with Drell–Yan-type contributions computed at N³LO, i.e. at $\mathcal{O}(\alpha_s^4)$. This is presently beyond theoretical computational possibilities.

2.4.3 Distributions

In Figures 2.7 and 2.8 we present a few selected differential distributions for the production of W⁺ and W⁻ bosons in association with a Higgs boson and a hard jet, using the experimental setup discussed previously in Section 2.4.1. In particular, Figures 2.7a and 2.8a display the distribution of the transverse momentum of the W⁺ and W⁻ bosons. Figures 2.7b and 2.8b

show the cross section as a function of the transverse momentum of the Higgs boson. Jet-related observables are presented in Figures 2.7c and 2.8c where the transverse momentum distribution of the leading jet is shown, and in Figures 2.7d and 2.8d where the cross section as function of the rapidity of the leading jet is displayed.

Besides the difference in magnitudes, the distributions of $W^+H+\text{jet}$ and $W^-H+\text{jet}$ look fairly similar, with the exception of the leading-jet rapidity distributions. The $W^-H+\text{jet}$ one of Figure 2.8d systematically shows larger K factors in forward regions than its $W^+H+\text{jet}$ sibling of Figure 2.7d. This feature has also been observed when comparing $W^++\text{jet}$ and $W^-+\text{jet}$ leading-jet rapidity distributions without a Higgs boson in ref. [67]. With the exception of these regions in the $W^-H+\text{jet}$ rapidity distribution, the K factors at NNLO are all close to flat and around one. Moreover, the scale uncertainties are also substantially reduced and contained within the uncertainty band of the NLO prediction, yet again indicating an excellent perturbative convergence.

2.5 Summary and Outlook

I presented the ingredients for the computation of precise predictions of differential observables related to the associated production of an on-shell Higgs boson with a vector boson decaying leptonically, along with always requiring a resolved hard jet in the final state. I carried out the simulation and showed its results for $W^\pm H+\text{jet}$ production for 13 TeV center-of-mass energy LHC collisions. Drell–Yan-like contributions are included up to $\mathcal{O}(\alpha_s^3)$ and top quark loop-induced parts up to $\mathcal{O}(\alpha_s^2)$. We found that the inclusion of these corrections improves the stability of the predictions for the differential distributions and contribute to a considerable reduction of the leftover theoretical uncertainties. Analyzing the relative size of the corrections in the two categories—top-loop and Drell–Yan-like—we saw that the inclusion of the top loop-induced contributions computed one order lower than their Drell–Yan-like counterparts are of phenomenological relevance, as both contribute equally to the fiducial cross section at percent level. As the phenomenological impact of top loop-induced parts is considerably different for the production processes of $W^\pm H$ and ZH with no hard jet in the final state, as seen in Sections 1.7.2 and 1.7.4, such observation may or may not hold for $ZH+\text{jet}$ production. It will be interesting to examine this once all runs for the $ZH+\text{jet}$ production finish.

Concerning future work related to this project in light of the recent report [25] of the ATLAS collaboration, an exciting way to proceed will be to produce predictions using the experimental setup of said publication. In particular, the $WH+\text{jet}$ setup in ref. [25] is exclusive in the jet content. Compared to our predictions in Section 2.4, which are inclusive

with respect to higher jet multiplicities, the effect of an additional jet veto on our differential distributions is worth further investigation.

A longer term goal is to equip VH+jet production with $H \rightarrow b\bar{b}$ decay and to add QCD corrections to both production and decay subprocesses, similarly to how it was done in Chapter 1. Despite having the infrastructure and almost all ingredients at our disposal, this is a more engaging task than it might seem at first. With this construction, QCD radiation could already occur on the decay side as well at leading order, i.e. the underlying Born cross sections include additional $\mathcal{O}(\alpha_s^0)$ production \times $\mathcal{O}(\alpha_s^1)$ decay contributions too, such as the ones in Section 1.4.3. If $\mathcal{O}(\alpha_s^3)$ corrections were included in a consistent manner, the final NNLO production \times decay VH+jet cross section with $H \rightarrow b\bar{b}$ decay would incorporate substantially more terms than even eq. 1.47. Nonetheless, adding the decay of the Higgs boson to a pair of bottom–antibottom quarks is a definite goal to pursue in future developments of the project.

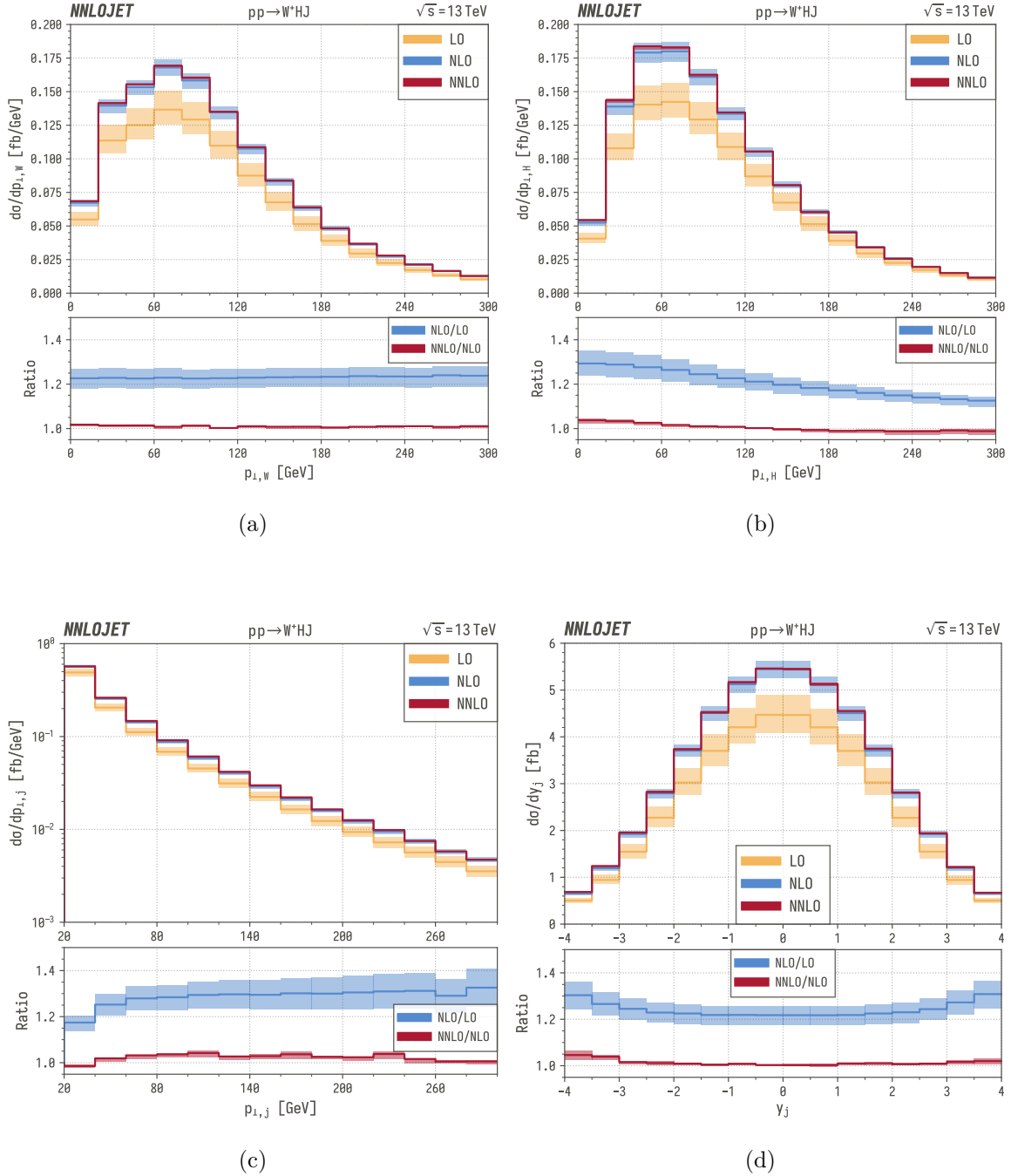


Figure 2.7: Differential distributions of the following W^+H +jet observables: transverse momentum distributions of the W^+ boson in (a), the Higgs boson in (b), and of the leading jet in (c). The rapidity distribution of the leading jet is shown in (d). The upper panel shows the absolute value of the distribution while the lower panel shows the bin-by-bin ratio to the previous order. The uncertainty band represent the envelope of values attained via the 7-point scale variation at the given order.

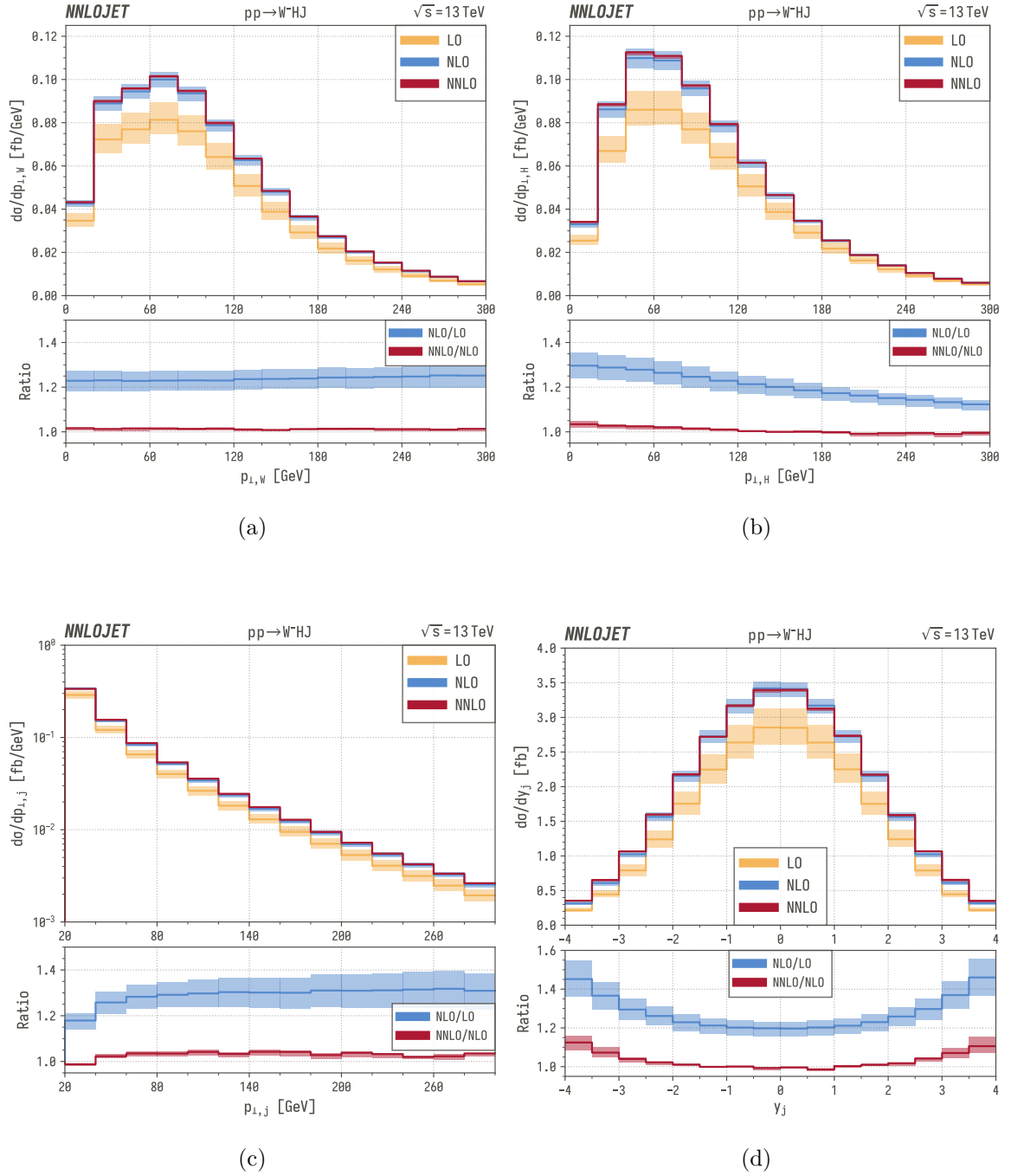


Figure 2.8: Differential distributions of the following W^-H +jet observables: transverse momentum distributions of the W^- boson in (a), the Higgs boson in (b), and of the leading jet in (c). The rapidity distribution of the leading jet is shown in (d). The upper panel shows the absolute value of the distribution while the lower panel shows the bin-by-bin ratio to the previous order. The uncertainty band represent the envelope of values attained via the 7-point scale variation at the given order.

Chapter 3

Flavour Tagging

This chapter is about obtaining predictions for collider experiments which are sensitive to quark flavour in the final states. Among others, it is an essential pillar for the results shown in Chapter 1 for associated Higgs production, when the Higgs boson decays to flavoured bottom quarks.

In Section 3.1, I will give an introduction to why flavour tagging is experimentally important to LHC processes alongside of the theoretical issues challenging a fixed-order prediction. Next, I will summarize the solution to the theory woes by introducing the flavour-aware flavour- k_t algorithm in Section 3.2. The following pages, starting with Section 3.3, give an overview on the modifications needed to implement a flavour-tagging layer into NNLOJET. Concrete technical details of this implementation are the topic of Section 3.4 where I will describe the extension of the Fortran codebase based on the principles described in earlier sections, along with the strategy that addresses the autogeneration of these subroutines. The goal of this technical section is not only to recount the coding complications we had to overcome when trying to interweave a new layer to the venerable codebase of NNLOJET but also to serve as a documentation that anyone who tries to engage in modifying or extending the flavour-tagging layer could use as their starting point. Lastly, I will summarize the chapter in Section 3.5.

As before, I will be using parts from previous publications on VH production [1] and some lines from our article on Z plus b-jet production [3]. Moreover, I will also insert parts of unpublished documents available only internally to NNLOJET collaborators [68–70] which were created either by Rhorry Gauld, myself, or with joint effort. All of these excerpts are often modified and/or extended to fit the train of thought of the thesis better.

3.1 Introduction

Besides measuring flavour-dependent observables in VH production and its subsequent $H \rightarrow b\bar{b}$ decay, the issue of appropriate jet-flavour definition is of great importance for other precision measurements at the LHC as well. Experimental collaborations have performed a huge number of physics analyses of final states that involved jets with identified flavour. The identification of jet flavour is crucial for these analyses because it provides suppression of otherwise overwhelming background processes, and offers insight into flavour-dependent physics dynamics—some examples being the flavour structure of the colliding protons and searches of new physics with a distinct flavour signature.

We are mostly interested in the identification of jets that are initiated by charm or bottom quarks, hence c - or b -tagging, respectively. The current algorithms used by the experimental collaborations for the flavour tagging of such jets have become complicated, relying upon sophisticated machine-learning techniques [71–73]. While the specific details of the various tagging algorithms employed by the LHC experiments differ widely, they each rely upon identifying universal signatures of B - and/or D -hadron decays in the detector. As these hadrons have a typical lifetime of picoseconds, they may travel several millimeters in the detector before decaying, resulting in secondary vertices. That is, the tracks of the hadron decay products are physically displaced with respect to the primary vertex of the hard scattering process. The tagging algorithms may use tracking information, such as the impact parameter between a track and the primary vertex, information related to reconstructed secondary vertices, the presence of soft leptons (from semileptonic decays), or a combination of all these. Regardless of the specifics, the experimental tagging for a given event proceeds in the following steps:

1. Identify a “particle list” associated with the primary vertex of the hard scattering.
2. Reconstruct anti- k_t jets with a given ΔR using this particle list as input.
3. Flavour-tagging algorithms are then applied to these reconstructed jets, after the jets have been reconstructed with the flavour-blind anti- k_t algorithm.

This procedure is extremely successful experimentally—as we already highlighted it for the discovery of the $H \rightarrow b\bar{b}$ decay via the VH production mode [22, 23] in Section 1.1.

While there is no experimental issue with the method described above, such an approach leads to problems on the theoretical side. Specifically, a fixed-order calculation for such observables with massless QCD partons is infrared unsafe at NNLO. The problem of infrared unsafety can be overcome by applying a “flavour-aware” jet reconstruction procedure such

the flavour- k_t algorithm proposed in ref. [43]. The main complication is that the experimental jet reconstruction described above is not flavour aware—the flavour assignment is applied after the infrared-safe jet clustering. Consequently, no direct comparison of data and NNLO flavoured-jet predictions is possible currently. It is highly desirable to overcome this issue for a number of reasons:

- Predictions for processes such as $Zq\bar{q}$ or $W^\pm q$, where q denotes a massive quark, are not available at NNLO: the complicated two-loop integrals are presently unknown. Therefore, the most precise fixed-order calculation for such processes will be those with massless partons, e.g. the Z+jet and W+jet calculations of refs. [63, 66].
- Even if fully massive predictions were available, calculations of this sort suffer from perturbative instabilities. For example, to n^{th} order in perturbation theory, contributions of collinear logarithms of the form $(\alpha_s \ln[Q/m_q])^n$ as well as double logarithms from final state $g \rightarrow q\bar{q}$ splittings of the form $(\alpha_s \ln^2[Q/m_q])^n$ appear [74]. The massless calculation naturally resums the collinear logarithms via PDF evolution while double logarithmic contributions are absent—in principle they are manifest as collinear singularities that cancel against the virtual contributions, provided we use an appropriate definition of jet flavour in the algorithm [43].
- Such precise fixed-order predictions are necessary in order to include V plus heavy flavour data in a global PDF fit at NNLO accuracy, which would allow for more precise studies of the flavour content of the proton.

There are a few different workarounds to overcome the problem of mismatch between the experimentally used and theoretically feasible jet algorithms. The one we employed and advocated in ref. [3] for Z plus b-jet predictions was an unfolding procedure with the RooUnfold package [75]. There, we converted experimental anti- k_t data into that of flavour- k_t using a conversion model provided by NLO+PS simulations using MadGraph [50] interfaced to Pythia8 [76].

From the theoretical point of view, however, the cleanest solution would be if experimental jet-reconstruction algorithms were altered to become flavour aware as well. This way, the same jet algorithm could be applied to both data and predictions in an infrared safe manner without resorting to workarounds, which themselves may introduce various issues and uncertainties.

3.2 Flavoured Jet Algorithm

As mentioned in the previous section, standard jet algorithms such as the k_t family [77] lead to an infrared-unsafe definition of jet flavour at relative order $\mathcal{O}(\alpha_s^2)$ for massless QCD calculations. The principal issue is that wide-angle soft quarks can be generated from a soft gluon emission. If the soft quark is considered flavoured, i.e. bottom or antibottom quarks for b-tagging, then this soft quark may be clustered together with a different parton/pseudojet which does not carry flavour. The resultant flavour of the jet would therefore be sensitive to the dynamics of long-distance physics effects.

A solution to overcome this problem is to incorporate a flavour-dependent clustering such as the flavour- k_t algorithm, which provides an infrared-safe definition of jet flavour. For completeness, we recapitulate the main steps of the algorithm for hadron-hadron collisions, which were originally presented in ref. [43] and also summarized in ref. [78].

The algorithm proceeds by assigning a net flavour to all pseudojets or jets based on their quark flavour content, attributing +1 (−1) if a quark (antiquark) of the flavour under consideration is present. In an experimental context, the presence of a quark flavour could be inferred from a fully/partially reconstructed hadron as described in Section 3.1. A criterion is then applied to these objects to determine if they carry flavour, possible examples being: the net flavour (sum of quarks and antiquarks); or the net flavour modulo two. Objects are considered to carry flavour if they have non-zero values of this criterion. The algorithm then proceeds by constructing distance measures for pairs of all final-state pseudojets i and j (d_{ij}) as well as beam distances (d_{iB} and $d_{i\bar{B}}$). These (flavour-dependent) distances are defined as

$$d_{ij} = \frac{\Delta y_{ij}^2 + \Delta\phi_{ij}^2}{R^2} \begin{cases} \max(k_{ti}, k_{tj})^\alpha \min(k_{ti}, k_{tj})^{2-\alpha} & \text{softer of } i, j \text{ is flavoured,} \\ \min(k_{ti}, k_{tj})^\alpha & \text{softer of } i, j \text{ is unflavoured,} \end{cases} \quad (3.1)$$

$$d_{iB} = \begin{cases} \max(k_{ti}, k_{tB}(y_i))^\alpha \min(k_{ti}, k_{tB}(y_i))^{2-\alpha} & \text{softer of } i, j \text{ is flavoured,} \\ \min(k_{ti}, k_{tB}(y_i))^\alpha & \text{softer of } i, j \text{ is unflavoured,} \end{cases} \quad (3.2)$$

and

$$d_{i\bar{B}} = \begin{cases} \max(k_{ti}, k_{t\bar{B}}(y_i))^\alpha \min(k_{ti}, k_{t\bar{B}}(y_i))^{2-\alpha} & \text{softer of } i, j \text{ is flavoured,} \\ \min(k_{ti}, k_{t\bar{B}}(y_i))^\alpha & \text{softer of } i, j \text{ is unflavoured.} \end{cases} \quad (3.3)$$

In these definitions, k_{ti} and k_{tj} are the transverse momentum of pseudojets i and j , and the rapidity difference and azimuthal angular separation between these pseudojets is given by Δy_{ij} and $\Delta\phi_{ij}$, respectively. The parameters R and α define a class of measures for the algorithm. The (rapidity-dependent) transverse momentum of the beam B at positive rapidity k_{tB} , and beam \bar{B} at negative rapidity $k_{t\bar{B}}$, are defined as:

$$k_{tB}(y) = \sum_i k_{ti} (\Theta(y_i - y) + \Theta(y - y_i) e^{y_i - y}), \quad (3.4)$$

$$k_{t\bar{B}}(y) = \sum_i k_{ti} (\Theta(y - y_i) + \Theta(y_i - y) e^{y - y_i}), \quad (3.5)$$

with $\Theta(0) = 1/2$ and the index i iterating over all pseudojets.

While this flavour-aware jet algorithm is substantially more complex than the flavour-blind anti- k_t algorithm [77], its use is unavoidable in fixed-order computations based on massless quarks. At NLO, the flavour criterion of a pseudojet ensures that a collinear splitting of the form $g \rightarrow q\bar{q}$ is indistinguishable from a gluon (or flavourless) jet. Any subtraction formalism would be spoiled without this criterion. At NNLO, the flavour-dependent distance measure in eq. (3.1) ensures that a pair of flavoured quarks originating from a wide-angle gluon splitting is clustered into a pseudojet *before* being combined with any other (harder) pseudojets. This avoids the situation where one of these soft quarks may be clustered with a hard pseudojet that carries zero flavour, which would lead to a definition of jet flavour sensitive to soft physics. These are issues which are otherwise insurmountable for fixed-order computations involving massless quarks.

There is another point related to our choice of flavour criterion during the clustering process. In the NNLOJET implementation, we have always chosen to define the flavour of pseudojets to be the net flavour of its constituents modulo two, which means that all pseudojets which contain an even flavour content are considered to have zero net flavour. The motivation for this choice is that, in our opinion, it is the most feasible realization of the flavour- k_t algorithm experimentally. Focusing on the case of b-jets, the main consideration is that most experimental approaches to flavour tagging are sensitive only to the absolute flavour [71–73] and do not additionally charge tag the jets. All realizations of the algorithm must consider the combination of a $b\bar{b}$ -quark pair (or equivalently a $B\bar{B}$ -hadron pair) to carry zero flavour, as required to guarantee its infrared safety. Therefore, in the absence of charge tagging, any (pseudo)jet which contains an even number of b (B) and/or \bar{b} (\bar{B}) quarks (hadrons) should also be considered to carry zero flavour, as experimentally these signatures are indistinguishable. Charge tagging of flavoured jets is also possible [79], for example in the presence of semileptonic B-hadron decays. However, the drawback is a large reduction

in event statistics (roughly an order of magnitude for each b-jet, as the branching fraction $\text{Br}(B \rightarrow \ell + X) \approx 10\%$) with little informational gain.

Accordingly, the NNLO results for VH observables presented in Section 1.7 use the version of the flavour- k_t algorithm where all even-tagged (pseudo)jets carry zero flavour. We provide an examination of the impact of the even-tag exclusion in the shape and normalization of flavour-sensitive VH observables in Appendix B.

We implemented the flavour- k_t algorithm with even-tag exclusion as its default mode into NNLOJET and validated it against the independent implementation using FastJet [80, 81], provided for us by Gavin Salam.

3.3 Flavour Dressing

The application of flavour- k_t requires tracking the flavour of individual partons that appear in the partonic cross sections at each perturbative order. In the following, we provide a description of how this is achieved within NNLOJET, but the discussion here can be easily generalized and is not particularly specific to the use of the antenna subtraction formalism.

The first step towards computing flavour-dependent jet observables is to ensure that the jet algorithm has access to both momentum and flavour information when evaluating the contributions from matrix elements and subtraction terms. To address this issue within NNLOJET, an additional “flavour-dressing” layer that tracks the flavours of all amplitudes as well as reduced matrix elements appearing in subtraction terms has been implemented.

To illustrate how this proceeds, we consider the construction of a generic NLO coefficient cross section for an n -body final state initiated by two partons i and j . We have seen before in Section 1.4 that we can write the contributions to the partonic cross section as

$$d\hat{\sigma}_{ij,\text{NLO coef.}} = \int_{\Phi_{n+1}} \left(d\hat{\sigma}_{ij}^{\text{R}} - d\hat{\sigma}_{ij}^{\text{SNLO}} \right) + \int_{\Phi_n} \left(d\hat{\sigma}_{ij}^{\text{V}} - d\hat{\sigma}_{ij}^{\text{TNLO}} \right). \quad (3.6)$$

As an example of the flavour-dressing procedure for the amplitudes, we consider the real-emission cross section (omitting the sum over potential colour orderings) which takes the general form

$$d\hat{\sigma}_{ij}^{\text{R}} = \frac{\mathcal{N}^{\text{R}}}{A_{ij} S_{n+1}} d\Phi_{n+1}(p_2, p_1; \{p_{n+1}\}) J_n^{(n+1)}(\{p_{n+1}\}, \{f_{n+1}\}) M_{n+3}^0(\{p_{n+3}\}, \{f_{n+3}\}), \quad (3.7)$$

where M_{n+3}^0 denotes a generic partial squared amplitude, following the notation of ref. [16]. The other symbols are identical to the ones throughout Chapters 1 and 2. The amplitude

M_{n+3}^0 is evaluated with the momentum set $\{p_{n+3}\}$ and a corresponding flavour set $\{f_{n+3}\}$. The flavour-sensitive jet algorithm $J_n^{(n+1)}$ builds n jets from $n+1$ final-state partons, which carry momentum and flavour labelled by the sets $\{p_{n+1}\}$ and $\{f_{n+1}\}$ respectively. In the previous chapters, we condensed these two separate sets of information into a single alphanumeric list of particles, but prior to the addition of the flavour-dressing layer the set $\{f_{n+1}\}$ was not available neither for the jet algorithm, nor associated to the partial squared amplitude.

The real-subtraction cross section can be written in a similar fashion:

$$\begin{aligned} d\hat{\sigma}_{ij}^{\text{SNLO}} &= \frac{\mathcal{N}^{\text{R}}}{A_{ij}} \frac{1}{S_{n+1}} d\Phi_{n+1}(p_2, p_1; \{p_{n+1}\}) \times \\ &\sum_k J_n^{(n)}(\{\tilde{p}_n\}, \{\tilde{f}_n\}) X_3^0(\cdot, k, \cdot) M_{n+2}^0(\{\tilde{p}_{n+2}\}, \{\tilde{f}_{n+2}\}), \end{aligned} \quad (3.8)$$

where the index k runs over all possible unresolved partons in $d\hat{\sigma}_{ij}^{\text{R}}$ and the symbol $X_3^0(\cdot, k, \cdot)$ denotes the three-parton antenna function that factorizes from the associated reduced squared matrix element M_{n+2}^0 . In this case, the jet algorithm acts upon mapped final-state momentum and flavour sets $\{\tilde{p}_n\}$ and $\{\tilde{f}_n\}$ associated with the reduced squared matrix element M_{n+2}^0 . As the total subtraction cross section must take into account all possible unresolved limits of parton k , this cross section may be composed of multiple flavour structures. The subtraction method is only effective if the evaluation of flavour-dependent observables in both the real and real-subtraction cross sections match in all possible unresolved limits. This is only ensured if an infrared-safe flavour-sensitive jet algorithm is applied, such as the flavour- k_t algorithm we reviewed in the previous Section 3.2.

To construct an NLO cross section according to eq. (3.6), a similar procedure must also be applied to both virtual and virtual-subtraction cross sections. This construction is carried out in a similar fashion, by tracking both the momentum and flavour sets associated to all partial squared amplitudes and reduced squared matrix elements then applying the flavour-sensitive jet algorithm to the of final-state particles within these sets. To allow the computation of flavour-dependent jet observables at NNLO, the same ideas straightforwardly propagate to one order higher, applying the outlined flavour-dressing procedure to all NNLO parton-level contributions and their corresponding subtraction terms.

3.4 Implementation

Realizing a flavour-tagging layer within NNLOJET required a rather significant overhaul of the entire infrastructure so we needed to lay down some guiding principles before attempting it. We required flavour tagging to be

- General—so that it can be applied all processes currently present within NNLOJET.
- Unobtrusive—the implementation should be such that it does not slow down the running of processes when not in flavour-tagging mode.
- Efficient—while running in flavour-tagging mode we wish to calculate only the pieces of the subtraction terms and matrix elements which contribute to the observables being evaluated.

In the remaining parts of this chapter, I will describe key points of the final implementation in a structured manner, often inserting relevant segments of the NNLOJET driver (i.e. the Fortran codebase that is compiled and executed during event generation) and the sources used in autogeneration. The working example will be the process Z+jet, which ultimately—among rather significant efforts in the mass-correction front—yielded us the publication [3].

3.4.1 Driver

During the early days of the project, we were considering dynamically deducing the flavour arrays $\{f\}$, such as those in eq. (3.8), based on inherent flavour mappings of the antenna functions. However, due to some limitations in the construction of the antennæ—specifically the D_4^0 antenna shown in ref. [9]—dynamic mapping resulted in illegal flavour assignments in some cases and thus a mismatch between real amplitudes and their corresponding subtraction terms.

The robust implementation we decided to pursue relied on storing each possible flavour set $\{f\}$ that appears for matrix elements and reduced matrix element in so-called *flavour blocks*. While this solution might be deemed less elegant and relies on a priori generating large amount of flavour information before executing an event simulation, it is also trivially applicable to all levels of amplitudes (B, R, V, RR, RV, VV) and subtraction terms (SNLO, TNLO, S, T, U).

For our working example, let us take a look at parts of the Fortran file `flavourZJ.f`, the autogenerated file containing the flavour information required for all partonic processes of Z+jet production. Specifically, consider the $d\bar{u}$ -initiated real–virtual channel bearing the process number `iproc=450` in the NNLOJET codebase. This is constructed similarly to

eq. (2.52) but with native NNLOJET amplitudes instead of the OpenLoops ones we used for ZH+jet. First, we have to expand the generic down- and up-type labelling that was used prior to flavour tagging into separate *subprocesses* (`isub`) that list all flavours individually. This expansion will yield the following six different *subprocesses*:

$$\begin{array}{ccccccc}
 d & \bar{u} & \rightarrow & \bar{u} & d & \ell & \bar{\ell} \\
 \hline
 d & \bar{u} & \rightarrow & \bar{u} & d & \ell & \bar{\ell} \\
 d & \bar{c} & \rightarrow & \bar{c} & d & \ell & \bar{\ell} \\
 s & \bar{u} & \rightarrow & \bar{u} & s & \ell & \bar{\ell} \\
 s & \bar{c} & \rightarrow & \bar{c} & s & \ell & \bar{\ell} \\
 b & \bar{u} & \rightarrow & \bar{u} & b & \ell & \bar{\ell} \\
 b & \bar{c} & \rightarrow & \bar{c} & b & \ell & \bar{\ell}
 \end{array}$$

as down-type quarks consist of down, strange, and bottom quarks and up-type quarks consist of up and charm quarks in the $n_F = 5$ scheme.

In the codebase, this is achieved by looping over *subprocesses* using different values for the integer variable `isub` under the given process (`iproc=450`) and running the jet algorithm separately for each of them before actually evaluating the amplitudes or subtraction terms. The number of *subprocesses* that need to be iterated over is stored in the variable `nflavourZJ`, which is also a part of the autogenerated file `flavourZJ.f`. In the case of our example, the number of *subprocesses* is six, therefore we find the following Snippet 3.1 in `flavourZJ.f`:

```

1 integer function nflavourZJ(iproc)
2   implicit none
3   integer, intent(in) :: iproc
4   select case(ip)
5   ...
6   !--- d ub → ub d lm lp
7   case(450)
8     nflavourZJ = 6
9   end select
10  ...
11 end function nflavourZJ

```

Snippet 3.1: The number of *subprocesses* inside the autogenerated file `flavourZJ.f` for the process `iproc=450`, a $d\bar{u}$ -initiated real-virtual channel contributing to Z+jet production.

Omission of parts of the code relevant to other processes (`iproc`) in Snippet 3.1 are marked with ellipses.

While the matrix element

$$C_0^{Z,1}(\hat{1}_d, \hat{2}_{\bar{u}}, 3_{\bar{u}}, 4_d; 5_\ell, 6_{\bar{\ell}}) \quad (3.9)$$

is evaluated on the flavour set of a *subprocess* as it is, the subtraction terms can have multiple flavour assignments depending on the reduced matrix element the amplitude collapses onto in a given unresolved limit. The subtraction amplitude

$$\text{qqpbC0g1ZT}(\hat{1}_d, \hat{2}_{\bar{u}}, 3_{\bar{u}}, 4_d; 5_\ell, 6_{\bar{\ell}}) \quad (3.10)$$

accompanying the matrix element (3.9) of our particular example is quite lengthy: it consists of 23 different terms of (integrated) antennæ and reduced matrix elements, therefore I will not give the explicit expression here. From the flavour-tagging perspective, it is enough to know that these 23 terms in total contain only the following 7 different reduced matrix elements:

1. C0g0Z: the tree-level $C_0^{Z,0}$,
2. f1B1g0Z: the tree-level $B_1^{Z,0}$ inheriting the flavour of the first quark line (*d*-type),
3. f1B1g1Z: the one-loop $B_1^{Z,1}$ inheriting the flavour of the first quark line (*d*-type),
4. f1B2g0Z: the tree-level $B_2^{Z,0}$ inheriting the flavour of the first quark line (*d*-type),
5. f2B1g0Z: the tree-level $B_1^{Z,0}$ inheriting the flavour of the second quark line (*u*-type),
6. f2B1g1Z: the one-loop $B_1^{Z,1}$ inheriting the flavour of the second quark line (*u*-type),
7. f2B2g0Z: the tree-level $B_2^{Z,0}$ inheriting the flavour of the second quark line (*u*-type).

These reduced matrix elements all come with specific flavour assignments which we organize into *flavour blocks* (`flav_block`). In this case, we created *flavour blocks 1–7* for the reduced matrix elements and one more *flavour block 0* for the actual amplitude (3.9). They are stored inside the `dress_flav_ZJ` subroutine according to Snippet 3.2, which is also part of the autogenerated file `flavourZJ.f`.

```

1 subroutine dress_flav_ZJ(iproc, isub, ipass, flav_block)
2   use Flavour_mod
3   implicit none
4   integer, intent(in) :: iproc, isub, flav_block
5   integer, intent(inout) :: ipass
```

```

6   if (ipass == 0) return
7   select case(iproc)
8   ...
9   !--- d ub → ub d lm lp
10  case(450)
11    select case (isub)
12      case(1) ! d ub → ub d lm lp
13      ...
14      case(2) ! d cb → cb d lm lp
15      ...
16      case(3) ! s ub → ub s lm lp
17      ...
18      case(4) ! s cb → cb s lm lp
19      ...
20      case(5) ! b ub → ub b lm lp
21      ...
22      case(6) ! b cb → cb b lm lp
23    select case (flav_block)
24      case(0) ! Matrix element: sC0g1Z matching to C0g1Z in FLAVlistZJ.map
25      call dress_flav( (/ -5,4, -4, 5, -99, 99 /), 6, ipass, (/ 5,-4 /))
26      case(1) ! Reduced matrix element: C0g0Z
27      call dress_flav( (/ -5,4, -4, 5, -99, 99 /), 6, ipass, (/ 5,-4 /))
28      case(2) ! Reduced matrix element: f1B1g0Z
29      call dress_flav( (/ -5,0, 5, -99, 99 /), 5, ipass, (/ 5,-4 /))
30      case(3) ! Reduced matrix element: f1B1g1Z
31      call dress_flav( (/ -5,0, 5, -99, 99 /), 5, ipass, (/ 5,-4 /))
32      case(4) ! Reduced matrix element: f1B2g0Z
33      call dress_flav( (/ -5,0, 0, 5, -99, 99 /), 6, ipass, (/ 5,-4 /))
34      case(5) ! Reduced matrix element: f2B1g0Z
35      call dress_flav( (/ -4,0, 4, -99, 99 /), 5, ipass, (/ 5,-4 /))
36      case(6) ! Reduced matrix element: f2B1g1Z
37      call dress_flav( (/ -4,0, 4, -99, 99 /), 5, ipass, (/ 5,-4 /))
38      case(7) ! Reduced matrix element: f2B2g0Z
39      call dress_flav( (/ -4,0, 0, 4, -99, 99 /), 6, ipass, (/ 5,-4 /))
40    end select
41    ...
42  end select
43 end select
44 end subroutine dress_flav_ZJ

```

Snippet 3.2: Flavour dressing of the matrix element (3.9) and all reduced matrix elements inside the subtraction amplitude (3.10) for the process $iproc=450$, a $d\bar{u}$ -initiated real–virtual channel contributing to Z +jet production. The subroutine is part of the autogenerated file `flavourZJ.f`.

In Snippet 3.2, we only highlighted the *flavour-block* decomposition for the *subprocess* $b\bar{c} \rightarrow \bar{c}b\ell\bar{\ell}$ ($isub=6$) through lines 22–40, i.e. when bottom and strange quarks are substi-

tuted into down-type and up-type quarks, respectively. A similar set of 7+1 *flavour blocks* are present for each of the other *subprocesses* from `isub=1` to `isub=5` through lines 12–21, which are replaced by ellipses. Each *flavour block* dresses up the (reduced) matrix elements with the appropriate flavour array: we use the integer set $\{1, 2, 3, 4, 5\}$ for the quarks $\{\text{d}, \text{u}, \text{s}, \text{c}, \text{b}\}$ and $\{-1, -2, -3, -4, -5\}$ for the antiquarks $\{\bar{\text{d}}, \bar{\text{u}}, \bar{\text{s}}, \bar{\text{c}}, \bar{\text{b}}\}$. The gluon is marked with 0 and the respective PDG [82] codes are assigned to the rest of the particles, such as -99 for the electron and 99 for the positron in our example.

Besides the flavour array as its first argument, the `dress_flav` subroutine takes the number particles as its second. The initial-state flavours in a reduced matrix element can change, as it is apparent throughout the *flavour blocks*, but the flavours of the initial states that select the appropriate PDFs for the convolution cannot. They are fixed inside a *subprocess* (`isub`), which is indicated by the slightly redundant last argument pair of the `dress_flav` subroutine. The example sets the PDFs to that of the bottom (5) and anticharm (-4) quarks in Snippet 3.2.

During the evaluation of the 23 different terms in the subtraction term (3.10) we need to refer to the particular *flavour block* that is associated to the given reduced matrix element and evaluate the jet function accordingly. If the given flavour set does not contain the quark flavour we are tagging in the final state at least as many times as many flavour-tagged jets we require, then we skip the evaluation of the jet function and move onto the next term. The `ipass` flag in Snippet 3.2 is used for this purpose, referring back to the efficiency principle we pointed out in the beginning.

Let us investigate the new additions to the subtraction amplitude (3.10) that flavour tagging brought about. Term 11 (out of the total 23) of our working example is

$$\begin{aligned}
\text{qqpbC0g1ZT}(\hat{1}_d, \hat{2}_{\bar{u}}, 3_{\bar{u}}, 4_d; 5_\ell, 6_{\bar{\ell}}) = \\
\quad \dots 10 \text{ terms} \dots \\
\quad + D_{3,gq}^0(\hat{2}, 3, \hat{1}) J_{2,GQ,q' \rightarrow g}^{(1),IF}(s_{14}) B_2^{Z,1}(4_u, \hat{1}_g, \hat{2}_{\bar{u}}; 5_\ell, 6_{\bar{\ell}}) \\
\quad + \dots 12 \text{ more terms} \dots
\end{aligned} \tag{3.11}$$

The Fortran code for the evaluation steps (momentum mapping, jet function, numerical value, etc.) of this term is shown in Snippet 3.3, an excerpt from the autogenerated file `autoqqpbC0g1ZT.f`.

```

1 function qqpbC0g1ZT(ix,x1,x2,i1,i2,i3,i4,i5,i6,rscale2,fscale2)
2 ...
3 ! II: {i4 = j3, i5 = j4, i6 = j5, [i1] = j1, [i2] = j2}
4   call set_map(6,5, (/i1,i3,i2/), (/i1,i2,i4,i5,i6/), ipass)
5 ! BLOCK 7
6   call ecuts_vj(0,5,ipass)
7   call set_flav_perm(5, (/ j3,j1,j2,j4,j5 /))
8   if(ipass.eq.1)then
9     call getqcdnorm(ix,partons,facnorm, 5, ipass_block, 5)
10    if(ipass_block/=0) then
11      kinwt = 0d0
12      do i=1,nAct_scl
13        wtcalX30=0d0
14        wtcalX30=wtcalX30+1d0*rJ21GQtogIF(ix,x1,x2,j1,j3,5,muR2_scl(i),muF2_scl(i))
15        kinwt(i)=FullgqD30II(i2,i3,i1,6)*f2B1g0Z(j3,j1,j2,j4,j5)*(wtcalX30)
16      enddo
17      wt(11)=bino(ix,partons,-kinwt*facnorm)
18    endif
19  endif
20  call unset_flav_perm()
21  ipass=1
22  ipass_block=1
23  call unset_map()
24 ...
25 end function qqpbC0g1ZT

```

Snippet 3.3: An excerpt of the autogenerated T-type `autoqqpbC0g1ZT.f` subtraction amplitude focusing on term 11 out of 23. The rest of the terms are replaced by ellipses.

Without delving too much into the inner workings of NNLOJET, let us focus on the additions of the flavour-tagging layer. These are the following subroutines:

- **set_flav_perm** (line 7): so far the flavour set of the matrix element (3.9) was easily matched to *flavour block 0* (`flav_block=0`) of Snippet 3.2. For demonstration purposes we chose a channel whose momentum ordering is simply (1, 2, 3, 4; 5, 6) as seen in (3.9). This actually defines what we call the canonical ordering of the flavours for a given matrix element. Flavour arrays shown in Snippet 3.2 are *always* generated in their canonical ordering. The various permutations for channel crossings or those appearing in different unresolved limits of the subtraction terms, such as in our example (3.10), require performing the same permutation on the canonical flavour set as well.¹ This is the role of the `set_flav_perm` subroutine. Besides the subtraction terms, it is always

¹The momentum mappings of the unresolved limit must be performed first, i.e. we must first map the set (1, 2, 3, 4; 5, 6) onto $(j_1, j_2, j_3; j_4, j_5)$ and then perform the permutation $(j_3, j_1, j_2; j_4, j_5)$.

called in front of the amplitudes as well, which I will not show here in a separate code snippet.

- **unset_flav_perm** (line 20): resets the permutation before moving onto the next term inside the subtraction amplitude.
- **getqcdnorm** (line 9): this subroutine is not a new addition in flavour tagging, but its roles have significantly been extended by it. As its name suggests, it originally only multiplied amplitudes and subtraction terms with their normalization prefactor \mathcal{N} but now it also calls the relevant subroutines of `flavourZJ.f` and therefore we will examine its structure—shown in Snippet 3.4—in more detail. Before doing so, the main point that I wish to accentuate here is that the reduced matrix element for our example is `f2B1g0Z`, as seen in line 12 of Snippet 3.4 or in eq. (3.11). This reduced matrix element is found in *flavour block 5* (`flav_block=5`) as shown in line 35 of Snippet 3.2, which is why this number is passed as the last argument of `getqcdnorm`. Similarly to `set_flav_perm`, this subroutine is also called before evaluating regular matrix elements not part of subtraction terms.

Besides multiplying the (reduced) matrix elements with the correct normalization factor, the `getqcdnorm` subroutine also dresses them with the appropriate flavour set, calls the correct PDFs, and executes the flavour-sensitive jet algorithm. Traditionally, these roles are the responsibilities of other subroutines in NNLOJET but overloading `getqcdnorm` was the most convenient point in the codebase where the flavour-tagging layer could be linked in a uniform way into every implemented process. Let us therefore inspect the lines of the subroutine `getqcdnormZJ` (directly called by `getqcdnorm` for Z+jet) which are important to flavour tagging in Snippet 3.4.

```

1  subroutine getqcdnormZJ(ix, partons, factor, npar, ipass, flav_block)
2  ...
3  if (.not.isActive_flav()) then
4      call get_lumi_scl(ix, ip1_chan, ip2_chan, partons)
5      relfactor = 1d0
6  else
7  #IFDEF FLAVZJ
8      ipass = 0
9      partons = 0d0
10     relfactor = 1d0/relfacflavourZJ(current_chan)
11     do isub = 1, nflavourZJ(current_chan)
12         ipass_sub = 1
13
14         !> this dresses the flavours, does permutations, makes coffee

```

```

15     call dress_flav_ZJ(current_chan, isub, ipass_sub, flav_block)
16     if (ipass_sub == 0) cycle
17     call ecuts_flav(0, npar, ipass_sub)
18     if (ipass_sub == 0) cycle
19     ipass = 1
20
21     ip1_chan = getPDF_flav(npar, 1)
22     ip2_chan = getPDF_flav(npar, 2)
23
24     call get_lumi_scl(ix, ip1_chan, ip2_chan, partons_sub)
25     if ( isActive_hist() ) call push_flav(partons_sub)
26     partons = partons + partons_sub
27 end do
28 if (ipass == 0) return
29 #ELSE
30 print*, "flavour-tagging routines not compiled for this process"
31 print*, "run: make flav=ZJ"
32 stop
33 #ENDIF
34 end if
35 ...
36 end

```

Snippet 3.4: Segments of the autogenerated file `qcdnormZJ.f` responsible for flavour tagging of the Z+jet process.

For the sake of efficacy, NNLOJET often evaluates the sum of various PDFs where it is appropriate. An example is when only up-type and down-type quarks are distinguished due to the Z coupling, in which case there is no need to evaluate the amplitudes separately multiple times for the individual quark flavours. Lines 3–5 of the Snippet 3.4 above guarantee that if flavour tagging is not active, then usual PDF sums are used and the rest of the lines relevant to flavour tagging are skipped. This upholds the unobtrusiveness principle, as the rest of the subroutine reverts back to its traditional role of only providing the normalization factor whenever flavour tagging is turned off.

Lines 8–33 are called in order when flavour tagging is active. First of all, the statements `#IFDEF`, `#ELSE`, and `#ENDIF` ensure that flavour tagging for the Z+jet process is only compiled if the `FLAVZJ` preprocessor flag is given during compilation time. The autogenerated `flavourZJ.f` is a monstrously large file—43905 lines—which increases the size of the executable substantially. Given that we are usually focusing on evaluating observables for a single process at a time, it is reasonable to only compile flavour tagging for the given process when necessary instead of needlessly bloating the executable by enabling it for all processes.

Line 10 of Snippet 3.4 divides out the relative factor that accompanies amplitudes when-

ever identical final states that only differ in quark flavour are present. For example, such factors are n_{up} and n_{down} in eq. (1.68) for ZH production and n_{F} in eq. (1.67) for WH production. The value `relfacflavourZJ` is once again stored inside `flavourZJ.f` for every given `iproc`. As our working example (`iproc=450`) does not have such a final-state configuration, `relfacflavourZJ` is set to its default value: one.

The loop encapsulated within lines 11–27 of Snippet 3.4 is where *subprocesses* (`isub`) are being iterated over one-by-one. The flavour dressing for the fixed *flavour block* (`flav_block`) is done within the loop on line 15, after which the flavour-sensitive jet algorithm (*flavour- k_t*) is executed and subsequently the experimental cuts are applied, both within the subroutine `ecuts_flav` on line 17.

Finally, if the event passes the experimental cuts, then lines 21–24 get the PDFs from the dressed array (the last argument pair of `dress_flav_ZJ` in Snippet 3.2) and accumulate them for multiplying the (reduced) matrix elements. The values of PDFs are optionally stacked for histograms of observables when binning is active.

Figure 3.1 summarizes all of the aforementioned and illustrates the driver side (Fortran code) of the flavour-tagging layer. The Fortran subroutines throughout this section are all autogenerated and therefore not the end of the story. They were, however, the ones we first conceptualized and the autogeneration scripts were adjusted to them in order to produce the desired files for all processes. In the next section we will look at the structure of the autogeneration layer for flavour tagging, written mostly in Maple, as it is conventional in NNLOJET.

3.4.2 Autogeneration

One of properties of the flavour-dressing layer is storing fixed flavour assignments for matrix elements, regardless of whether they are called from inside a subtraction term or not. Using Z+jet as our working example as usual, this assignment is contained within the file `flavourZJ.f` in a canonical ordering as shown in Snippet 3.2. The process-specific shuffling of the flavours due to crossings or various unresolved limits inside a subtraction term is performed by the `set_flav_perm` subroutine inside the Fortran code, which follows the permutation of the momentum indices. Consequently, this permutation is already something that the NNLOJET Maple scripts knew how to generate prior to flavour tagging, we just extended them to the flavour-permuting `set_flav_perm` subroutine as well.

This scheme necessarily invokes the creation of a library that stores the flavour arrays associated with all matrix elements in a canonical ordering. Canonical assignment stands for the flavours of an all-outgoing momenta configuration in an order that is most natural to

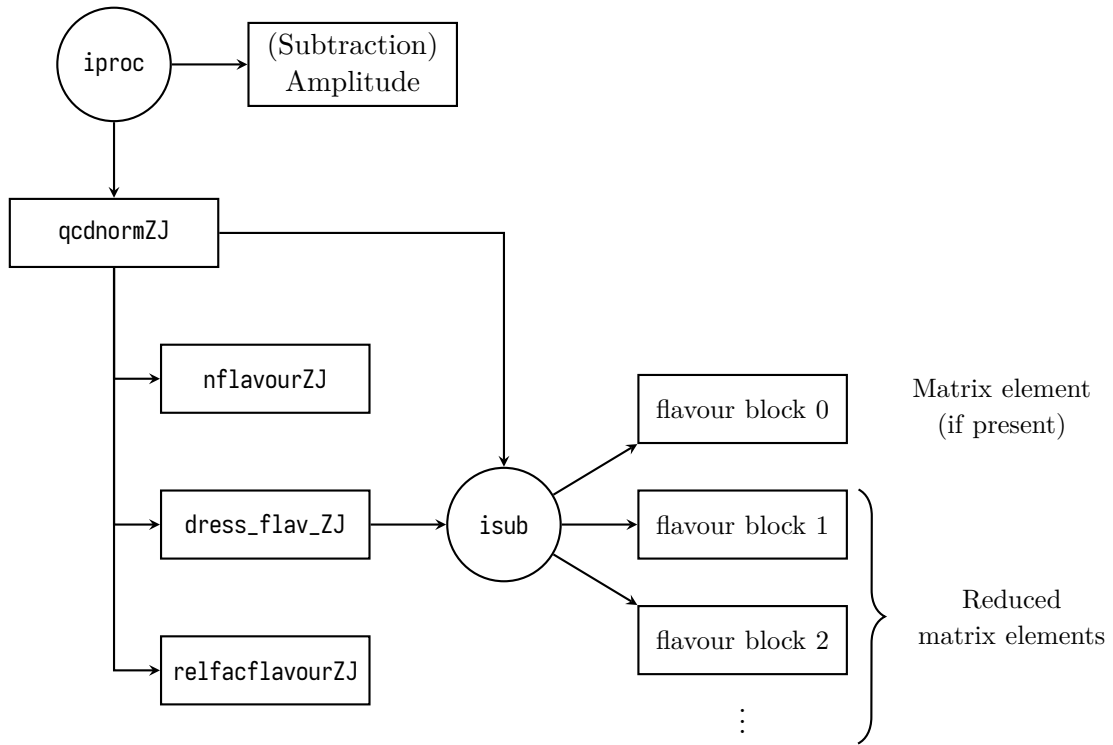


Figure 3.1: Flavour storage scheme in the NNLOJET driver for Z+jet production. The same scheme is autogenerated for all of the processes inside NNLOJET. Matrix elements are not always present if the given channel is a pure mass-factorization one (possible for TNLO and T subtraction terms).

the respective matrix element, i.e. the partonic process the matrix element describes if the momentum indices are in an increasing alphanumeric order, such as in eq. (3.9). This library that contains all possible matrix elements in the NNLOJET codebase is written manually and found in the Maple file `MElibrary.map`. Some of its lines containing familiar matrix elements that appeared in the previous chapters of the thesis are shown in Snippet 3.5.

```

1 MElibrary := table([
2 ...
3   # Z/W production matrix elements
4   B2g1Z = [-q, 0, 0, q, -99, 99],
5   B3g0W = [-qp, 0, 0, 0, q, 98, -99],
6   C0g0Z = [-q, Q, -Q, q, -99, 99],
7   C0g0W = [-qp, Q, -Q, q, 98, -99],
8   D1g0Z = [-q, 0, q, -q, q, -99, 99],
9   D1g0Wa = [-qp, 0, qp, -qp, q, 98, -99],
10  D1g0Wb = [-qp, 0, q, -q, q, 98, -99],
11 ...

```

```

12 # Higgs → b bbar decay matrix elements
13 By1g0H = [5, 0, -5],
14 Cy0g0H = [5, 0, -0, -5],
15 Dy0g0H = [5, 5, -5, -5],
16 ...
17 ]):

```

Snippet 3.5: Excerpts of the matrix element library `MElibrary.map` showing the storage of $V+\text{jet}$ and $H \rightarrow b\bar{b}$ decay amplitudes.

We can see in Snippet 3.5 that in case of multiple quarks or flavour-changing W^\pm coupling, similar notations are used as the one outlined in Section 1.5.1. For composite matrix elements such as the production \times decay VH ones, a separate script at the end of the file `MElibrary.map` concatenates the relevant flavour arrays.

The autogeneration of subtraction terms in the NNLOJET codebase is done via scripts written in Maple called `makefortRR` for SNLO and S, `makefortRV` for TNLO and T, and `makeformVV` for U subtraction terms. These scripts read in files containing analytical expressions for the subtraction terms such as eq. (3.10) and output respective Fortran code like Snippet 3.3. In order to know what reduced matrix elements appear in a given analytical subtraction term, a newly written `makeflavlist` Maple script combs through all of these analytical expressions and creates a dictionary of amplitudes and reduced matrix elements. For $Z+\text{jet}$, these are then stored in `FLAVlistZJ.map` according to Snippet 3.6.

```

1 FLAVlist:=[
2 ...
3 [[g, g], B1g1Z, [B1g0Z]],
4 [[g, qb], D1g0Z, [D0g0Z, f1B1g0Z]],
5 [[g, qb], Bth2g1Z, [B1g0Z, Bh1g1Z, Bt2g0Z]],
6 [[q, qpb], C0g1Z, [C0g0Z, f1B1g0Z, f1B1g1Z, f1B2g0Z, f2B1g0Z, f2B1g1Z, f2B2g0Z]],
7 [[q, qpb], Bt1g2Z, [f1B1g0Z, f2B1g0Z, f1Bt1g1Z, f2Bt1g1Z]],
8 ...
9 ]):

```

Snippet 3.6: List of reduced matrix elements that appear inside subtraction terms for the $Z+\text{jet}$ process, as generated by the Maple script `makeflavlist`. It is essential for generating the correct *flavour blocks* for `flavourZJ.f`.

Line 6 of Snippet 3.6 belongs to our working example: the subtraction term (3.10) of the process `ipro=450`. The first array pair indicates the initial states, which are a quark and

a non-identical antiquark,² the second is the matrix element. Both are deduced from the name of the subtraction term, i.e. from `qqpbC0g1ZT`. The list in the rest of the line shows the 7 different matrix elements that the script could identify while combing through all 23 terms of the subtraction amplitude. The ordering of reduced matrix elements inside `FLAVlistZJ.map` defines the order of *flavour blocks* seen in Snippet 3.2, therefore it is crucial to run the script `makeflavlist` before generating the Fortran subtraction terms, as they need to refer to the correct *flavour block* inside the argument of `getqcdnorm` (cf. line 9 of Snippet 3.3).

The last step is generating `flavourZJ.f` with the script `makeflavour`. The role of `makeflavour` is to first find the flavour configuration of the matrix elements of `FLAVlist` (Snippet 3.6) in the library `MElibrary` (Snippet 3.5) then fill up the placeholders q (`q`), Q (`Q`), and q' (`qp`)—paying attention to the possible flavour-changing configurations—and output the *flavour blocks* one-by-one into `flavourZJ.f`. As long as `FLAVlistZJ.map` is already present, the subtraction-term generation via the scripts `makefortRR`, `makefortRV`, and `makeformVV` can be run independently as the order of the *flavour blocks* are already fixed.

The autogeneration schematics discussed throughout this section is summarized diagrammatically by Figure 3.2. While there are a lot more technical details that could be discussed—mostly stemming from trying to bridge various conventions used throughout the codebase—these are not as important for the core strategy of outfitting NNLOJET with flavour tagging.

3.5 Summary

The study of flavour-sensitive jet observables with fixed-order predictions, such as those associated with b-jets from $H \rightarrow b\bar{b}$ decay in Chapter 1 must be performed in an infrared-safe way. For calculations based on massless QCD this can only be achieved with a flavour-aware jet algorithm (such as flavour- k_t), while for a massive calculation this is achievable with flavour-blind algorithms (such as anti- k_t). In many cases the corresponding massive calculation may not be available, or the massless calculation may actually be preferred due to the presence of large logarithmic corrections that can be easily resummed via PDF evolution. Future comparisons to measurements are only viable if a similar prescription is employed on the experimental side as well. The application of even-tag exclusion here was mainly motivated to facilitate this. The use of flavour-sensitive jet algorithms is of relevance for *any*

²Unfortunately NNLOJET sometimes mixes the notations q' (`qp`) and Q (`Q`), partially due to Fortran being oblivious to capitalization. While I usually tried to abide by using q' (`qp`) only for indicating a change in flavour due to W^\pm coupling, this was not always possible because of already established notational inconsistencies in the codebase.

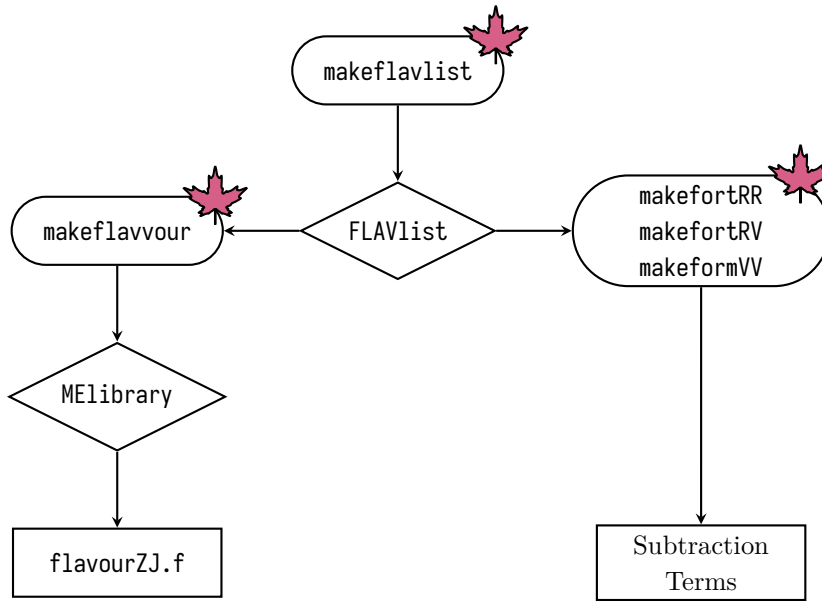


Figure 3.2: Strategy for the Maple autogeneration layer in NNLOJET for flavour tagging, illustrated for $Z+\text{jet}$ production.

flavour-sensitive jet observable, such as the ones identifying the associated production of the flavoured jet with a gauge boson or a $H \rightarrow b\bar{b}$ decay.

We gave an overview of the technicalities of a fully generic flavour-tagging implementation into the NNLOJET parton-level event generator that can be used for flavour-dependent observable predictions for any process within it. The use of the working example $Z+\text{jet}$ to indicate the key steps of this implementation was meant not just as a toy example, but it was what we used to simulate the first NNLO accurate predictions for b-jet observables associated with a Z boson. Although our publication [3] also contains crucial elements that are not strictly connected to the flavour tagging in NNLOJET—such as the bottom quark mass corrections—it is an irreplaceable constituent of the results. Together with VH production where the Higgs decays to a pair of bottom–antibottom quarks [1] they accentuate the importance and possibilities of flavour tagging in collider experiments.

Closing Thoughts

I have arrived to the last lines of my thesis. I hope I was able to give a systematic overview of my work and results during my doctoral studies at ETH Zürich, which I conducted as a member of the NNLOJET collaboration. I learned the intricacies of employing perturbative QCD calculations to produce high-precision, state-of-the-art predictions for particle physics collider experiments such as the ones conducted at the Large Hadron Collider.

Specifically, I gave detailed account on implementing next-to-next-to-leading order calculations for two classes of associated Higgs boson production into NNLOJET, a multiprocess parton-level event generator. The first class included the most abundant decay process of the Higgs boson into a pair of bottom and antibottom quarks and the requirement of at least two flavoured jets in the final state. This brought about a major extension of the NNLOJET framework that enabled identification of quark flavours and calculation of flavour-sensitive observables for all processes. The second class of associated Higgs production required at least a single final-state hard jet without the inclusion of the decay of the Higgs boson. As the precision of differential information on these processes ever increases on the experimental side, the relevance of both theoretical calculations in fundamental probes of the Standard Model rises accordingly as well.

Although it was slightly challenging to navigate the labyrinth of such a complex field as high-energy particle physics from time to time, all in all I can confidently say that I learned a lot over these years and grew to appreciate and respect the enormous effort of thousands of people who are working on a daily basis to expand this cutting-edge field, and with it, the collective knowledge of mankind.

Appendix A

Amplitudes

A common feature in all amplitudes is that the coupling strength of the Z and W^\pm bosons depend on the flavour and the helicity of the quarks and lepton lines. The W^\pm boson only couples to left-handed fermion currents between up-type and down-type quarks of the same generation with unit coupling strength—a consequence of using unity CKM matrix everywhere. The Z boson couples to fermion currents of the same flavour but its coupling strength depends on the flavour and helicity of said current. The coupling strength of a Z boson mediating between quark (q) and lepton (ℓ) currents of helicities h_q and h_ℓ can be described by the formula

$$C_{q\ell}^{h_q h_\ell} = \lambda_q^{h_q} \lambda_\ell^{h_\ell}, \quad (\text{A.1})$$

with individual couplings for left (L or $-$) and right (R or $+$) helicities being

$$\lambda_q^- = T_{3,q} - Q_q \sin^2 \theta_W, \quad \lambda_q^+ = -Q_q \sin^2 \theta_W, \quad (\text{A.2})$$

$$\lambda_\ell^- = -\frac{1}{2} + \sin^2 \theta_W, \quad \lambda_\ell^+ = \sin^2 \theta_W, \quad (\text{A.3})$$

where the third component of the weak isospin and the electric charge are

$$T_{3,u} = -\frac{1}{2}, \quad Q_u = -\frac{1}{3}, \quad (\text{A.4})$$

$$T_{3,d} = +\frac{1}{2}, \quad Q_d = +\frac{2}{3}, \quad (\text{A.5})$$

for up- and down-type quarks, respectively. The couplings being defined, we can start enumerating the variety of amplitudes which we used in the computations of VH and $VH+\text{jet}$

production.

As outlined throughout Chapters 1 and 2, we only need to give the relevant non-momentum-conserving V and V +jet amplitudes for all the Drell–Yan-like contributions, as the full VH and VH +jet ones can be simply derived by virtue of eqs. (1.5) and (1.9).

Most of the amplitudes are given in spinor–helicity formalism [83, 84] with the conventions of ref. [85]. I extensively made use of the Mathematica packages S@M [86] and SpinorsExtras [87], which are tailored towards arithmetics in spinor–helicity formalism. Furthermore, this is also how the amplitudes are numerically implemented into NNLOJET. A left-handed fermion current of particle labels i and j is given by the notation (i_f^-, j_f^+) and conversely a right-handed one with (i_f^+, j_f^-) . Gluon helicities of label k are marked similarly by k_g^\pm . Lastly, the propagator of the gauge bosons \mathcal{P}_V are given by eq. (1.10).

A.1 $B_0^{V,0}$

The left-handed quark and left-handed lepton ($q_L \ell_L$) helicity amplitude is given by

$$\mathcal{B}_0^{V,0}(1_q^-, 2_{\bar{q}}^+; 3_\ell^-, 4_{\bar{\ell}}^+) = \langle 23 \rangle [41]. \quad (\text{A.6})$$

All other helicity configurations can be expressed with it via charge conjugation relations:

$$q_L \ell_R : \quad \mathcal{B}_0^{V,0}(1_q^-, 2_{\bar{q}}^+; 3_\ell^+, 4_{\bar{\ell}}^-) = \mathcal{B}_0^{V,0}(1_q^-, 2_{\bar{q}}^+; 4_\ell^-, 3_{\bar{\ell}}^+), \quad (\text{A.7})$$

$$q_R \ell_L : \quad \mathcal{B}_0^{V,0}(1_q^+, 2_{\bar{q}}^-; 3_\ell^-, 4_{\bar{\ell}}^+) = \mathcal{B}_0^{V,0}(2_q^-, 1_{\bar{q}}^+; 3_\ell^-, 4_{\bar{\ell}}^+), \quad (\text{A.8})$$

$$q_R \ell_R : \quad \mathcal{B}_0^{V,0}(1_q^+, 2_{\bar{q}}^-; 3_\ell^+, 4_{\bar{\ell}}^-) = \mathcal{B}_0^{V,0}(2_q^-, 1_{\bar{q}}^+; 4_\ell^-, 3_{\bar{\ell}}^+). \quad (\text{A.9})$$

The non-momentum-conserving squared amplitudes for W and Z respectively are

$$B_0^{W,0}(1_q, 2_{\bar{q}}; 3_\ell, 4_{\bar{\ell}}) = |\mathcal{P}_W(s_{34})|^2 \left| \mathcal{B}_0^{V,0}(1_q^-, 2_{\bar{q}}^+; 3_\ell^-, 4_{\bar{\ell}}^+) \right|^2, \quad (\text{A.10})$$

$$B_0^{Z,0}(1_q, 2_{\bar{q}}; 3_\ell, 4_{\bar{\ell}}) = |\mathcal{P}_Z(s_{34})|^2 \sum_{h_q, h_\ell} \left| C_{q\ell}^{h_q h_\ell} \mathcal{B}_0^{V,0}(1_q^{h_q}, 2_{\bar{q}}^{-h_q}; 3_\ell^{h_\ell}, 4_{\bar{\ell}}^{-h_\ell}) \right|^2. \quad (\text{A.11})$$

The implementation in the codebase is found in the `B0g0Znmc.f90` and the autogenerated `autoB0g0Wnmc.f90` Fortran files.

A.2 $B_1^{V,0}$

The left-handed quark and left-handed lepton ($q_L \ell_L$) helicity amplitudes for both gluon helicities are given by

$$\mathcal{B}_1^{V,0}(1_q^-, 2_g^-, 3_{\bar{q}}^+; 4_\ell^-, 5_{\bar{\ell}}^+) = \langle 34 \rangle \frac{\langle 13 \rangle [51] + \langle 23 \rangle [52]}{\langle 12 \rangle \langle 23 \rangle}, \quad (\text{A.12})$$

$$\mathcal{B}_1^{V,0}(1_q^-, 2_g^+, 3_{\bar{q}}^+; 4_\ell^-, 5_{\bar{\ell}}^+) = -\mathcal{B}_1^{V,0}(3_q^-, 2_g^-, 1_{\bar{q}}^+; 5_\ell^-, 4_{\bar{\ell}}^+)^*, \quad (\text{A.13})$$

where the second line exploited parity and charge conjugation. All other helicity configurations ($h = \pm$) can be expressed with them via charge conjugation relations:

$$q_L \ell_R : \quad \mathcal{B}_1^{V,0}(1_q^-, 2_g^h, 3_{\bar{q}}^+; 4_\ell^+, 5_{\bar{\ell}}^-) = \mathcal{B}_1^{V,0}(1_q^-, 2_g^h, 3_{\bar{q}}^+; 5_\ell^-, 4_{\bar{\ell}}^+), \quad (\text{A.14})$$

$$q_R \ell_L : \quad \mathcal{B}_1^{V,0}(1_q^+, 2_g^h, 3_{\bar{q}}^-; 4_\ell^-, 5_{\bar{\ell}}^+) = -\mathcal{B}_1^{V,0}(3_q^-, 2_g^h, 1_{\bar{q}}^+; 4_\ell^-, 5_{\bar{\ell}}^+), \quad (\text{A.15})$$

$$q_R \ell_R : \quad \mathcal{B}_1^{V,0}(1_q^+, 2_g^h, 3_{\bar{q}}^-; 4_\ell^+, 5_{\bar{\ell}}^-) = -\mathcal{B}_1^{V,0}(3_q^-, 2_g^h, 1_{\bar{q}}^+; 5_\ell^-, 4_{\bar{\ell}}^+). \quad (\text{A.16})$$

The non-momentum-conserving squared amplitudes for W and Z respectively are

$$B_1^{W,0}(1_q, 2_g, 3_{\bar{q}'}; 4_\ell, 5_{\bar{\ell}}) = |\mathcal{P}_W(s_{45})|^2 \sum_h \left| \mathcal{B}_1^{V,0}(1_q^-, 2_g^h, 3_{\bar{q}'}^+; 4_\ell^-, 5_{\bar{\ell}}^+) \right|^2, \quad (\text{A.17})$$

$$B_1^{Z,0}(1_q, 2_g, 3_{\bar{q}}; 4_\ell, 5_{\bar{\ell}}) = |\mathcal{P}_Z(s_{45})|^2 \sum_{h, h_q, h_\ell} \left| C_{q\ell}^{h_q h_\ell} \mathcal{B}_1^{V,0}(1_q^{h_q}, 2_g^h, 3_{\bar{q}}^{-h_q}, 4_\ell^{h_\ell}, 5_{\bar{\ell}}^{-h_\ell}) \right|^2. \quad (\text{A.18})$$

The implementation in the codebase is found in the `B1g0Znmc.f90` and the autogenerated `autoB1g0Wnmc.f90` Fortran files.

A.3 $B_0^{V,1}$

The one-loop amplitudes are expressed with the tree-level ones of Section A.1 as

$$B_0^{V,1}(1_q, 2_{\bar{q}}; 3_\ell, 4_{\bar{\ell}}) = B_0^{V,0}(1_q, 2_{\bar{q}}; 3_\ell, 4_{\bar{\ell}}) \times \left\{ -\frac{1}{\epsilon^2} + \left[\ln\left(\frac{s_{12}}{\mu_R^2}\right) - \frac{3}{2} \right] \frac{1}{\epsilon} - \frac{1}{2} \ln^2\left(\frac{s_{12}}{\mu_R^2}\right) + \frac{3}{2} \ln\left(\frac{s_{12}}{\mu_R^2}\right) + \frac{7}{12} \pi^2 - 4 \right\}. \quad (\text{A.19})$$

The implementation in the codebase is found in the `B0g1Znmc.f90` and the autogenerated `autoB0g1Wnmc.f90` Fortran files.

A.4 $B_2^{V,0}$

The left-handed quark and left-handed lepton ($q_L \ell_L$) helicity amplitudes for all four gluon helicities are given by

$$\mathcal{B}_2^{V,0}\left(1_q^-, 2_g^-, 3_g^-, 4_q^+; 5_\ell^-, 6_\ell^+\right) = -[61] \frac{\langle 25 \rangle [21] + \langle 35 \rangle [31] + \langle 45 \rangle [41]}{[43][32][21]}, \quad (\text{A.20})$$

$$\begin{aligned} \mathcal{B}_2^{V,0}\left(1_q^-, 2_g^-, 3_g^+, 4_q^+; 5_\ell^-, 6_\ell^+\right) &= -\frac{1}{\langle 12 \rangle [42] + \langle 13 \rangle [43]} \times \\ &\left[[42] \frac{\langle 35 \rangle [32] + \langle 45 \rangle [42]}{[43][32]} \left([61] \frac{\langle 13 \rangle [32] + \langle 14 \rangle [42]}{s_{234}} + [62] \right) \right. \\ &\left. + \langle 13 \rangle \frac{\langle 13 \rangle [61] + \langle 23 \rangle [62]}{\langle 12 \rangle \langle 23 \rangle} \left(\langle 45 \rangle \frac{\langle 13 \rangle [41] + \langle 23 \rangle [42]}{s_{123}} + \langle 35 \rangle \right) \right], \end{aligned} \quad (\text{A.21})$$

$$\begin{aligned} \mathcal{B}_2^{V,0}\left(1_q^-, 2_g^+, 3_g^-, 4_q^+; 5_\ell^-, 6_\ell^+\right) &= -\frac{1}{\langle 24 \rangle [21] + \langle 34 \rangle [31]} \times \\ &\left[\langle 45 \rangle [31]^3 \frac{\langle 14 \rangle [61] + \langle 24 \rangle [62] + \langle 34 \rangle [63]}{s_{123} [32][21]} \right. \\ &\left. + [61] \langle 24 \rangle^3 \frac{\langle 25 \rangle [21] + \langle 35 \rangle [31] + \langle 45 \rangle [41]}{s_{234} \langle 23 \rangle \langle 34 \rangle} \right], \end{aligned} \quad (\text{A.22})$$

$$\mathcal{B}_2^{V,0}\left(1_q^-, 2_g^+, 3_g^+, 4_q^+; 5_\ell^-, 6_\ell^+\right) = \mathcal{B}_2^{V,0}\left(4_q^-, 3_g^-, 2_g^-, 1_q^+; 6_\ell^-, 5_\ell^+\right)^*, \quad (\text{A.23})$$

where the last line exploited parity and charge conjugation. All other helicity configurations ($h_1, h_2 = \pm$) can be expressed with them via charge conjugation relations:

$$q_L \ell_R : \quad \mathcal{B}_2^{V,0}\left(1_q^-, 2_g^{h_1}, 3_g^{h_2}, 4_q^+; 5_\ell^+, 6_\ell^-\right) = \mathcal{B}_2^{V,0}\left(1_q^-, 2_g^{h_1}, 3_g^{h_2}, 4_q^+; 6_\ell^-, 5_\ell^+\right), \quad (\text{A.24})$$

$$q_R \ell_L : \quad \mathcal{B}_2^{V,0}\left(1_q^+, 2_g^{h_1}, 3_g^{h_2}, 4_q^-; 5_\ell^-, 6_\ell^+\right) = \mathcal{B}_2^{V,0}\left(4_q^-, 3_g^{h_2}, 2_g^{h_1}, 1_q^+; 5_\ell^-, 6_\ell^+\right), \quad (\text{A.25})$$

$$q_R \ell_R : \quad \mathcal{B}_2^{V,0}\left(1_q^+, 2_g^{h_1}, 3_g^{h_2}, 4_q^-; 5_\ell^+, 6_\ell^-\right) = \mathcal{B}_2^{V,0}\left(4_q^-, 3_g^{h_2}, 2_g^{h_1}, 1_q^+; 6_\ell^-, 5_\ell^+\right). \quad (\text{A.26})$$

The non-momentum-conserving squared amplitudes for W and Z respectively are

$$B_2^{W,0}(1_q, 2_g, 3_g, 4_{\bar{q}'}; 5_\ell, 6_{\bar{\ell}}) = |\mathcal{P}_W(s_{56})|^2 \sum_{h_1, h_2} \left| \mathcal{B}_2^{V,0} \left(1_q^-, 2_g^{h_1}, 3_g^{h_2}, 4_{\bar{q}'}^+; 5_\ell^-, 6_{\bar{\ell}}^+ \right) \right|^2, \quad (\text{A.27})$$

$$B_2^{Z,0}(1_q, 2_g, 3_g, 4_{\bar{q}}; 5_\ell, 6_{\bar{\ell}}) = |\mathcal{P}_Z(s_{56})|^2 \sum_{\substack{h_q, h_\ell \\ h_1, h_2}} \left| C_{q\ell}^{h_q h_\ell} \mathcal{B}_2^{V,0} \left(1_q^{h_q}, 2_g^{h_1}, 3_g^{h_2}, 4_{\bar{q}}^{-h_q}; 5_\ell^{h_\ell}, 6_{\bar{\ell}}^{-h_\ell} \right) \right|^2. \quad (\text{A.28})$$

The subleading-colour helicity amplitude is the sum of two different gluon permutations of the leading-colour helicity amplitudes (A.20)–(A.23)

$$\begin{aligned} \tilde{\mathcal{B}}_2^{V,0} \left(1_q^{h_q}, 2_g^{h_1}, 3_g^{h_2}, 4_{\bar{q}}^{-h_q}; 5_\ell^{h_\ell}, 6_{\bar{\ell}}^{-h_\ell} \right) = \\ \mathcal{B}_2^{V,0} \left(1_q^{h_q}, 2_g^{h_1}, 3_g^{h_2}, 4_{\bar{q}}^{-h_q}; 5_\ell^{h_\ell}, 6_{\bar{\ell}}^{-h_\ell} \right) + \mathcal{B}_2^{V,0} \left(1_q^{h_q}, 3_g^{h_2}, 2_g^{h_1}, 4_{\bar{q}}^{-h_q}; 5_\ell^{h_\ell}, 6_{\bar{\ell}}^{-h_\ell} \right), \end{aligned} \quad (\text{A.29})$$

from which the final squared amplitudes are derived similarly to eqs. (A.27) and (A.28). The implementation in the codebase for both colour levels is found in the `B2g0Znmc.f90` and the autogenerated `autoB2g0Wnmc.f90` Fortran files.

A.5 $C_0^{V,0}$

The helicity amplitude where both quark lines and the lepton current are left-handed ($q_L Q_L \ell_L$) and the gauge boson couples to the outer q ($1_q 4_{\bar{q}}$) quark line is given by

$$\begin{aligned} C_0^{V,0} \left(1_q^-, 2_Q^+, 3_Q^-, 4_{\bar{q}}^+; 5_\ell^-, 6_{\bar{\ell}}^+ \right) = \\ \frac{1}{s_{32}} \left[\langle 24 \rangle [61] \frac{\langle 25 \rangle [32] - \langle 45 \rangle [43]}{s_{234}} + \langle 45 \rangle [31] \frac{\langle 12 \rangle [61] - \langle 23 \rangle [63]}{s_{123}} \right]. \end{aligned} \quad (\text{A.30})$$

All other helicity configurations with the vector boson still only coupling to the outer quark line q are expressed using charge conjugation relations as

$$q_L Q_L \ell_R : \quad C_0^{V,0} \left(1_q^-, 2_Q^+, 3_Q^-, 4_{\bar{q}}^+; 5_\ell^+, 6_{\bar{\ell}}^- \right) = C_0^{V,0} \left(1_q^-, 2_Q^+, 3_Q^-, 4_{\bar{q}}^+; 6_{\bar{\ell}}^-, 5_\ell^+ \right), \quad (\text{A.31})$$

$$q_L Q_R \ell_L : \quad C_0^{V,0} \left(1_q^-, 2_Q^-, 3_Q^+, 4_{\bar{q}}^+; 5_\ell^-, 6_{\bar{\ell}}^+ \right) = C_0^{V,0} \left(1_q^-, 3_Q^+, 2_Q^-, 4_{\bar{q}}^+; 5_\ell^-, 6_{\bar{\ell}}^+ \right), \quad (\text{A.32})$$

$$q_L Q_R \ell_R : \quad C_0^{V,0} \left(1_q^-, 2_Q^-, 3_Q^+, 4_{\bar{q}}^+; 5_\ell^+, 6_{\bar{\ell}}^- \right) = C_0^{V,0} \left(1_q^-, 3_Q^+, 2_Q^-, 4_{\bar{q}}^+; 6_{\bar{\ell}}^-, 5_\ell^+ \right), \quad (\text{A.33})$$

$$q_R Q_L \ell_L : \quad C_0^{V,0} \left(1_q^+, 2_{\bar{Q}}^+, 3_Q^-, 4_{\bar{q}}^-; 5_{\ell}^-, 6_{\bar{\ell}}^+ \right) = -C_0^{V,0} \left(4_{\bar{q}}^-, 2_{\bar{Q}}^+, 3_Q^-, 1_q^+; 5_{\ell}^-, 6_{\bar{\ell}}^+ \right), \quad (\text{A.34})$$

$$q_R Q_L \ell_R : \quad C_0^{V,0} \left(1_q^+, 2_{\bar{Q}}^+, 3_Q^-, 4_{\bar{q}}^-; 5_{\ell}^+, 6_{\bar{\ell}}^- \right) = -C_0^{V,0} \left(4_{\bar{q}}^-, 2_{\bar{Q}}^+, 3_Q^-, 1_q^+; 6_{\ell}^-, 5_{\bar{\ell}}^+ \right), \quad (\text{A.35})$$

$$q_R Q_R \ell_L : \quad C_0^{V,0} \left(1_q^+, 2_{\bar{Q}}^-, 3_Q^+, 4_{\bar{q}}^-; 5_{\ell}^-, 6_{\bar{\ell}}^+ \right) = -C_0^{V,0} \left(4_{\bar{q}}^-, 3_Q^+, 2_{\bar{Q}}^-, 1_q^+; 5_{\ell}^-, 6_{\bar{\ell}}^+ \right), \quad (\text{A.36})$$

$$q_R Q_R \ell_R : \quad C_0^{V,0} \left(1_q^+, 2_{\bar{Q}}^-, 3_Q^+, 4_{\bar{q}}^-; 5_{\ell}^+, 6_{\bar{\ell}}^- \right) = -C_0^{V,0} \left(4_{\bar{q}}^-, 3_Q^+, 2_{\bar{Q}}^-, 1_q^+; 6_{\ell}^-, 5_{\bar{\ell}}^+ \right). \quad (\text{A.37})$$

The squared amplitude for W is then

$$C_0^{W,0} \left(1_q, 2_{\bar{Q}}, 3_Q, 4_{\bar{q}'}; 5_{\ell}, 6_{\bar{\ell}} \right) = |\mathcal{P}_W(s_{56})|^2 \sum_{h_Q} \left| C_0^{V,0} \left(1_q^-, 2_{\bar{Q}}^{-h_Q}, 3_Q^{h_Q}, 4_{\bar{q}'}^+; 5_{\ell}^-, 6_{\bar{\ell}}^+ \right) \right|^2. \quad (\text{A.38})$$

The Z amplitude requires adding terms with the interchange $(1_q \leftrightarrow 3_Q)$ and $(4_{\bar{q}} \leftrightarrow 2_{\bar{Q}})$ to ensure that the neutral gauge boson can couple to both quark lines:

$$\begin{aligned} C_0^{Z,0} \left(1_q, 2_{\bar{Q}}, 3_Q, 4_{\bar{q}}; 5_{\ell}, 6_{\bar{\ell}} \right) &= |\mathcal{P}_Z(s_{56})|^2 \times \\ &\sum_{h_q, h_Q, h_{\ell}} \left| C_{q\ell}^{h_q h_{\ell}} C_0^{V,0} \left(1_q^{h_q}, 2_{\bar{Q}}^{-h_Q}, 3_Q^{h_Q}, 4_{\bar{q}}^{-h_q}; 5_{\ell}^{h_{\ell}}, 6_{\bar{\ell}}^{-h_{\ell}} \right) \right. \\ &\quad \left. + C_{Q\ell}^{h_Q h_{\ell}} C_0^{V,0} \left(3_Q^{h_Q}, 4_{\bar{q}}^{-h_q}, 1_q^{h_q}, 2_{\bar{Q}}^{-h_Q}; 5_{\ell}^{h_{\ell}}, 6_{\bar{\ell}}^{-h_{\ell}} \right) \right|^2. \end{aligned} \quad (\text{A.39})$$

The implementation in the codebase is found in the `C0g0Znmc.f90` and the autogenerated `autoC0g0Wnmc.f90` Fortran files.

A.6 $D_0^{V,0}$

The subleading-colour interference terms are assembled from the complex amplitudes of Section A.5. The W squared amplitudes for the two different identical-quark configurations are

$$\begin{aligned} D_{b,0}^{W,0} \left(1_q, 2_{\bar{q}'}, 3_{q'}, 4_{\bar{q}'}; 5_{\ell}, 6_{\bar{\ell}} \right) \\ = -|\mathcal{P}_W(s_{56})|^2 2 \operatorname{Re} \left\{ C_0^{V,0} \left(1_q^-, 2_{\bar{q}'}^+, 3_{q'}^-, 4_{\bar{q}'}^+; 5_{\ell}^-, 6_{\bar{\ell}}^+ \right) C_0^{V,0} \left(1_q^-, 4_{\bar{q}'}^+, 3_{q'}^-, 2_{\bar{q}'}^+; 5_{\ell}^-, 6_{\bar{\ell}}^+ \right)^* \right\}, \end{aligned} \quad (\text{A.40})$$

$$D_{a,0}^{W,0} \left(1_q, 2_{\bar{q}}, 3_q, 4_{\bar{q}'}; 5_{\ell}, 6_{\bar{\ell}} \right) = D_{b,0}^{W,0} \left(4_{q'}, 3_{\bar{q}}, 2_q, 1_{\bar{q}}; 6_{\ell}, 5_{\bar{\ell}} \right). \quad (\text{A.41})$$

As the quarks are identical, helicity flips are not allowed for the Z squared amplitude:

$$D_0^{Z,0}(1_q, 2_{\bar{q}}, 3_q, 4_{\bar{q}}; 5_\ell, 6_{\bar{\ell}}) = -|\mathcal{P}_Z(s_{56})|^2 \sum_{h_q, h_\ell} \left| C_{q\ell}^{h_q h_\ell} \right|^2$$

$$2 \operatorname{Re} \left\{ \left[\mathcal{C}_0^{V,0} \left(1_q^{h_q}, 2_{\bar{q}}^{-h_q}, 3_q^{h_q}, 4_{\bar{q}}^{-h_q}; 5_\ell^-, 6_{\bar{\ell}}^+ \right) + \mathcal{C}_0^{V,0} \left(3_q^{h_q}, 4_{\bar{q}}^{-h_q}, 1_q^{h_q}, 2_{\bar{q}}^{-h_q}; 5_\ell^-, 6_{\bar{\ell}}^+ \right) \right] \right.$$

$$\left. \times \left[\mathcal{C}_0^{V,0} \left(1_q^{h_q}, 4_{\bar{q}}^{-h_q}, 3_q^{h_q}, 2_{\bar{q}}^{-h_q}; 5_\ell^-, 6_{\bar{\ell}}^+ \right) + \mathcal{C}_0^{V,0} \left(3_q^{h_q}, 2_{\bar{q}}^{-h_q}, 1_q^{h_q}, 4_{\bar{q}}^{-h_q}; 5_\ell^-, 6_{\bar{\ell}}^+ \right) \right]^* \right\}. \quad (\text{A.42})$$

The negative sign preceding the amplitudes is due to the NNLOJET convention of having one in front of subleading-colour pieces. The implementation in the codebase is found in the `D0g0Znmc.f90` and the autogenerated `autogD0Wnmc.f90` Fortran files.

A.7 $B_1^{V,1}$ and $B_1^{V,2}$

The structure of the one-loop $\mathcal{B}_1^{V,1}$ and the two-loop $\mathcal{B}_1^{V,2}$ helicity amplitudes are very similar and both rely on the formulation given in ref. [88]. The left-handed quark and left-handed lepton ($q_L \ell_L$) complex amplitudes for both gluon helicities are expressed as

$$\mathcal{B}_1^{V,N} \left(1_q^-, 2_g^-, 3_{\bar{q}}^+, 4_\ell^-, 5_{\bar{\ell}}^+ \right) = \mathcal{A}_\alpha \alpha(u, v) + \mathcal{A}_\beta \beta(u, v) + \mathcal{A}_\gamma \gamma(u, v), \quad (\text{A.43})$$

$$\mathcal{B}_1^{V,N} \left(1_q^-, 2_g^+, 3_{\bar{q}}^+, 4_\ell^-, 5_{\bar{\ell}}^+ \right) = -\mathcal{B}_1^{V,N} \left(3_q^-, 2_g^-, 1_{\bar{q}}^+, 5_\ell^-, 4_{\bar{\ell}}^+ \right)^*, \quad (\text{A.44})$$

where the second line exploited parity and charge conjugation. The helicity coefficients $\alpha(u, v)$, $\beta(u, v)$, and $\gamma(u, v)$ are presented in great detail in ref. [88] for both the one-loop ($N = 1$) and two-loop ($N = 2$) cases, but the partial helicity amplitudes \mathcal{A}_α , \mathcal{A}_β , and \mathcal{A}_γ are different due to not respecting momentum conservation.¹ They are

$$\mathcal{A}_\alpha = \frac{\langle 13 \rangle \langle 34 \rangle [51]}{\langle 12 \rangle \langle 23 \rangle} + \langle 13 \rangle [21] \frac{\langle 14 \rangle [51] + \langle 24 \rangle [52] + \langle 34 \rangle [53]}{2s_{123} \langle 12 \rangle}, \quad (\text{A.45})$$

$$\mathcal{A}_\beta = \frac{\langle 34 \rangle [52]}{\langle 12 \rangle} - \langle 13 \rangle [21] \frac{\langle 14 \rangle [51] + \langle 24 \rangle [52] + \langle 34 \rangle [53]}{2s_{123} \langle 12 \rangle}, \quad (\text{A.46})$$

$$\mathcal{A}_\gamma = \frac{\langle 14 \rangle [21] [52]}{\langle 12 \rangle [32]} - \langle 13 \rangle [21] \frac{\langle 14 \rangle [51] + \langle 24 \rangle [52] + \langle 34 \rangle [53]}{2s_{123} \langle 12 \rangle}. \quad (\text{A.47})$$

¹The last terms in eqs. (A.45)–(A.47) vanish when momentum is conserved, restoring the values in ref. [88]. This can be seen more explicitly in eq. (2.22) of ref. [89] as well.

The renormalization-scale dependence is not indicated in eq. (A.43) but it is also given explicitly in ref. [88]. All other helicity configurations ($h = \pm$) can be expressed with eqs. (A.43) and (A.44) via charge conjugation:

$$q_L \ell_R : \quad \mathcal{B}_1^{V,N} \left(1_q^-, 2^h, 3_{\bar{q}}^+; 4_\ell^+, 5_{\bar{\ell}}^- \right) = \mathcal{B}_1^{V,N} \left(1_q^-, 2^h, 3_{\bar{q}}^+; 5_{\bar{\ell}}^-, 4_\ell^+ \right), \quad (\text{A.48})$$

$$q_R \ell_L : \quad \mathcal{B}_1^{V,N} \left(1_q^+, 2^h, 3_{\bar{q}}^-; 4_\ell^-, 5_{\bar{\ell}}^+ \right) = -\mathcal{B}_1^{V,N} \left(3_{\bar{q}}^-, 2^h, 1_q^+; 4_\ell^-, 5_{\bar{\ell}}^+ \right), \quad (\text{A.49})$$

$$q_R \ell_R : \quad \mathcal{B}_1^{V,N} \left(1_q^+, 2^h, 3_{\bar{q}}^-; 4_\ell^+, 5_{\bar{\ell}}^- \right) = -\mathcal{B}_1^{V,N} \left(3_{\bar{q}}^-, 2^h, 1_q^+; 4_\ell^+, 5_{\bar{\ell}}^- \right). \quad (\text{A.50})$$

The non-momentum-conserving leading-colour one-loop squared amplitudes $B_1^{V,1}$ are the following (tree) \times (one-loop) interferences:

$$B_1^{W,1}(1_q, 2_g, 3_{\bar{q}'}; 4_\ell, 5_{\bar{\ell}}) = |\mathcal{P}_W(s_{45})|^2 \times \sum_h 2 \operatorname{Re} \left[\mathcal{B}_1^{V,0} \left(1_q^-, 2^h, 3_{\bar{q}'}^+; 4_\ell^-, 5_{\bar{\ell}}^+ \right) \mathcal{B}_1^{V,1} \left(1_q^-, 2^h, 3_{\bar{q}'}^+; 4_\ell^-, 5_{\bar{\ell}}^+ \right)^* \right], \quad (\text{A.51})$$

$$B_1^{Z,1}(1_q, 2_g, 3_{\bar{q}}; 4_\ell, 5_{\bar{\ell}}) = |\mathcal{P}_Z(s_{45})|^2 \times \sum_{h, h_q, h_\ell} \left| C_{q\ell}^{h_q h_\ell} \right|^2 2 \operatorname{Re} \left[\mathcal{B}_1^{V,0} \left(1_q^{h_q}, 2^h, 3_{\bar{q}}^{-h_q}; 4_\ell^{h_\ell}, 5_{\bar{\ell}}^{-h_\ell} \right) \mathcal{B}_1^{V,1} \left(1_q^{h_q}, 2^h, 3_{\bar{q}}^{-h_q}; 4_\ell^{h_\ell}, 5_{\bar{\ell}}^{-h_\ell} \right)^* \right], \quad (\text{A.52})$$

where the tree-level helicity amplitudes $\mathcal{B}_1^{V,0}$ are those of Section A.2.

The structure for deriving the subleading-colour $\tilde{B}_1^{V,1}$ and n_F -proportional $\hat{B}_1^{V,1}$ amplitudes is very similar, except that the correct colour decomposition of the helicity coefficients $\alpha(u, v)$, $\beta(u, v)$, and $\gamma(u, v)$ need to be substituted into eq. (A.43).² This is also given in ref. [88]. The implementation in the codebase for all colour levels is found in the `B1g1Znmc.f90` and the autogenerated `autoB1g1Wnmc.f90` Fortran files.

The leading-colour two-loop amplitudes $B_1^{V,2}$ consist of (tree) \times (two-loop) and (one-loop)² interferences according to

$$B_1^{W,1}(1_q, 2_g, 3_{\bar{q}'}; 4_\ell, 5_{\bar{\ell}}) = |\mathcal{P}_W(s_{45})|^2 \left\{ \sum_h \left| \mathcal{B}_1^{V,1} \left(1_q^-, 2^h, 3_{\bar{q}'}^+; 4_\ell^-, 5_{\bar{\ell}}^+ \right) \right|^2 \right.$$

²The subleading-colour contributions acquire a negative sign in eqs. (A.51) and (A.52), as customary in NNLOJET.

$$+ \sum_h 2 \operatorname{Re} \left[\mathcal{B}_1^{V,0} \left(1_q^-, 2_g^h, 3_{q'}^+, 4_\ell^-, 5_{\bar{\ell}}^+ \right) \mathcal{B}_1^{V,2} \left(1_q^-, 2_g^h, 3_{q'}^+, 4_\ell^-, 5_{\bar{\ell}}^+ \right)^* \right] \Big\}, \quad (\text{A.53})$$

$$\begin{aligned} B_1^{Z,1}(1_q, 2_g, 3_{\bar{q}}; 4_\ell, 5_{\bar{\ell}}) &= |\mathcal{P}_Z(s_{45})|^2 \left\{ \sum_{h, h_q, h_\ell} \left| C_{q\ell}^{h_q h_\ell} \right|^2 \left| \mathcal{B}_1^{V,1} \left(1_q^{h_q}, 2_g^h, 3_{\bar{q}}^{-h_q}; 4_\ell^{h_\ell}, 5_{\bar{\ell}}^{-h_\ell} \right) \right|^2 \right. \\ &\quad \left. + \sum_{h, h_q, h_\ell} \left| C_{q\ell}^{h_q h_\ell} \right|^2 2 \operatorname{Re} \left[\mathcal{B}_1^{V,0} \left(1_q^{h_q}, 2_g^h, 3_{\bar{q}}^{-h_q}; 4_\ell^{h_\ell}, 5_{\bar{\ell}}^{-h_\ell} \right) \mathcal{B}_1^{V,2} \left(1_q^{h_q}, 2_g^h, 3_{\bar{q}}^{-h_q}; 4_\ell^{h_\ell}, 5_{\bar{\ell}}^{-h_\ell} \right)^* \right] \right\}. \end{aligned} \quad (\text{A.54})$$

Using the appropriate interferences and colour decomposition of the helicity coefficients, the partial squared amplitudes $\tilde{B}_2^{VH,1}$, $\hat{B}_2^{VH,1}$, $\hat{\hat{B}}_2^{VH,1}$, $\tilde{\tilde{B}}_2^{VH,1}$, $\hat{B}_2^{VH,1}$, and $\hat{\hat{B}}_2^{VH,1}$ are derived very similarly. Additionally, the colour-decomposed Catani pole structures need to be subtracted to match conventions used in subtraction terms. The implementation in the codebase for all colour levels is found in the `B1g2Znmc.f90` and the autogenerated `autoB1g2Wnmc.f90` Fortran files.

For both $N = 1$ and $N = 2$ cases, the helicity coefficients in eq. (A.43) are evaluated through subroutines in the file `B1gNZnmcAux.f90`.

A.8 $B_1^{VH,1top}$

This amplitude was imported from Appendix B.3 of ref. [33] and modified to fit conventions in NNLOJET. The left-handed quark and left-handed lepton ($q_L \ell_L$) helicity amplitudes for both gluon helicities are given by

$$\begin{aligned} \mathcal{B}_1^{VH,1top} \left(1_q^-, 2_g^-, 3_{q'}^+, 4_\ell^-, 5_{\bar{\ell}}^+ \right) &= \\ &= \frac{1}{s_{1345}} \left[[51] \frac{\langle 14 \rangle [21] + \langle 45 \rangle [52]}{s_{145}} \left(\langle 13 \rangle [21] + \langle 34 \rangle [42] + \langle 35 \rangle [52] \right) \right. \\ &\quad \left. - \langle 34 \rangle [21] \left([52] + [21] \frac{\langle 13 \rangle [53] + \langle 14 \rangle [54]}{s_{345}} \right) \right], \end{aligned} \quad (\text{A.55})$$

$$\mathcal{B}_1^{VH,1top} \left(1_q^-, 2_g^+, 3_{q'}^+, 4_\ell^-, 5_{\bar{\ell}}^+ \right) = -\mathcal{B}_1^{VH,1top} \left(3_{q'}^-, 2_g^-, 1_{q'}^+, 5_{\bar{\ell}}^-, 4_\ell^+ \right)^*, \quad (\text{A.56})$$

where the second line exploited parity and charge conjugation. All other helicity configurations ($h = \pm$) can be expressed with them via charge conjugation relations:

$$q_L \ell_R : \quad \mathcal{B}_1^{VH,1top} \left(1_q^-, 2_g^h, 3_{\bar{q}}^+, 4_\ell^+, 5_{\bar{\ell}}^- \right) = \mathcal{B}_1^{VH,1top} \left(1_q^-, 2_g^h, 3_{\bar{q}}^+, 5_{\bar{\ell}}^-, 4_\ell^+ \right), \quad (\text{A.57})$$

$$q_R \ell_L : \quad \mathcal{B}_1^{VH,1top} \left(1_q^+, 2_g^h, 3_{\bar{q}}^-, 4_\ell^-, 5_{\bar{\ell}}^+ \right) = -\mathcal{B}_1^{VH,1top} \left(3_q^-, 2_g^h, 1_{\bar{q}}^+, 4_\ell^-, 5_{\bar{\ell}}^+ \right), \quad (\text{A.58})$$

$$q_R \ell_R : \quad \mathcal{B}_1^{VH,1top} \left(1_q^+, 2_g^h, 3_{\bar{q}}^-, 4_\ell^+, 5_{\bar{\ell}}^- \right) = -\mathcal{B}_1^{VH,1top} \left(3_q^-, 2_g^h, 1_{\bar{q}}^+, 5_{\bar{\ell}}^-, 4_\ell^+ \right). \quad (\text{A.59})$$

The non-momentum-conserving squared amplitudes are the following (tree) \times (one-loop) interferences:

$$B_1^{WH,1top} (1_q, 2_g, 3_{\bar{q}'}; 4_\ell, 5_{\bar{\ell}}) = \sum_h 2 \operatorname{Re} \left\{ \mathcal{P}_W(s_{45}) \mathcal{B}_1^{VH,0} \left(1_q^-, 2_g^h, 3_{\bar{q}'}^+, 4_\ell^-, 5_{\bar{\ell}}^+ \right) \left[\mathcal{I}^{\text{FT}} \mathcal{B}_1^{VH,1top} \left(1_q^-, 2_g^h, 3_{\bar{q}'}^+, 4_\ell^-, 5_{\bar{\ell}}^+ \right) \right]^* \right\}, \quad (\text{A.60})$$

$$B_1^{ZH,1top} (1_q, 2_g, 3_{\bar{q}}; 4_\ell, 5_{\bar{\ell}}) = \sum_{h, h_q, h_\ell} \left| C_{q\ell}^{h_q h_\ell} \right|^2 \times 2 \operatorname{Re} \left\{ \mathcal{P}_Z(s_{45}) \mathcal{B}_1^{VH,0} \left(1_q^{h_q}, 2_g^h, 3_{\bar{q}}^{-h_q}, 4_\ell^{h_\ell}, 5_{\bar{\ell}}^{-h_\ell} \right) \left[\mathcal{I}^{\text{FT}} \mathcal{B}_1^{VH,1top} \left(1_q^{h_q}, 2_g^h, 3_{\bar{q}}^{-h_q}, 4_\ell^{h_\ell}, 5_{\bar{\ell}}^{-h_\ell} \right) \right]^* \right\}, \quad (\text{A.61})$$

where the tree-level helicity amplitudes $\mathcal{B}_1^{VH,0}$ are

$$\mathcal{B}_1^{VH,0} = \mathcal{P}_V(s_{45}) \mathcal{B}_1^{V,0}, \quad (\text{A.62})$$

i.e. those of Section A.2 equipped with the extra gauge-boson propagator, similarly how it was outlined in eq. (1.9) for squared amplitudes. The factor \mathcal{I}^{FT} contains a combination of scalar loop integrals and it is given by eq. (B.11) of ref. [33] with an index swap ($2 \leftrightarrow 5$) due to differences between notations. These scalar integrals within \mathcal{I}^{FT} are evaluated with the ONELOOP [54] library that comes bundled together with OpenLoops [53].

The implementation in the codebase is found in the `B1g1topZnmc.f90` and the autogenerated `autoB1g1topWnmc.f90` Fortran files.

A.9 $B_0^{V,2}$

The leading-colour, subleading-colour, and n_F -proportional two-loop amplitudes with their Catani pole structures subtracted are expressed proportional to the tree-level amplitudes as

$$\begin{aligned}
B_0^{V,2}(1_q, 2_{\bar{q}}; 3_\ell, 4_{\bar{\ell}}) &= B_0^{V,0}(1_q, 2_{\bar{q}}; 3_\ell, 4_{\bar{\ell}}) \times \\
&\left\{ \frac{1}{2} \frac{1}{\epsilon^4} + \left[\frac{23}{8} + \ln\left(\frac{\mu_R^2}{s_{12}}\right) \right] \frac{1}{\epsilon^3} + \left[\frac{401}{72} + \frac{47}{12} \ln\left(\frac{\mu_R^2}{s_{12}}\right) + \ln^2\left(\frac{\mu_R^2}{s_{12}}\right) - \frac{13}{24} \pi^2 \right] \frac{1}{\epsilon^2} \right. \\
&+ \left[\frac{10093}{864} + \frac{151}{18} \ln\left(\frac{\mu_R^2}{s_{12}}\right) + 3 \ln^2\left(\frac{\mu_R^2}{s_{12}}\right) + \frac{2}{3} \ln^3\left(\frac{\mu_R^2}{s_{12}}\right) - \frac{7}{12} \zeta_3 - \frac{89}{48} \pi^2 - \frac{13}{12} \pi^2 \ln\left(\frac{\mu_R^2}{s_{12}}\right) \right] \frac{1}{\epsilon} \\
&\left. - \frac{60923}{5184} - \frac{22}{3} \ln\left(\frac{\mu_R^2}{s_{12}}\right) + \frac{389}{72} \zeta_3 - \frac{5}{36} \pi^2 + \frac{49}{1440} \pi^4 \right\}, \tag{A.63}
\end{aligned}$$

$$\begin{aligned}
\tilde{B}_0^{V,2}(1_q, 2_{\bar{q}}; 3_\ell, 4_{\bar{\ell}}) &= B_0^{V,0}(1_q, 2_{\bar{q}}; 3_\ell, 4_{\bar{\ell}}) \times \\
&\left\{ \frac{1}{2} \frac{1}{\epsilon^4} + \left[\frac{3}{2} + \log\left(\frac{\mu_R^2}{s_{12}}\right) \right] \frac{1}{\epsilon^3} + \left[\frac{41}{8} + 3 \log\left(\frac{\mu_R^2}{s_{12}}\right) + \log^2\left(\frac{\mu_R^2}{s_{12}}\right) - \frac{7}{12} \pi^2 \right] \frac{1}{\epsilon^2} \right. \\
&+ \left[\frac{445}{32} + \frac{41}{4} \log\left(\frac{\mu_R^2}{s_{12}}\right) + 3 \log^2\left(\frac{\mu_R^2}{s_{12}}\right) + \frac{2}{3} \log^3\left(\frac{\mu_R^2}{s_{12}}\right) - \frac{23}{6} \zeta_3 - \frac{13}{8} \pi^2 - \frac{7}{6} \pi^2 \log\left(\frac{\mu_R^2}{s_{12}}\right) \right] \frac{1}{\epsilon} \\
&\left. + \frac{511}{64} - \frac{15}{4} \zeta_3 + \frac{29}{48} \pi^2 - \frac{11}{360} \pi^4 \right\}, \tag{A.64}
\end{aligned}$$

$$\begin{aligned}
\hat{B}_0^{V,2}(1_q, 2_{\bar{q}}; 3_\ell, 4_{\bar{\ell}}) &= B_0^{V,0}(1_q, 2_{\bar{q}}; 3_\ell, 4_{\bar{\ell}}) \times \\
&\left\{ -\frac{1}{4} \frac{1}{\epsilon^3} - \left[\frac{1}{9} + \frac{1}{6} \log\left(\frac{\mu_R^2}{s_{12}}\right) \right] \frac{1}{\epsilon^2} + \left[\frac{65}{216} + \frac{5}{18} \log\left(\frac{\mu_R^2}{s_{12}}\right) + \frac{1}{24} \pi^2 \right] \frac{1}{\epsilon} \right. \\
&\left. + \frac{4085}{1296} + \frac{4}{3} \log\left(\frac{\mu_R^2}{s_{12}}\right) - \frac{1}{36} \zeta_3 + \frac{7}{72} \pi^2 \right\}. \tag{A.65}
\end{aligned}$$

The implementation of all colour levels in the codebase is found in the `B0g2Znmc.f90` and the autogenerated `autoB0g2Wnmc.f90` Fortran files.

A.10 $B_3^{V,0}$

These amplitudes rely on the results presented in ref. [85]. The left-handed quark and left-handed lepton ($q_L \ell_L$) helicity amplitudes for gluon helicities $(+++)$, $(++-)$, $(+-+)$, and

(- + +) are given respectively by

$$\mathcal{B}_3^{V,0}\left(1_q^-, 2_g^+, 3_g^+, 4_g^+, 5_{\bar{q}}^+; 6_\ell^-, 7_{\bar{\ell}}^+\right) = \langle 56 \rangle \frac{\langle 15 \rangle [71] + \langle 25 \rangle [72] + \langle 35 \rangle [73] + \langle 45 \rangle [74]}{\langle 12 \rangle \langle 23 \rangle \langle 34 \rangle \langle 45 \rangle}, \quad (\text{A.66})$$

$$\begin{aligned} \mathcal{B}_3^{V,0}\left(1_q^-, 2_g^+, 3_g^+, 4_g^-, 5_{\bar{q}}^+; 6_\ell^-, 7_{\bar{\ell}}^+\right) = & \\ & - \frac{\langle 14 \rangle}{\langle 12 \rangle \langle 23 \rangle \langle 34 \rangle} \left[\langle 46 \rangle + \langle 56 \rangle \frac{\langle 14 \rangle [51] + \langle 24 \rangle [52] + \langle 34 \rangle [53]}{s_{1234}} \right] \frac{\langle 14 \rangle [71] + \langle 24 \rangle [72] + \langle 34 \rangle [73]}{\langle 21 \rangle [52] + \langle 31 \rangle [53] + \langle 41 \rangle [54]} \\ & + [53] \frac{\langle 46 \rangle [34] + \langle 56 \rangle [35]}{\langle 32 \rangle [53] + \langle 42 \rangle [54]} \frac{[71](\langle 41 \rangle [34] + \langle 51 \rangle [35]) + [72](\langle 42 \rangle [34] + \langle 52 \rangle [35]) + [73] s_{345}}{\langle 12 \rangle [54] [43] s_{345}} \\ & + \frac{1}{\langle 23 \rangle \langle 34 \rangle} \frac{\langle 24 \rangle [52] + \langle 34 \rangle [53]}{\langle 32 \rangle [53] + \langle 42 \rangle [54]} \left[\langle 46 \rangle + \langle 56 \rangle \frac{\langle 24 \rangle [52] + \langle 34 \rangle [53]}{s_{234}} \right] \\ & \times \left[\frac{\langle 14 \rangle [71] + \langle 24 \rangle [72] + \langle 34 \rangle [73]}{\langle 21 \rangle [52] + \langle 31 \rangle [53] + \langle 41 \rangle [54]} + \frac{\langle 45 \rangle [71]}{s_{2345}} \right], \quad (\text{A.67}) \end{aligned}$$

$$\begin{aligned} \mathcal{B}_3^{V,0}\left(1_q^-, 2_g^+, 3_g^-, 4_g^+, 5_{\bar{q}}^+; 6_\ell^-, 7_{\bar{\ell}}^+\right) = & \\ & - \frac{\langle 16 \rangle (\langle 43 \rangle [14] + \langle 53 \rangle [15]) + \langle 26 \rangle (\langle 43 \rangle [24] + \langle 53 \rangle [25]) + \langle 36 \rangle (s_{345} - s_{12345})}{s_{345} \langle 13 \rangle + \langle 12 \rangle (\langle 43 \rangle [24] + \langle 53 \rangle [25])} \\ & \times \frac{\langle 13 \rangle \langle 35 \rangle^3}{\langle 12 \rangle \langle 23 \rangle \langle 34 \rangle \langle 45 \rangle} \frac{\langle 13 \rangle [71] + \langle 23 \rangle [72]}{s_{123} \langle 35 \rangle + \langle 45 \rangle (\langle 13 \rangle [41] + \langle 23 \rangle [42])} \\ & - \frac{\langle 13 \rangle \langle 56 \rangle}{s_{123} s_{1234} \langle 12 \rangle \langle 23 \rangle} \frac{(\langle 13 \rangle [41] + \langle 23 \rangle [42])^3}{\langle 21 \rangle [42] + \langle 31 \rangle [43]} \frac{\langle 15 \rangle [71] + \langle 25 \rangle [72] + \langle 35 \rangle [73] + \langle 45 \rangle [74]}{s_{123} \langle 35 \rangle + \langle 45 \rangle (\langle 13 \rangle [41] + \langle 23 \rangle [42])} \\ & + \frac{\langle 35 \rangle^3}{s_{2345}} \frac{\langle 43 \rangle [24] + \langle 53 \rangle [25]}{\langle 35 \rangle [23] + \langle 45 \rangle [24]} \frac{\langle 36 \rangle [23] + \langle 46 \rangle [24] + \langle 56 \rangle [25]}{s_{345} \langle 34 \rangle \langle 45 \rangle} \\ & \times \frac{(\langle 31 \rangle [23] + \langle 41 \rangle [24] + \langle 51 \rangle [25]) [71] + [72] s_{2345}}{s_{345} \langle 13 \rangle + \langle 12 \rangle (\langle 43 \rangle [24] + \langle 53 \rangle [25])} \\ & + \frac{\langle 56 \rangle [42]^4}{s_{234} [32] [43]} \frac{\langle 15 \rangle [71] + \langle 25 \rangle [72] + \langle 35 \rangle [73] + \langle 45 \rangle [74]}{(\langle 35 \rangle [23] + \langle 45 \rangle [24]) (\langle 21 \rangle [42] + \langle 31 \rangle [43])}, \quad (\text{A.68}) \end{aligned}$$

$$\begin{aligned} \mathcal{B}_3^{V,0}\left(1_q^-, 2_g^-, 3_g^+, 4_g^+, 5_{\bar{q}}^+; 6_\ell^-, 7_{\bar{\ell}}^+\right) = & \\ & - \frac{\langle 25 \rangle^3 [71]}{s_{2345} \langle 23 \rangle \langle 34 \rangle \langle 45 \rangle} \frac{\langle 26 \rangle [21] + \langle 36 \rangle [31] + \langle 46 \rangle [41] + \langle 56 \rangle [51]}{\langle 25 \rangle [12] + \langle 35 \rangle [13] + \langle 45 \rangle [14]} \\ & - \frac{\langle 56 \rangle [31]^3}{s_{123} \langle 45 \rangle [21] [32]} \frac{\langle 15 \rangle [71] + \langle 25 \rangle [72] + \langle 35 \rangle [73] + \langle 45 \rangle [74]}{\langle 24 \rangle [12] + \langle 34 \rangle [13]} \end{aligned}$$

$$+ \frac{\langle 56 \rangle}{s_{234}s_{1234}\langle 23 \rangle \langle 34 \rangle} \frac{\langle 15 \rangle \langle 71 \rangle + \langle 25 \rangle \langle 72 \rangle + \langle 35 \rangle \langle 73 \rangle + \langle 45 \rangle \langle 74 \rangle}{\langle 25 \rangle \langle 12 \rangle + \langle 35 \rangle \langle 13 \rangle + \langle 45 \rangle \langle 14 \rangle} \frac{(\langle 32 \rangle \langle 13 \rangle + \langle 42 \rangle \langle 14 \rangle)^3}{\langle 24 \rangle \langle 12 \rangle + \langle 34 \rangle \langle 13 \rangle}. \quad (\text{A.69})$$

Helicity amplitudes of all other gluon helicity configurations—still for left-handed quark and lepton currents—can be expressed using parity and charge conjugation transformations. Performing the operations on the amplitudes in the same order as they are listed in eqs. (A.66)–(A.69) yields

$$\mathcal{B}_3^{V,0}(1_q^-, 2_g^-, 3_g^-, 4_g^+, 5_{\bar{q}}^+, 6_\ell^-, 7_{\bar{\ell}}^+) = -\mathcal{B}_3^{V,0}(5_q^-, 4_g^+, 3_g^+, 2_g^+, 1_{\bar{q}}^+; 7_\ell^-, 6_{\bar{\ell}}^+)^*, \quad (\text{A.70})$$

$$\mathcal{B}_3^{V,0}(1_q^-, 2_g^+, 3_g^-, 4_g^-, 5_{\bar{q}}^+, 6_\ell^-, 7_{\bar{\ell}}^+) = -\mathcal{B}_3^{V,0}(5_q^-, 4_g^+, 3_g^+, 2_g^-, 1_{\bar{q}}^+; 7_\ell^-, 6_{\bar{\ell}}^+)^*, \quad (\text{A.71})$$

$$\mathcal{B}_3^{V,0}(1_q^-, 2_g^-, 3_g^+, 4_g^-, 5_{\bar{q}}^+, 6_\ell^-, 7_{\bar{\ell}}^+) = -\mathcal{B}_3^{V,0}(5_q^-, 4_g^+, 3_g^-, 2_g^+, 1_{\bar{q}}^+; 7_\ell^-, 6_{\bar{\ell}}^+)^*, \quad (\text{A.72})$$

$$\mathcal{B}_3^{V,0}(1_q^-, 2_g^-, 3_g^-, 4_g^+, 5_{\bar{q}}^+, 6_\ell^-, 7_{\bar{\ell}}^+) = -\mathcal{B}_3^{V,0}(5_q^-, 4_g^-, 3_g^+, 2_g^+, 1_{\bar{q}}^+; 7_\ell^-, 6_{\bar{\ell}}^+)^*. \quad (\text{A.73})$$

Getting the amplitudes for the other fermion helicity configurations are just a matter of exploiting their symmetry under charge conjugation as usual:

$$q_L \ell_R : \quad \mathcal{B}_3^{V,0}(1_q^-, 2_g^{h_1}, 3_g^{h_2}, 4_g^{h_3}, 5_{\bar{q}}^+, 6_\ell^+, 7_{\bar{\ell}}^-) = \mathcal{B}_3^{V,0}(1_q^-, 2_g^{h_1}, 3_g^{h_2}, 4_g^{h_3}, 5_{\bar{q}}^+, 7_\ell^-, 6_{\bar{\ell}}^+), \quad (\text{A.74})$$

$$q_R \ell_L : \quad \mathcal{B}_3^{V,0}(1_q^+, 2_g^{h_1}, 3_g^{h_2}, 4_g^{h_3}, 5_{\bar{q}}^-, 6_\ell^-, 7_{\bar{\ell}}^+) = -\mathcal{B}_3^{V,0}(5_q^-, 4_g^{h_3}, 3_g^{h_2}, 2_g^{h_1}, 1_{\bar{q}}^+; 6_\ell^-, 7_{\bar{\ell}}^+), \quad (\text{A.75})$$

$$q_R \ell_R : \quad \mathcal{B}_3^{V,0}(1_q^+, 2_g^{h_1}, 3_g^{h_2}, 4_g^{h_3}, 5_{\bar{q}}^-, 6_\ell^+, 7_{\bar{\ell}}^-) = -\mathcal{B}_3^{V,0}(5_q^-, 4_g^{h_3}, 3_g^{h_2}, 2_g^{h_1}, 1_{\bar{q}}^+; 7_\ell^-, 6_{\bar{\ell}}^+), \quad (\text{A.76})$$

for all $h_1, h_2, h_3 = \pm$ gluon helicities. The non-momentum-conserving squared amplitudes for W and Z respectively are

$$B_3^{W,0}(1_q, 2_g, 3_g, 4_g, 5_{\bar{q}'}; 6_\ell, 7_{\bar{\ell}}) = |\mathcal{P}_W(s_{67})|^2 \sum_{h_1, h_2, h_3} \left| \mathcal{B}_3^{V,0}(1_q^-, 2_g^{h_1}, 3_g^{h_2}, 4_g^{h_3}, 5_{\bar{q}'}^+; 6_\ell^-, 7_{\bar{\ell}}^+) \right|^2, \quad (\text{A.77})$$

$$B_3^{Z,0}(1_q, 2_g, 3_g, 4_g, 5_{\bar{q}}; 6_\ell, 7_{\bar{\ell}}) = |\mathcal{P}_Z(s_{67})|^2 \sum_{\substack{h_q, h_\ell \\ h_1, h_2, h_3}} \left| C_{q\ell}^{h_q h_\ell} \mathcal{B}_3^{V,0}(1_q^{h_q}, 2_g^{h_1}, 3_g^{h_2}, 4_g^{h_3}, 5_{\bar{q}}^{-h_q}; 6_\ell^{h_\ell}, 7_{\bar{\ell}}^{-h_\ell}) \right|^2. \quad (\text{A.78})$$

The subleading-colour helicity amplitudes are generated by the sum of permutations

$$\begin{aligned} \tilde{\mathcal{B}}_3^{V,0}\left(1_q^-, 2_{\bar{g}}^{h_1}, 3_{\bar{g}}^{h_2}, 4_{\bar{g}}^{h_3}, 5_{\bar{q}'}^+, 6_\ell^-, 7_\ell^+\right) &= \mathcal{B}_3^{V,0}\left(1_q^-, 2_{\bar{g}}^{h_1}, 3_{\bar{g}}^{h_2}, 4_{\bar{g}}^{h_3}, 5_{\bar{q}'}^+, 6_\ell^-, 7_\ell^+\right) \\ &+ \mathcal{B}_3^{V,0}\left(1_q^-, 3_{\bar{g}}^{h_2}, 2_{\bar{g}}^{h_1}, 4_{\bar{g}}^{h_3}, 5_{\bar{q}'}^+, 6_\ell^-, 7_\ell^+\right) + \mathcal{B}_3^{V,0}\left(1_q^-, 3_{\bar{g}}^{h_2}, 4_{\bar{g}}^{h_3}, 2_{\bar{g}}^{h_1}, 5_{\bar{q}'}^+, 6_\ell^-, 7_\ell^+\right), \end{aligned} \quad (\text{A.79})$$

and

$$\tilde{\mathcal{B}}_3^{V,0}\left(1_q^-, 2_{\bar{g}}^{h_1}, 3_{\bar{g}}^{h_2}, 4_{\bar{g}}^{h_3}, 5_{\bar{q}'}^+, 6_\ell^-, 7_\ell^+\right) = \sum_{(3,4,5)} \mathcal{B}_3^{V,0}\left(1_q^-, 2_{\bar{g}}^{h_1}, 3_{\bar{g}}^{h_2}, 4_{\bar{g}}^{h_3}, 5_{\bar{q}'}^+, 6_\ell^-, 7_\ell^+\right). \quad (\text{A.80})$$

The implementation in the codebase is found in the `B3g0Znmc.f90` and the autogenerated `autoB3g0Wnmc.f90` Fortran files.

A.11 $B_0^{\text{H},0}$

The helicity amplitudes for the left- and right-handed quark currents are simply

$$\mathcal{B}_0^{\text{H},0}\left(i_q^-, j_{\bar{q}}^+\right) = [ji], \quad (\text{A.81})$$

$$\mathcal{B}_0^{\text{H},0}\left(i_q^+, j_{\bar{q}}^-\right) = \mathcal{B}_0^{\text{H},0}\left(i_q^-, j_{\bar{q}}^+\right)^*. \quad (\text{A.82})$$

The squared amplitude—including the Higgs boson propagator—is then

$$B_0^{\text{H},0}(i_q, j_{\bar{q}}) = |\mathcal{P}_{\text{H}}(s_{ij})|^2 \sum_{h_q} \left| \mathcal{B}_0^{\text{H},0}\left(i_q^{h_q}, j_{\bar{q}}^{-h_q}\right) \right|^2. \quad (\text{A.83})$$

The implementation in the codebase is found in the `By0g0H.f90` Fortran file.

A.12 $B_1^{\text{H},0}$

The left-handed quark helicity amplitudes for both gluon helicities are given by

$$\mathcal{B}_1^{\text{H},0}\left(i_q^-, j_{\bar{g}}^+, k_{\bar{q}}^+\right) = -\frac{\langle ik \rangle^2}{\langle ij \rangle \langle jk \rangle}, \quad (\text{A.84})$$

$$\mathcal{B}_1^{\text{H},0}\left(i_q^-, j_{\bar{g}}^-, k_{\bar{q}}^+\right) = \frac{s_{ijk}}{[ij][jk]}. \quad (\text{A.85})$$

The right-handed ones are expressed via parity transformations³ as

$$\mathcal{B}_1^{\text{H},0}(i_q^+, j_g^h, k_{\bar{q}}^-) = \mathcal{B}_1^{\text{H},0}(i_q^-, j_g^{-h}, k_{\bar{q}}^+)^*. \quad (\text{A.86})$$

The squared amplitude—including the Higgs boson propagator—is then

$$B_1^{\text{H},0}(i_q, j_g, k_{\bar{q}}) = |\mathcal{P}_{\text{H}}(s_{ijk})|^2 \sum_{h, h_q} \left| \mathcal{B}_1^{\text{H},0}(i_q^{h_q}, j_g^h, k_{\bar{q}}^{-h_q}) \right|^2. \quad (\text{A.87})$$

The implementation in the codebase is found in the `By1g0H.f90` Fortran file.

A.13 $B_0^{\text{H},1}$

The one-loop amplitude is expressed with the tree-level one of Section A.11 as

$$B_0^{\text{H},1}(i_q, j_{\bar{q}}) = B_0^{\text{H},0}(i_q, j_{\bar{q}}) \left\{ -\frac{1}{\epsilon^2} - \left[\frac{3}{2} + \ln\left(\frac{\mu_{\text{R}}^2}{s_{ij}}\right) \right] \frac{1}{\epsilon} - 1 - \frac{1}{2} \ln^2\left(\frac{\mu_{\text{R}}^2}{s_{ij}}\right) + \frac{7}{12} \pi^2 \right\}. \quad (\text{A.88})$$

The implementation in the codebase is found in the `By0g1H.f90` Fortran file.

A.14 $C_0^{\text{H},0}$

The helicity amplitude when both quark currents are right-handed ($q_{\text{R}}Q_{\text{R}}$) and the Higgs boson couples to the outer q ($i_q l_{\bar{q}}$) quark line is given by

$$C_0^{\text{H},0}(i_q^+, j_Q^+, k_{\bar{Q}}^-, l_{\bar{q}}^-) = \frac{1}{s_{jk}} \left[[j\bar{i}] \frac{\langle ki \rangle [i\bar{l}] + \langle kj \rangle [j\bar{l}]}{s_{ijk}} + [j\bar{l}] \frac{\langle kl \rangle [l\bar{i}] + \langle kj \rangle [j\bar{i}]}{s_{ljk}} \right]. \quad (\text{A.89})$$

All other helicity configurations with the vector boson still only coupling to the outer quark line can be expressed via charge conjugation⁴ and parity transformations according to

$$q_{\text{R}}Q_{\text{L}} : \quad C_0^{\text{H},0}(i_q^+, j_Q^-, k_Q^+, l_{\bar{q}}^-) = C_0^{\text{H},0}(i_q^+, k_Q^+, j_Q^-, l_{\bar{q}}^-), \quad (\text{A.90})$$

$$q_{\text{L}}Q_{\text{L}} : \quad C_0^{\text{H},0}(i_q^-, j_Q^-, k_Q^+, l_{\bar{q}}^+) = C_0^{\text{H},0}(i_q^+, j_Q^+, k_Q^-, l_{\bar{q}}^-)^*, \quad (\text{A.91})$$

³Charge conjugation of quark lines directly coupling to the Higgs boson is not useful because those currents do not exhibit “line-reversal” symmetry.

⁴The inner quark line Q ($j_Q k_{\bar{Q}}$) that does not couple to the Higgs boson exhibits line-reversal symmetry.

$$q_{\text{L}}Q_{\text{R}} : \quad C_0^{\text{H},0}(i_q^-, j_Q^+, k_{\bar{Q}}^-, l_{\bar{q}}^+) = C_0^{\text{H},0}(i_q^+, k_Q^+, j_{\bar{Q}}^-, l_{\bar{q}}^-)^* . \quad (\text{A.92})$$

The squared amplitude—including the Higgs boson propagator—is then

$$C_0^{\text{H},0}(i_q, j_Q, k_{\bar{Q}}, l_{\bar{q}}) = |\mathcal{P}_{\text{H}}(s_{ijkl})|^2 \sum_{h_q, h_Q} \left| C_0^{\text{H},0}(i_q^{h_q}, j_Q^{h_Q}, k_{\bar{Q}}^{-h_Q}, l_{\bar{q}}^{-h_q}) \right|^2 . \quad (\text{A.93})$$

This amplitude was also calculated and implemented into the codebase by Andrew Lifson as part of his semester project [55].⁵ It is found in the Fortran file `Cy0g0H.f90`.

A.15 $D_0^{\text{H},0}$

The subleading-colour interference terms for identical quarks are assembled from the helicity amplitudes of Section A.14 in the following way:

$$\begin{aligned} D_0^{\text{H},0}(j_q, j_Q, k_{\bar{Q}}, l_{\bar{q}}) &= -|\mathcal{P}_{\text{Z}}(s_{ijkl})|^2 \times \\ &\sum_{h_q} 2 \operatorname{Re} \left\{ \left[C_0^{\text{H},0}(i_q^{h_q}, j_q^{h_q}, k_{\bar{q}}^{-h_q}, l_{\bar{q}}^{-h_q}) + C_0^{\text{H},0}(j_q^{h_q}, i_q^{h_q}, l_{\bar{q}}^{-h_q}, k_{\bar{q}}^{-h_q}) \right] \right. \\ &\quad \left. \times \left[C_0^{\text{H},0}(i_q^{h_q}, j_q^{h_q}, l_{\bar{q}}^{-h_q}, k_{\bar{q}}^{-h_q}) + C_0^{\text{H},0}(j_q^{h_q}, i_q^{h_q}, k_{\bar{q}}^{-h_q}, l_{\bar{q}}^{-h_q}) \right]^* \right\} . \end{aligned} \quad (\text{A.94})$$

The negative sign preceding the amplitude is due to NNLOJET convention of having one in front of subleading-colour pieces. This amplitude was also calculated and implemented into the codebase by Andrew Lifson as part of his semester project [55]. It is found in the Fortran file `Dy0g0H.f90`.

A.16 $B_1^{\text{H},1}$

These amplitudes have been created from the result presented in eq. (A.6) of ref. [37]. To import it into the NNLOJET framework, colour-level separation had to be carried out. The resulting leading-colour, subleading-colour, and n_{F} -proportional pieces are expressed as

$$B_1^{\text{H},1}(i_q, j_g, k_{\bar{q}}) = \frac{y_{ij} + y_{jk}}{y_{ij}y_{jk}} |\mathcal{P}_{\text{H}}(s_{ijk})|^2 + B_1^{\text{H},0}(i_q, j_g, k_{\bar{q}}) \times$$

⁵This is the reason why conventions slightly differ from my implementations.

$$\begin{aligned}
& \left\{ -\frac{2}{\epsilon^2} + \left[-\frac{10}{3} + \ln(y_{ij}) + \ln(y_{jk}) + 2 \ln\left(\frac{s_{ijk}}{\mu_{\text{R}}^2}\right) \right] \frac{1}{\epsilon} \right. \\
& - 1 + \frac{7}{6} \pi^2 - \ln^2\left(\frac{s_{ijk}}{\mu_{\text{R}}^2}\right) - \frac{1}{2} [\ln^2(y_{ij}) + \ln^2(y_{jk})] \\
& \left. - \ln\left(\frac{s_{ijk}}{\mu_{\text{R}}^2}\right) [\ln(y_{ij}) + \ln(y_{jk})] - R(y_{ij}, y_{jk}) \right\}, \tag{A.95}
\end{aligned}$$

$$\begin{aligned}
\tilde{B}_1^{\text{H},1}(i_q, j_g, k_{\bar{q}}) &= -\frac{y_{ij} + y_{jk}}{y_{ij} y_{jk}} |\mathcal{P}_{\text{H}}(s_{ijk})|^2 + B_1^{\text{H},0}(i_q, j_g, k_{\bar{q}}) \times \\
& \left\{ -\frac{1}{\epsilon^2} + \left[-\frac{3}{2} + \ln(y_{ik}) + \ln\left(\frac{s_{ijk}}{\mu_{\text{R}}^2}\right) \right] \frac{1}{\epsilon} \right. \\
& - 1 + \frac{7}{12} \pi^2 - \frac{1}{2} \ln^2\left(\frac{s_{ijk}}{\mu_{\text{R}}^2}\right) - \frac{1}{2} \ln^2(y_{ik}) \\
& \left. - \ln\left(\frac{s_{ijk}}{\mu_{\text{R}}^2}\right) \ln(y_{ik}) - R(y_{ik}, y_{ij}) - R(y_{ik}, y_{jk}) \right\}, \tag{A.96}
\end{aligned}$$

$$\hat{B}_1^{\text{H},1}(i_q, j_g, k_{\bar{q}}) = \frac{1}{3} \frac{1}{\epsilon} B_1^{\text{H},0}(i_q, j_g, k_{\bar{q}}), \tag{A.97}$$

with definitions

$$y_{ij} = \frac{s_{ij}}{s_{ijk}}, \quad y_{jk} = \frac{s_{jk}}{s_{ijk}}, \quad \text{and} \quad y_{ik} = \frac{s_{ik}}{s_{ijk}}, \tag{A.98}$$

along with

$$R(x_1, x_2) = \text{Li}_2(1 - x_1) + \text{Li}_2(1 - x_2) + \ln(x_1) \ln(x_2) - \frac{\pi^2}{6}. \tag{A.99}$$

The implementation in the codebase is found in the `By1g1H.f90` Fortran file.

A.17 $B_0^{\text{H},2}$

These amplitudes have been created from results presented in eqs. (A.3)–(A.4) of ref. [37]. To import it into the NNLOJET framework, colour-level separation and Catani pole subtraction had to be carried out. The resulting leading-colour, subleading-colour, and n_{F} -proportional

pieces are expressed proportional to the tree-level amplitude as

$$\begin{aligned}
B_0^{\text{H},2}(i_q, j_{\bar{q}}) &= B_0^{\text{H},0}(i_q, j_{\bar{q}}) \times \\
&\left\{ \frac{1}{2} \frac{1}{\epsilon^4} + \left[\frac{28}{8} + \ln\left(\frac{\mu_{\text{R}}^2}{s_{ij}}\right) \right] \frac{1}{\epsilon^3} + \left[\frac{185}{72} + \frac{29}{12} \ln\left(\frac{\mu_{\text{R}}^2}{s_{ij}}\right) + \ln^2\left(\frac{\mu_{\text{R}}^2}{s_{ij}}\right) - \frac{13}{24} \pi^2 \right] \frac{1}{\epsilon^2} \right. \\
&+ \left[\frac{1021}{864} + \frac{5}{36} \ln\left(\frac{\mu_{\text{R}}^2}{s_{ij}}\right) + \frac{3}{4} \ln^2\left(\frac{\mu_{\text{R}}^2}{s_{ij}}\right) + \frac{2}{3} \ln^3\left(\frac{\mu_{\text{R}}^2}{s_{ij}}\right) - \frac{7}{12} \zeta_3 - \frac{47}{48} \pi^2 - \frac{13}{12} \pi^2 \ln\left(\frac{\mu_{\text{R}}^2}{s_{ij}}\right) \right] \frac{1}{\epsilon} \\
&\left. - \frac{143}{324} + \frac{43}{48} \ln\left(\frac{\mu_{\text{R}}^2}{s_{ij}}\right) + \frac{5}{2} \ln^2\left(\frac{\mu_{\text{R}}^2}{s_{ij}}\right) + \frac{65}{72} \zeta_3 + \frac{49}{1440} \pi^4 - \frac{179}{144} \pi^2 \right\}, \tag{A.100}
\end{aligned}$$

$$\begin{aligned}
\tilde{B}_0^{\text{H},2}(i_q, j_{\bar{q}}) &= B_0^{\text{H},0}(i_q, j_{\bar{q}}) \times \\
&\left\{ \frac{1}{2} \frac{1}{\epsilon^4} + \left[\frac{3}{2} + \ln\left(\frac{\mu_{\text{R}}^2}{s_{ij}}\right) \right] \frac{1}{\epsilon^3} + \left[\frac{17}{8} + \frac{3}{2} \ln\left(\frac{\mu_{\text{R}}^2}{s_{ij}}\right) + \ln^2\left(\frac{\mu_{\text{R}}^2}{s_{ij}}\right) - \frac{7}{12} \pi^2 \right] \frac{1}{\epsilon^2} \right. \\
&+ \left[\frac{109}{32} + 2 \ln\left(\frac{\mu_{\text{R}}^2}{s_{ij}}\right) + \frac{3}{4} \ln^2\left(\frac{\mu_{\text{R}}^2}{s_{ij}}\right) + \frac{2}{3} \ln^3\left(\frac{\mu_{\text{R}}^2}{s_{ij}}\right) - \frac{23}{6} \zeta_3 - \frac{3}{4} \pi^2 - \frac{7}{6} \pi^2 \ln\left(\frac{\mu_{\text{R}}^2}{s_{ij}}\right) \right] \frac{1}{\epsilon} \\
&\left. + 1 - \frac{21}{16} \ln\left(\frac{\mu_{\text{R}}^2}{s_{ij}}\right) + \frac{9}{8} \ln^2\left(\frac{\mu_{\text{R}}^2}{s_{ij}}\right) - \frac{15}{4} \zeta_3 - \frac{11}{360} \pi^4 + \frac{1}{3} \pi^2 \right\}, \tag{A.101}
\end{aligned}$$

$$\begin{aligned}
\hat{B}_0^{\text{H},2}(i_q, j_{\bar{q}}) &= B_0^{\text{H},0}(i_q, j_{\bar{q}}) \left\{ \frac{1}{4} \frac{1}{\epsilon^3} - \left[\frac{1}{9} + \frac{1}{6} \ln\left(\frac{\mu_{\text{R}}^2}{s_{ij}}\right) \right] \frac{1}{\epsilon^2} + \left[\frac{65}{216} + \frac{5}{18} \ln\left(\frac{\mu_{\text{R}}^2}{s_{ij}}\right) + \frac{1}{24} \pi^2 \right] \frac{1}{\epsilon} \right. \\
&\left. + \frac{50}{81} - \frac{1}{12} \ln\left(\frac{\mu_{\text{R}}^2}{s_{ij}}\right) - \frac{1}{4} \ln^2\left(\frac{\mu_{\text{R}}^2}{s_{ij}}\right) - \frac{1}{36} \zeta_3 + \frac{19}{72} \pi^2 \right\}. \tag{A.102}
\end{aligned}$$

The implementation in the codebase is found in the `By0g2H.f90` Fortran file.

Appendix B

Effects of Even-Tag Exclusion

The clustering outcome of the algorithm can be altered according to the criterion used to define the flavour of (pseudo)jets. Our results have been presented with the criterion that the flavour of (pseudo)jets is assigned as the net flavour of its constituents modulo two, which we believe is more motivated from an experimental point of view as discussed in Section 3.2. Such a variant of flavour- k_t was also first proposed in ref. [78].

To investigate the impact of this “Even-tag exclusion” on the fixed-order predictions, we have recomputed the fiducial cross sections and distributions reported in Section 1.7.2 and 1.7.4 without the additional modulo-two criterion—we refer to these results as “Regular flavour- k_t ”. This impact of the choice of this criterion is visualized in the case of the W^+H process in Figure B.1 for the $p_{\perp,b}$, $p_{\perp,bb}$, and ΔR_{bb} distributions. In that figure, the ratio of the two NNLO central values are divided bin-by-bin, demonstrating that this choice has no overall effect on the shape of these distributions. The small variation between bins can be

pp \rightarrow W ⁺ H	σ_{NNLO} [fb]
Even-tag exclusion	20.6828 ± 0.0055
Regular flavour- k_t	20.7093 ± 0.0063
Ratio	99.87%

Table B.1: Fiducial cross sections for W^+H at NNLO for both the original flavour- k_t algorithm and our modified version where all even-tagged jets are excluded from the list of b-jets. The values are shown only for the central scales and their error represents the statistical uncertainty of the Monte Carlo integrations.

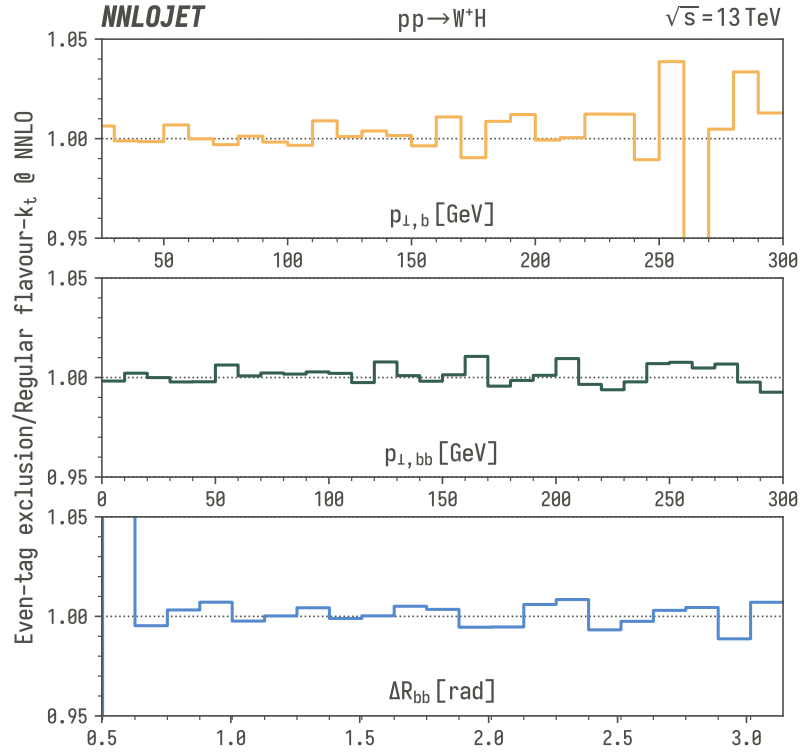


Figure B.1: Bin-by-bin ratio between distributions that were calculated with the even-tag-excluded and the original variants of the flavour- k_t algorithm for three observables of W^+H : the $p_{\perp,b}$, $p_{\perp,bb}$, and ΔR_{bb} distributions at NNLO for central scale values.

attributed to statistical fluctuations. This unnoticeable effect between the results obtained using either variants of the flavour- k_t algorithm is also confirmed by the fiducial cross sections reported in Table B.1, where the results are consistent within statistical uncertainties.

This supports our claim that no significant portion of the events are discarded by switching to the even-tag-excluded version of flavour- k_t in our fixed-order predictions.

Bibliography

- [1] Gauld, R. and Gehrmann-De Ridder, A. and Glover, E.W.N. and Huss, A. and Majer, I. “Associated production of a Higgs boson decaying into bottom quarks and a weak vector boson decaying leptonically at NNLO in QCD.” *JHEP* 10 (2019), p. 002. DOI: [10.1007/JHEP10\(2019\)002](https://doi.org/10.1007/JHEP10(2019)002). arXiv: [1907.05836](https://arxiv.org/abs/1907.05836) [hep-ph].
- [2] Gauld, R. and Gehrmann-De Ridder, A. and Glover, E.W.N. and Huss, A. and Majer, I. “NNLO predictions for WH plus jet production at LHC (in preparation).” 2020.
- [3] Gauld, R. and Gehrmann-De Ridder, A. and Glover, E.W. N. and Huss, A. and Majer, I. “Predictions for Z-boson production in association with a b-jet at $\mathcal{O}(\alpha_s^3)$ ” (May 2020). arXiv: [2005.03016](https://arxiv.org/abs/2005.03016) [hep-ph].
- [4] S.F. Novaes. “Standard model: An Introduction.” *10th Jorge Andre Swieca Summer School: Particle and Fields*. Jan. 1999, pp. 5–102. arXiv: [hep-ph/0001283](https://arxiv.org/abs/hep-ph/0001283).
- [5] Hyun Min Lee. “Lectures on Physics Beyond the Standard Model.” July 2019. arXiv: [1907.12409](https://arxiv.org/abs/1907.12409) [hep-ph].
- [6] Andrey Grozin. “Quantum Chromodynamics.” *11th International Baikal Summer School on Physics of Elementary Particles and Astrophysics*. May 2012. arXiv: [1205.1815](https://arxiv.org/abs/1205.1815) [hep-ph].
- [7] John C. Collins, Davison E. Soper, and George F. Sterman. “Factorization of Hard Processes in QCD.” Vol. 5. 1989, pp. 1–91. DOI: [10.1142/9789814503266_0001](https://doi.org/10.1142/9789814503266_0001). arXiv: [hep-ph/0409313](https://arxiv.org/abs/hep-ph/0409313).
- [8] A. Gehrmann-De Ridder, T. Gehrmann, and E. W. Nigel Glover. “Antenna subtraction at NNLO.” *JHEP* 09 (2005), p. 056. DOI: [10.1088/1126-6708/2005/09/056](https://doi.org/10.1088/1126-6708/2005/09/056). arXiv: [hep-ph/0505111](https://arxiv.org/abs/hep-ph/0505111) [hep-ph].
- [9] A. Gehrmann-De Ridder, T. Gehrmann, and E. W. Nigel Glover. “Gluon-gluon antenna functions from Higgs boson decay.” *Phys. Lett. B* 612 (2005), pp. 49–60. DOI: [10.1016/j.physletb.2005.03.003](https://doi.org/10.1016/j.physletb.2005.03.003). arXiv: [hep-ph/0502110](https://arxiv.org/abs/hep-ph/0502110) [hep-ph].

- [10] A. Gehrmann-De Ridder, T. Gehrmann, and E. W. Nigel Glover. “Quark-gluon antenna functions from neutralino decay.” *Phys. Lett.* B612 (2005), pp. 36–48. DOI: [10.1016/j.physletb.2005.02.039](https://doi.org/10.1016/j.physletb.2005.02.039). arXiv: [hep-ph/0501291](https://arxiv.org/abs/hep-ph/0501291) [hep-ph].
- [11] A. Daleo, T. Gehrmann, and D. Maitre. “Antenna subtraction with hadronic initial states.” *JHEP* 04 (2007), p. 016. DOI: [10.1088/1126-6708/2007/04/016](https://doi.org/10.1088/1126-6708/2007/04/016). arXiv: [hep-ph/0612257](https://arxiv.org/abs/hep-ph/0612257) [hep-ph].
- [12] Alejandro Daleo, Aude Gehrmann-De Ridder, Thomas Gehrmann, and Gionata Luisoni. “Antenna subtraction at NNLO with hadronic initial states: initial-final configurations.” *JHEP* 01 (2010), p. 118. DOI: [10.1007/JHEP01\(2010\)118](https://doi.org/10.1007/JHEP01(2010)118). arXiv: [0912.0374](https://arxiv.org/abs/0912.0374) [hep-ph].
- [13] Radja Boughezal, Aude Gehrmann-De Ridder, and Mathias Ritzmann. “Antenna subtraction at NNLO with hadronic initial states: double real radiation for initial-initial configurations with two quark flavours.” *JHEP* 02 (2011), p. 098. DOI: [10.1007/JHEP02\(2011\)098](https://doi.org/10.1007/JHEP02(2011)098). arXiv: [1011.6631](https://arxiv.org/abs/1011.6631) [hep-ph].
- [14] Thomas Gehrmann and Pier Francesco Monni. “Antenna subtraction at NNLO with hadronic initial states: real-virtual initial-initial configurations.” *JHEP* 12 (2011), p. 049. DOI: [10.1007/JHEP12\(2011\)049](https://doi.org/10.1007/JHEP12(2011)049). arXiv: [1107.4037](https://arxiv.org/abs/1107.4037) [hep-ph].
- [15] Aude Gehrmann-De Ridder, Thomas Gehrmann, and Mathias Ritzmann. “Antenna subtraction at NNLO with hadronic initial states: double real initial-initial configurations.” *JHEP* 10 (2012), p. 047. DOI: [10.1007/JHEP10\(2012\)047](https://doi.org/10.1007/JHEP10(2012)047). arXiv: [1207.5779](https://arxiv.org/abs/1207.5779) [hep-ph].
- [16] James Currie, E. W. N. Glover, and Steven Wells. “Infrared Structure at NNLO Using Antenna Subtraction.” *JHEP* 04 (2013), p. 066. DOI: [10.1007/JHEP04\(2013\)066](https://doi.org/10.1007/JHEP04(2013)066). arXiv: [1301.4693](https://arxiv.org/abs/1301.4693) [hep-ph].
- [17] Georges Aad et al. “Observation of a new particle in the search for the Standard Model Higgs boson with the ATLAS detector at the LHC.” *Phys. Lett.* B716 (2012), pp. 1–29. DOI: [10.1016/j.physletb.2012.08.020](https://doi.org/10.1016/j.physletb.2012.08.020). arXiv: [1207.7214](https://arxiv.org/abs/1207.7214) [hep-ex].
- [18] Serguei Chatrchyan et al. “Observation of a new boson at a mass of 125 GeV with the CMS experiment at the LHC.” *Phys. Lett.* B716 (2012), pp. 30–61. DOI: [10.1016/j.physletb.2012.08.021](https://doi.org/10.1016/j.physletb.2012.08.021). arXiv: [1207.7235](https://arxiv.org/abs/1207.7235) [hep-ex].
- [19] Georges Aad et al. “Search for Invisible Decays of a Higgs Boson Produced in Association with a Z Boson in ATLAS.” *Phys. Rev. Lett.* 112 (2014), p. 201802. DOI: [10.1103/PhysRevLett.112.201802](https://doi.org/10.1103/PhysRevLett.112.201802). arXiv: [1402.3244](https://arxiv.org/abs/1402.3244) [hep-ex].

-
- [20] Georges Aad et al. “Search for the Standard Model Higgs boson produced in association with a vector boson and decaying to a b -quark pair with the ATLAS detector.” *Phys. Lett.* B718 (2012), pp. 369–390. DOI: [10.1016/j.physletb.2012.10.061](https://doi.org/10.1016/j.physletb.2012.10.061). arXiv: [1207.0210](https://arxiv.org/abs/1207.0210) [hep-ex].
- [21] Serguei Chatrchyan et al. “Search for the standard model Higgs boson produced in association with a W or a Z boson and decaying to bottom quarks.” *Phys. Rev.* D89.1 (2014), p. 012003. DOI: [10.1103/PhysRevD.89.012003](https://doi.org/10.1103/PhysRevD.89.012003). arXiv: [1310.3687](https://arxiv.org/abs/1310.3687) [hep-ex].
- [22] Morad Aaboud et al. “Observation of $H \rightarrow b\bar{b}$ decays and VH production with the ATLAS detector.” *Phys. Lett.* B786 (2018), pp. 59–86. DOI: [10.1016/j.physletb.2018.09.013](https://doi.org/10.1016/j.physletb.2018.09.013). arXiv: [1808.08238](https://arxiv.org/abs/1808.08238) [hep-ex].
- [23] A. M. Sirunyan et al. “Observation of Higgs boson decay to bottom quarks.” *Phys. Rev. Lett.* 121.12 (2018), p. 121801. DOI: [10.1103/PhysRevLett.121.121801](https://doi.org/10.1103/PhysRevLett.121.121801). arXiv: [1808.08242](https://arxiv.org/abs/1808.08242) [hep-ex].
- [24] Morad Aaboud et al. “Measurement of VH , $H \rightarrow b\bar{b}$ production as a function of the vector-boson transverse momentum in 13 TeV pp collisions with the ATLAS detector.” *JHEP* 05 (2019), p. 141. DOI: [10.1007/JHEP05\(2019\)141](https://doi.org/10.1007/JHEP05(2019)141). arXiv: [1903.04618](https://arxiv.org/abs/1903.04618) [hep-ex].
- [25] Georges Aad et al. “Measurements of WH and ZH production in the $H \rightarrow b\bar{b}$ decay channel in pp collisions at 13 TeV with the ATLAS detector” (July 2020). arXiv: [2007.02873](https://arxiv.org/abs/2007.02873) [hep-ex].
- [26] Oliver Brein, Robert V. Harlander, and Tom J. E. Zirke. “vh@nnlo - Higgs Strahlung at hadron colliders.” *Comput. Phys. Commun.* 184 (2013), pp. 998–1003. DOI: [10.1016/j.cpc.2012.11.002](https://doi.org/10.1016/j.cpc.2012.11.002). arXiv: [1210.5347](https://arxiv.org/abs/1210.5347) [hep-ph].
- [27] Robert V. Harlander and William B. Kilgore. “Next-to-next-to-leading order Higgs production at hadron colliders.” *Phys. Rev. Lett.* 88 (2002), p. 201801. DOI: [10.1103/PhysRevLett.88.201801](https://doi.org/10.1103/PhysRevLett.88.201801). arXiv: [hep-ph/0201206](https://arxiv.org/abs/hep-ph/0201206) [hep-ph].
- [28] Oliver Brein, Robert Harlander, Marius Wiesemann, and Tom Zirke. “Top-Quark Mediated Effects in Hadronic Higgs-Strahlung.” *Eur. Phys. J.* C72 (2012), p. 1868. DOI: [10.1140/epjc/s10052-012-1868-6](https://doi.org/10.1140/epjc/s10052-012-1868-6). arXiv: [1111.0761](https://arxiv.org/abs/1111.0761) [hep-ph].
- [29] M. L. Ciccolini, S. Dittmaier, and M. Kramer. “Electroweak radiative corrections to associated WH and ZH production at hadron colliders.” *Phys. Rev.* D68 (2003), p. 073003. DOI: [10.1103/PhysRevD.68.073003](https://doi.org/10.1103/PhysRevD.68.073003). arXiv: [hep-ph/0306234](https://arxiv.org/abs/hep-ph/0306234) [hep-ph].

- [30] Ansgar Denner, Stefan Dittmaier, Stefan Kallweit, and Alexander Muck. “Electroweak corrections to Higgs-strahlung off W/Z bosons at the Tevatron and the LHC with HAWK.” *JHEP* 03 (2012), p. 075. DOI: [10.1007/JHEP03\(2012\)075](https://doi.org/10.1007/JHEP03(2012)075). arXiv: [1112.5142](https://arxiv.org/abs/1112.5142) [hep-ph].
- [31] Giancarlo Ferrera, Massimiliano Grazzini, and Francesco Tramontano. “Associated ZH production at hadron colliders: the fully differential NNLO QCD calculation.” *Phys. Lett. B* 740 (2015), pp. 51–55. DOI: [10.1016/j.physletb.2014.11.040](https://doi.org/10.1016/j.physletb.2014.11.040). arXiv: [1407.4747](https://arxiv.org/abs/1407.4747) [hep-ph].
- [32] Giancarlo Ferrera, Massimiliano Grazzini, and Francesco Tramontano. “Associated WH production at hadron colliders: a fully exclusive QCD calculation at NNLO.” *Phys. Rev. Lett.* 107 (2011), p. 152003. DOI: [10.1103/PhysRevLett.107.152003](https://doi.org/10.1103/PhysRevLett.107.152003). arXiv: [1107.1164](https://arxiv.org/abs/1107.1164) [hep-ph].
- [33] John M. Campbell, R. Keith Ellis, and Ciaran Williams. “Associated production of a Higgs boson at NNLO.” *JHEP* 06 (2016), p. 179. DOI: [10.1007/JHEP06\(2016\)179](https://doi.org/10.1007/JHEP06(2016)179). arXiv: [1601.00658](https://arxiv.org/abs/1601.00658) [hep-ph].
- [34] Giancarlo Ferrera, Gábor Somogyi, and Francesco Tramontano. “Associated production of a Higgs boson decaying into bottom quarks at the LHC in full NNLO QCD.” *Phys. Lett. B* 780 (2018), pp. 346–351. DOI: [10.1016/j.physletb.2018.03.021](https://doi.org/10.1016/j.physletb.2018.03.021). arXiv: [1705.10304](https://arxiv.org/abs/1705.10304) [hep-ph].
- [35] Fabrizio Caola, Gionata Luisoni, Kirill Melnikov, and Raoul Röntsch. “NNLO QCD corrections to associated WH production and $H \rightarrow b\bar{b}$ decay.” *Phys. Rev. D* 97.7 (2018), p. 074022. DOI: [10.1103/PhysRevD.97.074022](https://doi.org/10.1103/PhysRevD.97.074022). arXiv: [1712.06954](https://arxiv.org/abs/1712.06954) [hep-ph].
- [36] Charalampos Anastasiou, Franz Herzog, and Achilleas Lazopoulos. “The fully differential decay rate of a Higgs boson to bottom-quarks at NNLO in QCD.” *JHEP* 03 (2012), p. 035. DOI: [10.1007/JHEP03\(2012\)035](https://doi.org/10.1007/JHEP03(2012)035). arXiv: [1110.2368](https://arxiv.org/abs/1110.2368) [hep-ph].
- [37] Vittorio Del Duca, Claude Duhr, Gábor Somogyi, Francesco Tramontano, and Zoltán Trócsányi. “Higgs boson decay into b-quarks at NNLO accuracy.” *JHEP* 04 (2015), p. 036. DOI: [10.1007/JHEP04\(2015\)036](https://doi.org/10.1007/JHEP04(2015)036). arXiv: [1501.07226](https://arxiv.org/abs/1501.07226) [hep-ph].
- [38] Roberto Mondini, Matthew Schiavi, and Ciaran Williams. “N³LO predictions for the decay of the Higgs boson to bottom quarks” (2019). arXiv: [1904.08960](https://arxiv.org/abs/1904.08960) [hep-ph].
- [39] Werner Bernreuther, Long Chen, and Zong-Guo Si. “Differential decay rates of CP-even and CP-odd Higgs bosons to top and bottom quarks at NNLO QCD.” *JHEP* 07 (2018), p. 159. DOI: [10.1007/JHEP07\(2018\)159](https://doi.org/10.1007/JHEP07(2018)159). arXiv: [1805.06658](https://arxiv.org/abs/1805.06658) [hep-ph].

-
- [40] Keith Hamilton, Paolo Nason, Carlo Oleari, and Giulia Zanderighi. “Merging H/W/Z + 0 and 1 jet at NLO with no merging scale: a path to parton shower + NNLO matching.” *JHEP* 05 (2013), p. 082. DOI: [10.1007/JHEP05\(2013\)082](https://doi.org/10.1007/JHEP05(2013)082). arXiv: [1212.4504](https://arxiv.org/abs/1212.4504) [hep-ph].
- [41] Gionata Luisoni, Paolo Nason, Carlo Oleari, and Francesco Tramontano. “ HW^\pm/HZ + 0 and 1 jet at NLO with the POWHEG BOX interfaced to GoSam and their merging within MiNLO.” *JHEP* 10 (2013), p. 083. DOI: [10.1007/JHEP10\(2013\)083](https://doi.org/10.1007/JHEP10(2013)083). arXiv: [1306.2542](https://arxiv.org/abs/1306.2542) [hep-ph].
- [42] William Astill, Wojciech Bizoń, Emanuele Re, and Giulia Zanderighi. “NNLOPS accurate associated HZ production with $H \rightarrow b\bar{b}$ decay at NLO.” *JHEP* 11 (2018), p. 157. DOI: [10.1007/JHEP11\(2018\)157](https://doi.org/10.1007/JHEP11(2018)157). arXiv: [1804.08141](https://arxiv.org/abs/1804.08141) [hep-ph].
- [43] Andrea Banfi, Gavin P. Salam, and Giulia Zanderighi. “Infrared safe definition of jet flavor.” *Eur. Phys. J. C* 47 (2006), pp. 113–124. DOI: [10.1140/epjc/s2006-02552-4](https://doi.org/10.1140/epjc/s2006-02552-4). arXiv: [hep-ph/0601139](https://arxiv.org/abs/hep-ph/0601139) [hep-ph].
- [44] Stefano Catani and Massimiliano Grazzini. “An NNLO subtraction formalism in hadron collisions and its application to Higgs boson production at the LHC.” *Phys. Rev. Lett.* 98 (2007), p. 222002. DOI: [10.1103/PhysRevLett.98.222002](https://doi.org/10.1103/PhysRevLett.98.222002). arXiv: [hep-ph/0703012](https://arxiv.org/abs/hep-ph/0703012) [hep-ph].
- [45] Vittorio Del Duca, Claude Duhr, Adam Kardos, Gábor Somogyi, Zoltán Szőr, Zoltán Trócsányi, and Zoltán Tulipánt. “Jet production in the CoLoRFulNNLO method: event shapes in electron-positron collisions.” *Phys. Rev. D* 94.7 (2016), p. 074019. DOI: [10.1103/PhysRevD.94.074019](https://doi.org/10.1103/PhysRevD.94.074019). arXiv: [1606.03453](https://arxiv.org/abs/1606.03453) [hep-ph].
- [46] Fabrizio Caola, Kirill Melnikov, and Raoul Röntsch. “Nested soft-collinear subtractions in NNLO QCD computations.” *Eur. Phys. J. C* 77.4 (2017), p. 248. DOI: [10.1140/epjc/s10052-017-4774-0](https://doi.org/10.1140/epjc/s10052-017-4774-0). arXiv: [1702.01352](https://arxiv.org/abs/1702.01352) [hep-ph].
- [47] Fabrizio Caola, Kirill Melnikov, and Raoul Röntsch. “Analytic results for decays of color singlets to gg and $q\bar{q}$ final states at NNLO QCD with the nested soft-collinear subtraction scheme” (2019). arXiv: [1907.05398](https://arxiv.org/abs/1907.05398) [hep-ph].
- [48] M. Czakon and D. Heymes. “Four-dimensional formulation of the sector-improved residue subtraction scheme.” *Nucl. Phys. B* 890 (2014), pp. 152–227. DOI: [10.1016/j.nuclphysb.2014.11.006](https://doi.org/10.1016/j.nuclphysb.2014.11.006). arXiv: [1408.2500](https://arxiv.org/abs/1408.2500) [hep-ph].
- [49] James Currie, Aude Gehrmann-De Ridder, Thomas Gehrmann, Nigel Glover, Alexander Huss, and Joao Pires. “Jet cross sections at the LHC with NNLOJET.” *PoS LL2018* (2018), p. 001. DOI: [10.22323/1.303.0001](https://doi.org/10.22323/1.303.0001). arXiv: [1807.06057](https://arxiv.org/abs/1807.06057) [hep-ph].

- [50] J. Alwall, R. Frederix, S. Frixione, V. Hirschi, F. Maltoni, O. Mattelaer, H. -S. Shao, T. Stelzer, P. Torrielli, and M. Zaro. “The automated computation of tree-level and next-to-leading order differential cross sections, and their matching to parton shower simulations.” *JHEP* 07 (2014), p. 079. DOI: [10.1007/JHEP07\(2014\)079](https://doi.org/10.1007/JHEP07(2014)079). arXiv: [1405.0301](https://arxiv.org/abs/1405.0301) [hep-ph].
- [51] Radja Boughezal, John M. Campbell, R. Keith Ellis, Christfried Focke, Walter Giele, Xiaohui Liu, Frank Petriello, and Ciaran Williams. “Color singlet production at NNLO in MCFM.” *Eur. Phys. J. C* 77.1 (2017), p. 7. DOI: [10.1140/epjc/s10052-016-4558-y](https://doi.org/10.1140/epjc/s10052-016-4558-y). arXiv: [1605.08011](https://arxiv.org/abs/1605.08011) [hep-ph].
- [52] Fabio Cascioli, Philipp Maierhofer, and Stefano Pozzorini. “Scattering Amplitudes with Open Loops.” *Phys. Rev. Lett.* 108 (2012), p. 111601. DOI: [10.1103/PhysRevLett.108.111601](https://doi.org/10.1103/PhysRevLett.108.111601). arXiv: [1111.5206](https://arxiv.org/abs/1111.5206) [hep-ph].
- [53] Federico Buccioni, Jean-Nicolas Lang, Jonas M. Lindert, Philipp Maierhöfer, Stefano Pozzorini, Hantian Zhang, and Max F. Zoller. “OpenLoops 2.” *Eur. Phys. J. C* 79.10 (2019), p. 866. DOI: [10.1140/epjc/s10052-019-7306-2](https://doi.org/10.1140/epjc/s10052-019-7306-2). arXiv: [1907.13071](https://arxiv.org/abs/1907.13071) [hep-ph].
- [54] A. van Hameren. “OneLOop: For the evaluation of one-loop scalar functions.” *Comput. Phys. Commun.* 182 (2011), pp. 2427–2438. DOI: [10.1016/j.cpc.2011.06.011](https://doi.org/10.1016/j.cpc.2011.06.011). arXiv: [1007.4716](https://arxiv.org/abs/1007.4716) [hep-ph].
- [55] Andrew Lifson. “Tree-Level NNLO QCD Corrections to $Z + H$ Production with H Decaying to $b\bar{b}$ and Leptonic Z Decay.” Semester project. June 2017.
- [56] Sandro Della Torre. “ VH +jet production at order α_s^2 .” MA thesis. ETH Zürich, May 2017.
- [57] “Search for $H^0 \rightarrow b\bar{b}$ or $c\bar{c}$ in association with a W or Z boson in the forward region of pp collisions” (Sept. 2016). URL: <http://cds.cern.ch/record/2209531>.
- [58] Andy Buckley, James Ferrando, Stephen Lloyd, Karl Nordström, Ben Page, Martin Rufenacht, Marek Schönherr, and Graeme Watt. “LHAPDF6: parton density access in the LHC precision era.” *Eur. Phys. J. C* 75 (2015), p. 132. DOI: [10.1140/epjc/s10052-015-3318-8](https://doi.org/10.1140/epjc/s10052-015-3318-8). arXiv: [1412.7420](https://arxiv.org/abs/1412.7420) [hep-ph].
- [59] J.A.M. Vermaseren, S.A. Larin, and T. van Ritbergen. “The four loop quark mass anomalous dimension and the invariant quark mass.” *Phys. Lett. B* 405 (1997), pp. 327–333. DOI: [10.1016/S0370-2693\(97\)00660-6](https://doi.org/10.1016/S0370-2693(97)00660-6). arXiv: [hep-ph/9703284](https://arxiv.org/abs/hep-ph/9703284).
- [60] D. de Florian et al. “Handbook of LHC Higgs Cross Sections: 4. Deciphering the Nature of the Higgs Sector” (2016). DOI: [10.23731/CYRM-2017-002](https://doi.org/10.23731/CYRM-2017-002). arXiv: [1610.07922](https://arxiv.org/abs/1610.07922) [hep-ph].

-
- [61] James Currie, Aude Gehrmann-De Ridder, Thomas Gehrmann, E. W. Nigel Glover, Alexander Huss, and João Pires. “Infrared sensitivity of single jet inclusive production at hadron colliders.” *JHEP* 10 (2018), p. 155. DOI: [10.1007/JHEP10\(2018\)155](https://doi.org/10.1007/JHEP10(2018)155). arXiv: [1807.03692](https://arxiv.org/abs/1807.03692) [hep-ph].
- [62] Federico Granata, Jonas M. Lindert, Carlo Oleari, and Stefano Pozzorini. “NLO QCD+EW predictions for HV and HV +jet production including parton-shower effects.” *JHEP* 09 (2017), p. 012. DOI: [10.1007/JHEP09\(2017\)012](https://doi.org/10.1007/JHEP09(2017)012). arXiv: [1706.03522](https://arxiv.org/abs/1706.03522) [hep-ph].
- [63] A. Gehrmann-De Ridder, T. Gehrmann, E. W. N. Glover, A. Huss, and T. A. Morgan. “Precise QCD predictions for the production of a Z boson in association with a hadronic jet.” *Phys. Rev. Lett.* 117.2 (2016), p. 022001. DOI: [10.1103/PhysRevLett.117.022001](https://doi.org/10.1103/PhysRevLett.117.022001). arXiv: [1507.02850](https://arxiv.org/abs/1507.02850) [hep-ph].
- [64] Aude Gehrmann-De Ridder, T. Gehrmann, E. W. N. Glover, A. Huss, and T. A. Morgan. “The NNLO QCD corrections to Z boson production at large transverse momentum.” *JHEP* 07 (2016), p. 133. DOI: [10.1007/JHEP07\(2016\)133](https://doi.org/10.1007/JHEP07(2016)133). arXiv: [1605.04295](https://arxiv.org/abs/1605.04295) [hep-ph].
- [65] A. Gehrmann-De Ridder, T. Gehrmann, E. W. N. Glover, A. Huss, and T. A. Morgan. “NNLO QCD corrections for Drell-Yan p_T^Z and ϕ^* observables at the LHC.” *JHEP* 11 (2016), p. 094. DOI: [10.1007/JHEP11\(2016\)094](https://doi.org/10.1007/JHEP11(2016)094). arXiv: [1610.01843](https://arxiv.org/abs/1610.01843) [hep-ph].
- [66] A. Gehrmann-De Ridder, T. Gehrmann, E. W. N. Glover, A. Huss, and D. M. Walker. “Next-to-Next-to-Leading-Order QCD Corrections to the Transverse Momentum Distribution of Weak Gauge Bosons.” *Phys. Rev. Lett.* 120.12 (2018), p. 122001. DOI: [10.1103/PhysRevLett.120.122001](https://doi.org/10.1103/PhysRevLett.120.122001). arXiv: [1712.07543](https://arxiv.org/abs/1712.07543) [hep-ph].
- [67] A. Gehrmann-De Ridder, T. Gehrmann, E.W.N. Glover, A. Huss, and D.M. Walker. “Vector Boson Production in Association with a Jet at Forward Rapidities.” *Eur. Phys. J. C* 79.6 (2019), p. 526. DOI: [10.1140/epjc/s10052-019-7010-2](https://doi.org/10.1140/epjc/s10052-019-7010-2). arXiv: [1901.11041](https://arxiv.org/abs/1901.11041) [hep-ph].
- [68] Gauld, R. “Flavour-tagging jets: from nature to fixed-order.” NNLOJET Internal Document. 2018.
- [69] Gauld, R., Majer, I. “Document summarising the method for flavour tagging.” NNLOJET Internal Document. 2018.
- [70] Majer, I. “Proposal for the Maple Workflow of Flavour Tagging.” NNLOJET Internal Document. 2018.

- [71] Roel Aaij et al. “Identification of beauty and charm quark jets at LHCb.” *JINST* 10.06 (2015), P06013. DOI: [10.1088/1748-0221/10/06/P06013](https://doi.org/10.1088/1748-0221/10/06/P06013). arXiv: [1504.07670](https://arxiv.org/abs/1504.07670) [hep-ex].
- [72] Georges Aad et al. “Performance of b -Jet Identification in the ATLAS Experiment.” *JINST* 11.04 (2016), P04008. DOI: [10.1088/1748-0221/11/04/P04008](https://doi.org/10.1088/1748-0221/11/04/P04008). arXiv: [1512.01094](https://arxiv.org/abs/1512.01094) [hep-ex].
- [73] A. M. Sirunyan et al. “Identification of heavy-flavour jets with the CMS detector in pp collisions at 13 TeV.” *JINST* 13.05 (2018), P05011. DOI: [10.1088/1748-0221/13/05/P05011](https://doi.org/10.1088/1748-0221/13/05/P05011). arXiv: [1712.07158](https://arxiv.org/abs/1712.07158) [physics.ins-det].
- [74] Michelangelo L. Mangano and Paolo Nason. “Heavy quark multiplicities in gluon jets.” *Phys. Lett.* B285 (1992), pp. 160–166. DOI: [10.1016/0370-2693\(92\)91316-2](https://doi.org/10.1016/0370-2693(92)91316-2).
- [75] Tim Adye. “Unfolding algorithms and tests using RooUnfold.” *Proceedings, PHYSTAT 2011 Workshop on Statistical Issues Related to Discovery Claims in Search Experiments and Unfolding, CERN, Geneva, Switzerland 17-20 January 2011*. CERN. Geneva: CERN, 2011, pp. 313–318. DOI: [10.5170/CERN-2011-006.313](https://doi.org/10.5170/CERN-2011-006.313). arXiv: [1105.1160](https://arxiv.org/abs/1105.1160) [physics.data-an].
- [76] Torbjörn Sjöstrand, Stefan Ask, Jesper R. Christiansen, Richard Corke, Nishita Desai, et al. “An Introduction to PYTHIA 8.2.” *Comput.Phys.Commun.* 191 (2015), pp. 159–177. DOI: [10.1016/j.cpc.2015.01.024](https://doi.org/10.1016/j.cpc.2015.01.024). arXiv: [1410.3012](https://arxiv.org/abs/1410.3012) [hep-ph].
- [77] Matteo Cacciari, Gavin P. Salam, and Gregory Soyez. “The anti- k_t jet clustering algorithm.” *JHEP* 04 (2008), p. 063. DOI: [10.1088/1126-6708/2008/04/063](https://doi.org/10.1088/1126-6708/2008/04/063). arXiv: [0802.1189](https://arxiv.org/abs/0802.1189) [hep-ph].
- [78] Andrea Banfi, Gavin P. Salam, and Giulia Zanderighi. “Accurate QCD predictions for heavy-quark jets at the Tevatron and LHC.” *JHEP* 07 (2007), p. 026. DOI: [10.1088/1126-6708/2007/07/026](https://doi.org/10.1088/1126-6708/2007/07/026). arXiv: [0704.2999](https://arxiv.org/abs/0704.2999) [hep-ph].
- [79] Roel Aaij et al. “First measurement of the charge asymmetry in beauty-quark pair production.” *Phys. Rev. Lett.* 113.8 (2014), p. 082003. DOI: [10.1103/PhysRevLett.113.082003](https://doi.org/10.1103/PhysRevLett.113.082003). arXiv: [1406.4789](https://arxiv.org/abs/1406.4789) [hep-ex].
- [80] Matteo Cacciari and Gavin P. Salam. “Dispelling the N^3 myth for the k_t jet-finder.” *Phys. Lett.* B641 (2006), pp. 57–61. DOI: [10.1016/j.physletb.2006.08.037](https://doi.org/10.1016/j.physletb.2006.08.037). arXiv: [hep-ph/0512210](https://arxiv.org/abs/hep-ph/0512210) [hep-ph].
- [81] Matteo Cacciari, Gavin P. Salam, and Gregory Soyez. “FastJet User Manual.” *Eur. Phys. J.* C72 (2012), p. 1896. DOI: [10.1140/epjc/s10052-012-1896-2](https://doi.org/10.1140/epjc/s10052-012-1896-2). arXiv: [1111.6097](https://arxiv.org/abs/1111.6097) [hep-ph].

-
- [82] M. Tanabashi et al. “Review of Particle Physics.” *Phys. Rev. D* 98 (3 Aug. 2018), p. 030001. DOI: [10.1103/PhysRevD.98.030001](https://doi.org/10.1103/PhysRevD.98.030001). URL: <https://link.aps.org/doi/10.1103/PhysRevD.98.030001>.
- [83] Lance J. Dixon. “Calculating scattering amplitudes efficiently.” *Theoretical Advanced Study Institute in Elementary Particle Physics (TASI 95): QCD and Beyond*. Jan. 1996, pp. 539–584. arXiv: [hep-ph/9601359](https://arxiv.org/abs/hep-ph/9601359).
- [84] Lance J. Dixon. “A Brief Introduction to Modern Amplitude Methods.” *Theoretical Advanced Study Institute in Elementary Particle Physics: Journeys Through the Precision Frontier: Amplitudes for Colliders*. 2015, pp. 39–97. DOI: [10.1142/9789814678766_0002](https://doi.org/10.1142/9789814678766_0002).
- [85] S.D. Badger, E.W.Nigel Glover, and Valentin V. Khoze. “Recursion relations for gauge theory amplitudes with massive vector bosons and fermions.” *JHEP* 01 (2006), p. 066. DOI: [10.1088/1126-6708/2006/01/066](https://doi.org/10.1088/1126-6708/2006/01/066). arXiv: [hep-th/0507161](https://arxiv.org/abs/hep-th/0507161).
- [86] D. Maitre and P. Mastrolia. “S@M, a Mathematica Implementation of the Spinor-Helicity Formalism.” *Comput. Phys. Commun.* 179 (2008), pp. 501–574. DOI: [10.1016/j.cpc.2008.05.002](https://doi.org/10.1016/j.cpc.2008.05.002). arXiv: [0710.5559](https://arxiv.org/abs/0710.5559) [hep-ph].
- [87] Jakub Kuczmarski. “SpinorsExtras - Mathematica implementation of massive spinor-helicity formalism.” June 2014. arXiv: [1406.5612](https://arxiv.org/abs/1406.5612) [hep-ph].
- [88] L.W. Garland, T. Gehrmann, E.W.Nigel Glover, A. Koukoutsakis, and E. Remiddi. “The Two loop QCD matrix element for $e^+ e^- \rightarrow 3$ jets.” *Nucl. Phys. B* 627 (2002), pp. 107–188. DOI: [10.1016/S0550-3213\(02\)00057-3](https://doi.org/10.1016/S0550-3213(02)00057-3). arXiv: [hep-ph/0112081](https://arxiv.org/abs/hep-ph/0112081).
- [89] Thomas Gehrmann and Lorenzo Tancredi. “Two-loop QCD helicity amplitudes for $q\bar{q} \rightarrow W^\pm\gamma$ and $q\bar{q} \rightarrow Z^0\gamma$.” *JHEP* 02 (2012), p. 004. DOI: [10.1007/JHEP02\(2012\)004](https://doi.org/10.1007/JHEP02(2012)004). arXiv: [1112.1531](https://arxiv.org/abs/1112.1531) [hep-ph].